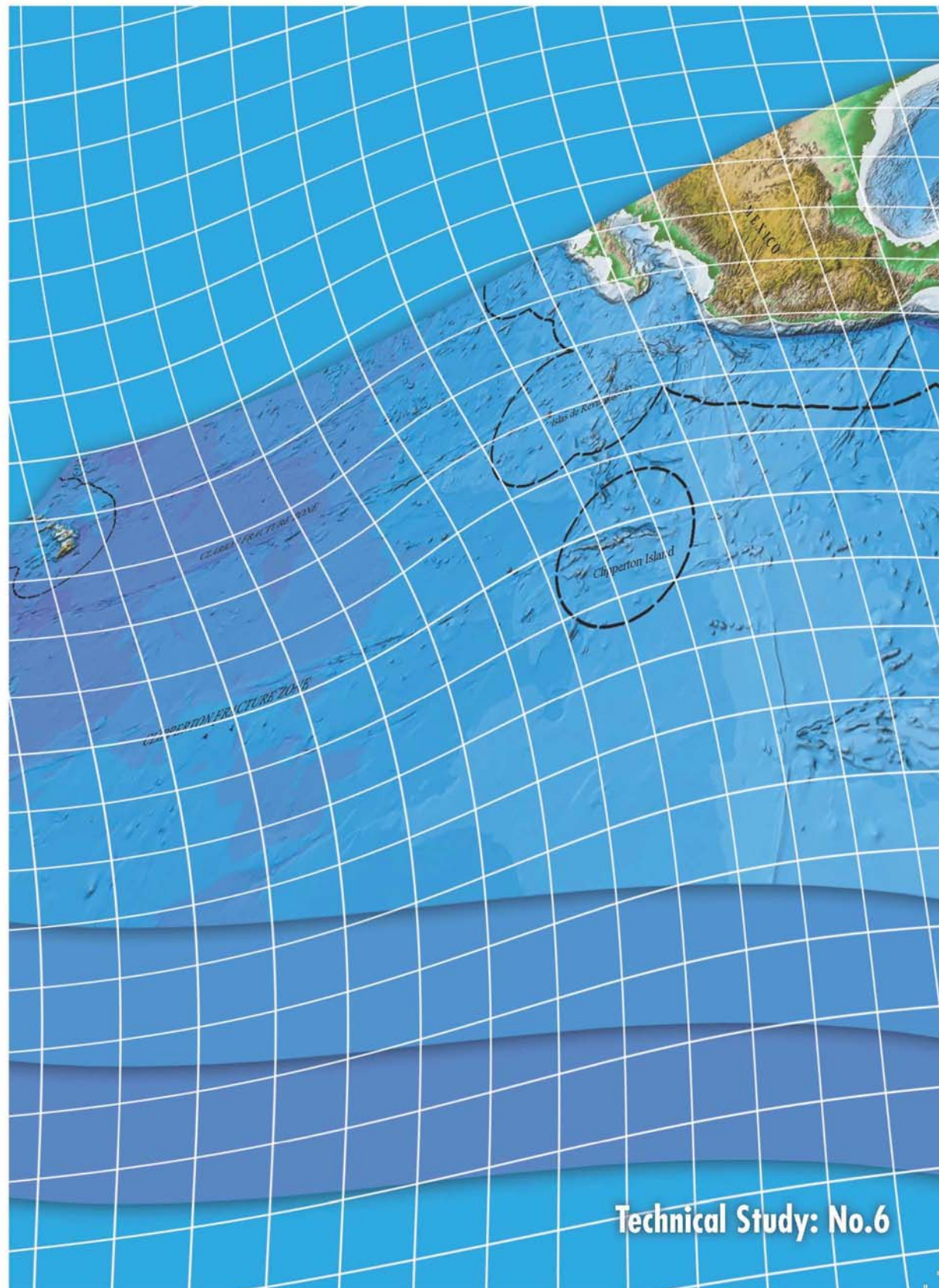




# A GEOLOGICAL MODEL OF POLYMETALLIC NODULE DEPOSITS IN THE CLARION CLIPPERTON FRACTURE ZONE



Technical Study: No.6

**A GEOLOGICAL MODEL OF  
POLYMETALLIC NODULE DEPOSITS IN THE  
CLARION-CLIPPERTON FRACTURE ZONE**

## ISA TECHNICAL STUDY SERIES

### *Technical Study No. 1*

Global Non-Living Resources on the Extended Continental Shelf: Prospects  
at the year 2000

### *Technical Study No. 2*

Polymetallic Massive Sulphides and Cobalt-Rich Ferromanganese Crusts:  
Status and Prospects

### *Technical Study No. 3*

Biodiversity, Species Ranges and Gene Flow in the Abyssal Pacific Nodule  
Province: Predicting and Managing the Impacts of Deep Seabed Mining

### *Technical Study No. 4*

Issues associated with the Implementation of Article 82 of the United  
Nations Convention on the Law of the Sea

### *Technical Study No. 5*

Non-Living resources of the Continental Shelf beyond 200 nautical miles:  
Speculations on the Implementation of Article 82 of the United Nations  
Convention on the Law of the Sea



# A GEOLOGICAL MODEL OF POLYMETALLIC NODULE DEPOSITS IN THE CLARION-CLIPPERTON FRACTURE ZONE

This report contains a summary of two documents – *A Geological Model of Polymetallic Nodule Deposits in the Clarion-Clipperton Fracture Zone* and a *Prospector's Guide* prepared under the project 'Development of a Geological Model of Polymetallic Nodule Deposits in the Clarion-Clipperton Fracture Zone, Pacific Ocean'.

ISA TECHNICAL STUDY: NO. 6

International Seabed Authority  
Kingston, Jamaica

The designation employed and the presentation of materials in this publication do not imply the expression of any opinion whatsoever on the part of the Secretariat of the International Seabed Authority concerning the legal status of any country or territory or of its authorities, or concerning the delimitation of its frontiers or maritime boundaries.

All rights reserved. No part of this publication may be reproduced, stored in a retrieval system, or transmitted in any form or by any means, electronic, mechanical, photocopying or otherwise, without the prior permission of the copyright owner. Application for such permission, with a statement of purpose and the extent of the reproduction, should be addressed to the International Seabed Authority, 14-20 Port Royal Street, Kingston, Jamaica.

**National Library of Jamaica Cataloguing-in-Publication Data**

International Seabed Authority

Development of geological models for the Clarion-Clipperton Zone polymetallic nodule deposits

p. ; ill., maps; cm. – (ISA technical study ; no.6)

ISBN: 978-976-95268-2-2 (pkb)

1. Oceanography. 2. Marine mineral resources.  
I. Title. II. Series

551.46 – dc 22

Copyright © International Seabed Authority 2010

International Seabed Authority

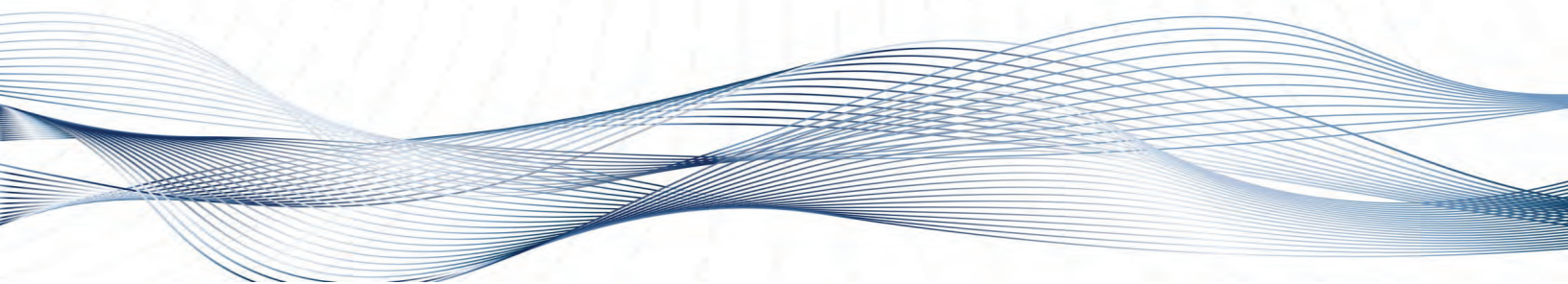
14-20 Port Royal Street

Kingston, Jamaica

Tel: (876) 9229105, Fax: (876) 9220195

URL: <http://www.isa.org.jm>

# EXECUTIVE SUMMARY



Polymetallic nodule resources contain nickel, cobalt, manganese and copper. While they occur in all oceans, deposits in the Clarion-Clipperton Fracture Zone (CCZ) are considered to be among the richest, containing high grade and high abundance nodules. Presently, seven of the eight exploration contractors with the International Seabed have exploration contracts in this area. As part of its mandate to conduct resource assessments of prospective mineral deposits in the Area, the Authority met with representatives of the seven contractors to discuss ways of improving the results of resource assessments of polymetallic nodule deposits in the CCZ. In the absence of sampling data across much of this vast geographic area, participants in the meeting suggested that if the suspected relationships between high nodule grade and abundance, and factors such as sediments, volcanism, topography and Primary Productivity etc. could be established, they could be used as proxies for grade and abundance in poorly sampled nodulized areas. They therefore recommended that the Authority should establish a geologic model of polymetallic nodule deposits in the CCZ. At the ninth session of the Authority, its Legal and Technical Commission, recognizing that such a model would be useful for prospectors, contractors and the Authority, endorsed this cause of action. Between 13 and 20 May 2003, the Authority convened a workshop in Nadi, Fiji to consider the data that could be taken into account to develop such a model. It identified candidate proxy variables and devised a programme for the development of the model and a Prospector's guide.

Taking into account the results of the Fiji workshop, the seven member Group of Technical Experts identified the approach that it would use to generate the model, specified the proxy data that would be tested for use in predicting nodule grade and abundance, and devised a programme of work over a thirty month period to complete the work. The programme commenced in the 2005-2006 biennium. The area of interest for this study is 110° - 160° W Longitude and 0° - 20° North Latitude. Five different data sets of polymetallic nodule abundance and metal content are used in the modeling work, including both publicly available and proprietary data sets.

The Authority served as the link between the contractors, their scientists and the Group of Technical Experts for the development of the Geological Model of polymetallic nodule deposits in the CCZ and Prospector's Guide. It set up a closed ftp site for the use of the consultants and contractor scientists (project members). It also uploaded to the ftp site all the data, reports and other related notes concerning the project and made them accessible to all project members.

The Authority regularly monitored the progress of the project by evaluating the interim reports and facilitating the resolution of any matters that arose during project implementation. The Authority conducted a mid-course review of the programme at the East-west Centre, Hawaii during

October 2006. At the mid-term review meeting, the consultants and the Secretariat discussed the progress of the work under the project and the future course of action to complete it. To facilitate the project's completion and undertake a final review of the model and prospector's guide tasks were reassigned to the team members.

The primary products from the effort are (1) a Geological Model of polymetallic nodule deposits in the CCZ and (2) a Prospector's Guide containing a narrative description of the key factors relevant to exploration for polymetallic nodules in the CCZ, including data and available information on known deposits. Both reports have been completed and reviewed by the Authority and by the contributing consultants. They were further reviewed during a workshop on the matter at the Authority during December 2009. This technical study provides concise version of the two products. The contents and main results from the reports are presented in the following paragraphs.

## 1. Geological Model of polymetallic nodule deposits in the CCZ

In this report, the results of three independent approaches to establishing a Geological Model for CCZ polymetallic deposits are presented. No undisclosed or proprietary algorithms are used so that the Model can be subject to peer review in the short term and available for updating as better data or better algorithms become available.

### i. PRIMARY RESOURCE DATA SET

The area of interest for this study is 110° - 160° W Longitude and 0° - 20° North Latitude. Five different data sets of polymetallic nodule abundance and metal content are used in the modeling work, including both publicly available and proprietary data sets. The methods used to produce this integrated data set and its basic characteristics are described in the report.

In order to preserve the spatial information inherent in these data while accommodating the proprietary concerns of the data owners, the data were assembled into groups representing all data collected within a defined grid with dimensions of one-tenth of a degree of both longitude and latitude. For each grid block where data are available, the data values are averaged. For each resource parameter (abundance and metal content), the number of stations within the grid bounds, mean, minimum, and maximum values, and, where at least three stations are present, the standard deviation of the values are reported. The report presents the interpolated maps generated for the abundance and the metal values.

### ii. INFERRRED RESOURCES

Several methods of estimating the quantities of polymetallic nodules and contained metals within portions of the study area were utilized. These methods range from interpolations made using standard kriging methods to extrapolations from the existing data to predict quantities outside of the areas covered by the available data. Table 1 lists representative values of these estimates. The first three rows of this table are derived from different interpolation schemes, while the last row uses extrapolations based on predictions from a linear regression model that uses specific proxy variables to predict metal content in the CCZ where no data are available.

**Table 1. Inferred resources**

| Source                                    | <i>Included<br/>Area (km<sup>2</sup> X<br/>10<sup>6</sup>)</i> | <i>Estimated Tons (metric tons X 10<sup>6</sup>)</i> |        |       |      |      |
|---|--|--|--------|-------|------|------|
|   |  | Nodules  | Mn     | Co    | Ni   | Cu   |
| <b>Total study area</b>                   | 4.19   | 30,700   | 8,657* | 67.5* | 393* | 341* |
| <b>Reduced area</b>                       | 3.83   | 21,100   | 5,950* | 46.4* | 270* | 234* |
| <b>Biogeochemical<br/>model</b>           | 4.85   | 27,100   | 7,300  | 58.0  | 340  | 290  |
| <b>Potential resources<br/>of nodules</b> | 12.57  | 62,000   | 17,500 | 134.0 | 761  | 669  |

\*Estimated using mean metal content values

### iii. BIOGEOCHEMICAL MODELING

The model presented here predicts the geographical distribution of the metal content of nodules (Mn, Co, Ni, Cu, and Ni concentrations) and abundance (kilograms of ore deposits per square meter of seafloor) using as model components the values of other, known variables, including chlorophyll concentrations in surface waters, distance from the East Pacific Rise, and Carbonate Compensation Depth (CCD).

The primary sources of metals for the nodule deposits of the CCZ are terrigenous or volcanogenic sources on the North and Central American continents and the East Pacific Rise. The metals are adsorbed to the surfaces of fine-grained sediments and carried westward by the North Pacific Current. The sediments are consumed by filter-feeding zooplankton en route and converted into silt-and sand-sized fecal matter that are large enough to sink to the seafloor in the deep tropical Pacific waters. These fecal pellets can then be metabolized by benthic animal communities and bacterial processes after they reach the sea floor, processes that remove the organic materials that bind the metals and reduce them to cationic species that are readily absorbed by the anionic manganese oxide matrix that constitutes the bulk of these deposits.

### iv. SPATIAL DECISION SUPPORT SYSTEM MODELING

Spatial Decision Support System (SDSS) modeling was employed to estimate the mineralization potential in selected areas of the CCZ where nodule abundance and metal content data are not available. The study is based on data sets that include bathymetry, topography, sediment type, CCD, and surface chlorophyll. Specific techniques employed in the study include Weights of Evidence Modeling, Fuzzy Logic, Logistic Regression and Artificial Neural Network (ANN) techniques. The results of this work provide differing assessments of the spatial distribution of areas within the study area where the occurrence of nodule deposits is likely. The results consistently indicate that better prospects can be found in the center and northern parts of the CCZ, while the southern, southwestern and eastern parts of the CCZ are likely to be unfavorable for nodule deposit

occurrence. Likely prospects of nodule occurrence in CCZ from Weights of Evidence Modeling, Logistic Regression and from Fuzzy Logic are shown in Figures 27, 28 and 29. Future explorers might expect to get better results from exploration efforts that focus on the center and northern areas of the CCZ than the southern, southwestern, or eastern area.

## 2. The Prospector's Guide

Included in this report are the results of nine independent studies that provide extensive geophysical, geological, oceanographic, and biological information related to the CCZ deposits and general guidance, based on many years of study of these deposits, of why these deposits occur where they do and criteria for seeking undiscovered deposits elsewhere.

### i. *GRIDDED BATHYMETRY OF THE CCZ*

The seafloor of the CCZ lies mostly between 4,000 and 6,000 meters water depth. The seafloor is characterized by a number of seamounts, some of which reach depths of less than 3,000 meters. The wide-spread seafloor spreading fabric, oriented approximately orthogonal to the trend of the bounding fracture zones, provides a large number of flat floored valleys, separated by irregular, often discontinuous ridges a few hundred meters high. The study used the Smith and Sandwell data set as the base map and incorporated proprietary data and paper maps from ISA Contractors to derive a series of bathymetric grids of the CCZ at resolutions of 1, 0.5 and 0.1 minutes of latitude and longitude. These data files are available at the ISA's Central Data Repository.

### ii. *VOLCANIC, TECTONIC, AND SEDIMENTARY FACTORS*

This study provides an analysis of the maps of volcanic and tectonic structural elements of the CCZ. The objective is to estimate the possible influences of static factors, (i.e. bathymetry, geomorphology, tectonic structure, and lithology), and dynamic factors (i.e. dynamic geological events such as tectonic movements and volcanogenic, hydrothermal, sedimentary, and erosive processes) on the growth of polymetallic nodules in the CCZ.

The bathymetric characteristics within the CCZ follow a pronounced order, most commonly consisting of trends that line up with the overall movement of the Pacific Plate and trends perpendicular to this direction. Generally, water depths and crustal age increase with distance from the East Pacific Rise (EPR). Recent seismic activity in the region has been also aligned with or perpendicular to the plate motion, suggesting that it is caused by strike-slip and normal faulting associated with the relief of stress caused by the rifting of the Pacific Plate to the northwest

The sediment facies exhibit a unidirectional gradient perpendicular to the fracture zones, trending from predominant carbonate sediments in the southeastern extreme to predominant siliceous red clay in the west-northwest. There are also regional-scale non-conformities, including latitudinal zonation of a variety of young (Pleistocene-Holocene) sediment facies; and a pronounced surface unconformity of Middle Miocene age, denoting an interruption in the sediment accumulation, dislocation and erosion of the earlier accumulated sediments

Analysis of the spatial distribution of nodule abundance and metal concentration suggests an axial line of maximum abundance that is approximately parallel to and midway between the

bounding fracture zones. The spatial distribution of metal content is different. The Manganese to Iron ratio clearly increases from north to south, while, less distinct, it decreases from east to west. These observations suggest that volcanogenic-hydrothermal activity of the EPR is one of the main sources of the ore components, which, finally, are included in manganese nodule composition as the result of complicated processes of dispersion and transportation to the bottom in dissolved and organic-fixed forms.

*iii. GROWTH MODEL FOR POLYMETALLIC NODULES*

Polymetallic nodules are composed of both nuclei and concentric layers of iron and manganese hydroxides. Generally, according to their morphology, size and texture etc., polymetallic nodules are classified into three types: S-type (Smooth type), R-type (Rough type) and S-R-type (Smooth-Rough mixed type). They generally grow very slowly, at rates of 1-10 mm per 10<sup>6</sup> yr. Six factors are believed to be important to nodule formation. These factors are:

- a. Supply of metals to growing surface;
- b. Presence of nucleus;
- c. The corrosive and erosive forces caused by benthic currents of the Antarctic Bottom water;
- d. Occurrence of semi-liquid surface layer on the seafloor ( sediment water interface);
- e. Bioturbation; and
- f. Internal Stratigraphy of individual nodules.

*iv. NODULE COVERAGE, MORPHOLOGY, AND DISTRIBUTION IN THE EASTERN CCZ*

In order to understand the nodule distribution within this study area, an analysis was made to determine the correlations among such nodule parameters as coverage, abundance, morphology, size, genetic type, and the water depth, bottom morphology, and geographic region. A classification system for nodule morphology and formation mechanism separates hydrogenetic from diagenetic nodules, and isolates different morphological types (discoidal, spheroidal, etc.).

Throughout the eastern part of the CCZ diagenetic, discoidal and ellipsoidal nodules are the dominant types. In the areas of highest nodule abundance, nodules with multiple nuclei are the most common morphology. The highest percentages of seafloor covered by nodules are found in water depths between 4,100 – 4,200 m, and the highest abundance values are found between 12° to 16° N latitude.

*v. SEDIMENTS IN THE EASTERN CCZ*

A detailed examination of bathymetry and sediment distribution and composition in the eastern CCZ was carried out. The topography of the area is characterized by NW-SE to NNW-SSE trending elongated seabed structures. Two predominant acoustic reflectors delineate Miocene and Oligocene unconformities. The surface sediments consist of Pleistocene-Holocene siliceous silty clay and ooze underlain by Miocene to Pliocene pelagic clay, zeolitic clay and zeolitic crust and hiatuses of Paleo-Pleistocene and Late Miocene ages. The ocean floor is a hilly plain - plateau, crossed by a strictly north-south system of horst and graben structures. The surface relief of this hilly plain is generally less than 100 m in extent, with hills and ridges exceeding 100 m in plains.

The most common sediment types in this region include reddish brown clay zeolitic clay (less than 5% amorphous silica content), slightly siliceous (with 5-10% amorphous silica content), siliceous (10-30% amorphous silica content) silty clay as well as slightly calcareous (5-10% CaCO<sub>3</sub> content) and calcareous (10-30% CaCO<sub>3</sub> content) silty clay. The uppermost part of the sediment profile features predominantly siliceous, silty clay, which, down core grades into slightly siliceous, silty clay. Calcareous, silty clay and calcareous oozes are observed only in the southern part of the study area. Metal contents in these sediments generally follow the trend of decreasing concentrations- Fe > Mn > Cu > Ni > Zn > Co

vi. *NODULE GENESIS & SEDIMENT DISTRIBUTION IN KOREA'S ALLOCATED AREA*

Nodule genesis and growth are affected by many environmental factors, especially (1) supply of biogenic, terrigenous and hydrogenetic material to the sediment and to the nodules; (2) deposition and reworking of sediments due to seafloor morphology; (3) bottom water composition and movement; and (4) bioturbation. The northern block (KR2) is characterized by relatively high nodule abundance, low Mn/Fe ratios, low Cu and Ni content, and high Fe and Co content. With regard to morphologies, poly-nucleated and irregular-shaped nodules are dominant. With regard to texture, smooth and transitional types between smooth and rough are abundant. All these characteristics indicate that the hydrogenetic process has dominated the diagenetic process one in the northern block. Taking account of the relatively slow growth rate of hydrogenetic nodules, the presence of smaller nodules in the northern block is consistent with other chemical, morphological, and textural characteristics of nodules.

In contrast with the northern block, the southern block (KR5) is characterized by relatively low nodule abundances, high Mn/Fe ratio, Cu, and Ni, and low Fe and Co contents. Differing from the northern block, rough-surface and dimorphic (rough on one side, smooth on the other), discoidal and ellipsoidal nodules are the dominant morphological and textural nodule types in the southern block. All these characteristics indicate that diagenetic processes have dominated hydrogenetic processes in the southern block

The sediments in the study area consist of three major lithological units: Units 1, 2, and 3, which are distinctive in color and textures. Unit 1 comprises the topmost layer and varies in colour from dark grayish brown to dark brown. It is homogenous mud and characterized by a very high water content with dominant occurrences of quartz and illite. Unit 2 lies below or alternates with Unit 1 in most cores. It consists of yellowish brown to brown colored mud and includes lots of burrows filled with overlying Unit 1 sediments. Burrow densities decrease with depth. Unit 3 is overlain by Unit 2 in most cores where it occurs and varies in colour from very dark brown to black color. Both Units 2 and 3 contain abundant smectite minerals. Sedimentation rates for all units are estimated to be near 0.1 mm/1,000 yr.

The distribution of different nodule genetic types in the northern and southern blocks can be explained by topography and sedimentation rate. It is known that hydrogenetic nodules are formed preferentially in areas with high topographic variation and low sedimentation rates, consistent with dominant nodule types and geological settings found in the northern block. Diagenetic nodules are known to be formed preferentially in flat abyssal areas with high sedimentation rates. The southern block has a geological setting more favourable to diagenetic nodule formation than the northern block.

*vii. BATHYMETRY AND SEDIMENTATION IN THE COMRA CONTRACT AREA.*

The area explored includes two non-contiguous portions, an east area and a west area. Water depth in the east area ranges from 3,901.8 m to 5,590.7 m. The west area ranges in depth from 2,969.1 m to 5,986.6 m. The area deeper than 5,300 m in water depth covers about 8.5% of the east area and about 11% of the west area. Water depth in the COMRA area, in both portions of the area, is mostly between 5,000 m to 5,300 m. There are generally four types of sediments in the surface layer of the seafloor of the COMRA area, including siliceous clay, siliceous ooze, siliceous-calcareous ooze and calcareous ooze. Siliceous sediments are the most abundant sedimentary types in the east area. Siliceous clay covers 72% of the area and siliceous ooze 22%. Siliceous clay is mainly distributed in abyssal hills and plains with an average water depth of 5,096 m. Siliceous ooze is mostly distributed in transitional areas between siliceous clay and calcareous ooze in the southeastern part of the east area. Calcareous sediment is limited to seamounts in southeastern and western parts of the east area. In general, calcareous sediments confined to the tops of seamounts, while the siliceous sediments cover the lower regions.

*viii. REGIONAL EXAMINATION OF SEDIMENTS.*

Data sets were provided to the study by three contractors in the Area, the French contractor (IFREMER), the Chinese contractor (COMRA), and the multi-national consortium IOM. In addition, publicly available sediment data within the CCZ study area were downloaded from the U.S. National Geophysical Data Center (NGDC). In order to investigate the relationships between sediment types, and nodule abundance and metal content, sediment types for each of the 0.1° grid points where nodule data are available were interpolated. The average metal content and abundance for each sediment type represented in the data set were then calculated. The results generally confirm the qualitative conclusions noted by scientists for many years, that the highest abundances of nodules occur in the siliceous sediments and not in the calcareous sediments. However, somewhat surprisingly it was derived that siliceous, calcareous mud host the highest abundances, and the siliceous oozes have surprisingly low abundances.

*ix. BENTHIC BIOLOGICAL DATA FROM THE CCZ*

A number of research programmes have sampled the abyssal North Pacific Ocean seafloor, and collected data for multiple parameters of interest to biogeochemical modeling efforts. Overall, meiofaunal (63-300 µm) and macrofaunal (300 µm-3 mm) abundances and/or biomass represent the most widely sampled biological parameters in this region, and these data sets also exhibit the greatest consistency in collection methods across field programmes. Preliminary examination of the data indicates that, in general, the abundance of these benthic fauna is roughly proportional to the flux of nutrients available in particles settling from the surface.

### 3. List of Contributors

|                      |  |
|----------------------|--|
| Dr Charles Morgan    | Planning Solutions Inc. Honolulu, Hawaii USA |
| Dr Ryszard Kotlinski | InterOcean Metal Joint Organization, Poland  |
| Dr Valcana Stoynova  | InterOcean Metal Joint Organization, Poland  |
| Dr H Zhou            | COMRA (Tongji University, China)             |
| Dr Wenzheng Lu       | COMRA  |
| Dr Ning Zhou         | COMRA  |
| Dr Deping Li         | COMRA  |
| Dr V Yubko           | Yuzmorgeologia, Russian Federation           |
| Dr Lindsay Parson    | Southampton Oceanographic Institute, UK      |
| Dr Peter M. Hunter   | Southampton Oceanographic Institute, UK      |
| Dr Craig Smith       | University of Hawaii, USA                    |
| Ms Sarah Mincks      | University of Hawaii, USA                    |
| Dr Jung-Keuk Kang    | KORDI, Republic of Korea                     |
| Dr Kiseong Hyeong    | KORDI, Republic of Korea                     |
| Dr Cheong-Kee Park   | KORDI, Republic of Korea                     |
| Dr Young Tak Ko      | KORDI, Republic of Korea                     |
| Dr Jonguk Kim        | KORDI, Republic of Korea                     |
| Mr Seungjin Yang     | KORDI, Republic of Korea                     |
| Dr D S Cronan        | Imperial College London                      |
| Dr Yuri Kazmin       | SEVERNEFTEGAS, Russian Federation            |
| Dr M Hoffert         | University of Strasbourg France              |



A GEOLOGICAL MODEL OF  
POLYMETALLIC NODULE DEPOSITS IN THE  
CLARION-CLIPPERTON FRACTURE ZONE



# TABLE OF CONTENTS

|   |           |
|---|-----------|
| <i>List of Tables</i>   | xviii     |
| <i>List of Figures</i>  | xix       |
| <b>1. INTRODUCTION</b>  | <b>1</b>  |
| 1.1 Background and Objectives   | 1         |
| <b>2. SUMMARY</b>   | <b>3</b>  |
| 2.1 Introduction  | 3         |
| 2.2 Primary Resource Data Set   | 3         |
| 2.3 Inferred Resources  | 4         |
| 2.4 SDSS Modelling  | 5         |
| <b>3. PRIMARY RESOURCE DATA SET</b>   | <b>6</b>  |
| 3.1 Original Data Sets  | 6         |
| 3.2 Tenth Degree Grid Data  | 8         |
| <b>4. GEOGRAPHIC INFORMATION SYSTEM AND GEOSTATISTICAL APPRAISAL<br/>OF RESOURCE POTENTIAL</b>  | <b>10</b> |
| 4.1 Introduction  | 10        |
| 4.2 Theory  | 11        |
| 4.3 Materials and Methods   | 11        |
| 4.3.1 Sites and Data Sets   | 11        |
| 4.3.2 Methods   | 15        |
| 4.4 Results   | 16        |
| 4.4.1 Resource Estimation Using ArcGIS  | 16        |
| 4.4.2 Resource Rstimation Using GSLIB   | 20        |
| <b>5. BIOGEOCHEMICAL MODEL OF THE MANGANESE, COPPER AND NICKEL<br/>CONTENT IN POLYMETALLIC NODULES IN THE CLARION-CLIPPERTON ZONE</b> | <b>24</b> |
| 5.1 Background and Organization   | 24        |
| 5.2 Kriging Methods and Results   | 24        |
| 5.3 Propagation of Errors   | 25        |
| 5.4 Hypothesis  | 25        |
| 5.5 Proxy Variables   | 28        |
| 5.5.1 Chlorophyl (Chlor)  | 28        |
| 5.5.2 Distance from East Pacific Rise and North American Continental<br>Slope ( $F_{epr}$ )   | 29        |

|           |  |           |
|-----------|--|-----------|
| 5.5.3     | Distance from CCD (del)  | 30        |
| 5.6       | Procedures   | 31        |
| 5.7       | Results  | 32        |
| 5.7.1     | Manganese  | 32        |
| 5.7.2     | Nickel   | 33        |
| 5.7.3     | Copper   | 33        |
| 5.8       | Predicted Metal Content  | 34        |
| 5.9       | Discussion and Conclusions   | 36        |
| <b>6.</b> | <b>SPATIAL DECISION SUPPORT SYSTEM MODELING</b>                    | <b>37</b> |
| 6.1       | Introduction   | 37        |
| 6.2       | Data Used in the Study   | 37        |
| 6.2.1     | Nodule Abundance and Metal Content                                 | 37        |
| 6.2.2     | Sediment Types   | 38        |
| 6.2.3     | Primary Productivity   | 39        |
| 6.2.4     | CCD Minus Water Depth  | 39        |
| 6.2.5     | Regional Bathymetric Regimes                                       | 40        |
| 6.3       | Theory   | 40        |
| 6.4       | Input Data Used in the SDSS Models                                 | 41        |
| 6.4.1     | Grid Cells   | 41        |
| 6.4.2     | Input Data, Weights of Evidence and Logistic Regression            | 41        |
| 6.4.3     | Input Data, Fuzzy Logic and Radial Basis Function Network Modeling | 42        |
| 6.5       | Modeling Results   | 43        |
| 6.5.1     | Weights of Evidence  | 43        |
| 6.5.2     | Logistic Regression  | 46        |
| 6.5.3     | Fuzzy Logic  | 47        |
| 6.5.4     | Radial Basis Function Network                                      | 48        |
| 6.6       | Maps of Potential Nodule Resource Areas                            | 49        |

|           |                         |           |
|-----------|-------------------------|-----------|
| <b>7.</b> | <b>REFERENCES CITED</b> | <b>52</b> |
| <b>8.</b> | <b>APPENDICES</b>       | <b>55</b> |
| 8.1       | Resource Maps           | 55        |
| 8.1.1     | Abundance               | 56        |
| 8.1.2     | Manganese               | 60        |
| 8.1.3     | Cobalt                  | 64        |
| 8.1.4     | Nickel                  | 68        |
| 8.1.5     | Copper                  | 72        |

## LIST OF TABLES

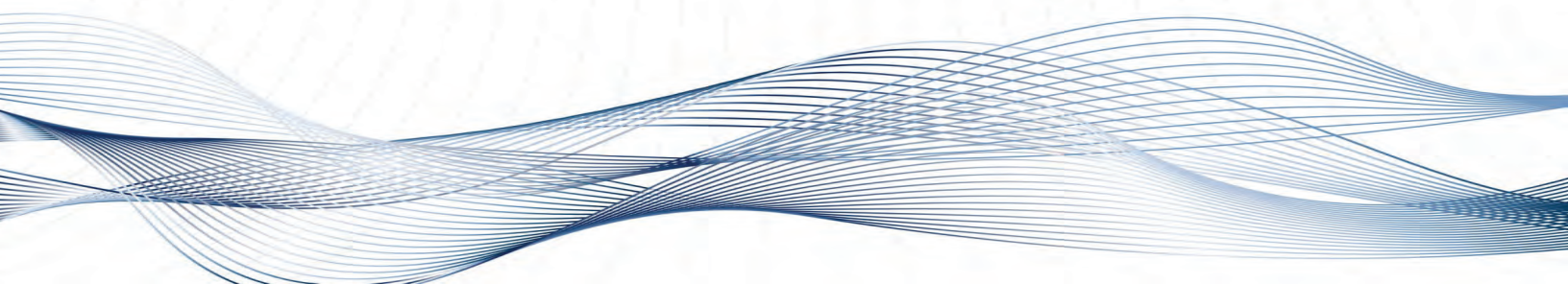
|          |  |    |
|----------|--|----|
| Table 1  | Inferred Resources in the Study Area                                   | 4  |
| Table 2  | Data Screening, Criteria for Elimination                               | 7  |
| Table 3  | Source Data for Resource Assessment (Screened Data)                    | 8  |
| Table 4  | Screened Data Set Elementary Statistics                                | 8  |
| Table 5  | Grid Data Elementary Statistics  | 9  |
| Table 6  | Statistics of Individual Blocks Used in this Study                     | 12 |
| Table 7  | Statistics for Total Study Area  | 18 |
| Table 8  | Statistics for ISA-1 Block   | 18 |
| Table 9  | Statistics for ISA-2 Block   | 18 |
| Table 10 | Statistics for ISA-3 Block   | 19 |
| Table 11 | Statistics for ISA-4 Block   | 19 |
| Table 12 | Polymetallic Nodule Tonnage Estimates in Total Study Area              | 19 |
| Table 13 | Polymetallic Nodule Tonnage Estimates in Reduced Area                  | 20 |
| Table 14 | Resource Assessment Summary of Results                                 | 25 |
| Table 15 | Manganese Regression Model Results                                     | 33 |
| Table 16 | Nickel Regression Model Results  | 33 |
| Table 17 | Copper Regression Model Results  | 34 |
| Table 18 | Comparison of R <sup>2</sup> Values Between Metals                     | 36 |
| Table 19 | Binary Transformations for Weights of Evidence and Logistic Regression | 42 |
| Table 20 | Transformations for Fuzzy Logic and Radial Basis Network Modeling      | 43 |
| Table 21 | Calculated Results from Weights of Evidence Modeling                   | 44 |
| Table 22 | Calculated Regression Coefficients, Logistical Regression              | 49 |

# LIST OF FIGURES

|           |   |    |
|-----------|---|----|
| Figure 1  | Clarion-Clipperton Zone (CCZ) Study Area (Sandwell, 2000)               | 10 |
| Figure 2  | Station Map, Showing Blocks Used in this Study                          | 11 |
| Figure 3  | Abundance Distributions within the four Blocks (ISA-1 and ISA-2)        | 13 |
| Figure 4  | Abundance Distributions within the four Blocks (ISA-3 and ISA-4)        | 14 |
| Figure 5  | Nodule Abundance, Entire Study Area (ArcGIS Software)                   | 16 |
| Figure 6  | Abundance, Individual Block Values, ArcGIS Software                     | 17 |
| Figure 7  | Analysis Blocks Used in Study Showing 0.1° Cells                        | 20 |
| Figure 8  | Abundance, Individual Block Values, GSLIB Kriging                       | 21 |
| Figure 9  | Predicted Abundance Distribution, SIS Realization 1                     | 22 |
| Figure 10 | Predicted Abundance Distribution SIS Realization 2                      | 22 |
| Figure 11 | Predicted Abundance Distribution, SIS Realization 3                     | 23 |
| Figure 12 | General Formation Model   | 26 |
| Figure 13 | Hypothesized Optimum Level of Biological Productivity for Nodule Growth | 28 |
| Figure 14 | Chlorophyll in Surface Waters of the Clarion-Clipperton Region          | 29 |
| Figure 15 | Points on East Pacific Rise and Coastal Shelf Used in Modeling          | 30 |
| Figure 16 | Water Depth minus CCD (del) in the Clarion-Clipperton Zone              | 31 |
| Figure 17 | Histograms of Proxy Variables   | 32 |
| Figure 18 | Predicted Mn Content in the CCZ   | 34 |
| Figure 19 | Predicted Ni Content in the CCZ   | 35 |
| Figure 20 | Predicted Cu Content in the CCZ   | 35 |
| Figure 21 | Distribution of Nodule Abundance in the CCZ                             | 38 |
| Figure 22 | Distribution of Seafloor Sediment Types in the CCZ                      | 38 |
| Figure 23 | Surface Chlorophyll Levels in the CCZ                                   | 39 |
| Figure 24 | Distribution of the value of the CCD minus water depth                  | 39 |
| Figure 25 | Bathymetric Regimes in the CCZ  | 40 |
| Figure 26 | Grid Cell Specification in the CCZ                                      | 41 |
| Figure 27 | Weights of Evidence Results, Posterior Probabilities in the CCZ         | 45 |
| Figure 28 | Logistic Regression Results, Posterior Probabilities in the CCZ         | 47 |
| Figure 29 | Fuzzy Logic Results, Combined Membership Function Values in the CCZ     | 48 |
| Figure 30 | RBF Network Modeling, Favorability for Deposit Occurrence in the CCZ    | 48 |
| Figure 31 | Prospects for Nodule Occurrence, Weights of Evidence Modeling           | 50 |
| Figure 32 | Prospects for Nodule Occurrence, Logistic Regression                    | 50 |
| Figure 33 | Prospects for Nodule Occurrence, Fuzzy Logic                            | 51 |
| Figure 34 | Prospects for Nodule Occurrence, Radial Basis Factor Network            | 51 |
| Figure 35 | Abundance (kg/m <sup>2</sup> ): Original Data Locations and Values      | 56 |
| Figure 36 | Abundance (kg/m <sup>2</sup> ): Grid Block Data Locations and Values    | 57 |
| Figure 37 | Abundance (kg/m <sup>2</sup> ): Original Data, Interpolated Contours    | 58 |
| Figure 38 | Abundance (kg/m <sup>2</sup> ): Grid Block Data, Interpolated Contours  | 59 |
| Figure 39 | Manganese (Dry weight percent): Original Data Locations and Values      | 60 |
| Figure 40 | Manganese (Dry weight percent): Grid Block Data Locations and Values    | 61 |
| Figure 41 | Manganese (Dry weight percent): Original Data Interpolated Contours     | 62 |
| Figure 42 | Manganese (Dry weight percent): Grid Block Data Interpolated Contours   | 63 |
| Figure 43 | Cobalt (dry weight percent): Original Block Data Locations and Values   | 64 |

|           |   |    |
|-----------|---|----|
| Figure 44 | Cobalt (dry weight percent): Grid Block Data Locations and Values   | 65 |
| Figure 45 | Cobalt (dry weight percent): Original Data Interpolated Contours    | 66 |
| Figure 46 | Cobalt (dry weight percent): Grid Block Data Interpolated Contours  | 67 |
| Figure 47 | Nickel (dry weight percent): Original Data Locations and Values     | 68 |
| Figure 48 | Nickel (dry weight percent): Grid Block Data Locations and Values   | 69 |
| Figure 49 | Nickel (dry weight percent): Original Data, Interpolated Contours   | 70 |
| Figure 50 | Nickel (dry weight percent): Grid Block Data, Interpolated Contours | 71 |
| Figure 51 | Copper (dry weight percent): Original Data Locations and Values     | 72 |
| Figure 52 | Copper (dry weight percent): Grid Block Data Locations and Values   | 73 |
| Figure 53 | Copper (dry weight percent): Original Data Interpolated Contours    | 74 |
| Figure 54 | Copper (dry weight percent): Grid Block Data Interpolated Contours  | 75 |

# 1. INTRODUCTION



## 1.1 Background and Objectives

Submarine ferromanganese concretions were first discovered in the Kara Sea off Siberia in 1868 (Earney, 1990). In the course of its round-the-world expedition from 1873 to 1876, HMS *Challenger* collected many small dark-brown balls, rich in manganese and iron, which were named manganese nodules (Murray and Reynard, 1891; Manheim, 1978; Earney, 1990). Since the 1960s, manganese nodules have been recognized as a potential source of nickel, copper, cobalt, and manganese, which are likely to assume increasing importance as land-based deposits of these metals become depleted.

Manganese nodules are found on the seabed in many areas, and have been comparatively well studied because of their potential economic importance (Mero, 1965). The Clarion-Clipperton Fracture Zone (CCZ), the study area for this project, has been the focus of much international attention for many years (Mero, 1965; McKelvey *et al.*, 1979; Bernhard and Blissenbach, 1988). To date, the greatest concentrations of nodule deposits have been found in this region.

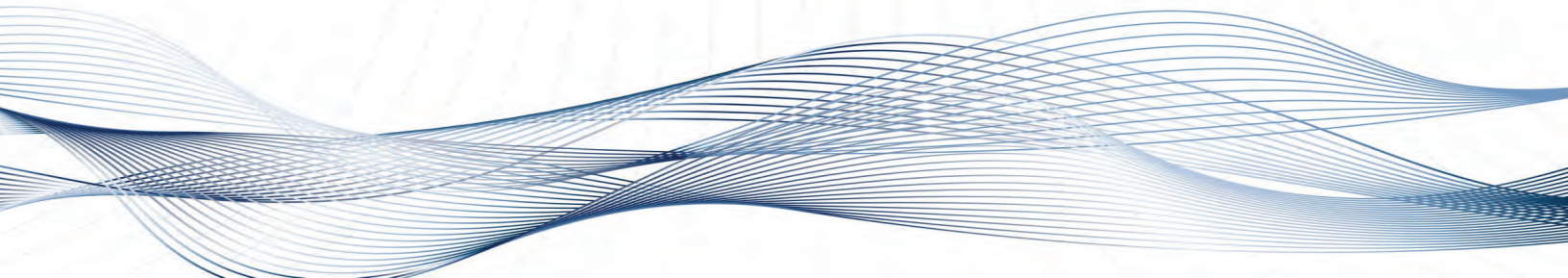
In March 2001, representatives of the International Seabed Authority (ISA) Secretariat met with representatives of the exploration Contractors (formerly known as 'registered pioneer investors') to discuss ways to improve the ISA's resource assessment of the CCZ. Some of the Contractor representatives suggested that the future work of the Secretariat would be enhanced through the development of a geological model of polymetallic nodule deposits in this region.

Participants at the meeting concluded that if the suspected relationships between certain parameters and nodule grade and abundance could be tested, they could be used as proxies for actual grade and abundance data for nodule bearing areas. The representatives of the Contractors also completed a questionnaire regarding the non-proprietary data and information, and technical expertise that they would be willing to contribute to the development of the model.

At the ninth session of the Authority in 2003, the members of the Authority's Legal and Technical Commission recognized that such a model could directly benefit Contractors and Prospectors working in the CCZ by improving the resource assessment for the area, and could also contribute to a better general understanding of how economically interesting deposits form. Between 13 and 20 May 2003, in Fiji, the Authority convened a workshop to consider the various data (available grade and abundance data and candidate proxy data types) that should be included in the effort. Experts from several disciplines delivered technical presentations that identified candidate proxies that could be used and the major tasks that the Authority should undertake to establish the Geological Model.

The workshop produced general recommendations, a project strategy and key project components for the development of the model. Between 6 and 10 December 2004, the Authority convened a Group of Technical Experts to: outline the scope of the work that would be involved; ascertain the availability of data on selected proxies; schedule the work required to gather, evaluate and incorporate suitable data sets into the model through mathematical algorithms; and produce the first iterations of the Geological Model and a draft of the Prospector's Guide.

Taking into account the results of the Fiji workshop, the Group of Technical Experts identified the approach that it would use to create the model and specified the proxy data that it would test for use in predicting nodule metal content and abundance. The primary products from the effort are (1) a ***Geological Model*** of polymetallic nodule deposits in the CCZ and (2) a ***Prospector's Guide*** containing a narrative description of the key factors relevant to exploration for polymetallic nodules in the CCZ, including data and available information on known deposits.



## 2. SUMMARY

### 2.1 Introduction

Manganese nodules are found on the seabed in many areas, and have been comparatively well studied because of their potential economic importance. The Clarion-Clipperton Fracture Zone (CCZ), the study area for this project, has been the focus of much international attention for many years. In March 2001, representatives of the International Seabed Authority (ISA) Secretariat met with representatives of the exploration Contractors (formerly known as 'registered pioneer investors') to discuss ways to improve the ISA's resource assessment for the CCZ. Participants at the meeting concluded that if the suspected relationships between data, such as nodule grade and abundance could be tested, they could be used as proxies for actual grade and abundance data for nodule-bearing areas. At the ninth session of the Authority in 2003, the members of the Authority's Legal and Technical Commission recognized that such a model could directly benefit Contractors and Prospectors working in the CCZ by improving the resource assessment for the area, and could also contribute to a better general understanding of how economically interesting deposits form. Between 13 and 20 May 2003, the Authority convened a workshop to consider the various data (available grade and abundance data and candidate proxy data types) that should be included in the effort.

The primary products from the effort are: (1) a **Geological Model** of polymetallic nodule deposits in the CCZ; and (2) a **Prospector's Guide** containing a narrative description of the key factors relevant to exploration for polymetallic nodules in the CCZ, including data and available information on known deposits. Included in this report are the results of three independent approaches to establishing the Geological Model for the CCZ deposits. No undisclosed or proprietary algorithms are used so that the Model can be subject to peer review in the short term and available for updating as better data or better algorithms become available.

### 2.2 Primary Resource Data Set

The area of interest for this study is 110° - 160° W Longitude and 0° - 20° North Latitude. Five different data sets of polymetallic nodule abundance and metal content are used in the modeling work, including both publicly available and proprietary data sets. The methods used to produce this integrated data set and its basic characteristics are described in Section 3. Maps showing the data locations, values, and interpolated contours are presented in Section 8.

In order to preserve the spatial information inherent in these data while accommodating the proprietary concerns of the data owners, the data were assembled into groups representing all

data collected within a defined grid with dimensions of one-tenth of a degree of longitude and latitude. For each grid block where data are available, the data values are averaged. For each resource parameter (abundance and metal content), the number of stations within the grid bounds, mean, minimum and maximum values of data where at least three stations are present, the standard deviation of the values are reported. These grid data are available for public distribution on the ISA's Central Data Repository.

## 2.3 Inferred Resources

Sections 4 and 5 of this report present several methods of estimating the quantities of polymetallic nodules and the metals they contain within portions of the study area. These methods range from interpolations made using standard kriging methods to extrapolate from the existing data to predict quantities outside the areas containing the required metal content and abundance.

Geostatistics is the generic name for a family of techniques which are used for the mapping of surfaces from limited sample data and the estimation of values at unsampled locations. First developed 40 years ago and named in honour of Danie Krige, these methods are now widely used in the minerals industry. Geostatistical estimation is a two stage process: (1) studying the gathered data to establish the predictability of values from place to place in the study area, resulting in a graph known as a 'semi variogram', which models the difference between the value at one location and the value at another location according to the distance and direction between them; and (2) estimating values at those locations which have not been sampled – this process is known as kriging. Table lists representative values of these estimates.

**Table 1. Inferred Resources in the Study Area**

| <b>Source</b>    | <b>Included Area<br/>(km<sup>2</sup> X 10<sup>6</sup>)</b> | <b>Estimated Tons (metric tons X 10<sup>6</sup>)</b> |                           |                        |                        |                        |
|------------------|--|--|---------------------------|------------------------|------------------------|------------------------|
|                  |  | <b>Nodules</b>                                       | <b>Manganese<br/>(Mn)</b> | <b>Cobalt<br/>(Co)</b> | <b>Nickel<br/>(Ni)</b> | <b>Copper<br/>(Cu)</b> |
| <b>Table 4.8</b> | 3.83   | 21,100   | 5,950*                    | 46.4*                  | 270*                   | 234*                   |
| <b>Table 4.7</b> | 4.19   | 30,700   | 8,657*                    | 67.5*                  | 393*                   | 341*                   |
| <b>Table 5.1</b> | 4.85   | 27,100   | 7,300                     | 58.0                   | 340                    | 290                    |

\*Estimated using mean metal content values from Table 3.3

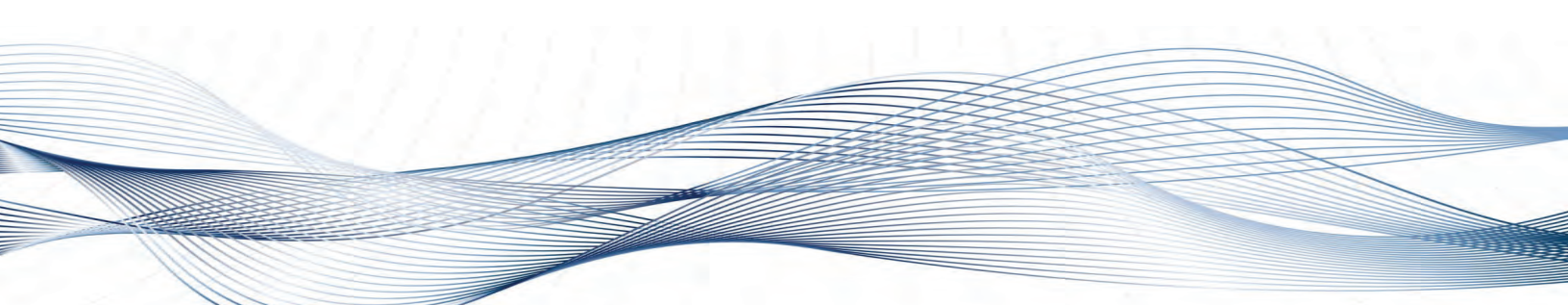
Section 5 includes a biogeochemical modeling study that concludes that the manganese, nickel and copper content in the CCZ polymetallic nodule deposits can be predicted using three proxy variables: (1) surface-water chlorophyll content; (2) distance of the deposit site from the East Pacific Rise and North American Continent; and (3) the differences between the water depth and Carbonate Compensation Depth at the deposit site. Non-linear regression techniques were used to test various relationships between these metal values and the proxy variables. Surface-water chlorophyll content proved to be the best regression fit for all three metals.

## 2.4 SDSS Modeling

Section 6 presents the results of Spatial Decision Support System (SDSS) modeling to estimate the mineralization potential in selected areas of the CCZ where nodule abundance and metal content data are not available. The study is based on data sets that include bathymetry, topography, sediment type, CCD and surface chlorophyll. Specific techniques employed in the study include Weights of Evidence Modeling, Fuzzy Logic, Logistic Regression and Artificial Neural Network (ANN).

The results of this work provide differing assessments of the spatial distribution of areas within the study area where the occurrence of nodule deposits is likely. The results consistently indicate that the better prospects can be found in the central and northern parts of the CCZ, while the southern, southwestern and eastern parts of the CCZ are likely to be unfavorable for nodule deposit occurrence.

### **3. PRIMARY RESOURCE DATA SET**



Several data sets of polymetallic nodule abundance and metal content, both publicly available and proprietary, are used in the modeling work, including. In order to be able to share the data among the international team of experts working on this project, it was necessary to convert the original data into a merged set that accommodates the proprietary concerns of the owners of the data sets while preserving their basic spatial structure. The methods used to produce this data set and its basic characteristics are described in this section. Maps showing the data locations, values, and interpolated contours are presented in Section 8, Figures 35-54.

#### **3.1 Original Data Sets**

These modeling efforts use five different data sets merged into one. They include:

1. All publicly available data in the Authority's Central Data Repository (CDR; <http://www.isa.org.jm>; Polymetallic Nodules - Major elements);
2. A proprietary database used with the permission of the Lockheed-Martin Corporation (Ocean Minerals Company; OMCO);
3. Data sets provided by the Government of the Republic of Korea;
4. Data sets provided by the China Ocean Mineral Resources Research and Development Association (COMRA) of China; and
5. Data sets provided by The Interoceanmetal Joint Organization (IOM), composed of Bulgaria, Cuba, the Czech Republic, Poland, the Russian Federation and Slovakia.

Virtually all the data were obtained from analysis of free-fall grab sampler recoveries, although a few results from box core recoveries are also included. Except for the data extracted from the Authority's Central Data Repository, the metal content estimates were determined by laboratories set up by the respective Contractors. Abundance (weight of nodules per unit area on the seafloor, (usually with units kg/m<sup>2</sup>) is estimated simply by dividing the weight of recovered nodules by the surface area covered by the open jaws of the sampler (~0.25 -0.5 m<sup>2</sup> coverage). As discussed in Hennigar, Dick and Foell (1986), free-fall grab samplers are the best tools available for the assessment of nodule abundance, but they consistently underestimate the actual abundance. Thus, the resource assessment values presented here are likely to be underestimated.

OMCO, and possibly other groups, conducted tank tests using artificial nodules to derive proprietary quantitative estimates of the actual free-fall grab recovery efficiencies and determined that the efficiency is a function of the size of the nodules being sampled. However, since size distributions are not available for most of the nodule samples used to assemble this data set, we have not attempted to adjust the abundance estimates for this study.

Metal content in the samples collected was determined by a variety of methods, including atomic absorption and X-ray fluorescence. During the 1970s and 1980s, the U.S. Bureau of Mines distributed standard nodule samples (labeled "A-1" and "P-1") that had been extensively analyzed by the Bureau and then mixed into a uniform powder. These standard samples were later transferred to the U.S. Geological Survey after the Bureau closed in 1996. The consortia that were exploring the CCZ deposits at that time all obtained sub-samples of these standards to evaluate the accuracy of their methods. No results of these standard tests are available; however, the fact that the scientists responsible for the analysis protocols were able to use state-of-the-art methods to ensure that their results were as accurate as possible benefited the consortia.

The data acquired were for the area 110° - 160° W Longitude and 0° - 20° North Latitude. The data were screened to eliminate clearly anomalous values (see Table 2).

**Table 2. Data Screening, Criteria for Elimination**

| <b>Statistic</b>                       | <b>Abundance<br/>(kg/m<sup>2</sup>)</b> | <b>Mn (%)</b> | <b>Co (%)</b> | <b>Ni (%)</b> | <b>Cu (%)</b> |
|--|---|---------------|---------------|---------------|---------------|
| <b><i>Remove if Value is Below</i></b> | 0.0                                     | 10            | 0.02          | 0.3           | 0.2           |
| <b><i>Remove if Value is Above</i></b> | 45                                      | 45            | 0.5           | 2             | 2             |

Table 3 summarizes the quantities of data from these sources after data screening. The large number of samples for abundance is the result of using the COMRA Multi-Frequency exploration system (MFES) data set (51,758 points) with the sample-based data from all the sources (9,825 points).

**Table 3. Source Data for Resource Assessment (Screened Data)**

| <b>Data Source</b>               | <b>CDR</b> | <b>KOREA</b> | <b>OMCO</b> | <b>COMRA</b> | <b>IOM</b> | <b>Totals</b> |
|----------------------------------|------------|--------------|-------------|--------------|------------|---------------|
| <b># Stations:<br/>Abundance</b> | 253        | 329          | 7,738       | 52,473       | 790        | 61,583        |
| <b># Stations:<br/>Manganese</b> | 879        | 258          | 5,875       | 716          | 664        | 8,392         |
| <b># Stations:<br/>Cobalt</b>    | 711        | 258          | 5,900       | 716          | 664        | 8,249         |
| <b># Stations:<br/>Nickel</b>    | 799        | 258          | 5,923       | 716          | 664        | 8,360         |
| <b># Stations:<br/>Copper</b>    | 882        | 258          | 5,924       | 714          | 664        | 8,442         |

Table 4 presents the elementary statistics of the merged data. This merged data set was used for the biogeochemical modeling presented in Section 5.

**Table 4. Screened Data Set Elementary Statistics**

| <b>Statistic</b>          | <b>Abundance<br/>(kg/m<sup>2</sup>)</b> | <b>Mn (%)</b> | <b>Co (%)</b> | <b>Ni (%)</b> | <b>Cu (%)</b> |
|---------------------------|---|---------------|---------------|---------------|---------------|
| <b>Number of stations</b> | 61,583                                  | 8,392         | 8,249         | 8,360         | 8,442         |
| <b>Minimum</b>            | 0.0                                     | 10.0          | 0.02          | 0.37          | 0.23          |
| <b>Maximum</b>            | 44.1                                    | 41.1          | 0.5           | 1.78          | 1.99          |
| <b>Median</b>             | 5.8                                     | 30.01         | 0.23          | 1.39          | 1.19          |
| <b>Mean</b>               | 7.2                                     | 29.0          | 0.23          | 1.34          | 1.14          |
| <b>Standard Deviation</b> | 6.1                                     | 3.8           | 0.05          | 0.20          | 0.24          |

The data set used for the other model development (Sections 4 and 6) was derived from the original data, without screening for anomalous values. The methods used to derive this data set are described in the following passages.

### 3.2 Tenth-Degree Grid Data

In order to preserve the spatial information inherent in these data while accommodating the proprietary concerns of the data owners, they were assembled into groups representing all data collected within a defined grid with dimensions of one-tenth of a degree of both longitude and latitude. For each grid block where data are available, the data values are averaged. For each resource parameter (abundance and metal content), the number of stations within the grid bounds, mean, minimum and maximum values of data, where at least three stations are present, the standard deviation of the values are reported.

These derived data preserve the basic regional information content, to the resolution of the grid dimension,<sup>1</sup> but cannot be used to infer the original data positions and values, which was the key concern of the owners of the data. Through inclusion of the maximum and minimum values and number of stations for each grid point, investigators were free to eliminate the extreme data values or specific grid blocks using whatever criteria they wish and then re-calculate the mean values for the affected grid locations.

**Table 5. Grid Data Elementary Statistics**

| <b>Grid Block Statistics</b>     | <b>Abundance<br/>(kg/m<sup>2</sup>)</b> | <b>Mn (%)</b> | <b>Co (%)</b> | <b>Ni (%)</b> | <b>Cu (%)</b> |
|----------------------------------|---|---------------|---------------|---------------|---------------|
| <b>No. Populated Blocks</b>      | 3,622                                   | 2,582         | 2,560         | 2,582         | 2,586         |
| <b>Median No. Stations/Block</b> | 5                                       | 1             | 1             | 1             | 1             |
| <b>Mean No. Stations/Block</b>   | 17                                      | 3.25          | 3.24          | 3.24          | 3.27          |
| <b>Minimum</b>                   | 0.0                                     | 10.0          | 0.05          | 0.40          | 0.20          |
| <b>Maximum</b>                   | 44.1                                    | 41.1          | 0.79          | 1.80          | 2.00          |
| <b>Median</b>                    | 5.47                                    | 29.2          | 0.22          | 1.30          | 1.19          |
| <b>Mean</b>                      | 6.72                                    | 28.2          | 0.22          | 1.28          | 1.11          |
| <b>Standard Deviation</b>        | 5.52                                    | 3.93          | 0.05          | 0.21          | 0.27          |

As shown in these tables, the elementary statistics of the original and grid data are very similar. As indicated by the median number of stations, except for abundance, over half of the grid blocks contain only a single station. Thus, we believe that, particularly for regional studies such as this one, the grid data can be used instead of the original data with insignificant loss in accuracy or interpretability.

---

<sup>1</sup> A tenth of a degree of latitude is 11.12 km. A tenth of a degree of longitude is approximately 11.08 km at 5° N and diminishes to 10.45 km at 20° N, using a spherical assumption for the shape of the Earth.

## 4. GEOGRAPHIC INFORMATION SYSTEM AND GEOSTATISTICAL APPRAISAL OF RESOURCE POTENTIAL

### 4.1 Introduction

The objective of this part of the study is to estimate the quantities of manganese nodules and their contained metal (Mn, Co, Ni and Cu) within the CCZ using Geographic Information System (GIS)<sup>2</sup> and geostatistical methods and the 0.1 degree grid block data described in Section 3.2 above.

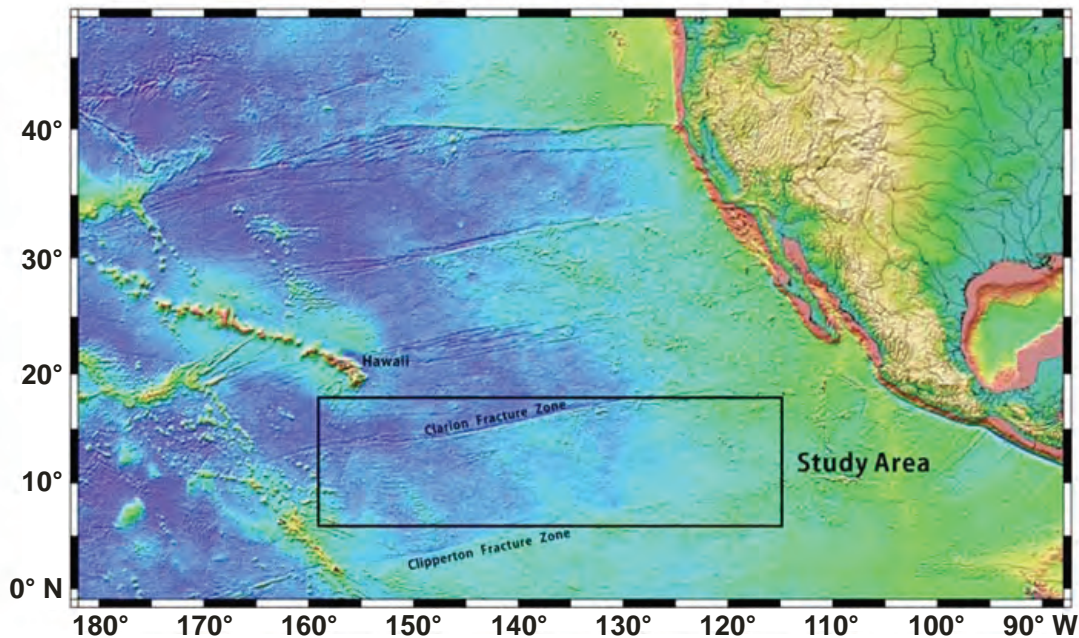


Figure 1. Clarion-Clipperton Zone (CCZ) Study Area (Sandwell, 2000)

<sup>2</sup> A geographic information system (GIS) is a system that captures, stores, analyses, manages and presents data that are limited to location. The term defines any information system that integrates, stores, edits, analyses, shows and displays geographic information. It is composed of the relevant software, hardware and data.

## 4.2 Theory

Two methods used for the study were Ordinary Kriging and Sequential Indicator Simulation (SIS). The entire theoretical background for the two methods is described in the full report.

## 4.3 Materials and Methods

### 4.3.1 Sites and Data Sets

The data set utilized for this study is a tenth-degree grid for the abundance data set described in Section 3.2. Because the study area is too broad for efficient analysis using the methods described above, the resource was evaluated by dividing the whole area into four blocks, ISA1 - ISA4, to improve the efficiency of data processing (see Figure 2). In this analysis, each station was given equal weight.

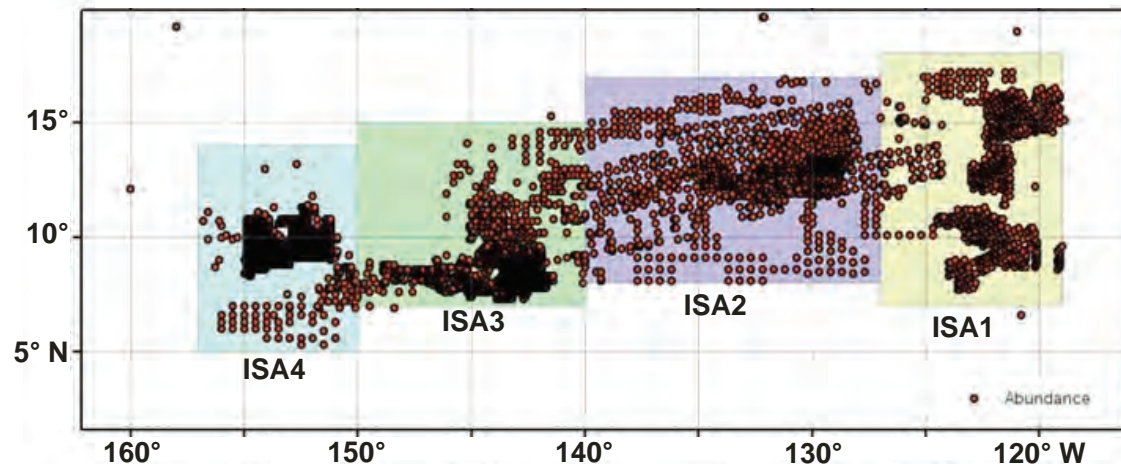
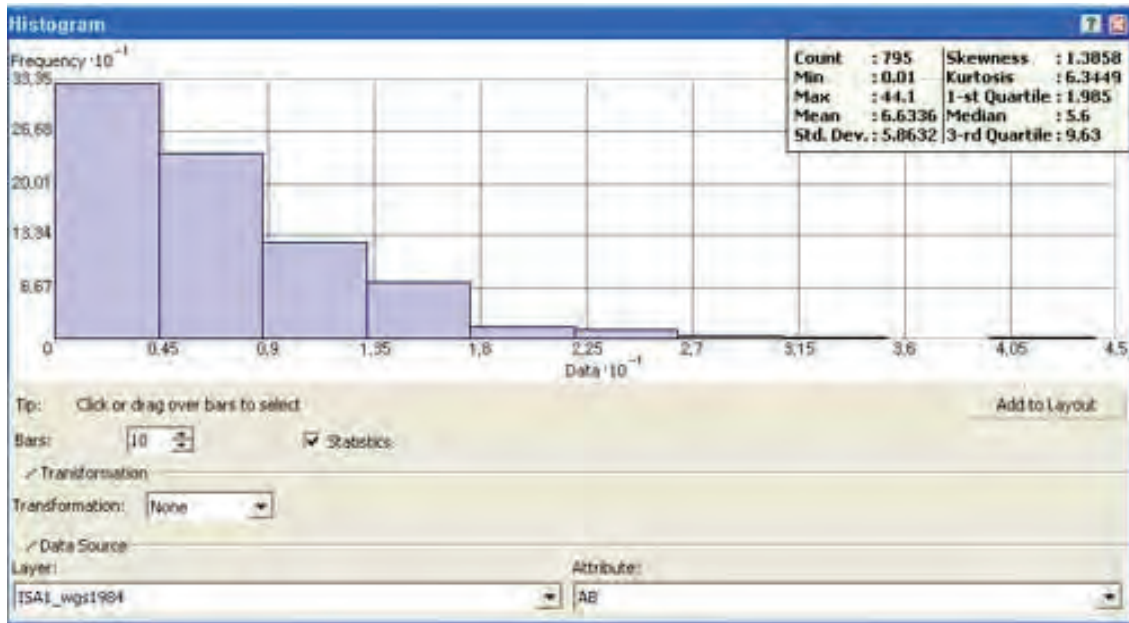


Figure 2. Station Map, Showing Blocks Used in this Study

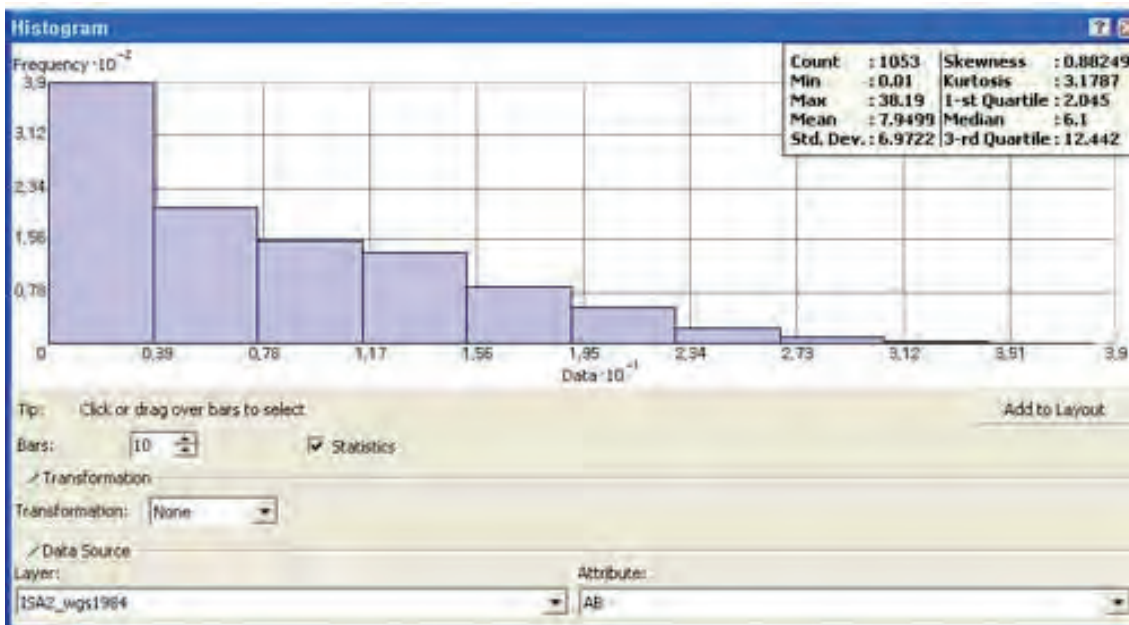
The data are distributed between 120°-160° W and 5.3° - 19.6°-N. There are 3,662 blocks containing data. As shown in Figure 2, the isolated, single stations are excluded from consideration in this study. The basic statistics from the total data set and the individual blocks used are shown in Table 6. As shown in this table, the abundance in the region varies between 0 and 44.1 kg/m<sup>2</sup> overall, and the mean abundance values for the study blocks vary between 5.0 kg/m<sup>2</sup> in ISA3 to 8.0 kg/m<sup>2</sup> in ISA 2. The separate distributions of abundance for these analysis blocks are presented in Figure 3 and Figure 4.

**Table 6. Statistics of Individual Blocks Used in this Study**

| Factor                 | Total                    | ISA 1        | ISA 2        | ISA 3        | ISA 4        |
|------------------------|--------------------------|--------------|--------------|--------------|--------------|
| <i>Longitude Range</i> | -160 to -118.9           | -127 to -119 | -140 to -127 | -150 to -140 | -157 to -150 |
| <i>Latitude Range</i>  | 5.3 to 19.6              | 7 to 18      | 8 to 17      | 7 to 15      | 5 to 14      |
| Number                 | <i>Total</i>             | 3,622        | 795          | 1,053        | 961          |
|                        | <i>Used for Analysis</i> | 3,593        | 791          | 1,051        | 958          |
|                        | <i>Excluded Data</i>     | 11           | 4            | 2            | 2            |
| <i>Minimum</i>         | 125.52                   | 44.10        | 38.2         | 21.0         | 22.2         |
| <i>Maximum</i>         | 6.8                      | 6.6          | 8.0          | 5.0          | 7.2          |
| <i>Mean</i>            | 20.6                     | 5.9          | 7.0          | 3.4          | 4.3          |
| <i>Std. Dev</i>        | 4.0                      | 1.4          | 0.88         | 1.4          | 0.40         |
| <i>Skewness</i>        | 18.2                     | 6.4          | 3.2          | 6.02         | 2.7          |
| <i>Kurtosis</i>        | 10.8                     | 2.0          | 2.0          | 2.9          | 3.9          |
| <i>1-st Quartile</i>   | 23.0                     | 5.6          | 6.1          | 4.5          | 6.8          |
| <i>Median</i>          | 38.7                     | 9.6          | 12.5         | 6.4          | 10.2         |
| <i>3-rd Quartile</i>   |                          |              |              |              |              |

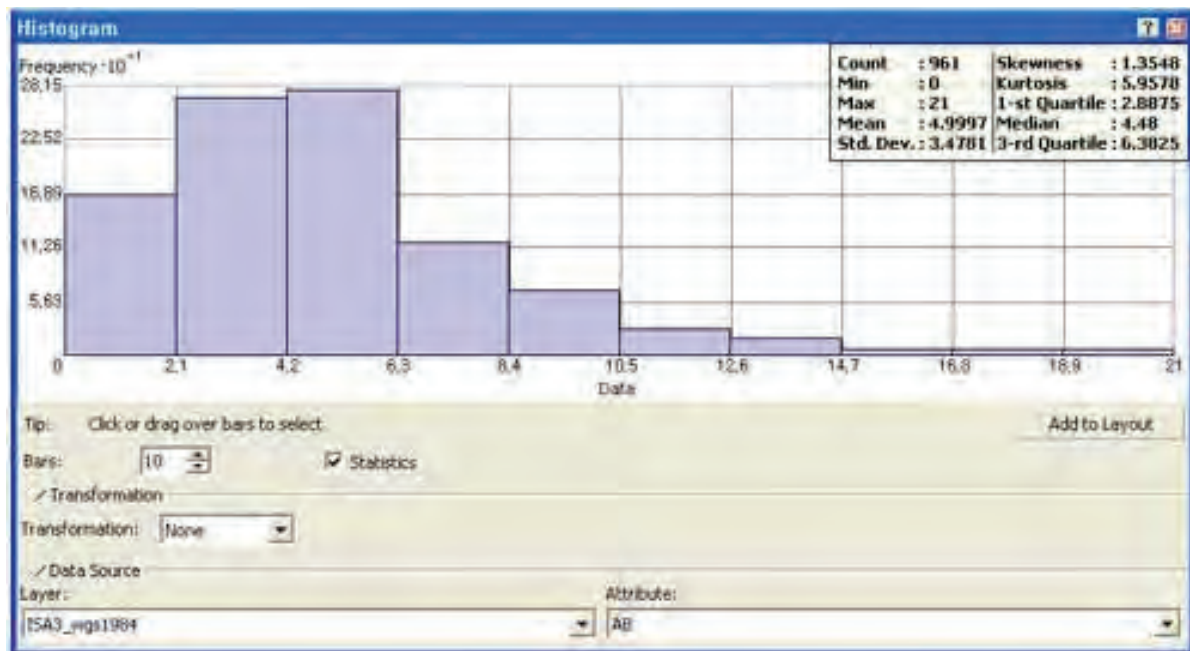


a) ISA-1

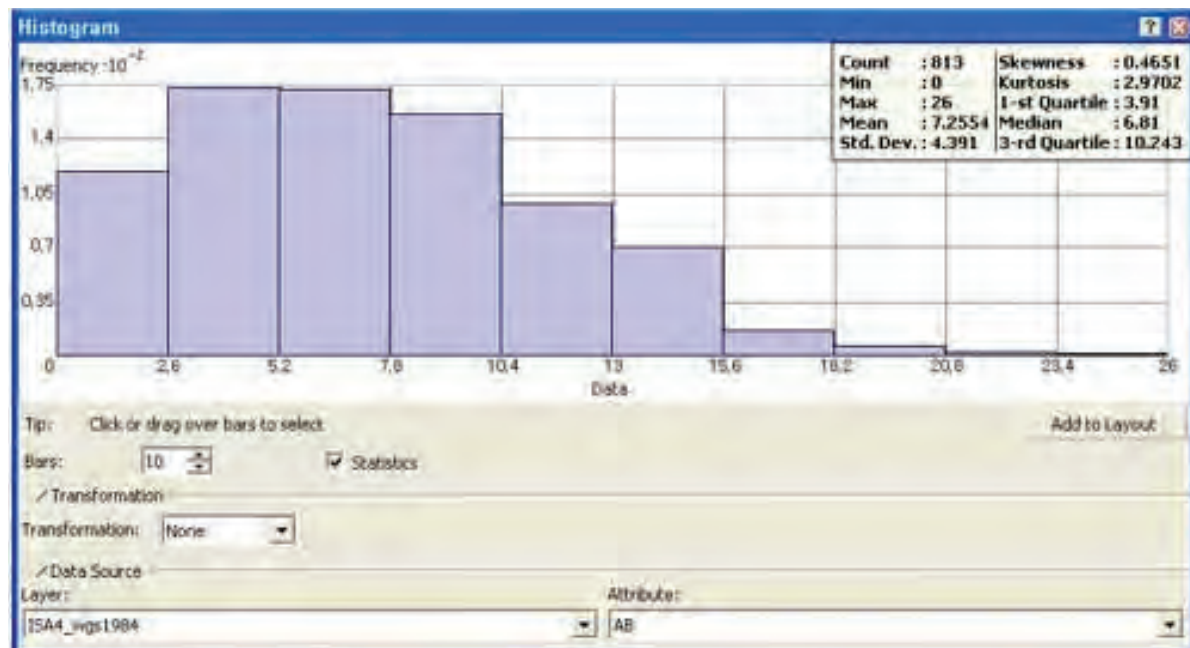


b) ISA-2

Figure 3. Abundance Distributions within the four Blocks (ISA-1 and ISA-2)



c) ISA - 3



d) ISA - 4

Figure 4. Abundance Distributions within the four Blocks (ISA-3 and ISA-4)

#### 4.3.2 Methods

The estimation of resource quantity was determined using the two methods indicated in Section 4.2, i.e. Ordinary Kriging (OK) and Sequential Indicator Simulation (SIS). First, parameters were acquired for kriging interpolation using the ESRI® Geostatistical Analyst module of the ArcGIS® software package, and then kriging interpolation was carried out using the ArcGIS® Spatial Analyst module to provide estimates of nodule tonnage. Second, the nodule tonnage estimate was estimated using OK and SIS using GSLIB software.

The projection used for calculating area for both methods is the Lambert Azimuthal Equal Area method. This projection preserves the area of individual polygons while simultaneously maintaining a true sense of direction from the center. Shape is minimally distorted (less than 2 per cent) within 15° from the focal point. Beyond that, angular distortion is more significant, and small shapes are compressed radially from the center and elongated perpendicularly. This method is used commonly for oceanic mapping of energy and mineral resources as well as for geological and geophysical applications (Johnston *et al.*, 2001).<sup>3</sup>

First, histogram analysis was performed for the univariate distribution of the data set. Then, for the appropriate interpolation of the data set, the kriging method was applied. The kriging method is one of the most commonly used methods to evaluate the quality of resources. Ordinary Kriging (OK) is the most general and widely used kriging method. It assumes that the constant mean is unknown. This is a reasonable assumption unless there is a scientific reason to reject it (Johnston *et al.*, 2001). Parameters for the ordinary kriging interpolation were arrived at using Geostatistical Analyst module in ArcGIS.<sup>4</sup>

ArcGIS Spatial Analyst provides circular, spherical, exponential, gaussian, and linear functions to fit to the empirical semivariogram. The selected model influences the prediction of the unknown values, particularly when the shape of the curve near the origin differs significantly. The steeper the curve near the origin, the more influence the closest neighbours will have on the prediction. As a result, the output surface will be less smooth. Each model is designed to fit different types of phenomena more accurately. The spherical model is one of the most commonly used models, and was used in this model.

The abundance value for each grid cell was produced to generate an object (shp file) using raw data. The Excel spreadsheet from ISA repository provided was converted to DBF4 format using MS Access so that it can be read in ArcGIS. For data processing and analysis, the data were organized and divided into a grid cell made of 100 nodes (10 x 10 window) by assigning an average value of each data set from 0.1° x 0.1° longitudinal and latitudinal area each grid cell. The average values were decided as the representative values for each grid cell. This estimation method was also used for the first, second and third relinquishments of the Republic of Korea's allocated area (reports submitted to ISA by KORDI 1997, 1999, 2002). Through statistical analysis using a Geostatistical analyst module, the nodule abundance for 0.1° X 0.1° grid cells was calculated.

---

<sup>3</sup> In the process of area calculation, the following ArcGIS procedures are used: Create Fishnet, checkered Polyline generation, and checkered Polygon were created using the polygon creation from Polyline data. For the exact area calculation of the created checkered polygon, Area field and X, Y coordinates were added to the Polygon feature table following Lambert Azimuthal Equal Area projection. Area value is then calculated in the polygon feature attribute table.

<sup>4</sup> 1) Sequence of ArcGIS commands: 1) Select point layer in the ArcMap table of contents to be analyzed; 2) Start Geostatistical Analyst Wizard; 3) Select abundance variable in Attribute dropdown menu; 4) Select Kriging method and click Next; 5) Click Next on all subsequent dialogs boxes; 6) click Finish on the Cross Validation dialog box; 7) Click OK on Output Layer information box.

Finally, the amount of manganese nodules was calculated by multiplying: 1) area data of  $0.1^\circ \times 0.1^\circ$  grid cell; and 2) abundance data of  $0.1^\circ \times 0.1^\circ$  grid cell which were acquired at the initial step for each block. Finally, the total resource was estimated by adding all results together.

## 4.4 Results

### 4.4.1 Resource Estimation Using ArcGIS

Resource estimation was completed by using first the ESRI<sup>®</sup> Geostatistical Analyst extension to derive kriging interpolations of nodule abundance for each of the four blocks, ISA1 – ISA4, then using Spatial Analyst extension to calculate the area for each  $0.1^\circ \times 0.1^\circ$  grid cell (see Figure 7), and then multiplying the abundance the area of each cell to determine the final estimates.

The spatial distribution of polymetallic nodule abundance was extrapolated over the whole study area using the OK method in the ArcGIS Geostatistical Analyst extension. The results are presented in 2D and 3D formats in Figure 5.

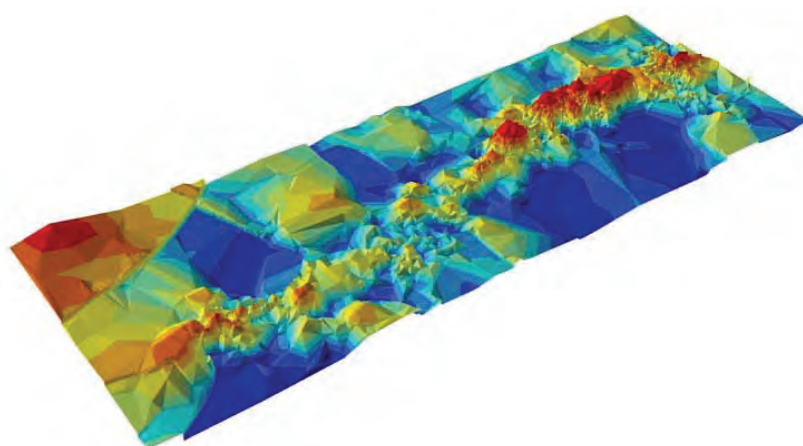
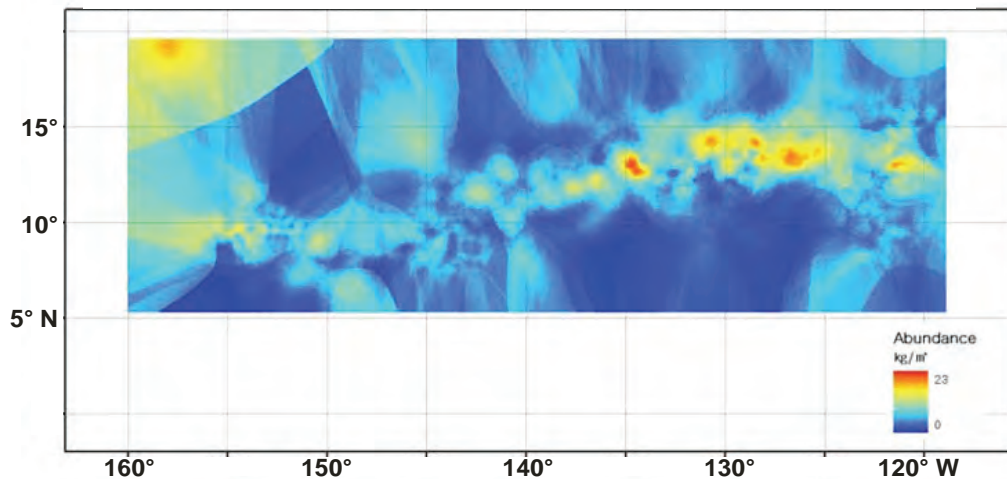


Figure 5. Nodule Abundance, Entire Study Area (ArcGIS Software)

Similar plots for the individual blocks are presented in Figure 6.

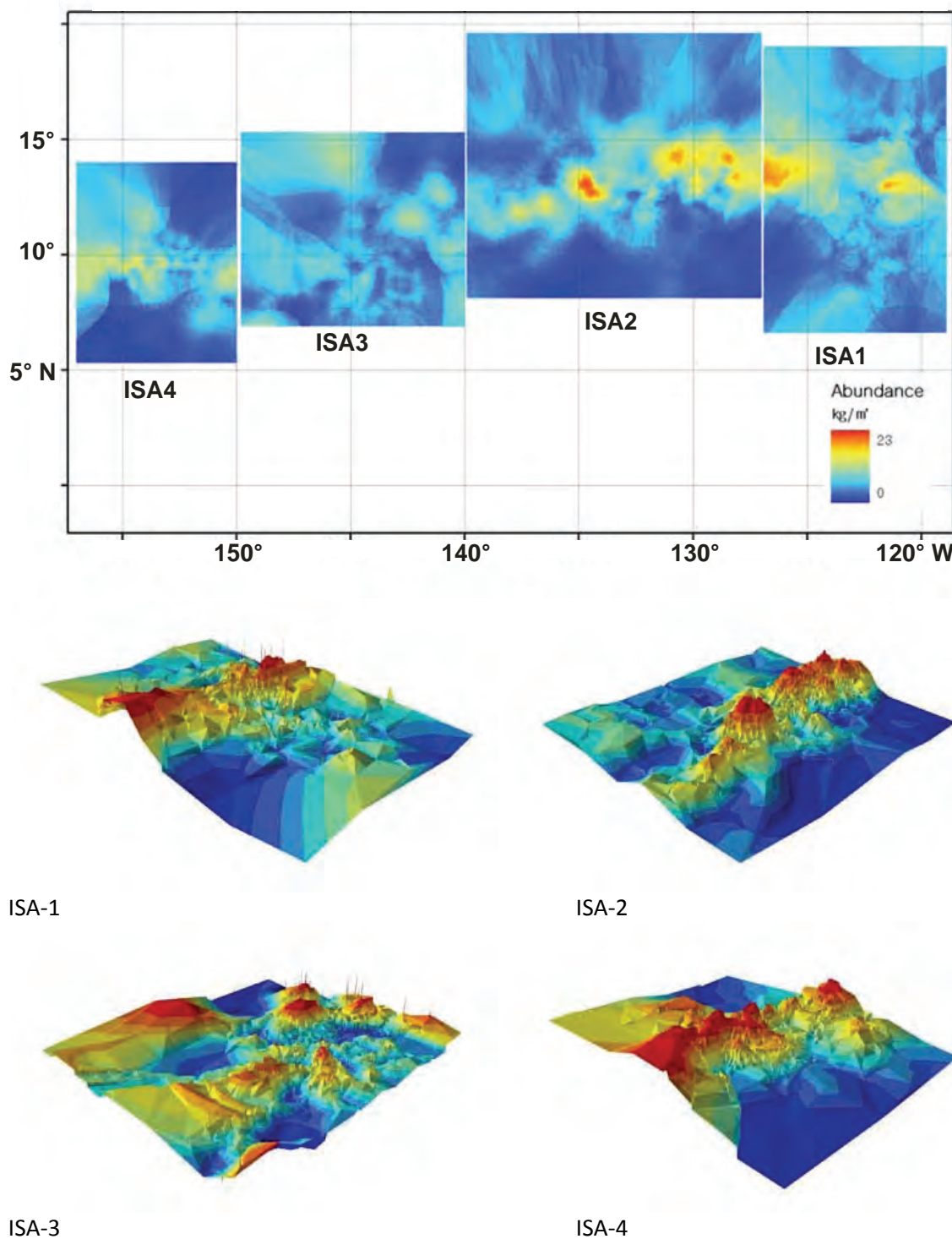


Figure 6. Abundance, Individual Block Values, ArcGIS Software

Statistics derived from the individual kriging blocks for the entire study area are presented in Table 7.

**Table 7. Statistics for Total Study Area**

| Abundance<br>(kg/m <sup>2</sup> ) | Raw Data | OK     | SIS Realizations |        |        |
|-----------------------------------|----------|--------|------------------|--------|--------|
|                                   |          |        | R1               | R2     | R3     |
| Mean                              | 6.72     | 5.29   | 7.26             | 6.9    | 7.23   |
| Std. Error                        | 0.09     | 0.01   | 0.03             | 0.03   | 0.03   |
| Median                            | 5.47     | 4.93   | 4.88             | 4.58   | 5      |
| Minimum                           | 0.01     | 0.01   | 0.01             | 0.01   | 0.01   |
| Std. Dev.                         | 5.52     | 3.17   | 8.03             | 7.78   | 7.94   |
| Range                             | 30.48    | 10.04  | 64.4             | 60.49  | 62.98  |
| No. Points                        | 3,622    | 57,819 | 63,571           | 63,571 | 63,571 |

Statistics for Blocks ISA-1 – ISA-4 are presented in Tables 8, 9, 10 and 11, respectively.

**Table 8. Statistics for ISA-1 Block**

| Abundance<br>(kg/m <sup>2</sup> ) | OK    | SIS Realizations |       |       |
|-----------------------------------|-------|------------------|-------|-------|
|                                   |       | R1               | R2    | R3    |
| Mean                              | 6.29  | 8.39             | 7.47  | 7.82  |
| Std. Error                        | 0.04  | 0.09             | 0.09  | 0.09  |
| Median                            | 5.69  | 5.85             | 4.96  | 5.35  |
| Minimum                           | 0.01  | 0.01             | 0.01  | 0.01  |
| Std. Dev.                         | 3.56  | 8.77             | 8.19  | 8.58  |
| Range                             | 12.65 | 76.96            | 67.07 | 73.55 |
| No. Points                        | 8,991 | 8,991            | 8,991 | 8,991 |

**Table 9. Statistics for ISA-2 Block**

| Abundance<br>(kg/m <sup>2</sup> ) | OK     | SIS Realizations |        |        |
|-----------------------------------|--------|------------------|--------|--------|
|                                   |        | R1               | R2     | R3     |
| Mean                              | 5.41   | 6.72             | 6.51   | 6.62   |
| Std. Error                        | 0.04   | 0.07             | 0.07   | 0.08   |
| Median                            | 4.43   | 4.03             | 3.52   | 3.49   |
| Minimum                           | 0.01   | 0.01             | 0.01   | 0.01   |
| Std. Dev.                         | 4.06   | 7.8              | 8.03   | 8.19   |
| Range                             | 16.51  | 60.81            | 64.44  | 67.07  |
| No. Points                        | 11,921 | 11,921           | 11,921 | 11,921 |

**Table 10. Statistics for ISA-3 Block**

| Abundance<br>(kg/m <sup>2</sup> ) | OK    | SIS Realizations |       |       |
|-----------------------------------|-------|------------------|-------|-------|
|                                   |       | R1               | R2    | R3    |
| Mean                              | 5.27  | 7.67             | 4.98  | 6.27  |
| Std. Error                        | 0.03  | 0.1              | 0.06  | 0.08  |
| Median                            | 5.1   | 4.74             | 3.45  | 4.3   |
| Minimum                           | 3.93  | 0.01             | 0.01  | 0.01  |
| Std. Dev.                         | 2.28  | 8.77             | 5.5   | 6.94  |
| Range                             | 5.18  | 76.93            | 30.28 | 48.21 |
| No. Points                        | 8,181 | 8,181            | 8,181 | 8,181 |

**Table 11. Statistics for ISA-4 Block**

| Abundance<br>(kg/m <sup>2</sup> ) | OK    | SIS Realizations |       |       |
|-----------------------------------|-------|------------------|-------|-------|
|                                   |       | R1               | R2    | R3    |
| Mean                              | 4.82  | 6.56             | 6.23  | 6.98  |
| Std. Error                        | 0.04  | 0.09             | 0.08  | 0.1   |
| Median                            | 4.45  | 4.54             | 4.86  | 5.03  |
| Minimum                           | 0.69  | 0.01             | 0.01  | 0.01  |
| Std. Dev.                         | 3.48  | 7.23             | 6.39  | 7.64  |
| Range                             | 12.1  | 52.32            | 40.77 | 58.44 |
| No. Points                        | 6,461 | 6,461            | 6,461 | 6,461 |

Tonnage estimates for the resources estimated for these Blocks are presented in Table 12.

**Table 12. Polymetallic Nodule Tonnage Estimates in Total Study Area**

| Block        | Area<br>(km <sup>2</sup> ) | ArcGIS<br>OK<br>(10 <sup>6</sup><br>ton) | GSILB<br>OK | SIS Realizations (10 <sup>6</sup> ton) |        |        |
|--------------|----------------------------|--|-------------|--|--------|--------|
|              |                            |  |             | R1                                     | R2     | R3     |
| ISA-1        | 1,056,000                  | 6,850                                    | 6,660       | 8,870                                  | 7,900  | 8,270  |
| ISA-2        | 1,405,000                  | 7,570                                    | 7,630       | 9,440                                  | 9,160  | 9,320  |
| ISA-3        | 966,000                    | 5,300                                    | 5,100       | 7,400                                  | 4,810  | 6,050  |
| ISA-4        | 764,000                    | 3,660                                    | 3,700       | 4,970                                  | 4,730  | 5,310  |
| <b>Total</b> | 4,190,000                  | 23,400                                   | 23,100      | 30,700                                 | 26,600 | 29,000 |

Tonnage estimates for a somewhat smaller area, adjusted to remove the outer margins of Blocks ISA-1, ISA-3 and ISA-4 where no data occur, are presented in Table 13.

**Table 13. Polymetallic Nodule Tonnage Estimates in Reduced Area**

| Block        | Area (km <sup>2</sup> ) | GSILB OK<br>(10 <sup>6</sup> ton) | SIS Realizations (10 <sup>6</sup> ton) |        |        |
|--------------|-------------------------|-----------------------------------|--|--------|--------|
|              |                         |                                   | R1                                     | R2     | R3     |
| ISA-1*       | 960,000                 | 6,170                             | 8,187.093                              | 7,400  | 7,150  |
| ISA-2        | 1,410,000               | 7,630                             | 9,442.066                              | 9,160  | 9,320  |
| ISA-3*       | 750,000                 | 3,960                             | 4,766.920                              | 3,930  | 4,580  |
| ISA-4*       | 716,000                 | 3,380                             | 4,645.463                              | 4,390  | 4,710  |
| <b>Total</b> | 3,830,000               | 21,100                            | 27,041.542                             | 24,900 | 25,800 |

\*Area reduced to eliminate margins with no resource data present

Each block was divided by a fishnet lattice into small sub-sections to facilitate the accurate calculation of areas. Each sub-section represents 120 to 121 km<sup>2</sup>. The numbers of these sub-sections are presented for each Block in Table 12. In summary, the mean abundance, determined using the ArcGIS software, varies between 4.8 (ISA-4) and 6.7 kg/m<sup>2</sup> (ISA-1), and the total estimated tonnage of nodules within the entire study area is estimated to be  $23.4 \times 10^9$  metric tons and the tonnage within the area contained by the study Blocks is estimated to be  $21.1 \times 10^9$  metric tons.

#### 4.4.2 Resource Estimation Using GSLIB

A separate variogram and OK analysis was carried out using the GSLIB 2.0 software package (Deutsch and Journel, 1998). This software was also used to perform a subsequent Sequential Indicator Simulation (SIS) with the kriging.

The 8 cutoffs used in the indicator variograms were chosen by taking high-rated 8 numbers besides the low-rated 2 numbers among numbers division in ten (0.43, 2.06, 3.32, 4.38, 5.47, 6.76, 8.50, 10.76 and 14.28). An abundance of 6 kg/m<sup>2</sup> is selected as the threshold. In these variograms, the range varies between 2.3° and 3.3° and the nugget value between 0.60 and 0.67 (kg/m<sup>2</sup>)<sup>2</sup>. The area used in the analysis consists of the four study Blocks, divided into 421 × 151 cells, each with dimensions of 0.1° × 0.1°. The range of results is computed within the area delimited by 160° to 118° W longitude and 5° to 20° North latitude (see Figure 7).

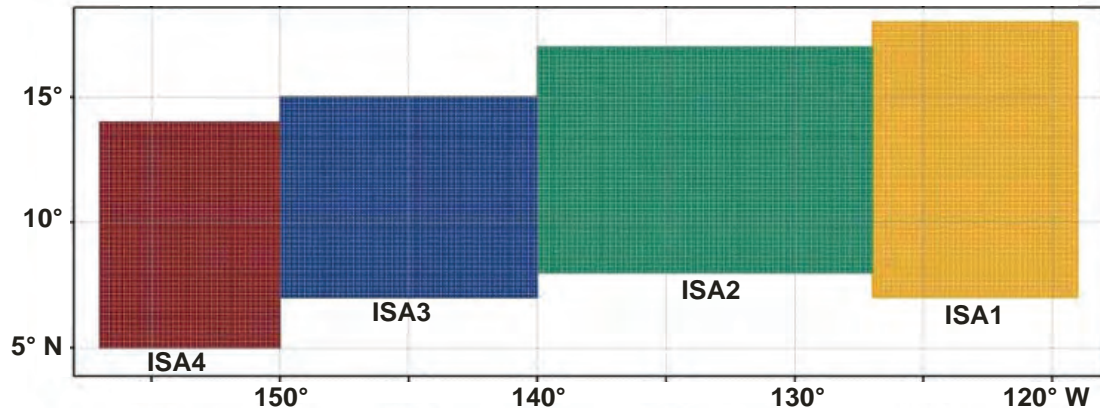


**Figure 7. Analysis Blocks Used in Study Showing 0.1°Cells**

The distribution of the abundance inferred from OK and SIS is presented in Figure 8. The results from the three realizations calculated using the SIS method are presented in Table 7 for the entire study area and in Table 8, Table 9, Table 10 and Table 11, respectively, for study Blocks ISA-1 – ISA-4. As shown in Table 7, Realization 2 produces a similar average value to the raw data, while all three realizations show generally higher averages than the ArcGIS results. In summary, as shown in Table 12 and Table 13, the tonnage of nodules within the four study Blocks is predicted by the SIS method to be between  $26.2$  and  $30.7 \times 10^9$  metric tons, considerably more than the tonnage predicted by the ArcGIS analysis. The estimate for the total tonnage in the reduced area, designed to eliminate the margins of Blocks ISA-1, ISA-3, and ISA-4 that contain no data, is estimated to be between  $24.9$  and  $30.7 \times 10^9$  metric tons. The predicted abundance distribution using SIS realization is presented in Figures 9, 10 and 11.

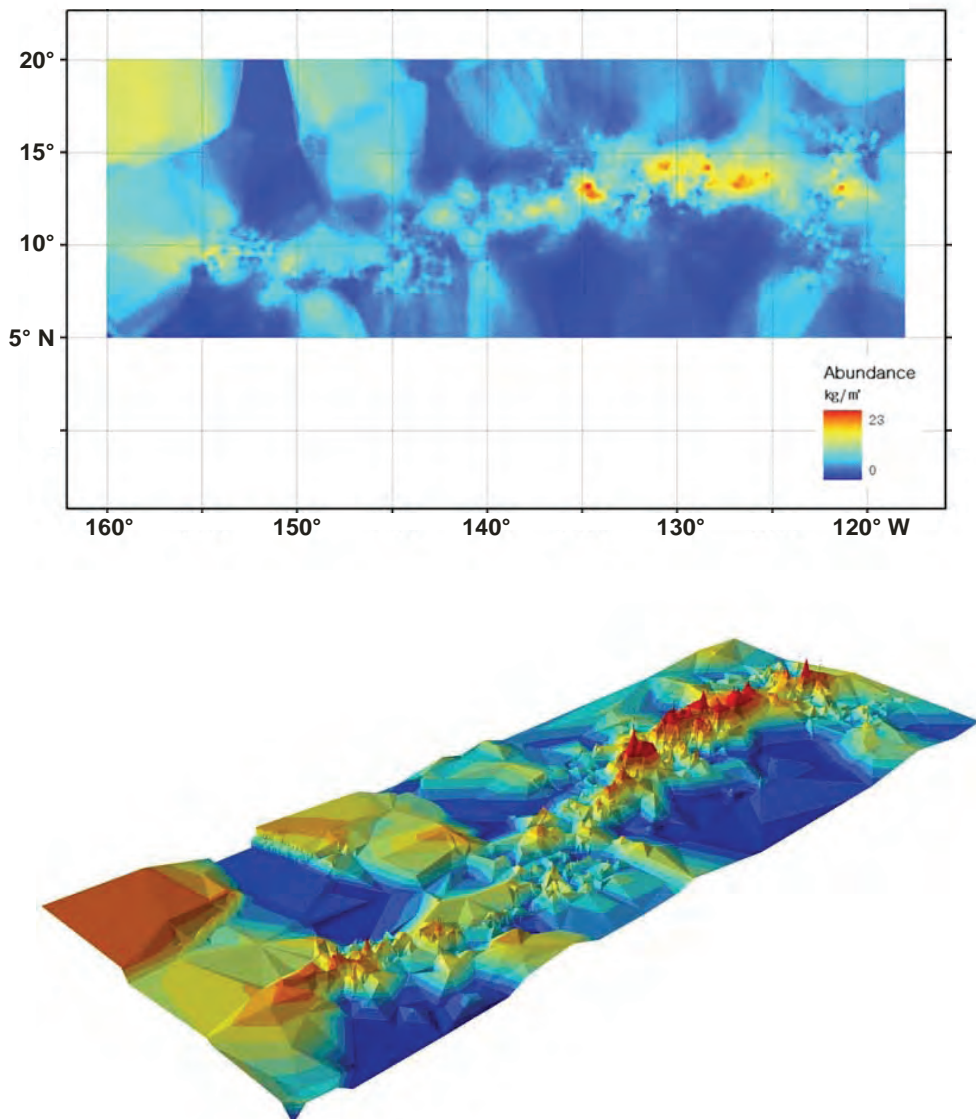


*Figure 8. Abundance, Individual Blocks, GSLIB Kriging*

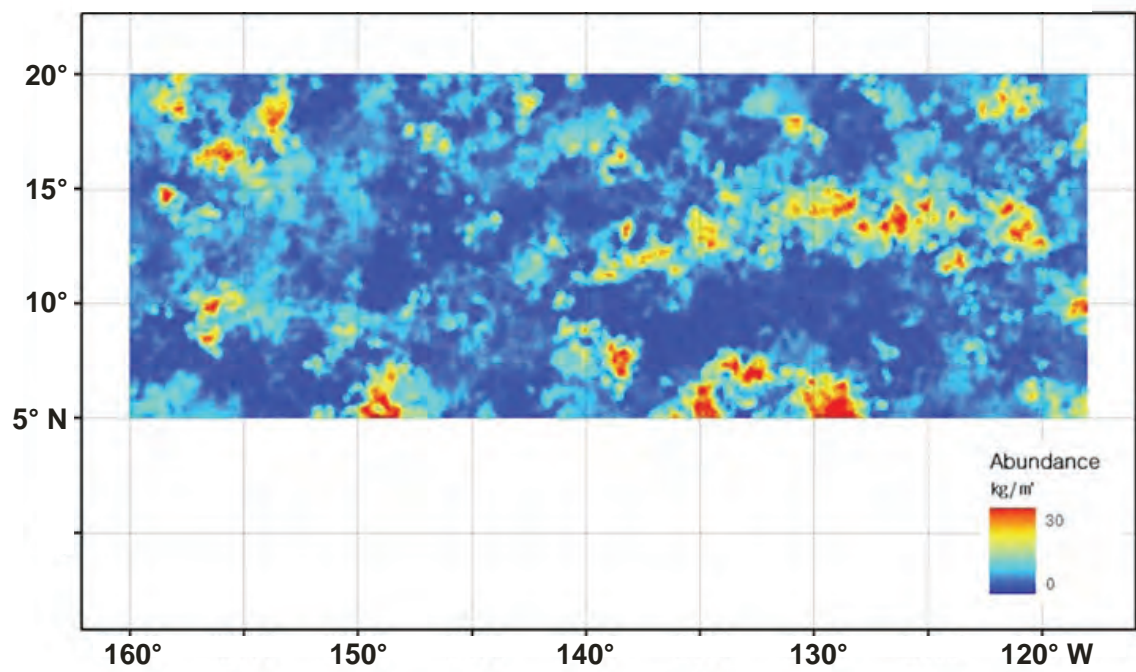


Figure 9. Predicted Abundance Distribution, SIS Realization 1

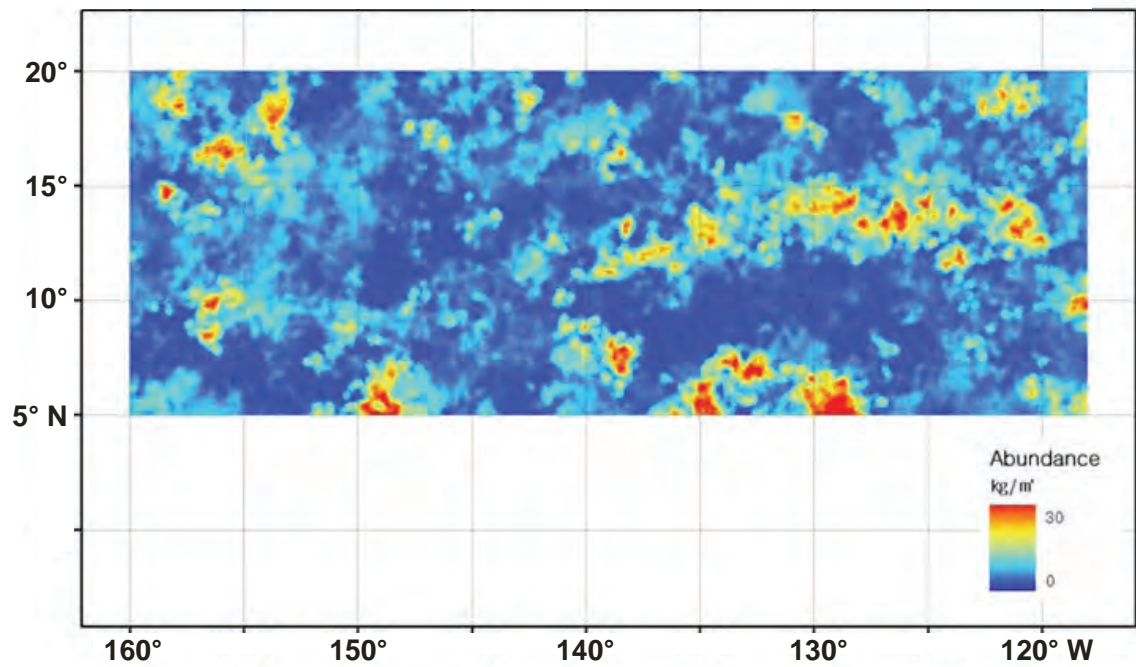
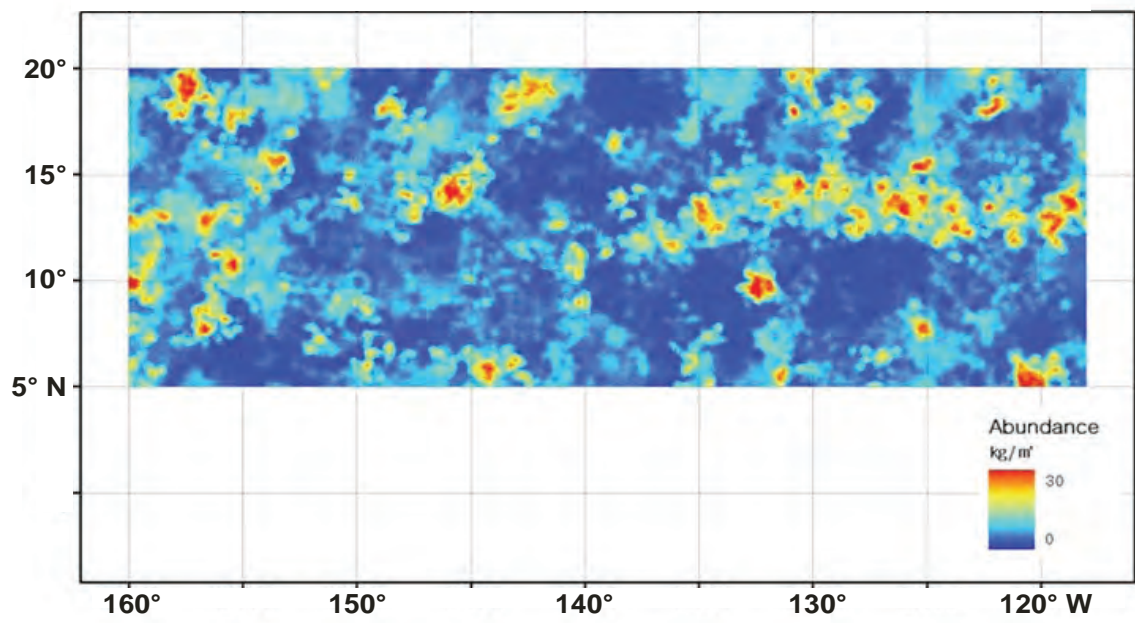


Figure 10. Predicted Abundance Distribution, SIS Realization 2



*Figure 11. Predicted Abundance Distribution, SIS Realization 3*

## 5. BIOGEOCHEMICAL MODEL OF THE MANGANESE, COPPER AND NICKEL CONTENT IN POLYMETALLIC NODULES IN THE CCZ

### 5.1 Background and Organization

The model presented here predicts the geographical distribution of the metal content of CCZ polymetallic nodules (Mn, Ni and Cu) using as independent variables the values of other known variables, including chlorophyll concentrations in surface waters, the distance from the East Pacific Rise and the North American Continental slope, and the carbonate compensation depth (CCD).

The estimates of metal content used for the modeling are the interpolated average values determined for each sample station using the kriging methods outlined in Section 5.2. Section 5.3 discusses the error estimates associated with the resource assessment derived from these kriging interpolations. Sections 5.4, 5.5 and 5.6 describe the scientific basis for the modeling work and the methods used. Sections 5.7 to 5.9 present the key model predictions and conclusions of the study.

### 5.2 Kriging Methods and Results

General aspects of kriging are described in Section 4. In this study, ordinary kriging<sup>5</sup> was used to generate contoured surfaces of predicted values within the areas that contain the sample data using the ESRI ArcGIS® geostatistical software. Maps of these surfaces are provided for each variable in the appendix.

Tonnage estimates apply only to the area ( $4.85 \times 10^6 \text{ km}^2$ ) included within the abundance predictions (i.e. the area that falls within one-half of the variogram range for the available survey data). Values for metal-content density (i.e. kg/m<sup>2</sup> of metal in nodules on seafloor) are estimated by multiplying the 1,549 half-degree grid point values for metal content by the associated grid values for abundance. Total tonnage for each metal is estimated by multiplying the mean values by the total area.

The values in Table 14 represent estimates for the tonnage of in-place polymetallic nodules within the Clarion-Clipperton region that are covered by available survey data. The rest of this

<sup>5</sup>  $Z(s) = \mu + \epsilon(s)$ , where  $Z$  is the predicted value at location,  $s$ ;  $\mu$  is the unknown population mean, and  $\epsilon$  is the local deviation from the mean at location  $s$ .

report uses geological modeling methods in an attempt to extend the area wherein resource estimates can be made.

**Table 14. Resource Assessment Summary of Results**

|   | <i>Abundance</i> | <i>Manganese</i> | <i>Cobalt</i> | <i>Nickel</i> | <i>Copper</i> |
|---|------------------|------------------|---------------|---------------|---------------|
| <b>Mean<br/>(kg/m<sup>2</sup>)</b>                            | 5.58             | 1.51             | 0.012         | 0.07          | 0.06          |
| <b>Median (kg/m<sup>2</sup>)</b>                              | 5.06             | 1.33             | 0.011         | 0.06          | 0.05          |
| <b>Maximum (kg/m<sup>2</sup>)</b>                             | 24.22            | 7.71             | 0.059         | 0.36          | 0.33          |
| <b>Minimum (kg/m<sup>2</sup>)</b>                             | 0.01             | 0.00             | 0.000         | 0.00          | 0.00          |
| <b>Std. Dev. (<math>\sigma</math>)<br/>(kg/m<sup>2</sup>)</b> | 5.38             | 2.61             | 0.036         | 0.15          | 0.15          |
| <b>Mean Standard<br/>Error (<math>\sigma/\sqrt{n}</math>)</b> | 0.137            | 0.066            | 0.001         | 0.004         | 0.004         |
| <b>Tonnage<br/>(10<sup>6</sup>-metric)</b>                    | 27,100           | 7,300            | 58            | 340           | 290           |
| <b>Estimated Error,<br/>tons (10<sup>6</sup>-metric)</b>      | 660              | 370              | 5             | 20            | 20            |

### 5.3 Propagation of Errors

Each resource estimate shown in Table 14 can be derived as the product of an estimated mean metal concentration ( $m$ ) and the mean nodule abundance ( $a$ ), multiplied by the area included in the kriging surface. The estimated relative error ( $e$ ) of this product for each metal (i.e. fraction of the calculated tonnage estimate) is calculated from the associated uncertainties (in this case, the mean standard error) of these terms ( $u_m$  and  $u_a$ ) as follows:

$$e = \sqrt{\left(\frac{u_m}{m}\right)^2 + \left(\frac{u_a}{a}\right)^2}$$

The estimated absolute errors (in tons of metals) are estimated by multiplying these relative errors by the tonnage estimates, as shown in the bottom row of this table.

### 5.4 Hypothesis

The general hypothesis for metal accumulation (specifically Mn, Ni and Cu) in the CCZ polymetallic nodule deposits is illustrated in Figure 12.

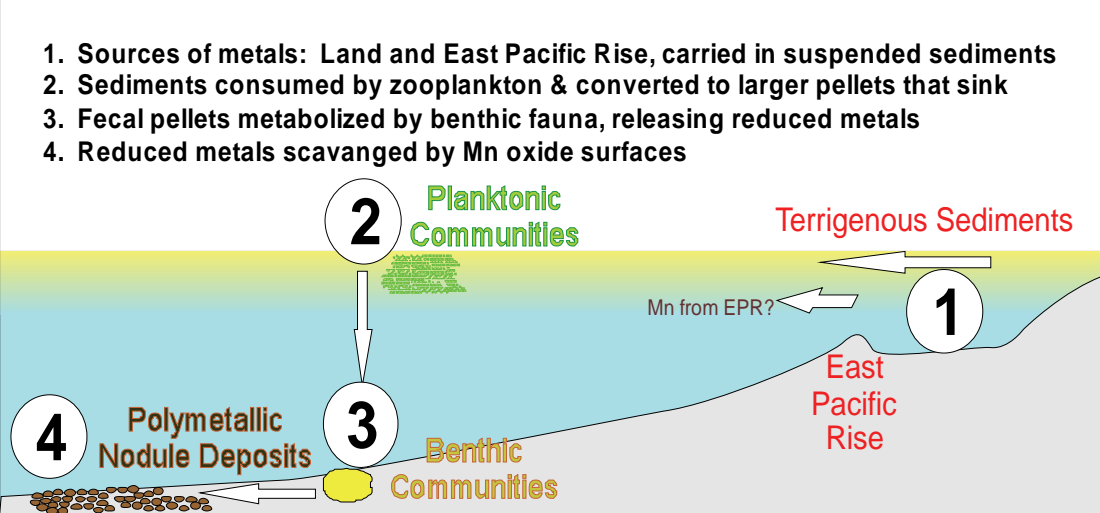


Figure 12. General Formation Model

It is based on ideas originally introduced by Greenslate, Frazer and Arrhenius (1973), which have been refined here as the basis of a regression model. Cobalt (Co), which also is an important valuable metal of nodule composition, is not included in this statistical study, since it is believed to accumulate via hydrogenetic processes that are independent from the biogeochemical model described below (Halbach 1986). Iron (Fe) which is the main antagonist to Mn in nodule composition, exists in ocean water as colloidal Fe-oxyhydroxide particles and is mainly supplied to Mn nodule growth after release to the water column due to dissolution of calcareous skeletons (Halbach and Putenanus 1984).

The general sequence of metal accumulation is proposed to be as follows:

The primary metal sources of Mn, Ni and Cu to the oceans, and presumably for these deposits, are believed to be from continental run-off, volcanogenic and atmospheric sources. The terrigenous metals exist as dissolved ions and complexes or are adsorbed to the surfaces of fine-grained particles that carry them westward within the North Pacific current. Volcanogenic metal injected into the water column from the East Pacific Rise probably consists predominantly of Mn (Koski, German and Hein, 2003). Some portion of the dissolved and/or adsorbed Mn may reach surface layers of the Pacific Ocean, and then be transported to the west (Kennett, 1982). By the time these metals reach the deposit sites in the CCZ, the postulated terrigenous, volcanogenic and atmospheric sources would not be distinguishable from each other.

Most of the fine-grained organic and inorganic particles in surface waters, which are mainly products of the biological processes in the photic zone, are too small to sink directly to the seafloor. However, these, as well as dissolved metals, can be taken up by the plankton in their organic tissue and shells during their life and growth, and later through adsorption processes after death. Some of the dissolved metals are also taken up at the particle surfaces and are released throughout the deeper water column (Chester, 2003). One very important particle type for the proposed vertical transport to the seafloor, especially for Mn, is fecal pellets.

Some portions of these metal-laden organic particles are deposited on the seafloor, where they are metabolized by benthic animals and are degraded through bacterial metabolic processes. These biological processes will reduce metals and make them soluble. The main process of metal fractionation takes place under early diagenetic conditions in the pelagic siliceous ooze sediment. The organic material of the fecal pellets gets degraded, causing suboxic conditions in the pore water environment of the upper sediment layer, which consists of a semi-liquid surface layer and a sublayer with suboxic to reducing conditions reaching down to about 30 cm (Müller, Hartmann and Suess, 1988).

Under these circumstances manganese is reduced, and other metals like nickel and copper are leached from their surface positions on sediment particles such as opaline skeletons. Thus, the pore water in the sub-layer contains enhanced concentrations of dissolved metals. Since oxidizing conditions prevail at the surface of the sediment, the metals migrate upwards via diffusion through this oxidation gradient. Mn is then oxidized in the uppermost surface layer and forms phyllosilicates like todorokite or birnessite. These phyllosilicates have interstitial layers that are able to scavenge metals like Cu<sup>2+</sup> and Ni<sup>2+</sup>. This results in a selective incorporation into these manganese oxide mineral lattices (Halbach and Puteanus 1988) and explains the particular enrichment of Mn, Ni, Cu, and also Zn in the diagenetic parts of the mixed-type nodules. On the other hand, the hydrogenetic portion of nodule growth is controlled by colloidal chemical and particle surface processes: the positively charged metal ions or metal complexes are readily absorbed by the negative surface charge of the hydrated manganese oxides at the pH of seawater.

If this diagenetic model of nodule growth has a basis in fact, and if the regional trends in surface water circulation and biological primary productivity have been persistent for the past several million years, then the metal content of the polymetallic nodules in the CCZ should reflect the intensity of the biological processes that are evoked to explain the metal transport from the surface waters to the deep water precipitation sites and the re-arrangement of metals during early sediment diagenesis.

Nodules richest in Cu and Ni have Mn/Fe ratios of about 5 and occur in the central part of the CCZ. Farther east, in the equatorial belt of high bio-productivity off the coast of the Americas, the surface primary productivity reaches very high levels, much higher than occur in the CCZ regions with high nodule occurrence. This results in the formation of diagenetic nodules with very high values of Mn. This is well documented in the Peru Basin (Halbach, Marchig, and Scherhag, 1980). Both areas (the CCZ as well as the Peru Basin) can be considered as one common biogeochemical system.

The main reason for the Mn enrichment in the nodules of the Peru Basin is the more pronounced diagenetic Mn flux to the sediments. Since reduced Mn<sup>2+</sup> can also be taken up by the phyllosilicate lattice, these Mn<sup>2+</sup> ions enter into the layered crystal structure and compete with Ni and Cu for interlayer positions. The result is that the nodules formed underneath areas of higher surface bioproductivity have more Mn and respectively a higher Mn/Fe ratio, but less Cu and Ni. These considerations show that the optimum conditions for developing nodules with high values of Ni and Cu is not related to maximum growth rates or maximum Mn concentrations, but rather to intermediate conditions.

Since the data from the very Mn-rich Peru Basin nodules are not included in this study, this enrichment in Mn and depletion in Ni and Cu caused by very high bioproductivity does not appear in the regression calculations presented here, and Mn, Ni and Cu coincide in the plot versus bioproductivity at intermediate surface chlorophyll values (Figure 13).

Also important to this model is a hypothesized balance between increasing supply of metals from biogenic sedimentation and the increasing dilution of metals from excess biogenic sedimentation (Figure 13).

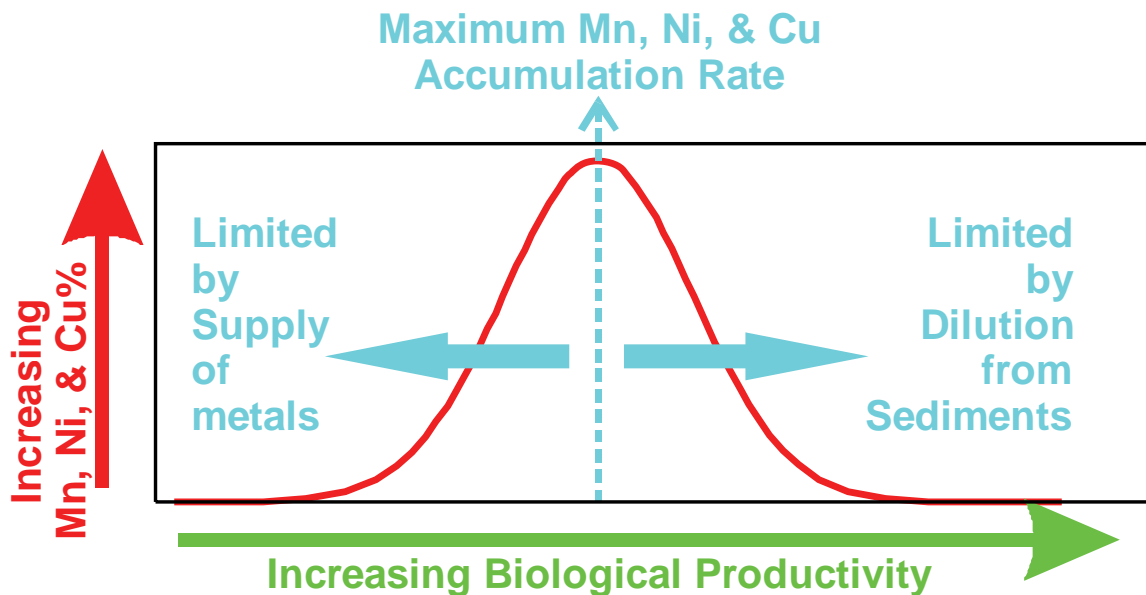


*Figure 13. Hypothesized Optimum Level of Biological Productivity for Nodule Growth*

At very low levels of biological activity, the supply of reduced metals to the seafloor is insufficient to produce substantial nodule deposits. At the other extreme, under regions with relatively high biological activity, as found in the eastern tropical Pacific and near the equator, the flux of organic matter will exceed the rates at which the benthic nodule-forming processes can extract the adsorbed metals, and deposits with high values of Mn, but low Ni and Cu, will form. The Peru Basin in the eastern tropical Pacific is one example of this high surface bioproductivity, which is about three times more than in the CCZ. The nodules there have Mn/Fe ratios up to about 20, thus representing a kind of end-member composition for the diagenetic type of manganese nodules (Halbach, Marchig and Scherhag, 1980).

The following section describes the method used in this study to test the applicability of these concepts to the CCZ polymetallic nodule deposits. The general objective is to use the environmental variables that characterize these processes as proxies for deposit formation and, using non-linear regression techniques, to establish quantitative relationships between them and deposit metal content.

## 5.5 Proxy Variables

The three proxy variables used in this study are:

### 5.5.1 Chlorophyll (Chlor)

The chlorophyll content in surface waters is closely related to the level of biological activity taking place and also to the export productivity at the site, (i.e. the flux rate of biogenic material out of surface waters). In this study we use the estimates of chlorophyll content that were determined by blending historical archives of in situ (National Oceanographic Data Center) and satellite (Coastal Zone Color Scanner) chlorophyll data, which were combined using the blended analysis method

(Reynolds, 1988) in an attempt to construct an improved climatological seasonal representation of global chlorophyll distributions (Gregg and Conkright, 2000). These data are available as seasonal and annual averages. Figure 14 shows the annual average used in the modeling runs described here.

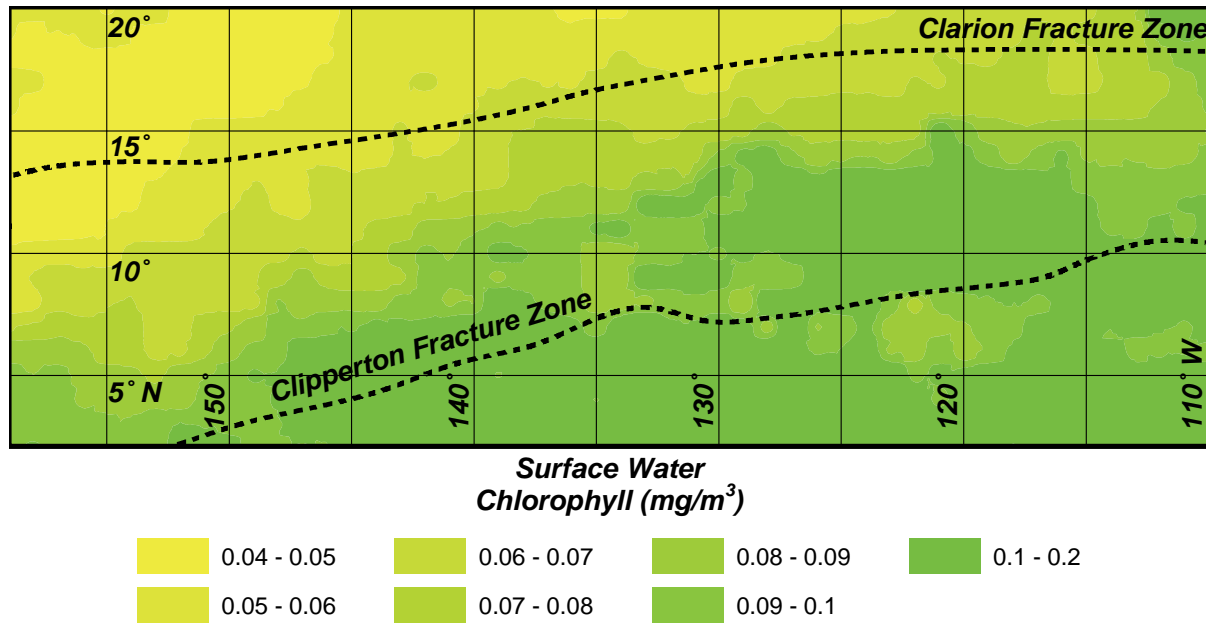


Figure 14. Chlorophyll in Surface Waters of the Clarion-Clipperton Region

### 5.5.2 Distance from East Pacific Rise and North American Continental Slope ( $F_{\text{epr}}$ )

If the sources of metals are to the east, then there should be some gradient of decreasing metal content from east to west as the deposit sites get farther from the EPR and West Coast of North America. For each sampling station, a factor ( $F_{\text{epr}}$ ) is calculated to be used in the modeling, which decreases with the square of the distance from the East Pacific Rist (EPR), which is used as a simple proxy for distance from both the EPR itself and West Coast of North America. The factor ( $F_{\text{epr}}$ ) is defined as follows:

$$F_{\text{epr}} = 10 * \sum(1/d^2)$$

Where  $d$  is the great-circle distance from the sample station to a point selected on the EPR or base of the North American slope. Sixty-three points were selected for this exercise, spaced approximately uniformly from about  $3^\circ \text{ S}, 130^\circ \text{ W}$  to  $35^\circ \text{ N}, 122^\circ \text{ W}$ . Figure 15 shows the points used to calculate this factor for the modeling runs.

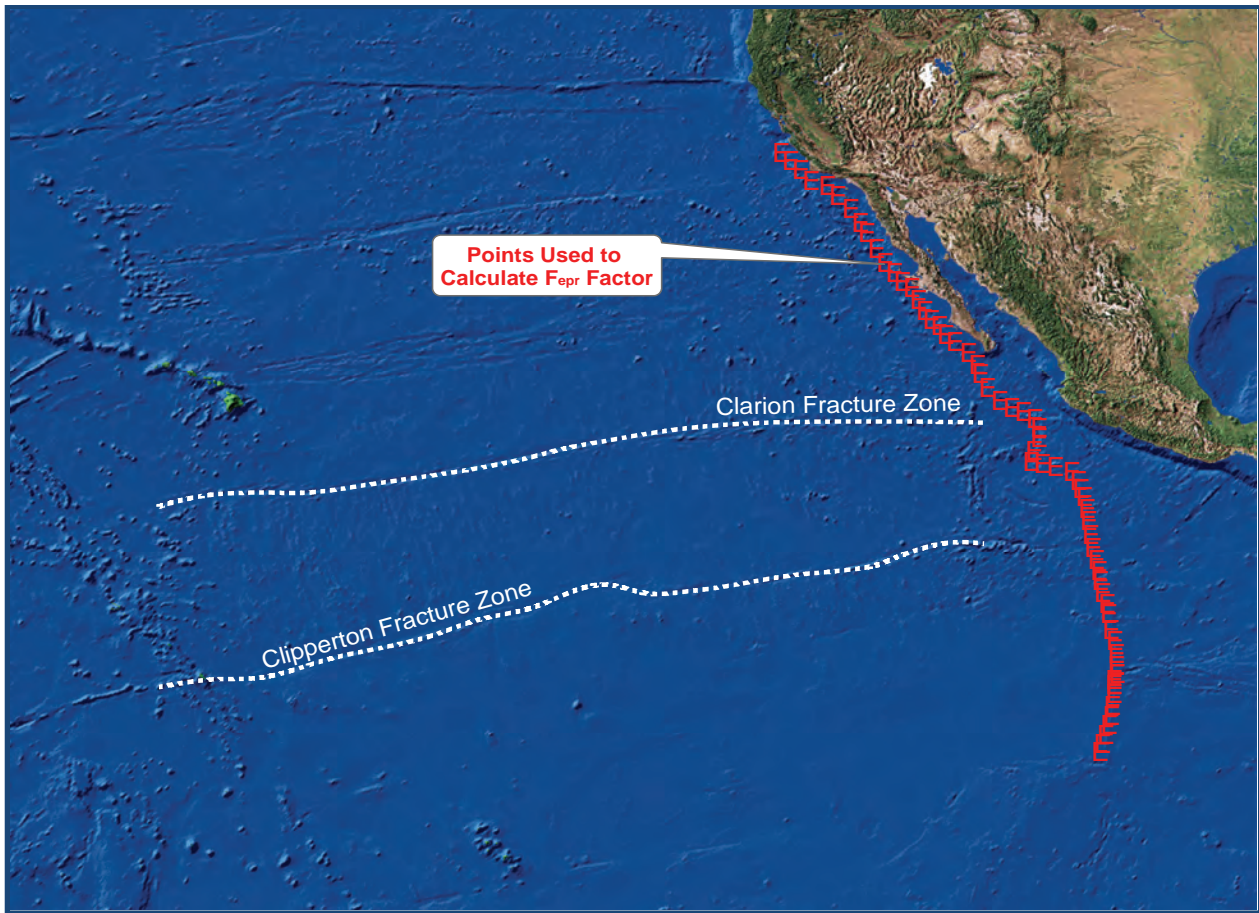


*Figure 15. Points on East Pacific Rise and Coastal Shelf Used in Modeling*

### **5.5.3 Distance from CCD (del)**

In order to estimate the depth of the CCD throughout the CCZ for this study, smear-slide data and chemical analyses of several hundred sediments collected mainly on Scripps Institution of Oceanography and Lamont-Doherty Geological Observatory cruises have been analyzed by Professor David Cronan of Imperial College, London. The method of Aplin and Cronan (1985) was used to estimate the CCD from these data. The sediment data were divided into three classes (carbonate rich, carbonate bearing and carbonate free), and plotted against depth and latitude. A best estimate of the CCD was then selected on the basis of the shallowest depth that low or zero calcium carbonate was found in the sediments. Some anomalies based on this approach could result from carbonate-rich sediments occurring below the CCD due to slumping, or carbonate-poor sediments occurring above the CCD due to outcrops of previously buried carbonate-poor strata at the seafloor exposed by erosion or tectonic activity. Nevertheless, the approach used gives a reasonable estimate of the CCD.

Professor Cronan generated a matrix of CCD values ( $5^{\circ}$  longitude  $\times 1^{\circ}$  latitude) for the entire CCZ area of interest. These values were used to generate a continuous surface of values for the CCZ using the kriging algorithms discussed before. The variable of interest is the difference between the water depth and the CCD for any particular seafloor location. Using the bathymetric data provided

to the project by Dr. Lindsay Parsons or, when available, the water depths measured for each sampling station, values of **del** (water depth – CCD) were determined. Figure 16 shows the distribution of **del** within the CCZ.

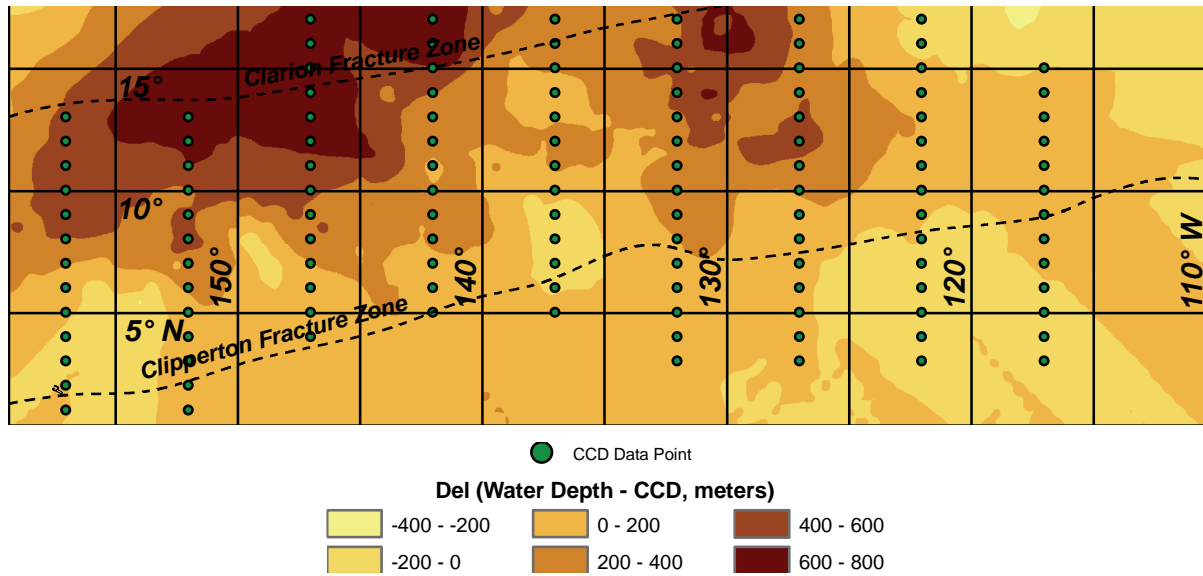


Figure 16. Water Depth minus CCD (**del**) in the Clarion-Clipperton Zone

## 5.6 Procedures

To identify empirical relationships between metal content and these proxy variables a non-linear Gauss-Newton regression method was used that was available in the Systat<sup>®</sup> statistical software package. Because the general hypothesis assumes that primary productivity (approximated using the chlorophyll concentration in surface waters) should be related in a non-linear way to metal content (Figure 13), we used a regression equation that is second order with respect to chlorophyll content. Because of the way we calculated  $F_{epr}$ , the regression should be linear with respect to this factor. Because we have no *a priori* reason to suspect that **del** should be related to metal content in a non-linear way, we also represent it as a linear term in the regression models. Regression equations were calculated using all possible combinations of these three proxy variables.

The statistic used to estimate the success of the regression is the ‘corrected’  $R^2$ .  $R^2$  is the square of the Pearson correlation coefficient ( $r$ ) between the observed values and the predicted values. It ranges between 0 and 1 and approximately represents the fraction of variance of the dependent variable (in this case metal content) that can be accounted for by the polynomial expression.

The general procedure is as follows:

For each sample station location in the database, the interpolated estimate of metal content using ordinary kriging was determined. The kriging value instead of the raw data was used in an effort to minimize the local variance (i.e. not related to spatial variation) that must be included in the regression. Previous runs using the raw metal content data returned  $R^2$  values ranging between 0.1 and 0.2.

An interpolated value for chlorophyll at the sample station locations was determined from the published values (a one-degree grid, see Section 5.5.1) using the ‘Prediction’ function in ArcView® and extracting the values of  $F_{epr}$  and **del** at each station. These data were then integrated into a spread-sheet that included both the dependent and proxy variables for every sampling station. The spreadsheet was inputted into the Systat® software and the non-linear regression module was used to test the hypothesized regression models.

## 5.7 Results

The **del** proxy variable is statistically independent from the other two (**del-Chlor**;  $r = -0.10$ ; **del-Fepr**;  $r = -0.17$ ), and Chlor exhibits only a weak positive correlation with Fepr ( $r = 0.54$ ), justifying their application as independent variables in the regression analysis. The value of **del** varies from -372 to +1,188m, indicating that polymetallic nodules deposits do occur both above and below the CCD. However, only 3.1 per cent of the values are less than zero (337 of 10,623 values), consistent with the common observation that the vast majority of the CCZ deposits occur below the CCD. Thus the regression is heavily weighted to the positive values. All but a single outlier are less than 800m. Chlor varies by a factor of about three, between 0.046 and 0.124 mg/m<sup>3</sup>. Fepr ranges between 1.1 and 6.2; however, all but two outliers are between 1.1 and 4.1. The histograms of these variable distributions are presented in Figure 17.

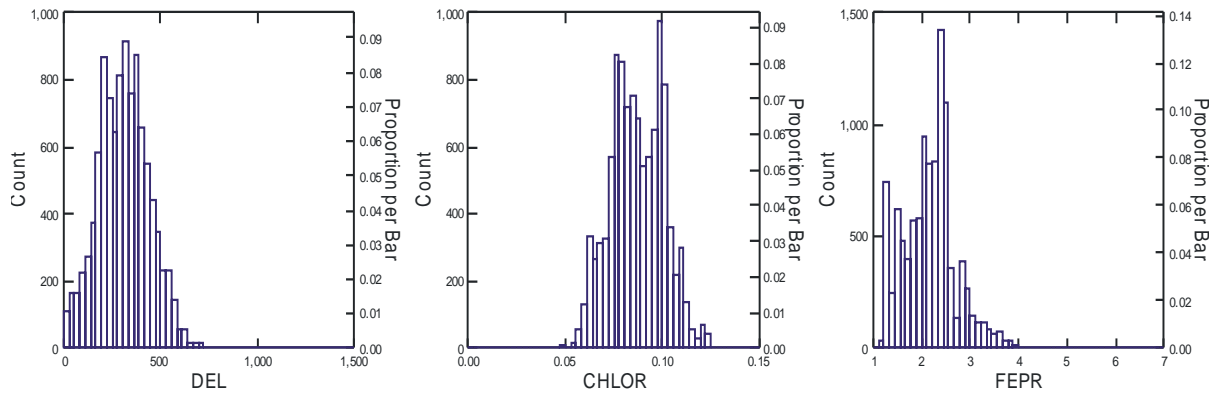


Figure 17. Histograms of Proxy Variables

### 5.7.1 Manganese

The results from the regression tests for manganese metal content are summarized in Table 15. As the table shows, the regression model using the proxy variables **Chlor** and **del** can account for about 56 per cent of the Mn variance, while using **Chlor** alone accounts for almost 50 per cent of the variance. The proxy variable  $F_{epr}$  appears to have little predictive value for Mn.

**Table 15. Manganese Regression Model Results**

| <b>Chlor</b> | <b>del</b> | <b>F<sub>epr</sub></b> | <b>r</b> | <b>R<sup>2</sup></b> |
|--------------|------------|------------------------|----------|----------------------|
| X            |            |                        | 0.70     | 0.49                 |
|              | X          |                        | 0.14     | 0.02                 |
|              |            | X                      | 0.34     | 0.13                 |
| X            | X          |                        | 0.75     | 0.56                 |
| X            |            | X                      | 0.70     | 0.49                 |
|              | X          | X                      | 0.41     | 0.17                 |
| X            | X          | X                      | 0.75     | 0.56                 |

r = Pearson Correlation Coefficient  
R<sup>2</sup> = Coefficient of Determination  
= r<sup>2</sup>

### 5.7.2 Nickel

The results from the regression tests for nickel content are summarized in Table 16. As the table shows, the regression model using the proxy variables **Chlor** and **del** or **Chlor** and **F<sub>epr</sub>** can account for about 48 per cent of the Ni variance, while using chlorophyll alone accounts for 44 per cent of the variance.

**Table 16. Nickel Regression Model Results**

| <b>Chlor</b> | <b>del</b> | <b>F<sub>epr</sub></b> | <b>r</b> | <b>R<sup>2</sup></b> |
|--------------|------------|------------------------|----------|----------------------|
| X            |            |                        | 0.66     | 0.44                 |
|              | X          |                        | 0.05     | 0.003                |
|              |            | X                      | 0.07     | 0.005                |
| X            | X          |                        | 0.69     | 0.48                 |
| X            |            | X                      | 0.69     | 0.48                 |
|              | X          | X                      | 0.07     | 0.005                |
| X            | X          | X                      | 0.69     | 0.48                 |

r = Pearson Correlation Coefficient  
R<sup>2</sup> = Coefficient of Determination  
= r<sup>2</sup>

### 5.7.3 Copper

The results from the regression tests for copper content are summarized in Table 17. As the table shows, the regression model using the proxy variables Chlor and del can account for about 49 per cent of the Cu variance, while using chlorophyll alone accounts for 39 per cent of the variance.

**Table 17. Copper Regression Model Results**

| <i>Chlor</i> | <i>del</i> | <i>F<sub>epr</sub></i> | <i>r</i> | <i>R<sup>2</sup></i> |
|--------------|------------|------------------------|----------|----------------------|
| X            |            |                        | 0.62     | 0.39                 |
|              | X          |                        | 0.46     | 0.21                 |
|              |            | X                      | 0.18     | 0.034                |
| X            | X          |                        | 0.70     | 0.49                 |
| X            |            | X                      | 0.65     | 0.42                 |
|              | X          | X                      | 0.32     | 0.10                 |
| X            | X          | X                      | 0.71     | 0.51                 |

*r* = Pearson Correlation Coefficient  
*R<sup>2</sup>* = Coefficient of Determination  
 $= r^2$

## 5.8 Predicted Metal Content

Figure 18, Figure 19 and Figure 20 present, respectively, the predicted Mn, Ni, and Cu concentrations in the CCZ polymetallic nodule deposits.

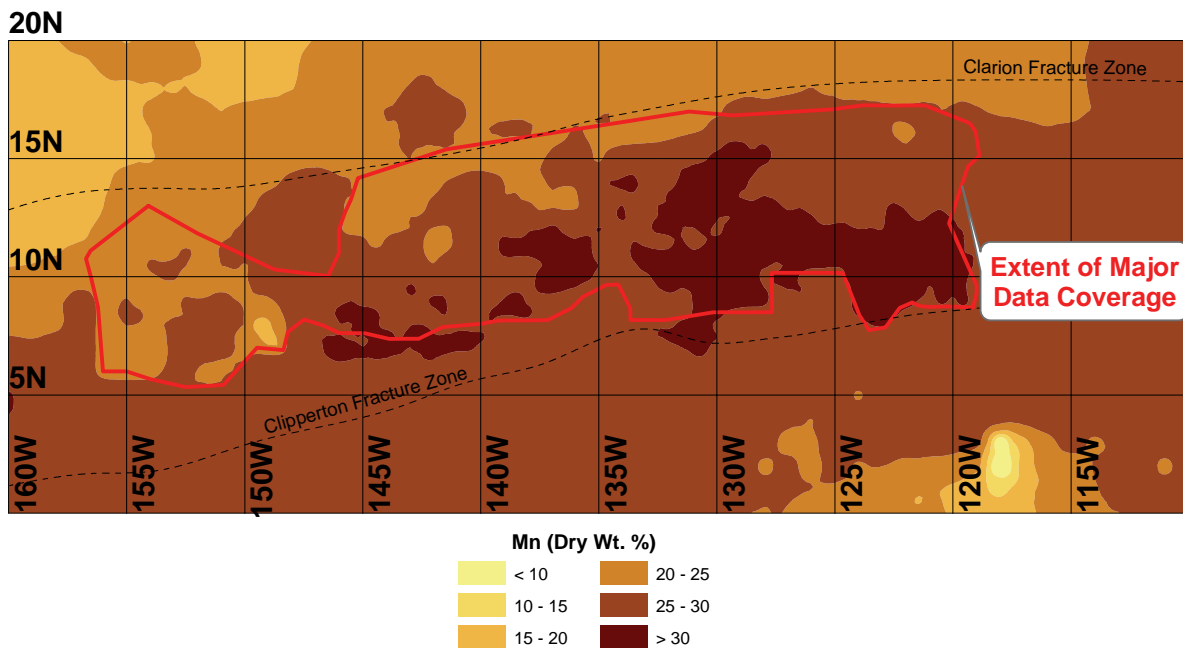


*Figure 18. Predicted Mn Content in the CCZ*

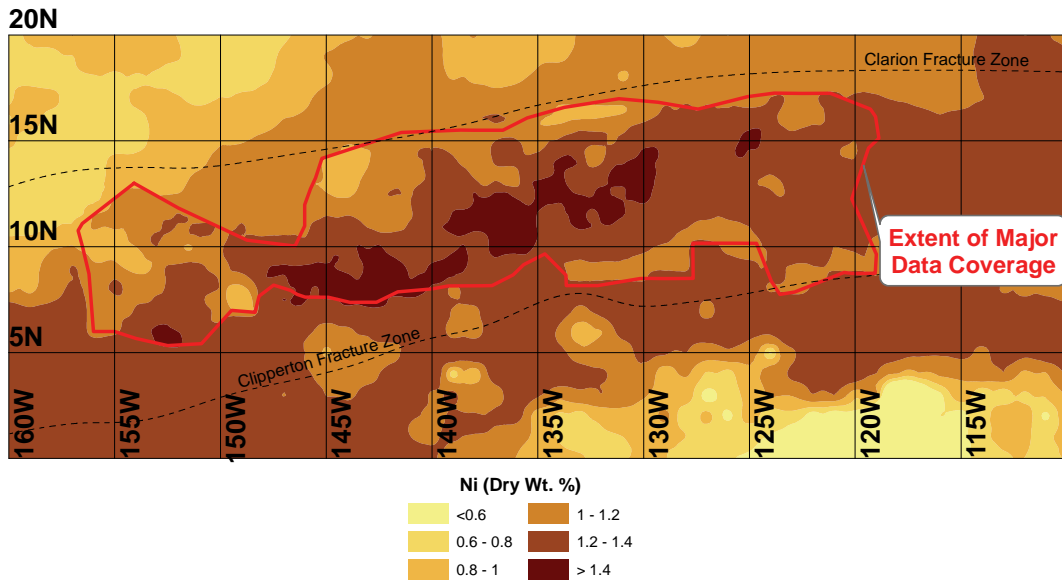


Figure 19. Predicted Ni Content in the CCZ

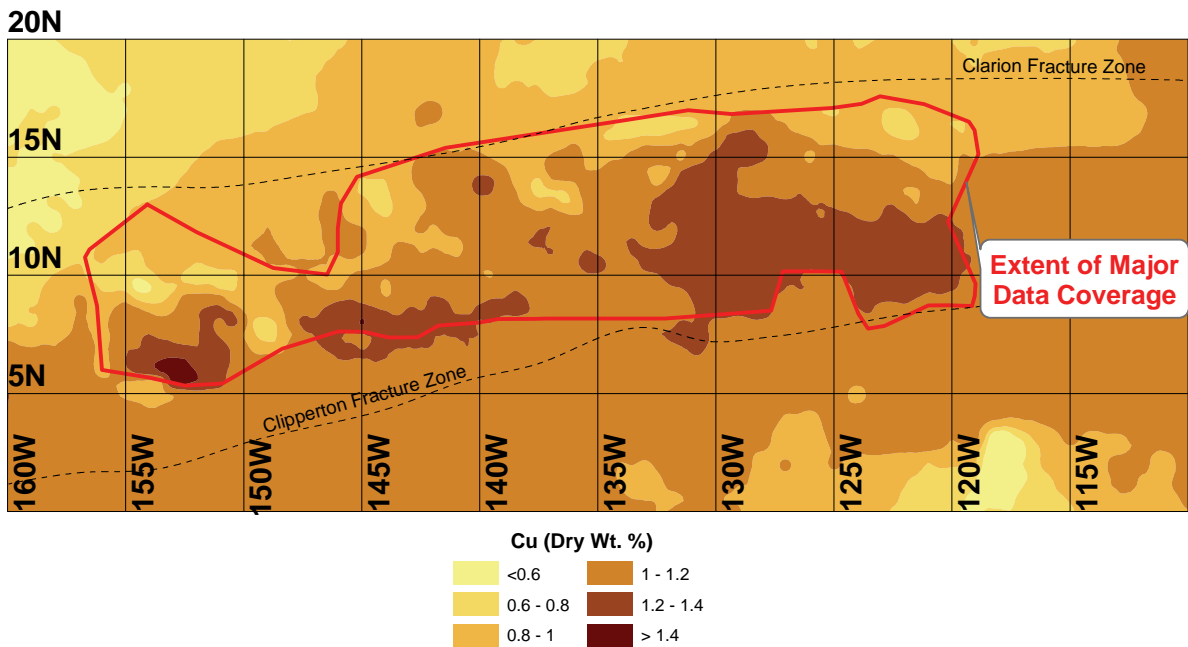


Figure 20. Predicted Cu Content in the CCZ

The contours are generated using ordinary kriging of a 0.5-degree grid. Grid points within the delimited 'Extent of Major Data Coverage' were generated by the original station data. Outside of this delimited area, the values at each grid point were calculated using the regression equation with the best fit.

## 5.9 Discussion and Conclusions

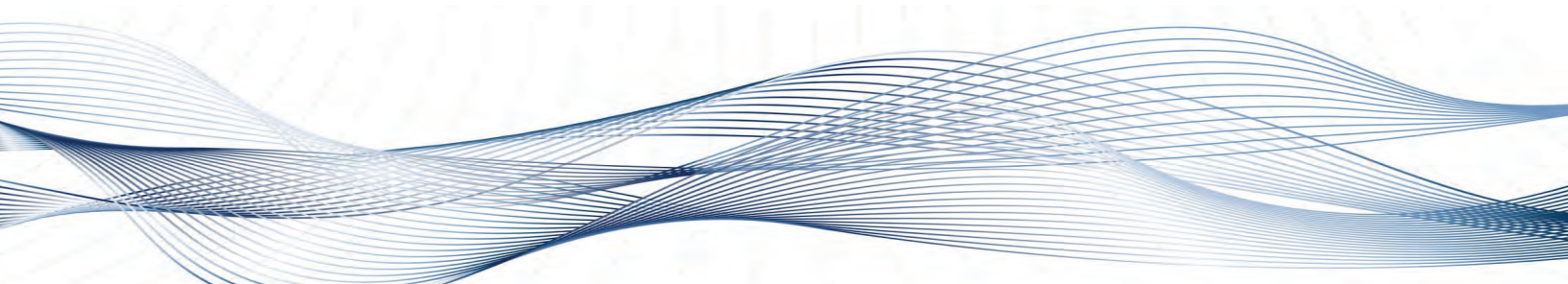
Given the diversity of sources for the samples used in the analysis and the intrinsic variability of geological samples in general, the quality of fit of the regression modeling with surface-water chlorophyll levels provides substantial support for the general model of metal accumulation (for Mn, Ni and Cu) presented above. As noted in Section 5.6, regression modeling using the raw metal values generated  $R^2$  values between 0.1 and 0.2. The kriging process assigns weights of interpolation on the basis of spatial covariance (i.e. through the variogram). Thus, the significant improvement of the fit when the kriging values, rather than the raw data are used, strongly suggests that the observed relationships between surface-water chlorophyll and metal content are real and not some statistical artifact.

The fact that the other two proxy variables used in the regression (**del** and **Fepr**) only improved the fit by at most a few percentage points suggests that they may not be as important in the concentration of these metals in the polymetallic nodule deposits. The regression using del and Chlor with Cu may be an exception to this general conclusion, since the R<sup>2</sup> value increases substantially, from 0.39 to 0.49 with the addition of this proxy variable to the regression (see Table 18). The regression coefficient with del is positive, indicating that the nodule Cu content is directly proportional to the vertical distance between the deposit site and the CCD. This suggests that Cu accumulation in the nodules is more sensitive than the other metals to the dissolution rate of carbonates on the seafloor, perhaps indicating that a relatively higher percentage of this metal is bound within the plankton shells rather than adsorbed on the surfaces of the sediments.

**Table 18. Comparison of  $R^2$  Values between Metals**

| <i>Proxy Variables in Regression</i> | <i>R<sup>2</sup></i> |           |           |
|--------------------------------------|----------------------|-----------|-----------|
|                                      | <i>Mn</i>            | <i>Ni</i> | <i>Cu</i> |
| <b><i>Chlor</i></b>                  | 0.49                 | 0.44      | 0.39      |
| <b><i>Chlor, del</i></b>             | 0.56                 | 0.48      | 0.49      |
| <b><i>Chlor, Fepr</i></b>            | 0.49                 | 0.48      | 0.42      |
| <b><i>Chlor, del, Fepr</i></b>       | 0.56                 | 0.48      | 0.51      |

## 6. SPATIAL DECISION SUPPORT SYSTEM MODELING



### 6.1 Introduction

The objective of this part of the study is to develop Spatial Decision Support System (SDSS) models to estimate the mineralization potential in selected areas of the CCZ where polymetallic nodule abundance and metal content data are not available. There are many key ore-forming controlling factors in nodule mineralization that potentially could be used in SDSS models as proxies for the occurrence of high-value nodule deposits. These include: age and growth rate of nodules; size and composition of the nodule nucleus; water depth and paleo-water depth; seafloor topography; Carbonate Compensation Depth (CCD); chemical composition of sea waters; deep water currents and paleo-currents; Eh at the interface between bottom water and sediments; the composition, thickness and age of sediments; the geothermal gradient of sediment profiles; fragmental or chemical sedimentation and biological productivity; and benthic biological activity.

The spatial decision support system (SDSS) is an interactive, computer based system designed to support users in achieving more effective decision making while solving semi-structured spatial decision problems. It was developed in response to the need to expand Geographic Information System (GIS) capabilities for tackling complex, ill defined special decision problems. However, according to the technical requirements of the input in SDSS modeling, every set of data used as a proxy for high-value deposit formation should cover the entire study area. Based on the actual available data, the data types selected in this SDSS modeling study included the spatial distribution, abundance and metal content of discovered nodule deposits, sediment types, primary productivity, CCD, water depth and topographical types of seafloor.

The study was based on data sets compiled by other experts that include bathymetry, topography, sediment type, CCD and surface chlorophyll. Specific techniques employed in the study include Weights of Evidence Modeling, Fuzzy Logic, Logistic Regression and Artificial Neural Network (ANN) techniques.

### 6.2 Data Used in the Study

The following data sets and protocols are used in this study.

#### 6.2.1 ***Nodule Abundance and Metal Content***

The spatial distribution of discovered nodule deposit abundance and metal content are the most fundamental guides to nodule occurrence at other locations and provide the first-order means

for prediction of the potential sites of undiscovered nodule resources. The data sets used in this study are the tenth degree grid data described above in Section 3.2. In order to distinguish the area that can be defined as the ‘ore deposit’ from the surrounding mineralized area, we choose those areas with abundance of manganese nodules higher than  $2 \text{ kg/m}^2$  as defining the area that contains the known deposit (Figure 21).

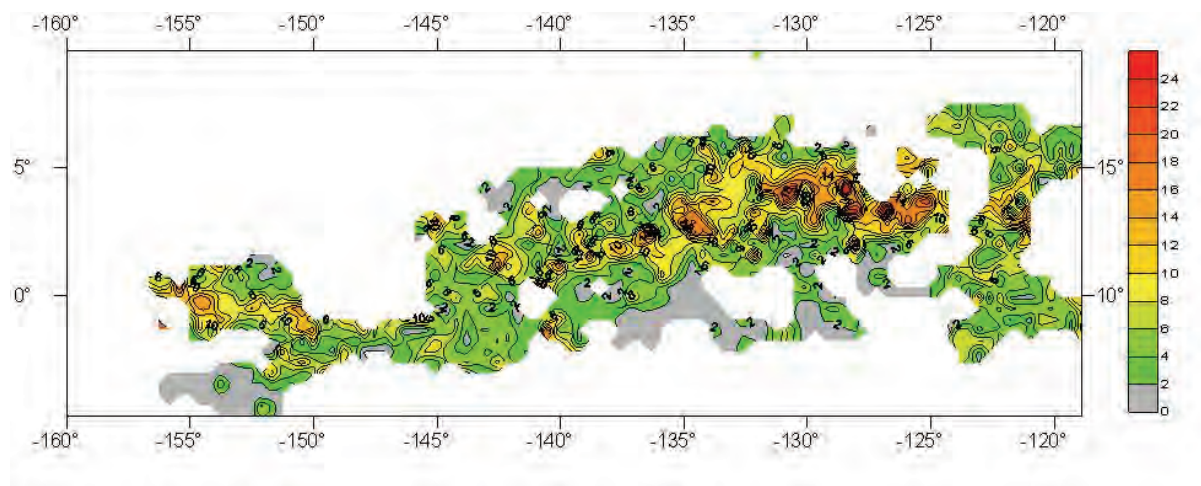
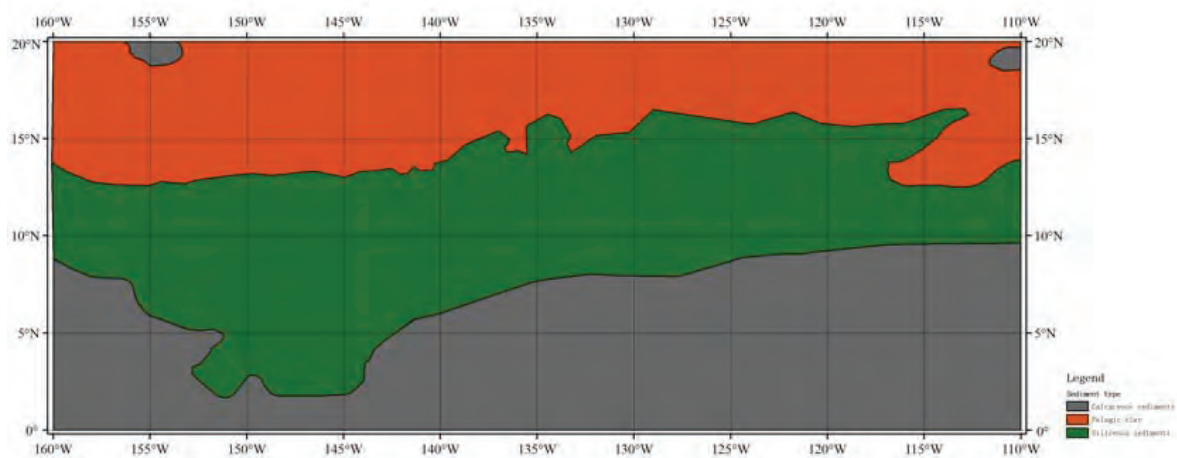


*Figure 21. Distribution of Nodule Abundance in the CCZ (edited after grid data from Morgan, 2008)*

### 6.2.2 Sediment types

Many studies have observed that nodules are hosted primarily by siliceous sediments, and secondarily on by pelagic clays, and occur much more rarely on calcareous sediments. Therefore in this study we have designated the areas covered with siliceous sediments as the most favourable for nodule formation, those areas covered with pelagic clays as less favourable, and those covered with calcareous sediments as unfavourable for deposit occurrence (Figure 22).



(Modified from Kazmin, 2003 and Halbach *et al.*, 1988)

*Figure 22. Distribution of Seafloor Sediment Types in the CCZ*

### 6.2.3 Primary productivity

As discussed in Section 5, biological activities, and particularly surface-water primary productivity levels, are believed to be very important in promoting nodule formation by providing metal inputs for nodule growth in the form of settling biogenic particles.

As shown through a comparison of Figure 21 with Figure 23, there are apparent similarities between the surface productivity (assumed here to be proportional to surface chlorophyll levels) and the distribution of nodule deposits in the CCZ.

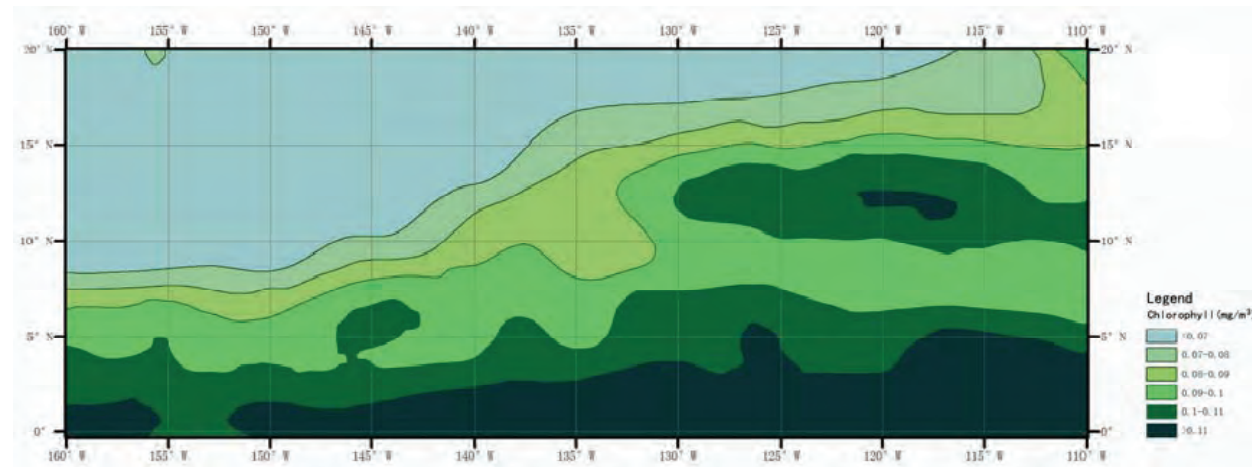


Figure 23. Surface Chlorophyll Levels in the CCZ

### 6.2.4 CCD Minus Water Depth

As discussed in more detail in Section 5.5.3, many researchers also believe that nodule formation is related to the Carbonate Compensation Depth (CCD). The CCD is the depth within the ocean water column at which the rate of dissolution of calcium carbonate (a rate that increases with water depth) is balanced by the rate of calcium carbonate sedimentation. If the seafloor lies above the CCD, nodule formation will be inhibited by dilution from precipitating carbonates; below the CCD this would not be the case. Therefore, in this study, sites where the CCD is at or above the seafloor are designated as favourable for the formation of nodules, while sites where the CCD is below the seafloor are designated as unfavourable for the formation of nodules (see Figure 24)

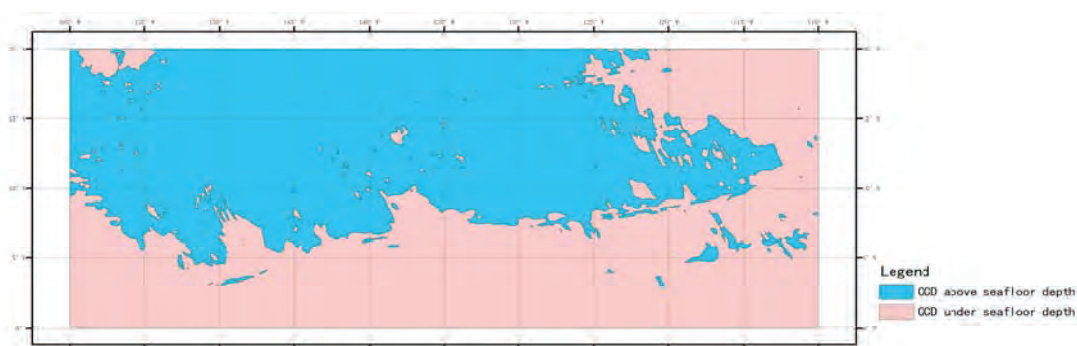


Figure 24. Distribution of the value of the CCD minus water depth

### 6.2.5 Regional Bathymetric Regimes

The bathymetric regimes in the CCZ can be classified into five types (see Figure 25):

- A. **Oceanic Rise:** Adjacent to and including the East Pacific Rise.
- B. **Seamount Chains:** Consisting of the Hawaiian and Line Island seamount chains in the northwest and west.
- C. **Abyssal Hill Province:** The region of sharply defined hills that rise from the abyssal plains to elevations no higher than about 1,000m.
- D. **Seamounts and Abyssal Hill Provinces:** Includes the two marginal regions to the east and west of the Abyssal Hill province. Includes volcanoes (seamounts) that rise more than 1,000 m above the ocean among bathymetry generally characterized as abyssal hills.
- E. **Transform Fracture Zones:** Clarion and Clipperton transform fault fracture zones.

The abundance and metal content of nodules are also related to seafloor bathymetry. Based on the distribution of the known deposits, the following designations for the above bathymetric regimes, ranging from most favorable for nodule deposit occurrence to least favorable are assigned.

$$C > D > A = B = E$$

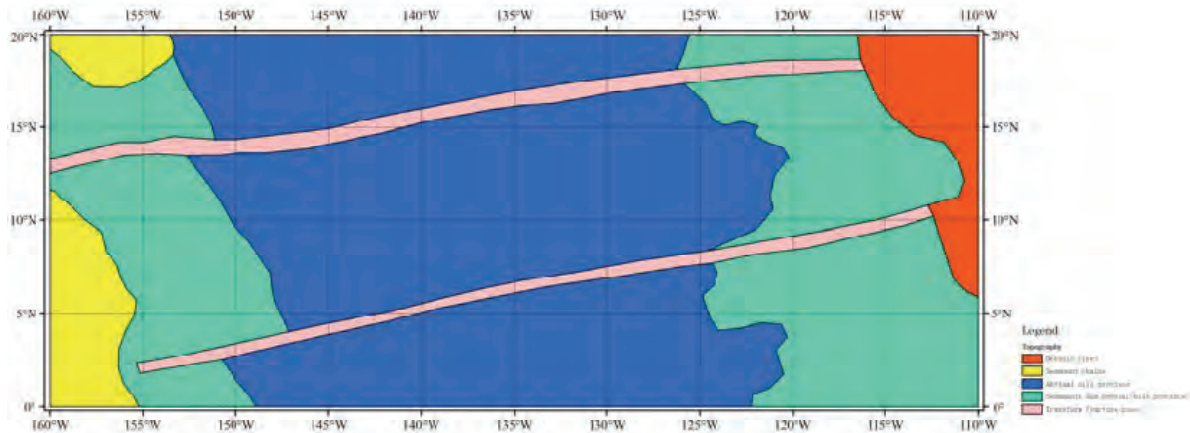


Figure 25. Bathymetric Regimes in the CCZ

## 6.3 Theory

For the SDSS modeling studies, four methods were employed- namely weights of evidence modeling, Logistic regression, Fuzzy logic and radial basis function (Artificial Neural Network method). The entire theoretical background of the methods is described in detail in the full report.

## 6.4 Input Data Used in the SDSS Models

### 6.4.1 Grid Cells

For this study, a grid unit size of 15' latitude  $\times$  15' longitude, resulting in a total of 16,000 grid cells in the study area was chosen. (see Figure 26). The following sections describe the data sets and protocols used to assign values to this grid for each analytical method.

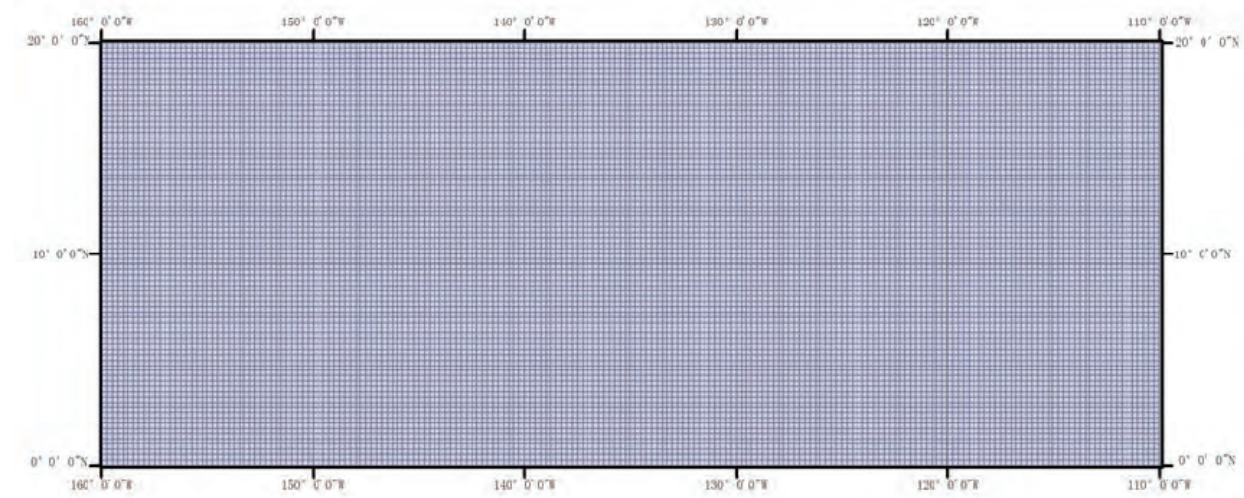


Figure 26. Grid Cell Specification in the CCZ

### 6.4.2 Input Data, Weights of Evidence and Logistic Regression

Original data from the geological evidence variable layers (see Section 6.2), were determined for each grid cell by overlapping the grid layer on these geological evidence variables respectively (Figure 21). As discussed above, input data were transformed from the original data to binary data (0 or 1), according to assumed relationships between the variable value and nodule formation. A value of 1 is assigned to values that are believed to correlate with nodule occurrence, and a value of 0 is assigned to values that are believed to indicate unfavourable conditions for nodule occurrence. By overlapping the geological evidence variables with the known deposit occurrences (defined here as areas with nodule abundance greater than  $2 \text{ kg/m}^2$ ; see Section 6.2.1), one can test the validity of these assumed relationships. Table 19 describes the criteria used to generate the transformed binary values used in the analysis for both Weights of Evidence and Logistic Regression.

**Table 19. Binary Transformations for Weights of Evidence and Logistic Regression**

| <i>Variable</i>  | <i>Criterion</i>                              | <i>Value Assigned</i> |
|--|---|-----------------------|
| <i>Abundance</i><br>(kg/m <sup>2</sup> )                 | ≥ 2   | 1                     |
|  | < 2   | 0                     |
| <i>Sediment Type</i>                                     | Siliceous                                     | 1                     |
|  | Pelagic clay                                  | 1                     |
|  | Calcareous                                    | 0                     |
| <i>Surface Water Chlorophyll</i><br>(mg/m <sup>3</sup> ) | < 0.07  | 0                     |
|  | 0.07 – 0.11                                   | 1                     |
|  | > 0.11  | 0                     |
| <i>Carbonate Compensation Depth (CCD)</i>                | CCD at or above seafloor                      | 1                     |
|  | CCD below seafloor                            | 0                     |
| <i>Bathymetric Regime</i>                                | Abyssal Hills                                 | 1                     |
|  | Seamounts & Abyssal Hills                     | 1                     |
|  | Oceanic Rise, Seamount chains, Fracture Zones | 0                     |

#### **6.4.3 Input Data, Fuzzy Logic and Radial Basis Function Network Modeling**

The approach here is similar to that employed above for Weights of Evidence and Logistic Regression modeling. However, fuzzy logic and radial basis function network modeling permit a relaxation of the strict binary transformation to accommodate any values between 0 and 1. The values assigned for each of the geological evidence variables are listed in Table 20.

**Table 20. Transformations for Fuzzy Logic and Radial Basis Network Modeling**

| <i>Variable</i>                                     | <i>Criterion</i>                              | <i>Value Assigned</i> |
|---|---|-----------------------|
| <i>Abundance (kg/m<sup>2</sup>)</i>                 | $\geq 2$                                      | 1                     |
|   | < 2   | 0                     |
| <i>Sediment Type</i>                                | Siliceous                                     | 0.9                   |
|   | Pelagic clay                                  | 0.3                   |
|   | Calcareous                                    | 0.1                   |
| <i>Surface Water Chlorophyll (mg/m<sup>3</sup>)</i> | < 0.07  | 0.1                   |
|   | 0.07 – 0.08                                   | 0.8                   |
|   | 0.08 – 0.09                                   | 0.9                   |
|   | 0.09 – 0.10                                   | 0.8                   |
|   | 0.10 – 0.11                                   | 0.4                   |
|   | > 0.11  | 0.2                   |
| <i>Carbonate Compensation Depth (CCD)</i>           | CCD at or above seafloor                      | 0.9                   |
|   | CCD below seafloor                            | 0.1                   |
| <i>Bathymetric Regime</i>                           | Abyssal Hills                                 | 0.8                   |
|   | Seamounts & Abyssal Hills                     | 0.7                   |
|   | Oceanic Rise, Seamount chains, Fracture Zones | 0.1                   |

## 6.5 Modeling Results

### 6.5.1 Weights of Evidence

Weights of Evidence Modeling (WoE) predicts favourable mineralized areas in a study area with posterior probability (Agterberg *et al.*, 1993; 1999). It is based on evidence layers. Based on Bayesian conditional probability, the weights of evidence layers related to a mineralization layer are mathematically calculated. Then the posterior probability in any position of the study area is calculated and target positions of undiscovered deposits are predicted. The advantage of the method is its operation on evidence layers – the most available and most direct expressive pattern to predict spatial positions.

Table 21 presents the results from this method for the CCZ deposits.

**Table 21. Calculated Results from Weights of Evidence Modeling**

| <b>Geological Evidence Variable</b>        | <b>Status</b> | <b>Total Grid Cells</b> | <b>Total with Deposit Present</b> | <b>Prior Probability (P)</b> | <b>Prior Odds (O)</b> | <b>Weight for Presence (<math>W^+</math>)</b> | <b>Weight for Absence (<math>W^-</math>)</b> | <b>Contrast (C)</b> |
|--|---------------|-------------------------|-----------------------------------|------------------------------|-----------------------|---|--|---------------------|
| Siliceous Sediments or Pelagic Clay        | Present       | 10,398                  | 3,046                             | 0.2929                       | 0.4143                | 0.5252  |  | 3.7235              |
|  | Absent        | 5,602                   | 103                               | 0.0099                       | 0.1000                |   | -3.1983                                      |                     |
| Surface Water Chlorophyll                  | Favorable     | 9,367                   | 2,617                             | 0.2794                       | 0.3877                | 0.4588  |  | 1.8623              |
|  | Unfavorable   | 6,633                   | 532                               | 0.0568                       | 0.0602                |   | -1.4035                                      |                     |
| CCD Above Seafloor                         | Present       | 8,081                   | 2,794                             | 0.3457                       | 0.5285                | 0.7686  |  | 2.4425              |
|  | Absent        | 7,919                   | 355                               | 0.0439                       | 0.0459                |   | -1.6739                                      |                     |
| Abyssal Hills or Seamounts & Abyssal Hills | Present       | 13,435                  | 3,052                             | 0.2272                       | 0.2939                | 0.1820  |  | 3.6993              |
|  | Absent        | 2,565                   | 97                                | 0.0072                       | 0.0073                |   | -3.5173                                      |                     |

Contrast values ( $W^+ - W^-$ ) indicate the correlation between a geological evidence variable and deposit occurrence. The higher the Contrast, the closer the correlation between the evidence variable and nodule occurrence. Contrasts from this table show decreasing correlations as follows:

Sediment Types > Bathymetric Regime > CCD minus water depth > surface water chlorophyll.

Figure 27 plots the posterior probability (i.e., predicted probability of finding nodule deposits) within the study area.

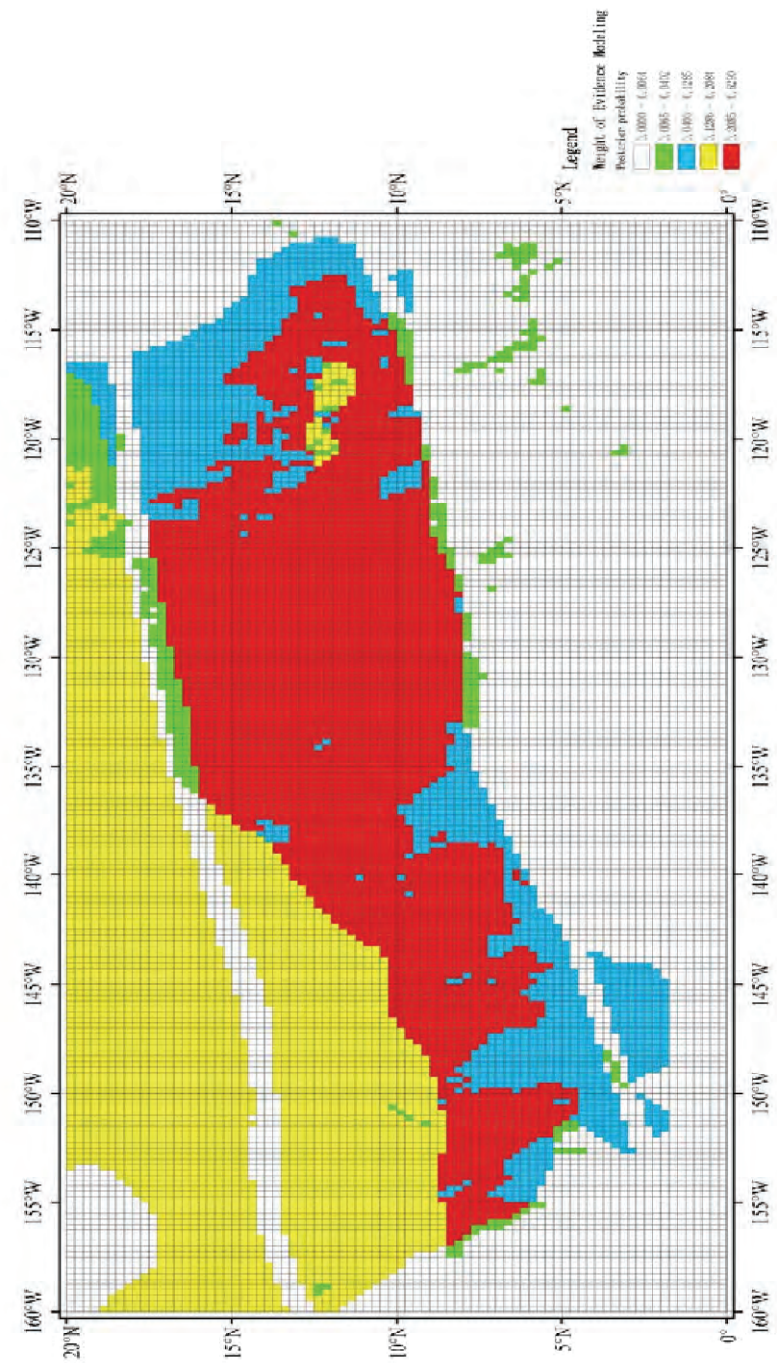


*Figure 27. Weights of Evidence Results, Posterior Probabilities in the CCZ*

This map shows that the highest probabilities are located at the middle and northern part of the CCZ and the lowest probabilities are located at the southern, southwestern, southeastern, northwestern and northeastern parts.

### **6.5.2 Logistic Regression**

Logistic Regression (LR) is a statistical method combining independent variables to generate a probability response to a dependent variable (Agterberg *et al.*, 1999). Though it may be applied to any categorical dependent variable, it is most frequently seen in the analysis of binary data, in which the dependent variable takes on only two values. Examples include survival beyond five years in a clinical trial, presence or absence of disease, responding to a specified dose of a toxin, voting for a political candidate, and participating in the labour force.

LR is also widely applied in the assessment of potential mineral resources. The posterior probabilities of mineralization in any position of the study area are calculated and target positions of undiscovered deposits are predicted by calculation of regression coefficients of the independent variables and the conditional probability in the model.

Table 22 presents the calculated regression coefficients from LR modeling. Similar to Weights of Evidence modeling, the regression coefficients show the correlations between geological evidence variables and known deposit occurrence. The higher the regression coefficient, the closer the correlation between the evidence variable and nodule occurrence. Regression coefficients from this table indicate the following sequence of decreasing correlation of the evidence variables with deposit occurrence:

Sediment Type > Surface Water Chlorophyll > Bathymetric Regime > CCD minus water depth

Though not completely consistent with the Weights of Evidence results, they both indicate that sediment type is the best indicator among the variables considered.

These regression coefficients can be used to calculate the predicted probability of finding nodule deposits, as discussed above. The resulting regression equation is:

$$P_{post} = \frac{\exp(-10.9658 + 3.3527x_1 + 3.2830x_2 + 2.4690x_3 + 2.6289x_4)}{1 + \exp(-10.9658 + 3.3527x_1 + 3.2830x_2 + 2.4690x_3 + 2.6289x_4)}$$

Using the appropriate input data for each grid cell in the CCZ we calculate the probability distribution shown in Figure 28.

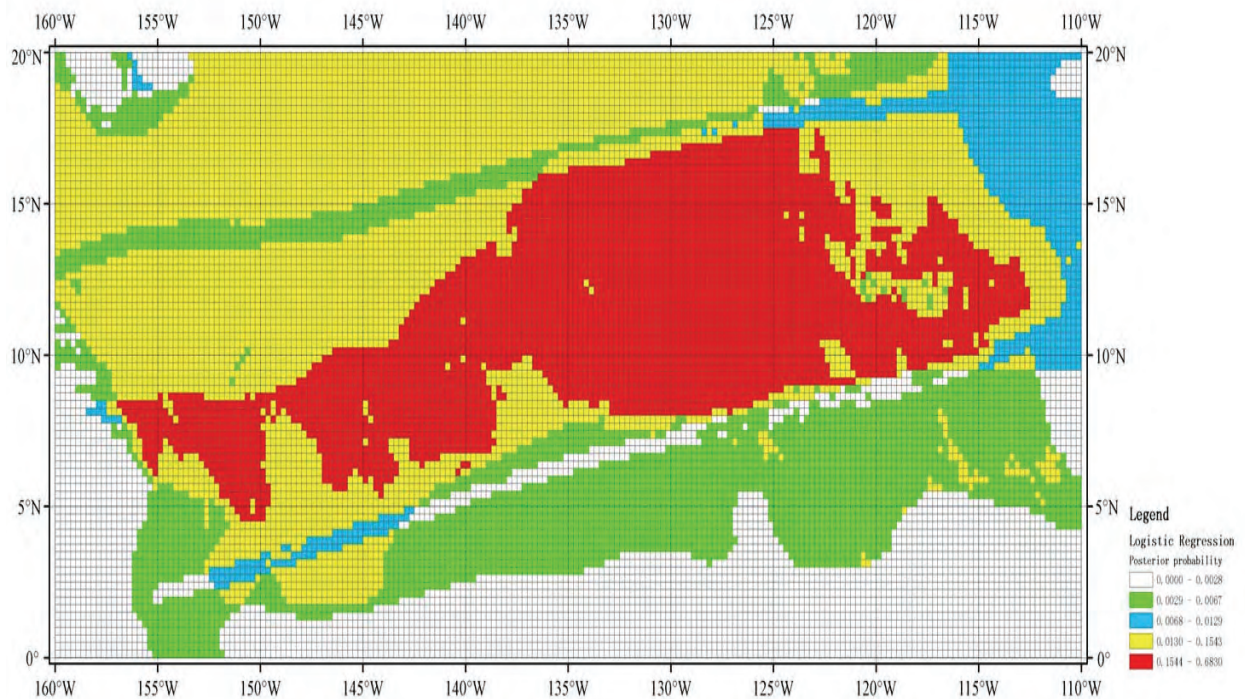


*Figure 28. Logistic Regression Results, Posterior Probabilities in the CCZ*

These results are similar to those for the Weights of Evidence calculations (Figure 27) and indicate that middle and northern parts of the CCZ are relatively favourable for finding undiscovered nodule deposits, while the southern, southwestern and southeastern parts of the CCZ are less likely to host nodule deposits.

### 6.5.3 Fuzzy Logic

The essence of Fuzzy Logic (FL) is the combination of propositions or evidence variables (Cheng *et al.*, 1999; Carranza *et al.*, 2001). The combination of fuzzy propositions is specifically the combination of membership functions

The key results from the fuzzy logic modeling, based on the same suite of geological evidence variables as above incorporated into the gamma operator ( $\gamma$ , set to 0.6 for this study), result in the estimated combined membership function values shown in Figure 29 .

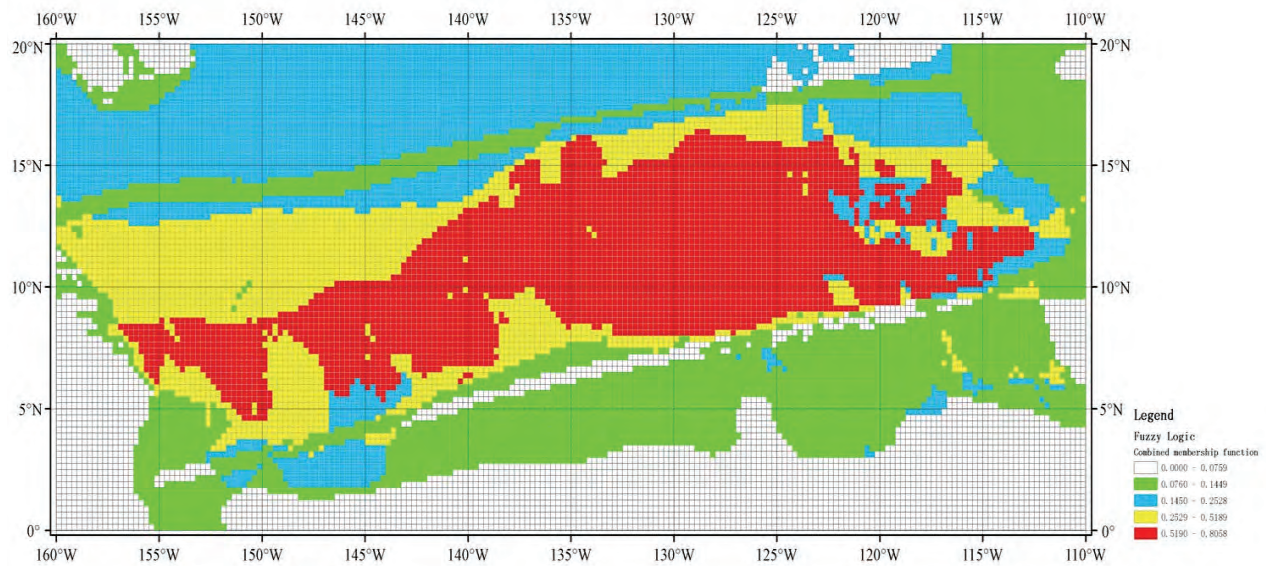


*Figure 29. Fuzzy Logic Results, Combined Membership Function Values in the CCZ*

This figure shows high combined membership function values located at the middle part of the CCZ, suggesting that these areas are favorable for nodule occurrence, but low combined membership function values located at the southern, northern, southwestern and southeastern parts of the CCZ, suggesting low favorability for nodule occurrence in these areas.

#### **6.5.4 Radial Basis Function Network**

The key results from the Radial Basis Function Network modeling, based on the geological evidence variables are presented in Figure 30.

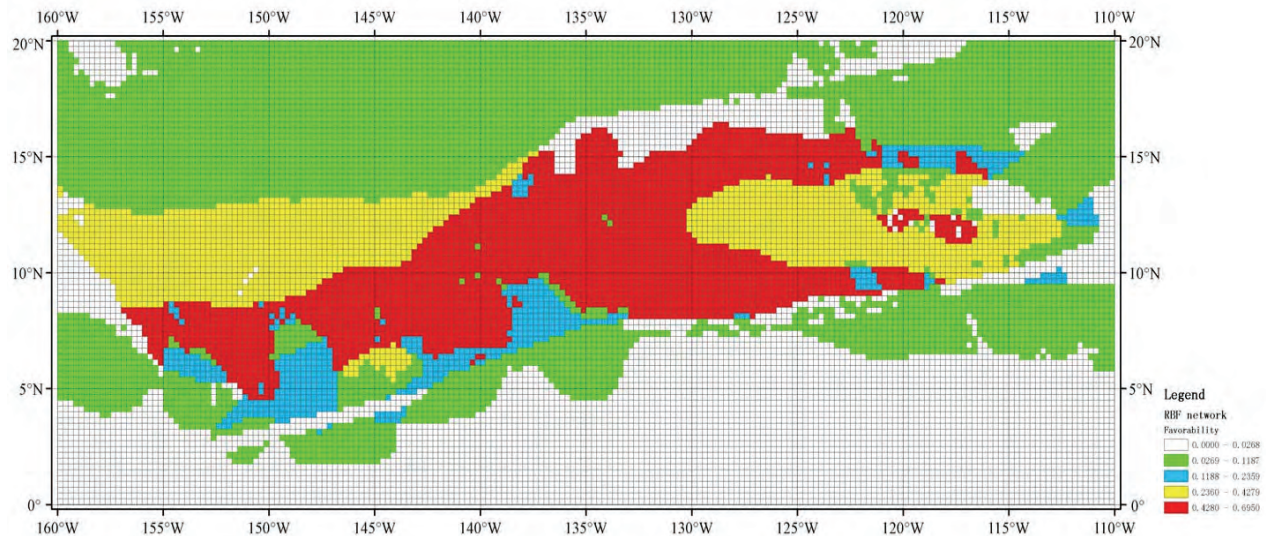


*Figure 30. RBF Network Modeling, Favorability for Deposit Occurrence in the CCZ*

They are similar to those from the fuzzy logic modeling, and suggest that the relatively high probabilities for finding nodules occur at the middle and northern parts of the CCZ, but low probabilities for finding nodules occur at the southern, southwestern and southeastern parts.

**Table 22. Calculated Regression Coefficients, Logistical Regression**

| <i>Geological Evidence Variable</i> | <i>Sediment Type (b<sub>1</sub>)</i> | <i>Primary Productivity (b<sub>2</sub>)</i> | <i>CCD minus Water Depth (b<sub>3</sub>)</i> | <i>Bathymetric Regime (b<sub>4</sub>)</i> | <i>Regression Constant (b<sub>0</sub>)</i> |
|-------------------------------------|--------------------------------------|---|--|---|--|
| <i>Regression Coefficient</i>       | 3.3527                               | 3.2830                                      | 2.4690                                       | 2.6289                                    | -10.9658                                   |

## 6.6 Maps of Potential Nodule Resource Areas

As discussed above (Section 6.5), the various indices (posterior probability, combined membership function value and favorability index) produced in these four methods of modeling (Figure 27 - Figure 30) provide differing assessments of the spatial distribution of areas within the study area where the occurrence of nodule deposits is likely. However, the results consistently indicate that the better prospects can be found in the central and northern parts of the CCZ, while the southern, southwestern and eastern parts are likely to be unfavorable for nodule deposits occurrence. Also, all the modeling results are consistent with the mapped deposit occurrence.

By eliminating the known occurrences of nodule deposits from the maps, the resulting distributions show the predicted likelihood of finding deposits at sites that have not been surveyed. These maps are shown in Figure 31 – Figure 34. These predictions are represented by colour from the most to least likely areas to host nodule deposits as follows:

Red > Yellow > Blue > Green

Thus, future explorers might expect to get better results from exploration efforts that focus on the central and northern areas of the CCZ than the southern, southwestern or eastern areas.

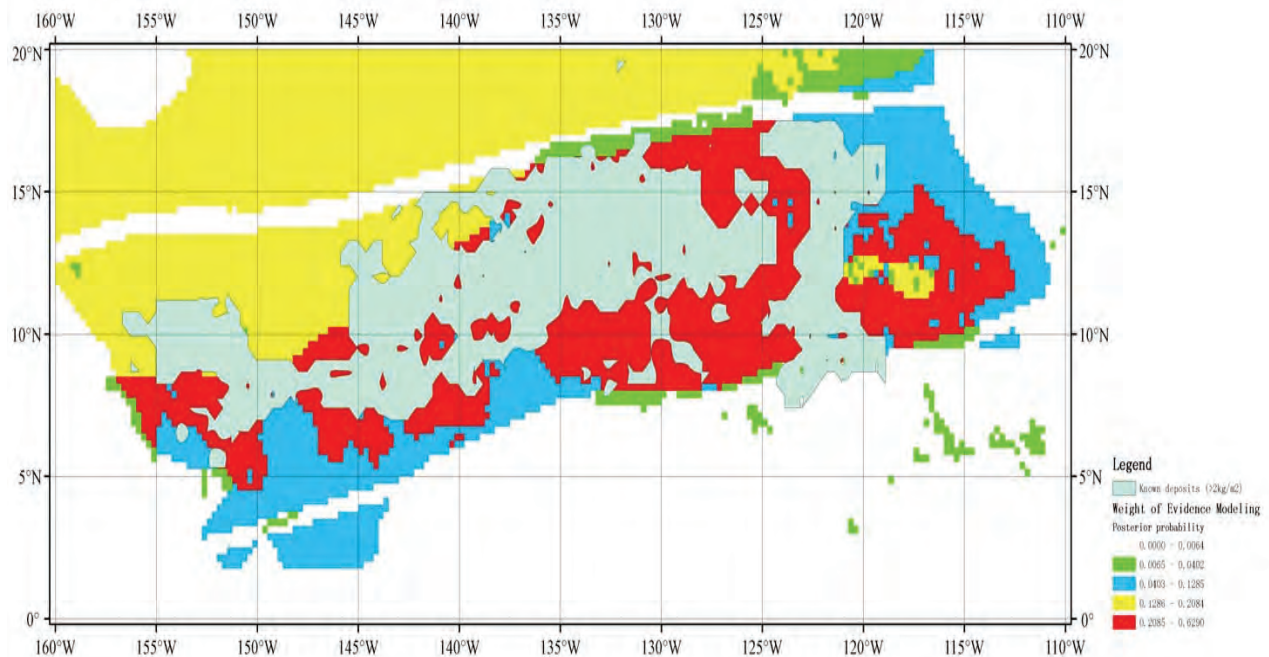


*Figure 31. Prospects for Nodule Occurrence, Weights of Evidence Modeling*

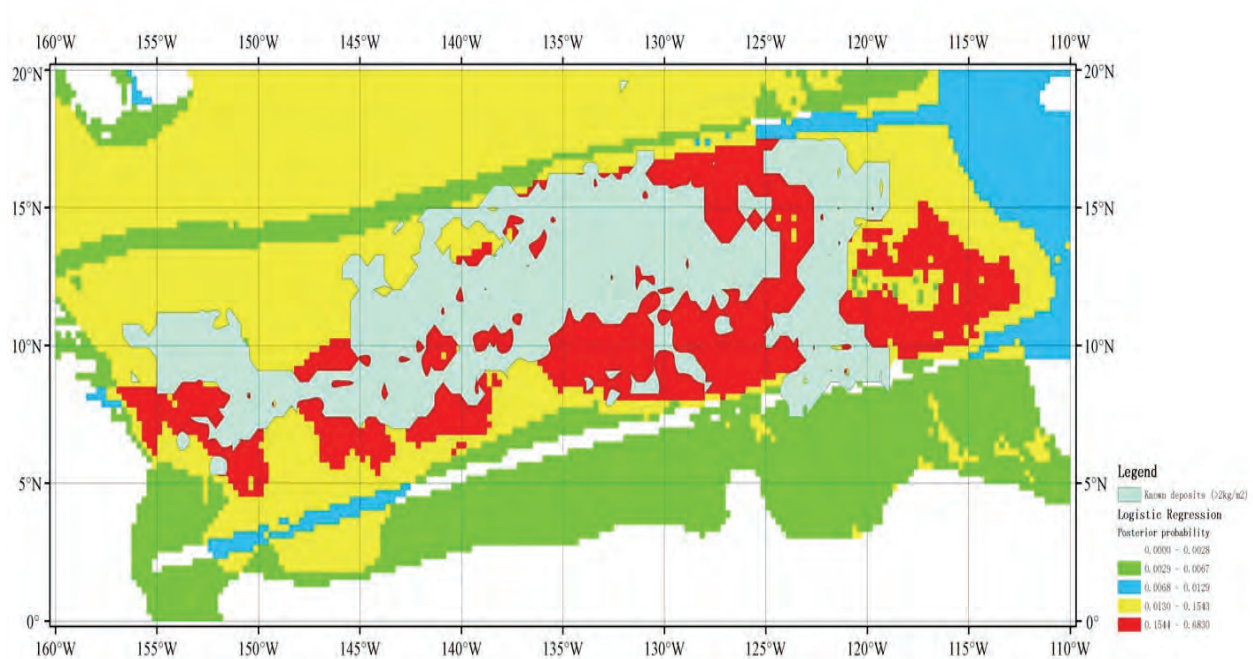


*Figure 32. Prospects for Nodule Occurrence, Logistic Regression*

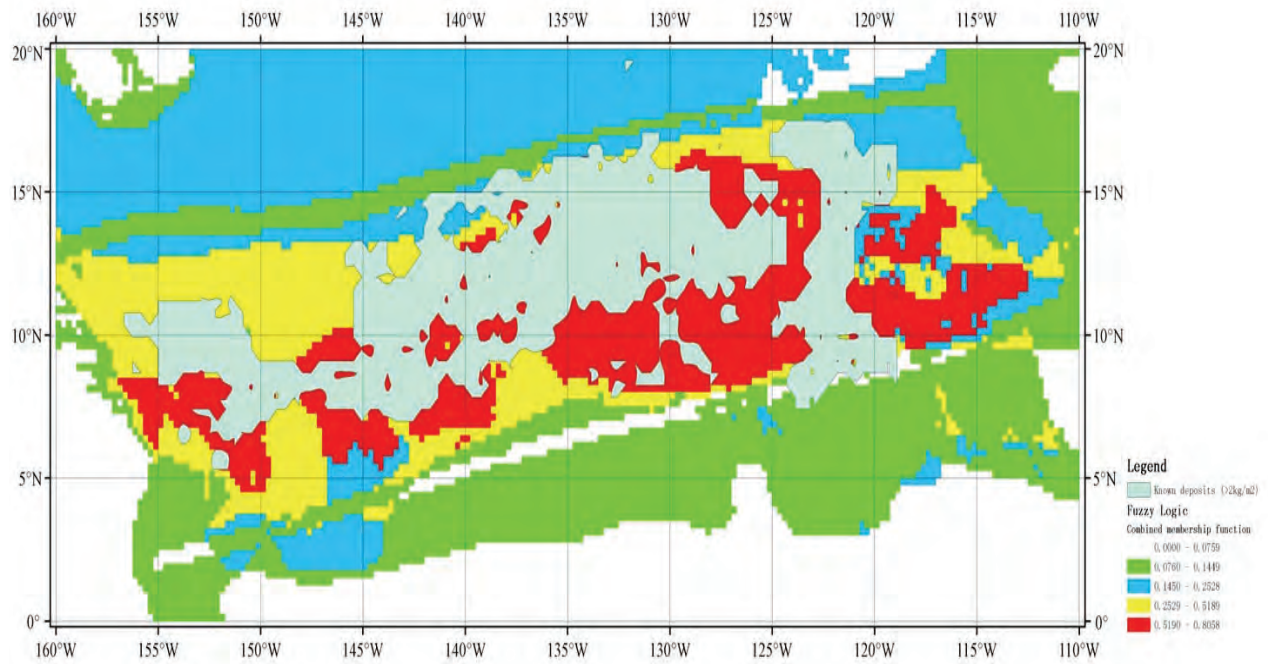


Figure 33. Prospects for Nodule Occurrence, Fuzzy Logic

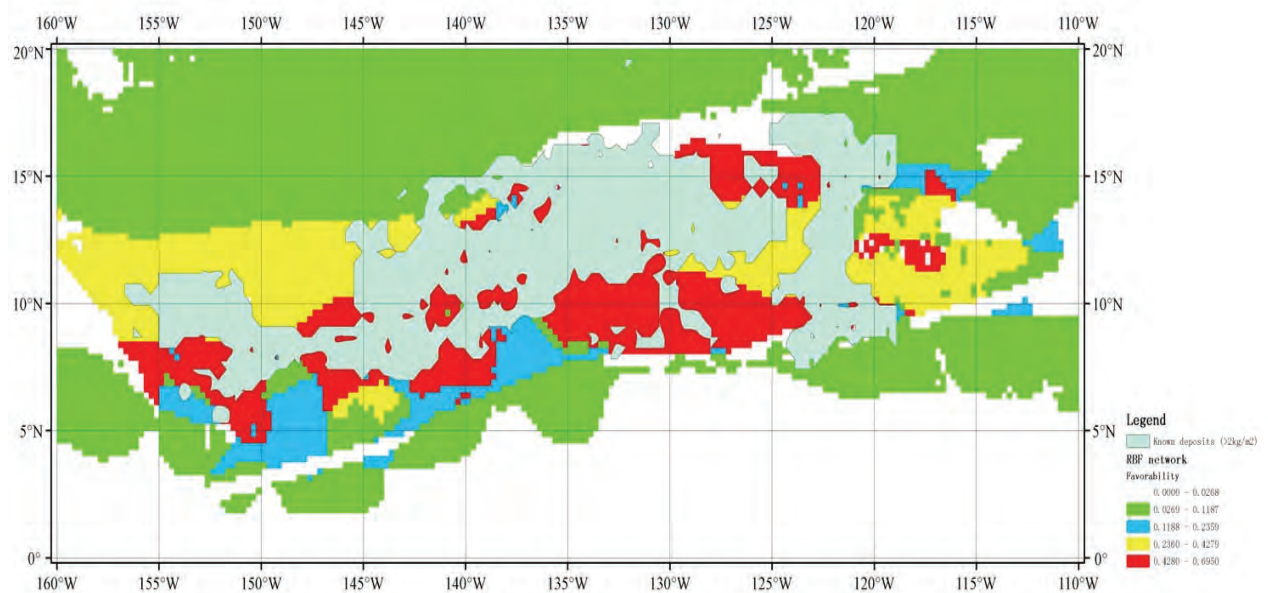
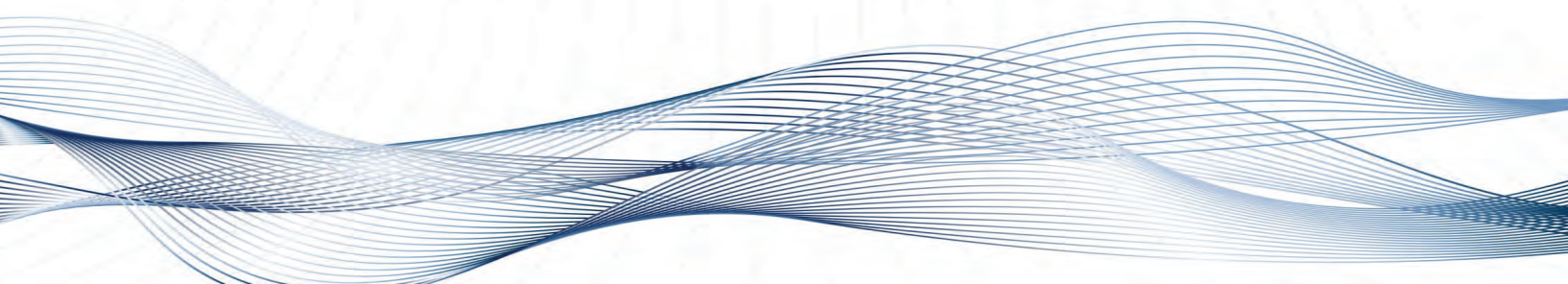


Figure 34. Prospects for Nodule Occurrence, Radial Basis Factor Network

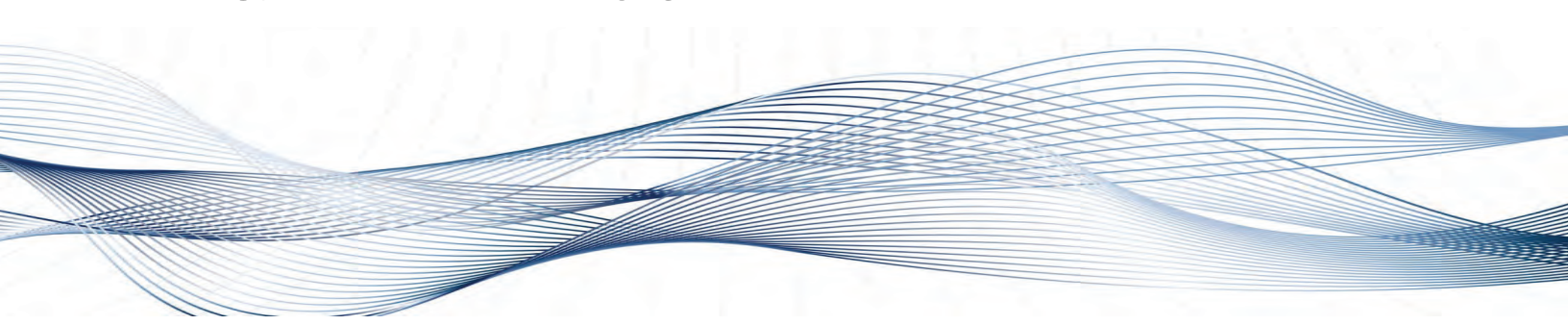
## 7. REFERENCES CITED

- 
- Agterberg F. P. and G.F. Bonham-Carter (1999), Logistic regression and weights of evidence modeling in mineral exploration, *Proc. 28th Interna. Symp. Computer Applications in the Mineral Industries*, Golden, Colorado, p 483-490.
- Agterberg F. P., G.F. Bonham-Carter, Q.M. Cheng *et al.* (1993), 'Weights of evidence modeling and weighted logistic regression for mineral potential mapping', in Davis J C and U.C. Herzfeld (eds.), *Computers in Geology: 25 years of progress*, New York, Oxford Univ. Press, p 13-32.
- Aplin, A. and D.S. Cronan (1985), Ferromanganese oxide deposits from the central Pacific Ocean II: Nodules and associated sediments, *Geochimica et Cosmochimica Acta* 49, p. 437-451.
- Asim R., G. Sandeep and M. Raymond (1995), An algorithm to generate Radial Basis Function (RBF)-Like nets for classification problems, *Neural Networks* 8(2), p 179-201.
- Bernhard, H. and H.E. Blissenbach (1988), 'Economic importance', in The Manganese nodule belt of the Pacific Ocean, P. Halbach, G. Friedrich and U. von Stackelberg (eds.), Stuttgart, Ferdinand Enke Verlag, p. 4-9.
- Carranza E. J. M. and M. Hale (2001), Geologically constrained fuzzy mapping of gold mineralization potential, Baguio district, Philippines, *Natural Resources Research* 10, p. 125-136.
- Cheng Q. and F.P. Agterberg (1999), Fuzzy weights of evidence method and its application in mineral potential mapping, *Natural Resources Research* 8, p. 27-35.
- Chester, R. (2003), *Marine Geochemistry*, Chapman & Hall, London, p. 699.
- Cronan, D. S. and R. Hodkinson (1994), Element supply to surface manganese nodules along the Aitutaki-Jarvis Transect, South Pacific, *Journal of the Geological Society of London*, 151, p. 391-401.
- Cronan, D.S. (1972), Regional geochemistry of ferromanganese nodules in the world ocean, in *Ferromanganese Deposits on the Ocean Floor*, Horn, D.R. (ed.), IDOE, NSF, Washington, D.C., p. 19-30.
- Deutsch, C.V. and A.G. Journel (1998), *GSLIB: Geostatistical software library and user's guide*, Oxford University Press, New York.
- Earney, F.C.F. (1990), *Marine Mineral Resources*, Routledge, p 387.
- Gomez Hernandez, J. J. and R.M. Strivastava (1990), ISIM3D: an ANSI-C three-dimensional multiple indicator conditional simulation program, *Computer and Geosciences* v.16, p.395-440.

- Greenslate, J.L., J.Z. Frazer and G. Arrhenius (1973), 'Origin and deposition of selected transition elements in the seabed', in Papers on the Origin and Distribution of Manganese Nodules in the Pacific and Prospects for Exploration, Morgenstein, M. (ed.), Hawai'i Institute of Geophysics, Honolulu, HI, July 23-24, 1973.
- Gregg, W.W. and M.E. Conkright (2000), *Blended In Situ-CZCS Chlorophyll Data Set*, Watson W. NASA/GSFC & NOAA/NODC.
- Halbach P., G. Friedrich and U.V. Stackelberg (1988), *The Manganese Nodule Belt of the Pacific Ocean: Geology, Environment, Nodule Formation, and Mining Aspects*, Stuttgart, Germany, Ferdinand Enke Verlag, p. 1-254.
- Halbach, P. (1986), Processes controlling the heavy metal distribution in Pacific ferromanganese nodules and crusts, *Geol. Rundsch.* 75/1, p 235-247.
- Halbach, P. and D. Puteanus (1984), The influence of the carbonate dissolution rate on the growth and composition of Co-rich ferromanganese crusts from Central Pacific seamount areas, *Earth Planet. Sci. Lett.* 68, p. 73-87.
- Halbach, P. and D. Puteanus (1988), 'Geochemical Trends of Different Genetic Types of Nodules and Crusts', in The Manganese Nodule Belt of the Pacific Ocean, Halbach, P., G. Friedrich and U. von Stackelberg (eds.), F. Enke Verlag, Stuttgart, Germany, p 61- 69.
- Halbach, P., V. Marchig and C. Scherhag (1980), Regional variations in Mn, Ni, Cu and Co of ferromanganese nodules from a basin in the Southeast Pacific, *Marine Geology* 38, M1-M9.
- Hennigar, H.F, R.E. Dick and E.J. Foell (1986), 'Derivation of Abundance Estimates for Manganese Nodule Deposits: Grab Sampler Recoveries to Ore Reserves', *Offshore Technology Conference*, OTC 5237, May 1986, Houston, TX, 5 p.
- Johnston, K. et al. (2001), *Using ArcGIS Geostatistical Analyst*, ESRI, California, 300 p.
- Journel, A. G. and C.J. Huijbregts (1978), *Mining Geostatistics*, Academic Press, London, 600 p.
- Kazmin, Y. B. (2003), 'Geology of the Clarion-Clipperton Fracture Zone (CCZ) – Existing Geologic Information in Respect of Polymetallic Nodules in the CCZ', in Meeting of Workshop to Develop a Geological Model of the Clarion-Clipperton Polymetallic Nodule Deposits, Fiji Islands, held by International Seabed Authority, May 13 - 20, 2003.
- Kennett, J.P. (1982), *Marine Geology*, Prentice-Hall, Inc. London, UK, Englewood Cliffs, N.J. 07632, p 813.
- Koski, R.A., C.R. German and J.R. Hein (2003), 'Fate of Hydrothermal Products from Mid-ocean Ridge Hydrothermal Systems – Near-field to Global Perspectives', in Energy and Mass Transfer in Marine and Hydrothermal Systems, Halbach, P., V. Tunnicliffe and J.R. Hein (eds.), *Dahlem Workshop Report 89*, Dahlem University Press, Berlin, Germany, 317-335..
- Krige, Danie G. (1951), A statistical approach to some basic mine valuation problems on the Witwatersrand, *J. of the Chem., Metal. and Mining Soc. of South Africa* 52 (6), p. 119–139.
- Manheim, F.T. (1978), Book review of G. P. Glasby, Marine Manganese Deposits, in *Geochemica et Cosmochimica Acta* 42(5), p 541.
- Matheron, G. (1962), *Traité de géostatistique appliquée*, Editions Technip.

- McKelvey, V.E., N.A. Wright and R.W. Rowland (1979), 'Manganese nodule resource in the northeastern equatorial Pacific', in *Marine Geology and Oceanography of the Pacific Manganese Nodule Province*, J.L. Bischoff and D. Z. Piper (eds.), Plenum, New York, p. 747-762.
- Mero, J.L. (1965), *The Mineral Resources of the Sea*. Elsevier, Amsterdam, 312 p
- MOMAF (1997), *A report on '97 deep seabed mineral resources exploration*, Seoul: MOMAF.
- MOMAF (1999), *A report on '99 deep seabed mineral resources exploration*, Seoul: MOMAF.
- MOMAF (2002), *A report on '02 deep seabed mineral resources exploration*, Seoul: MOMAF.
- Morgan, C. L. (2000), 'Resource estimates of the Clarion-Clipperton manganese nodule deposits', in Cronan, D. S. (ed.), *Handbook of Marine Mineral Deposits* 6, p. 145-170.
- Müller, P.J., M. Hartmann and E. Suess (1988), 'The Chemical Environment of Pelagic Sediments', in *The Manganese Nodule Belt of the Pacific Ocean*, Halbach, P.,G. Friedrich and U. von Stackelberg (eds.), F. Enke Verlag, Stuttgart, Germany, p. 70- 90,.
- Murray, J. and A.F. Renard (1891), *Deep Sea Deposits, Report of the Scientific Results of HMS Challenger, 1873–1876*.
- Porwal, A., E.J.M. Carranza and M. Hale (2003), Artificial neural networks for mineral-potential mapping: a case study from Aravalli province, Western India [J], *Natural Resources Research* 12, p. 155-171.
- Reynolds, R.W. (1988), A real-time global sea surface temperature analysis, *Journal of. Climatology* 1, p. 75-86.
- Royle, A. et al. (1980), *Geostatistics*, McGraw-Hill. 168 p.
- Sandwell, D.T. (2000), *Marine gravity from satellite altimetry* [Online], Available at: [http://topex.ucsd.edu/marine\\_grav/mar\\_grav.html](http://topex.ucsd.edu/marine_grav/mar_grav.html). [Cited 2003-04-20].

## 8. APPENDICES



### 8.1 Resource Maps

This section shows resource maps for abundance, Manganese, Copper, Cobalt and Nickel (maps generated using original data, grid data and interpolated contours).

### 8.1.1 Abundance

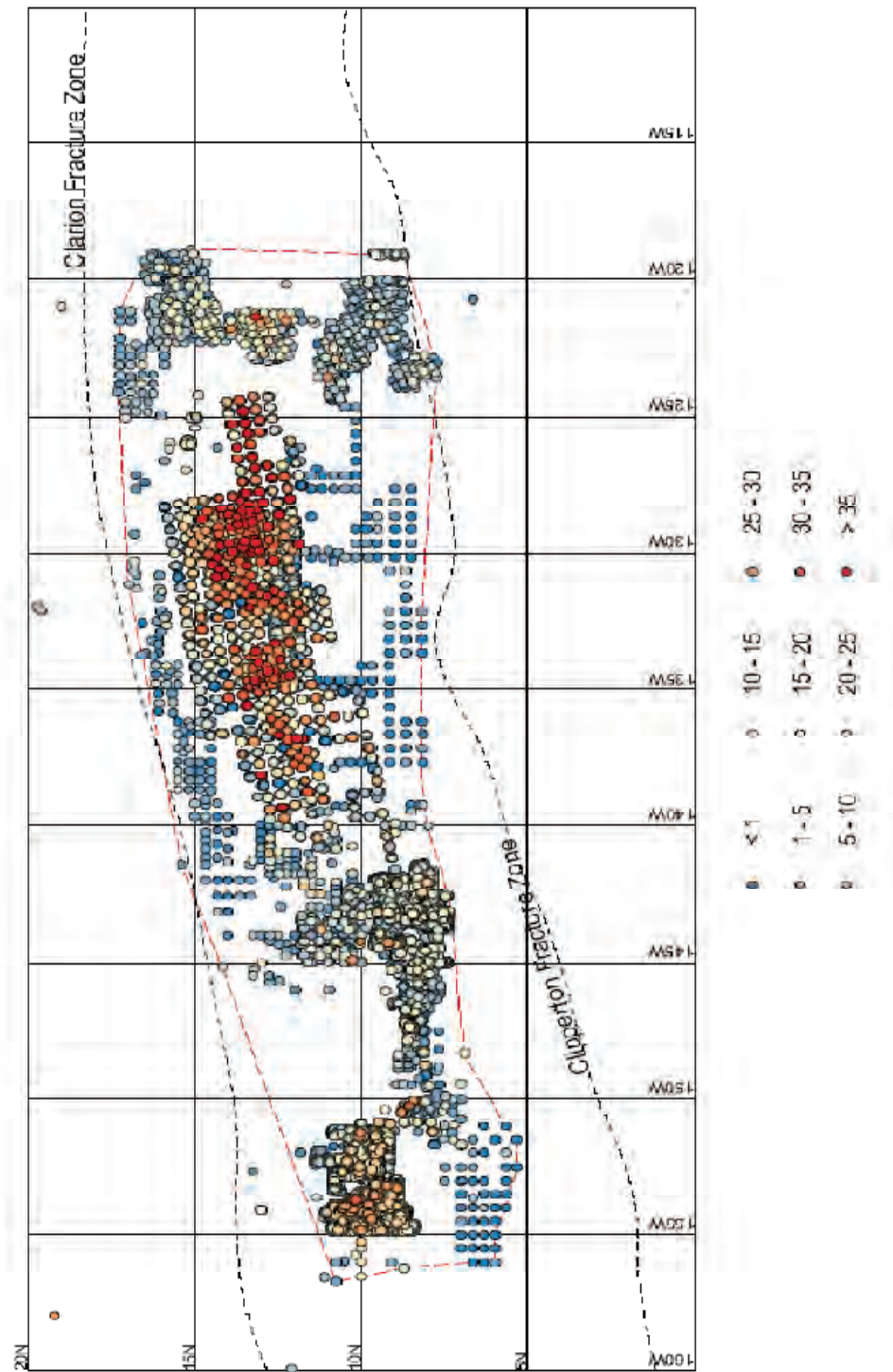


Figure 35. Abundance (kg/m<sup>2</sup>): Original Data Locations and Values

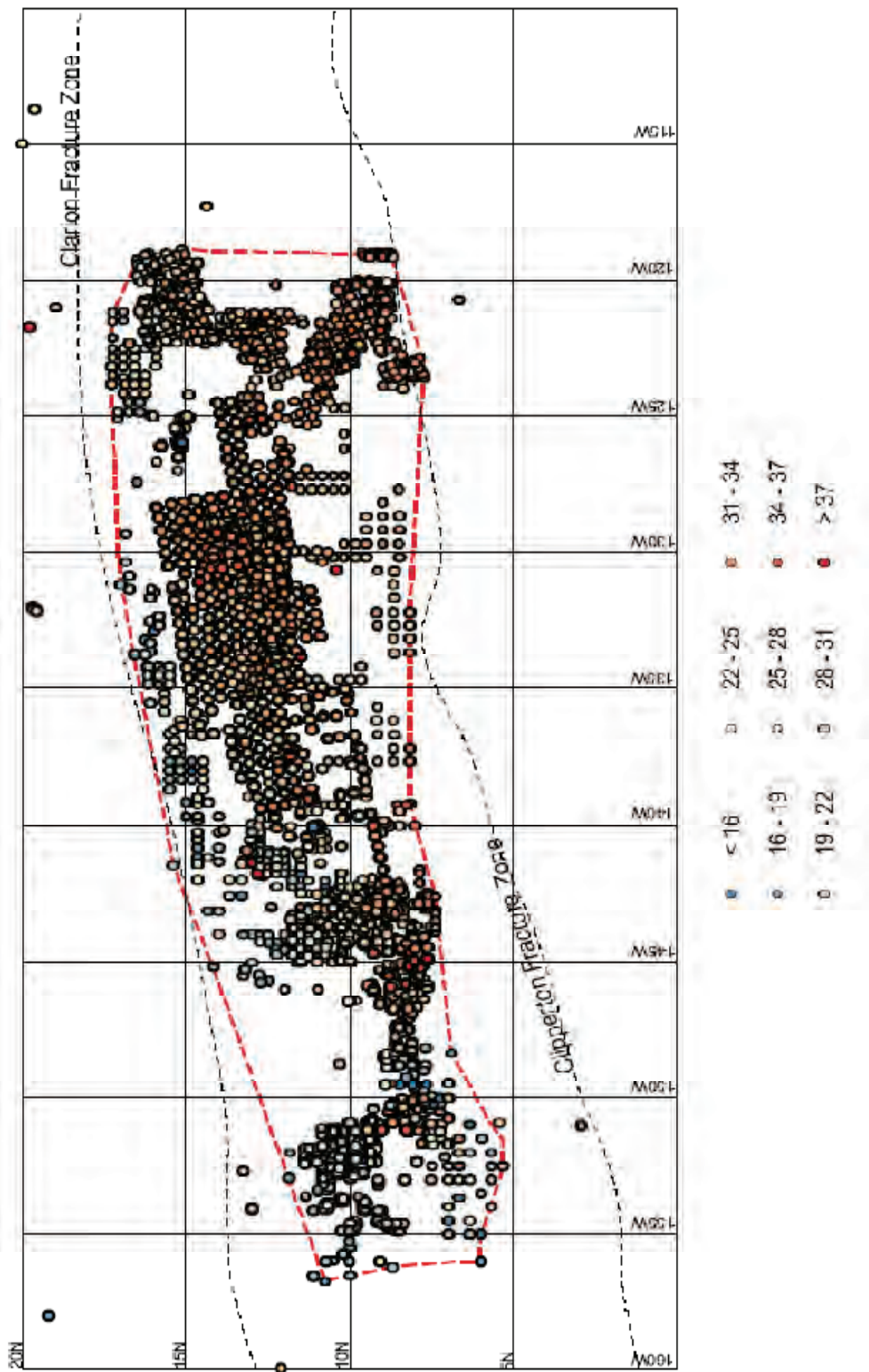


Figure 36. Abundance ( $\text{kg}/\text{m}^2$ ): Grid Block Data Locations and Values

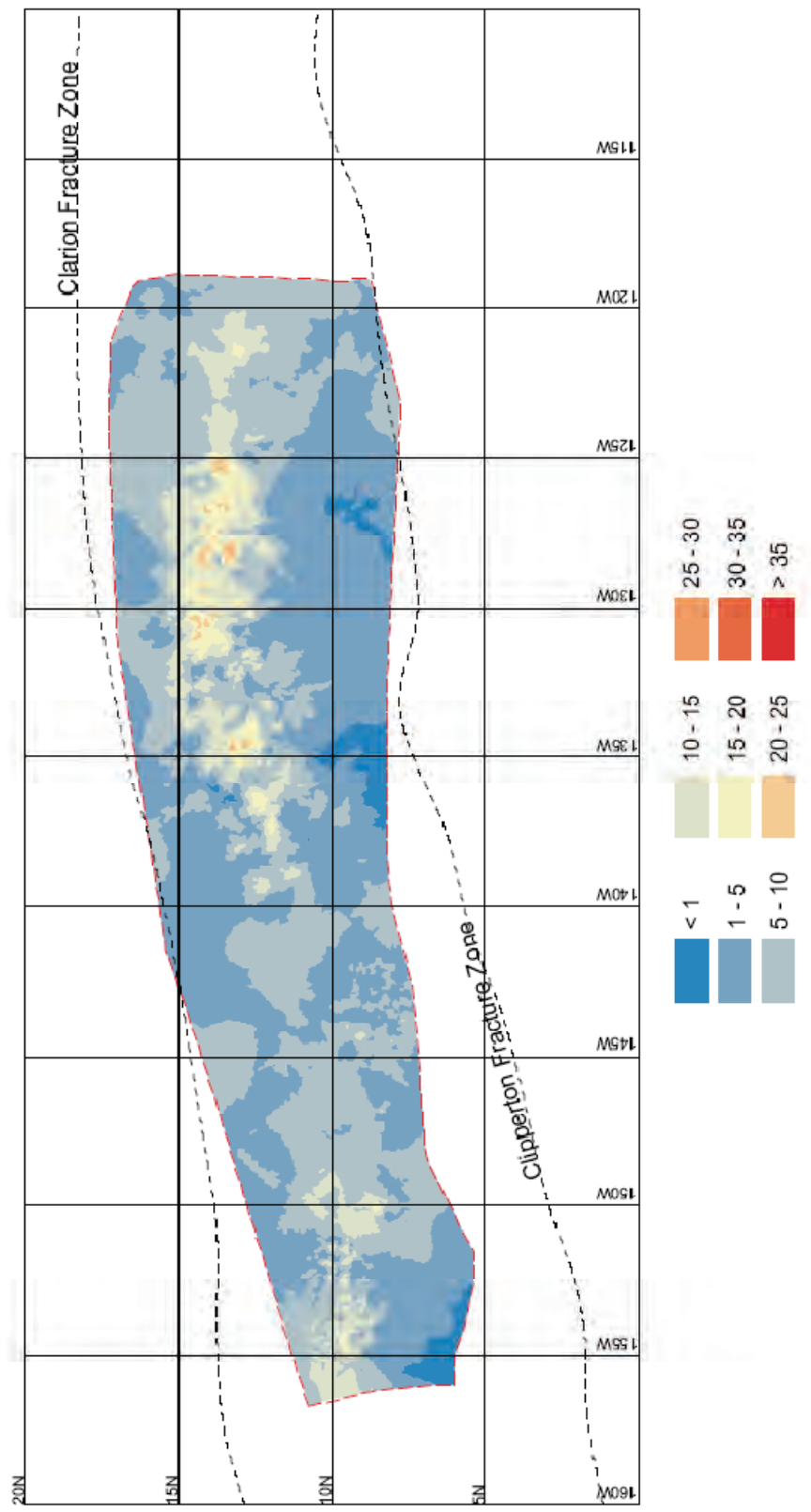


Figure 37. Abundance ( $\text{kg}/\text{m}^2$ ): Original Data, Interpolated Contours

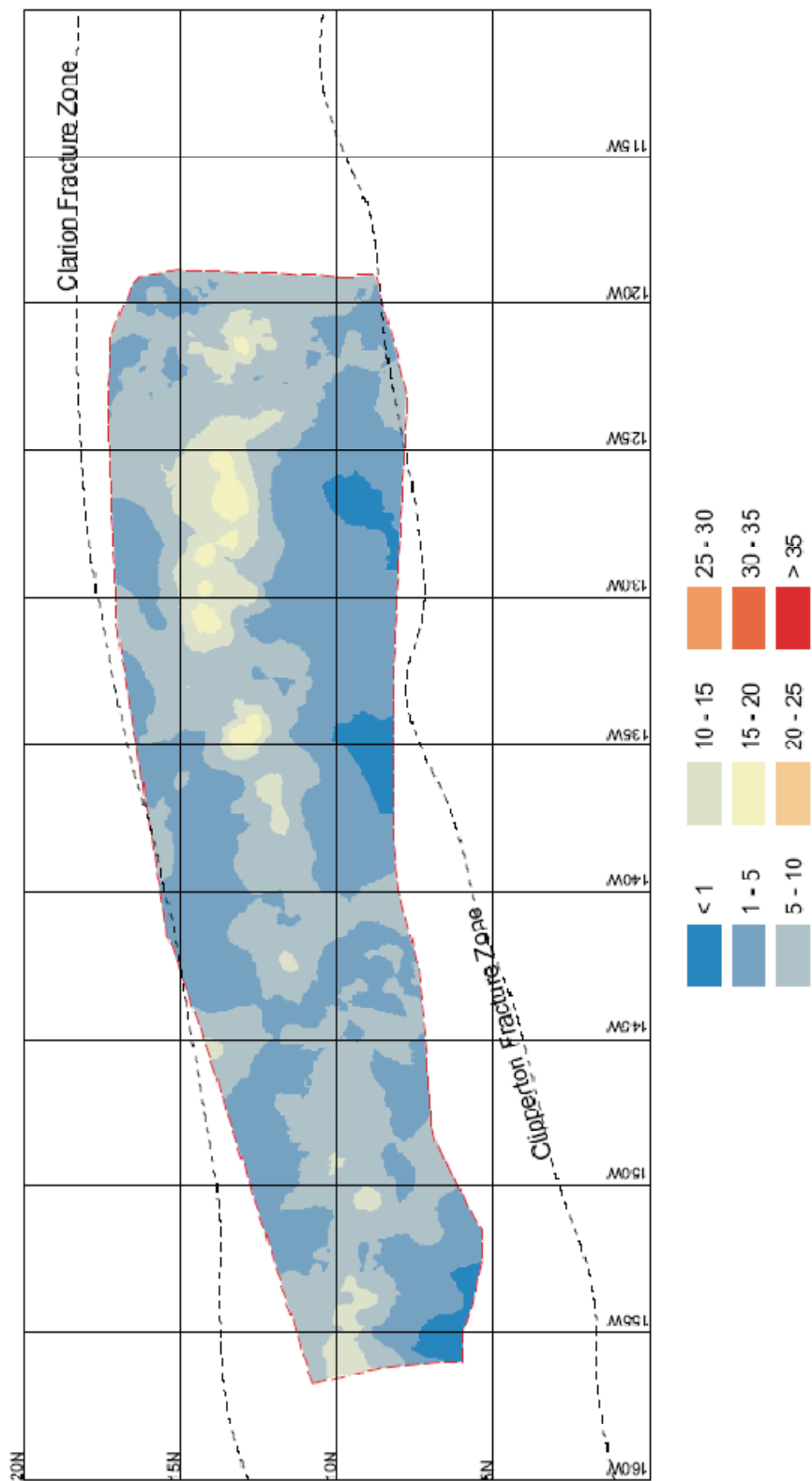


Figure 38. Abundance (kg/m<sup>2</sup>): Grid Block Data, Interpolated Contours

### 8.1.2 Manganese

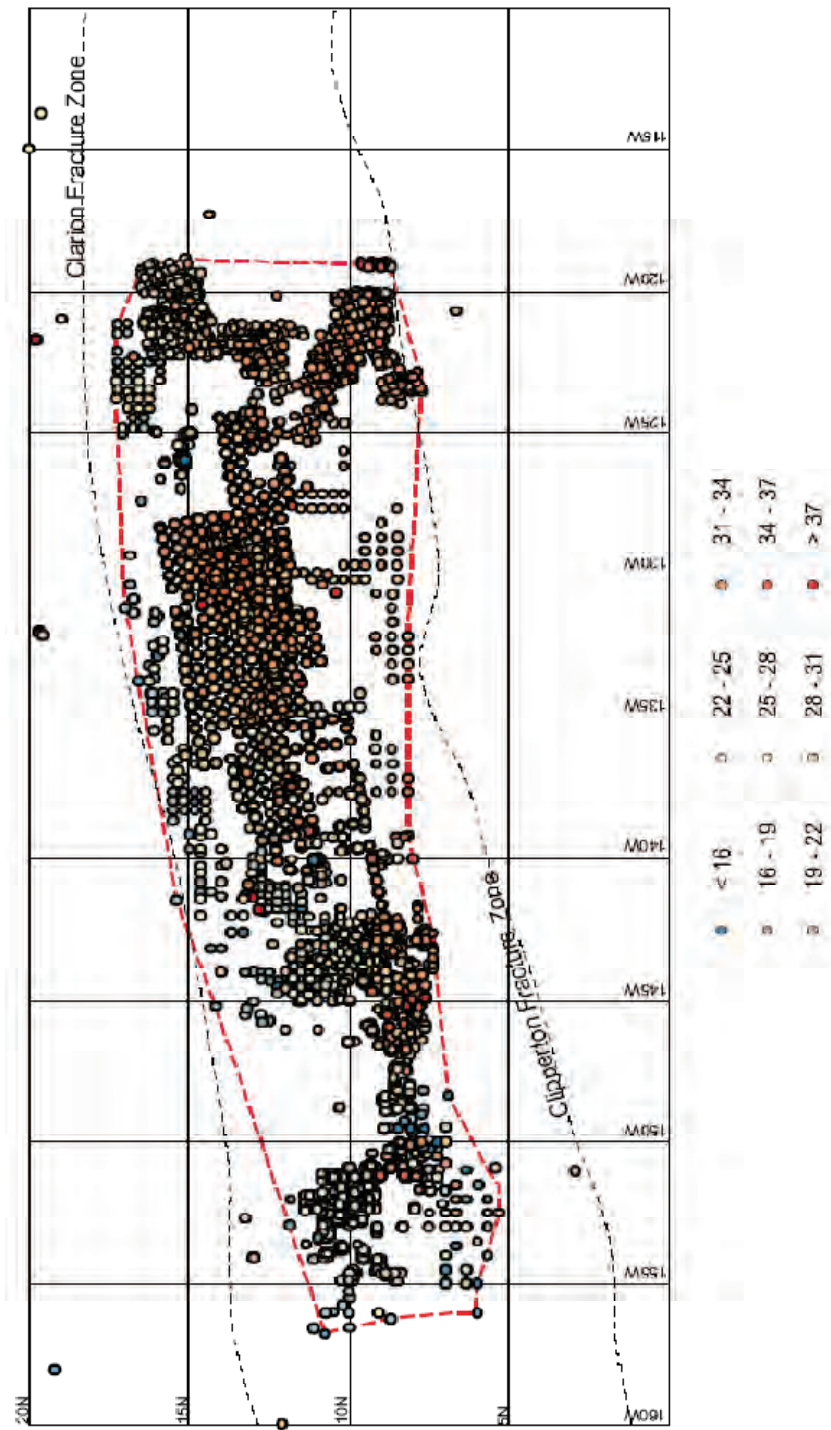


Figure 39. Manganese (dry weight percent): Original Data Locations and Values

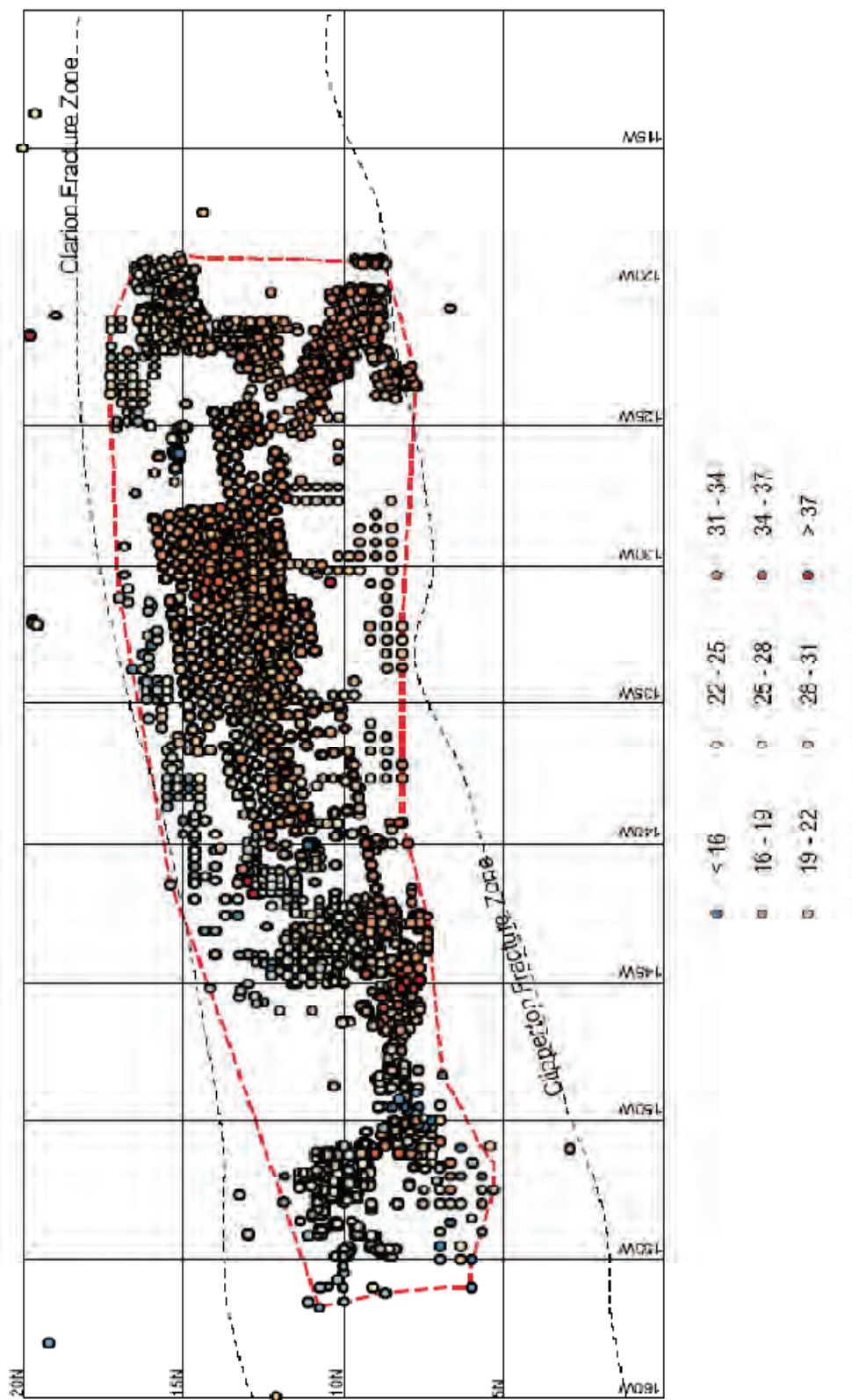
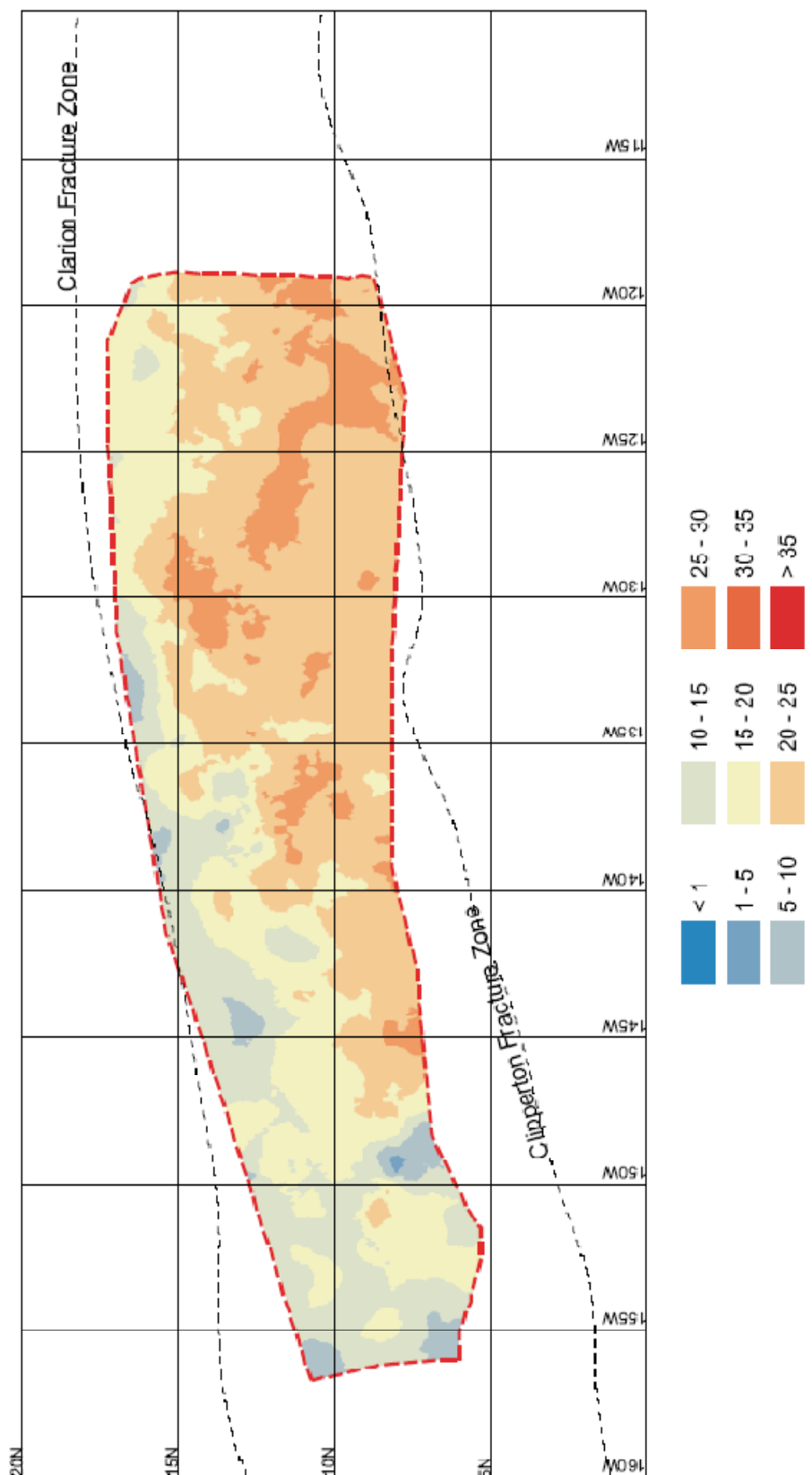
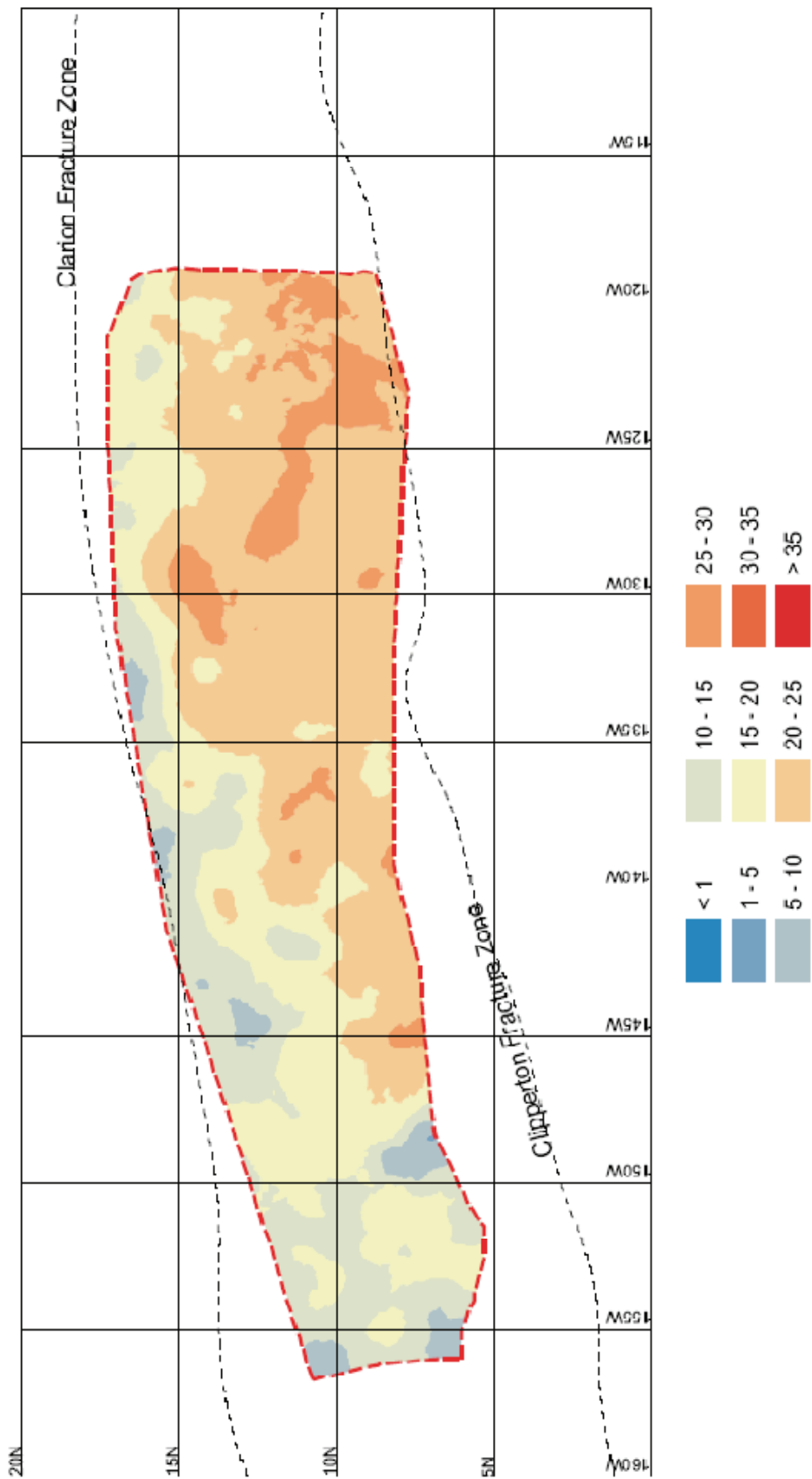


Figure 40. Manganese (dry weight percent): Grid Block Data Locations and Values



*Figure 41. Manganese (dry weight percent): Original Data, Interpolated Contours*



*Figure 42. Manganese (dry weight percent): Grid Block Data, Interpolated Contours*

### 8.1.3 Cobalt

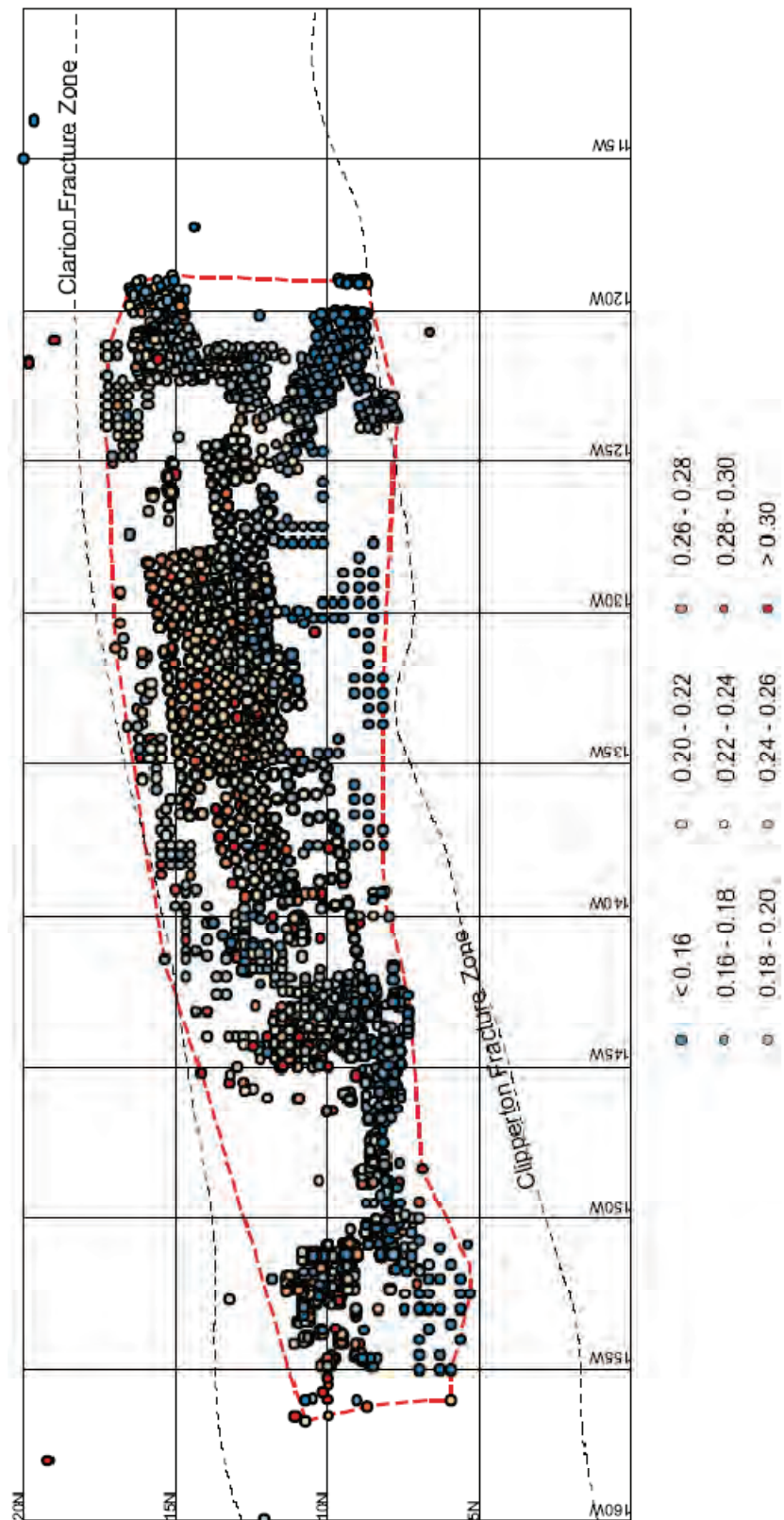


Figure 43. Cobalt (dry weight percent): Original Data Locations and Values

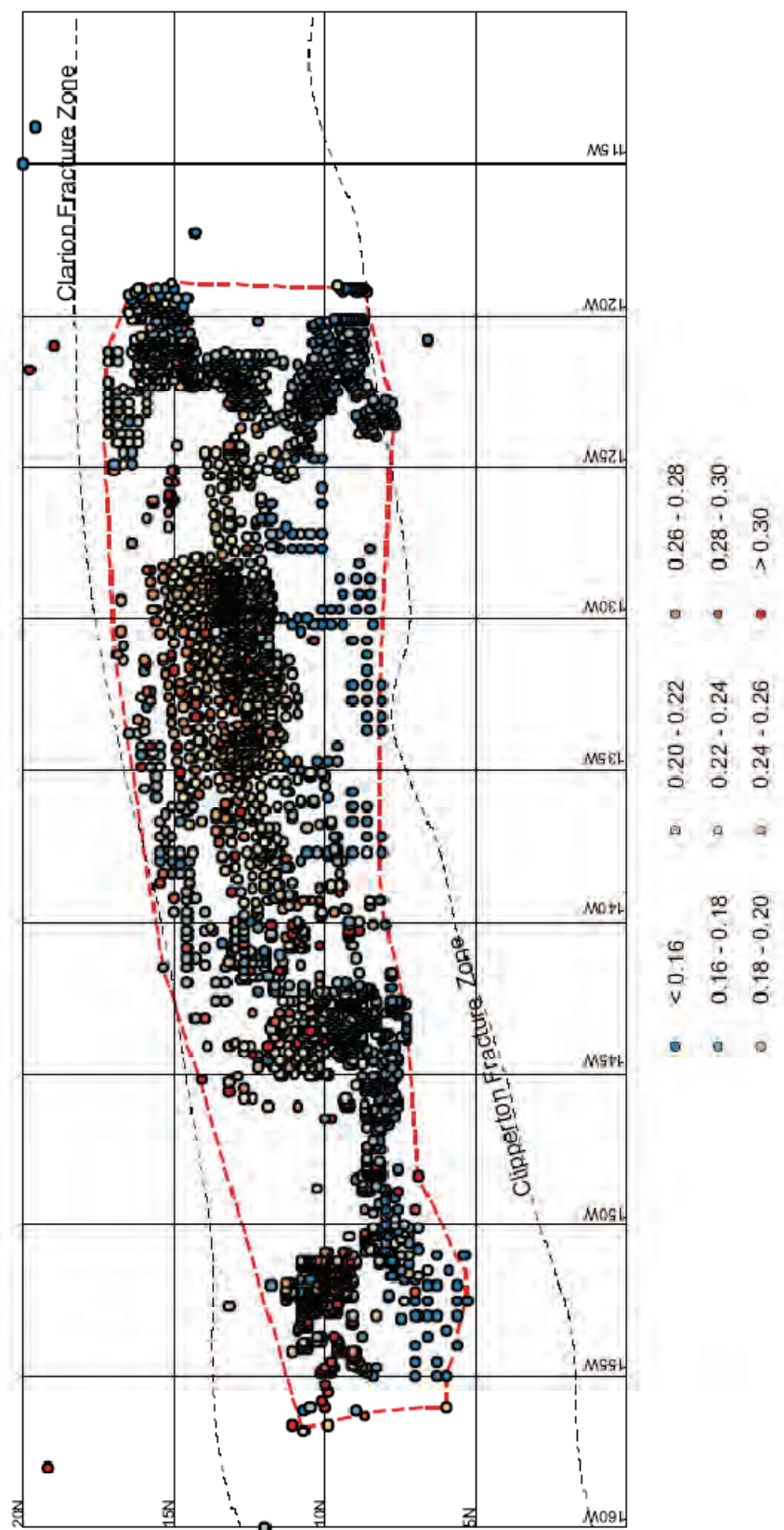


Figure 44. Cobalt (dry weight percent): Grid Block Data Locations and Values

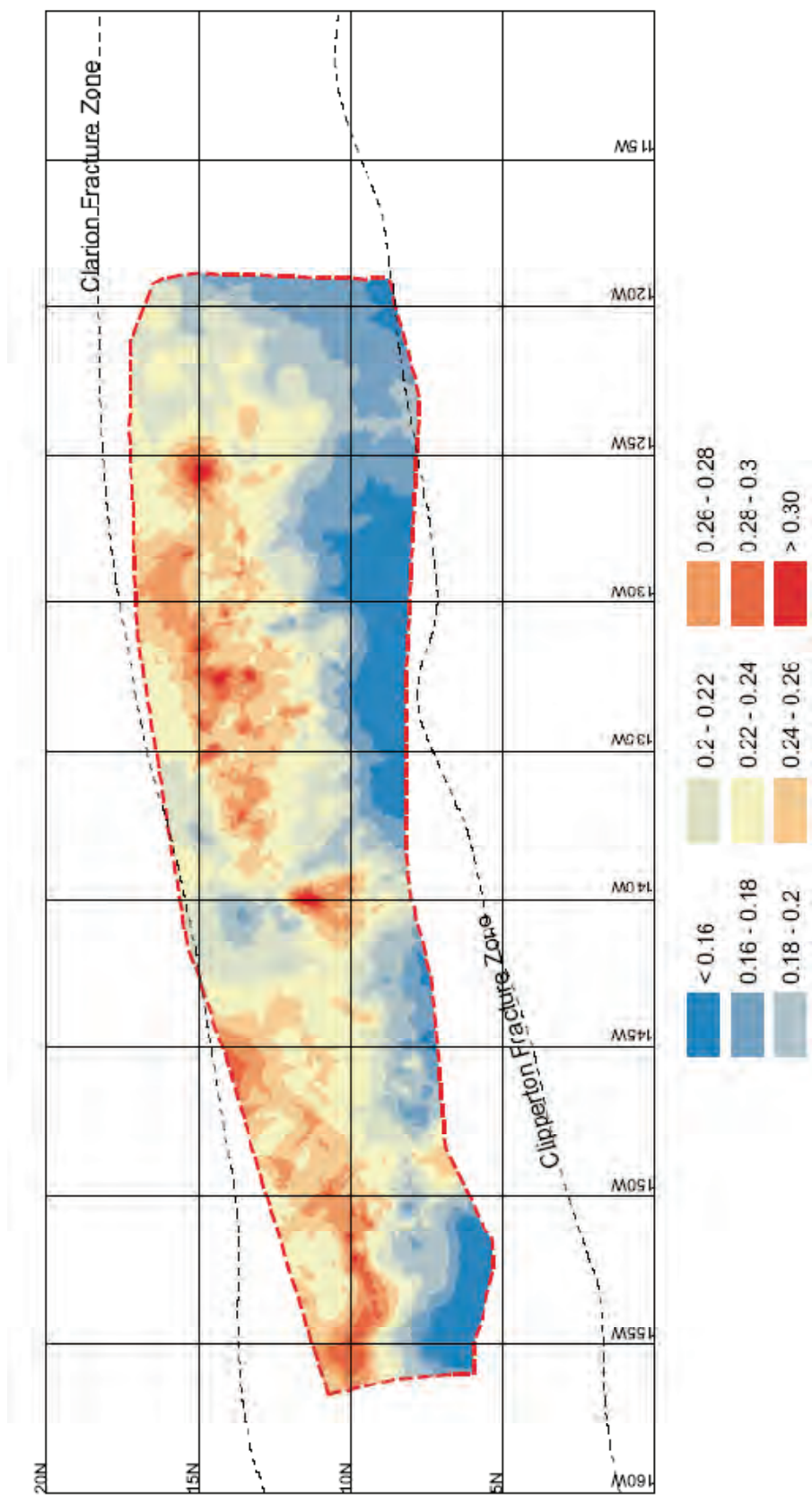


Figure 45. Cobalt (dry weight percent): Original Data, Interpolated Contours

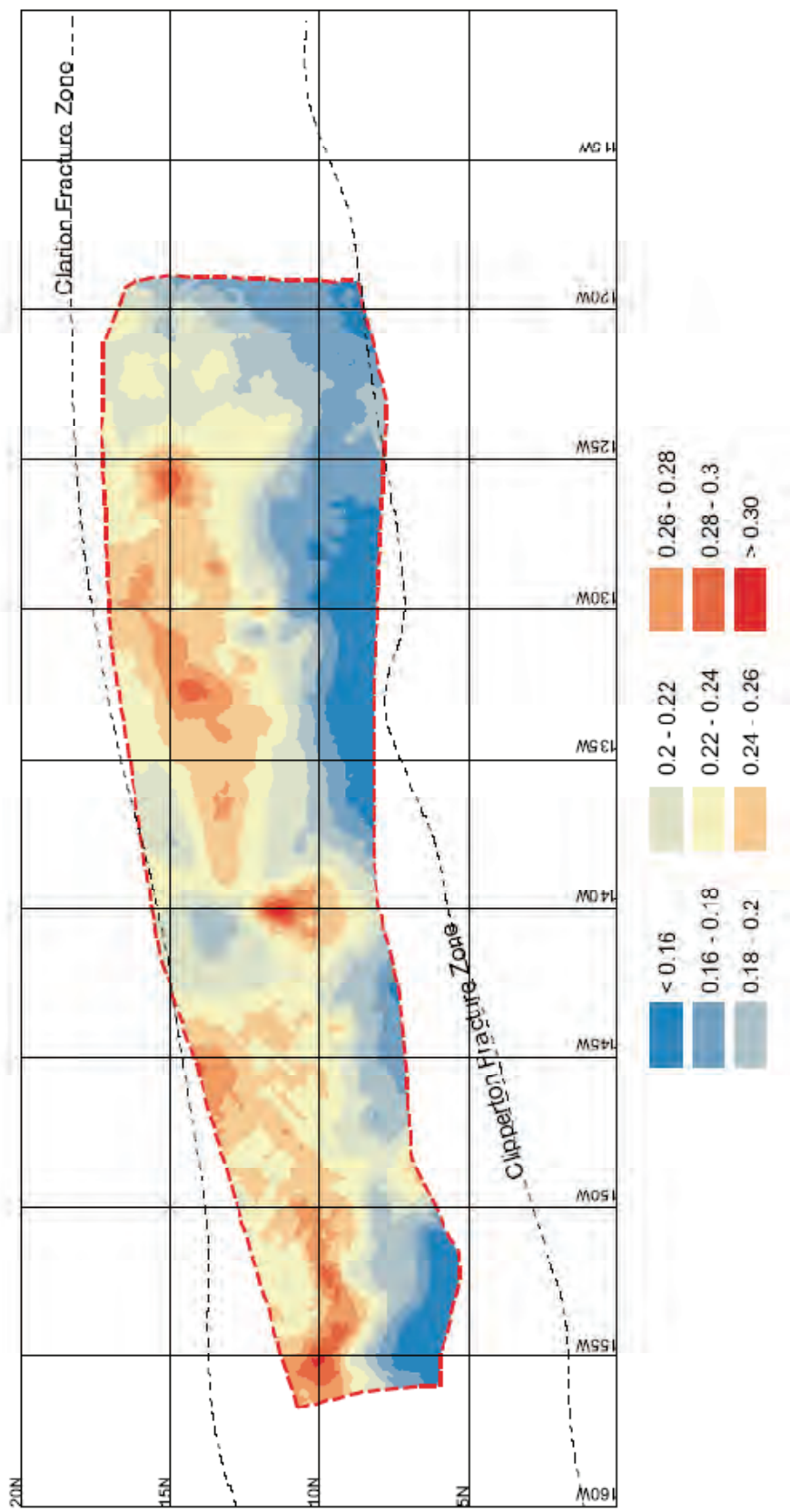


Figure 46. Cobalt (dry weight percent): Grid Block Data, Interpolated Contours

#### 8.1.4 Nickel

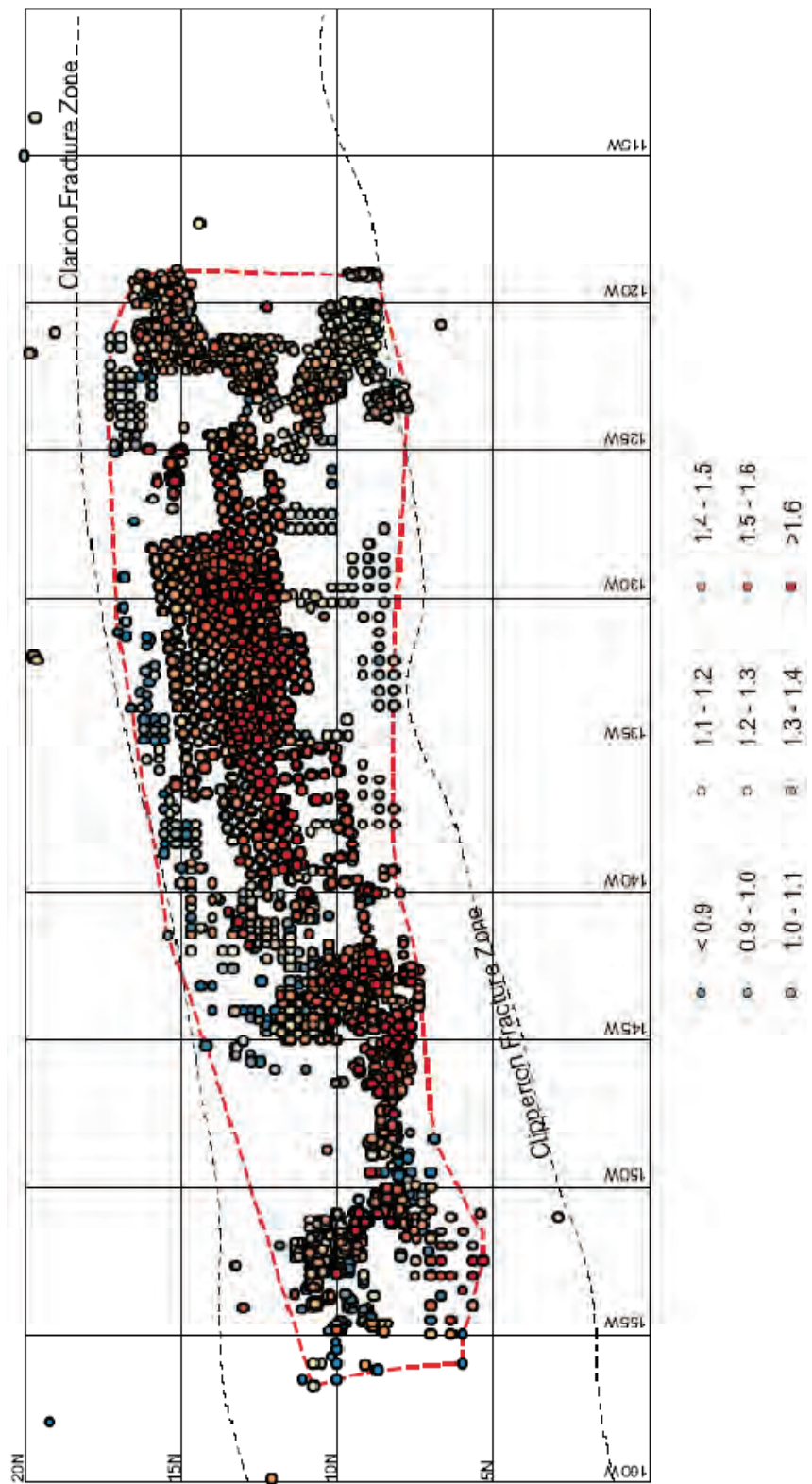


Figure 47. Nickel (dry weight percent): Original Data Locations and Values

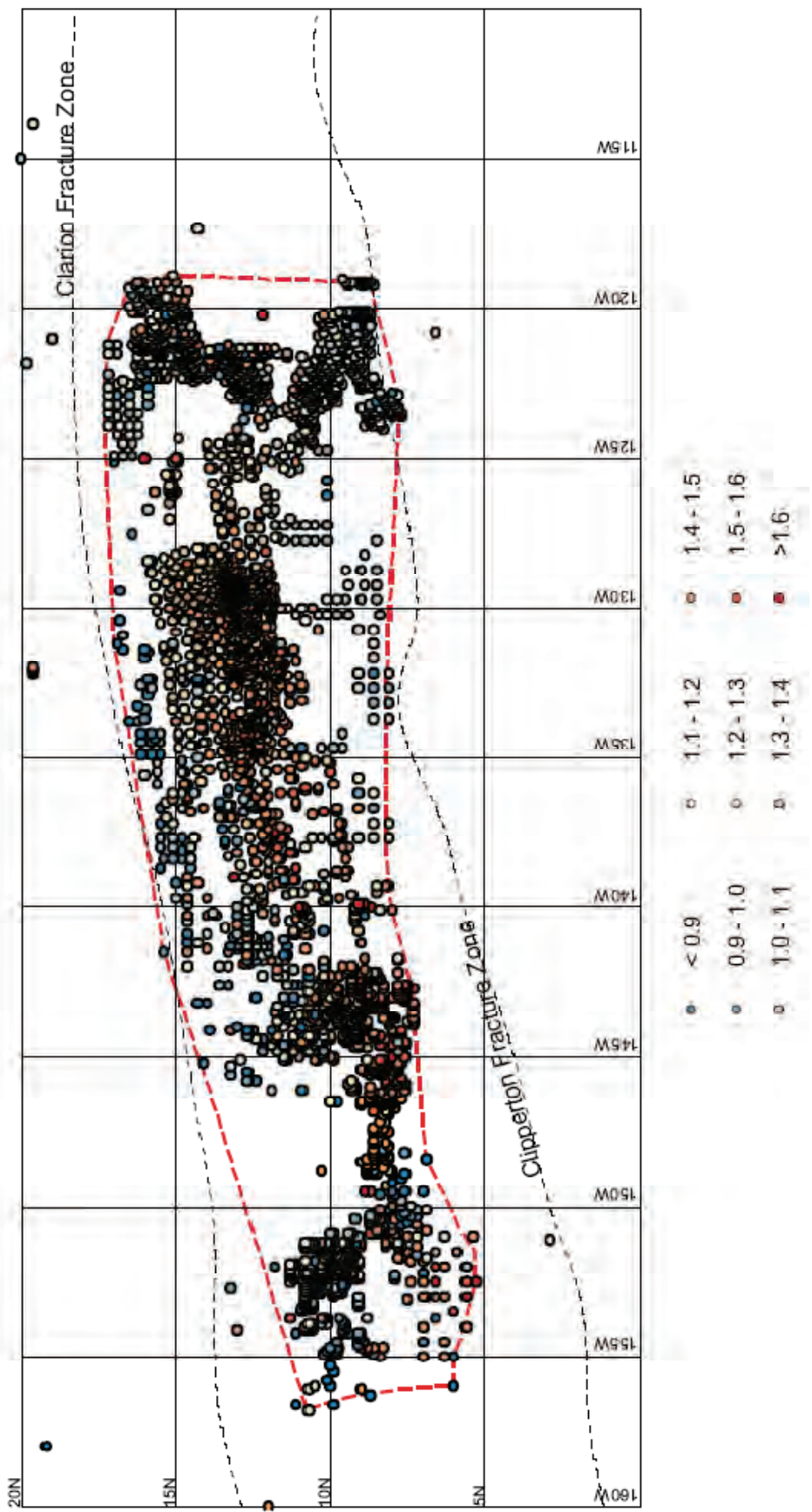


Figure 48. Nickel (dry weight percent): Grid Block Data Locations and Values

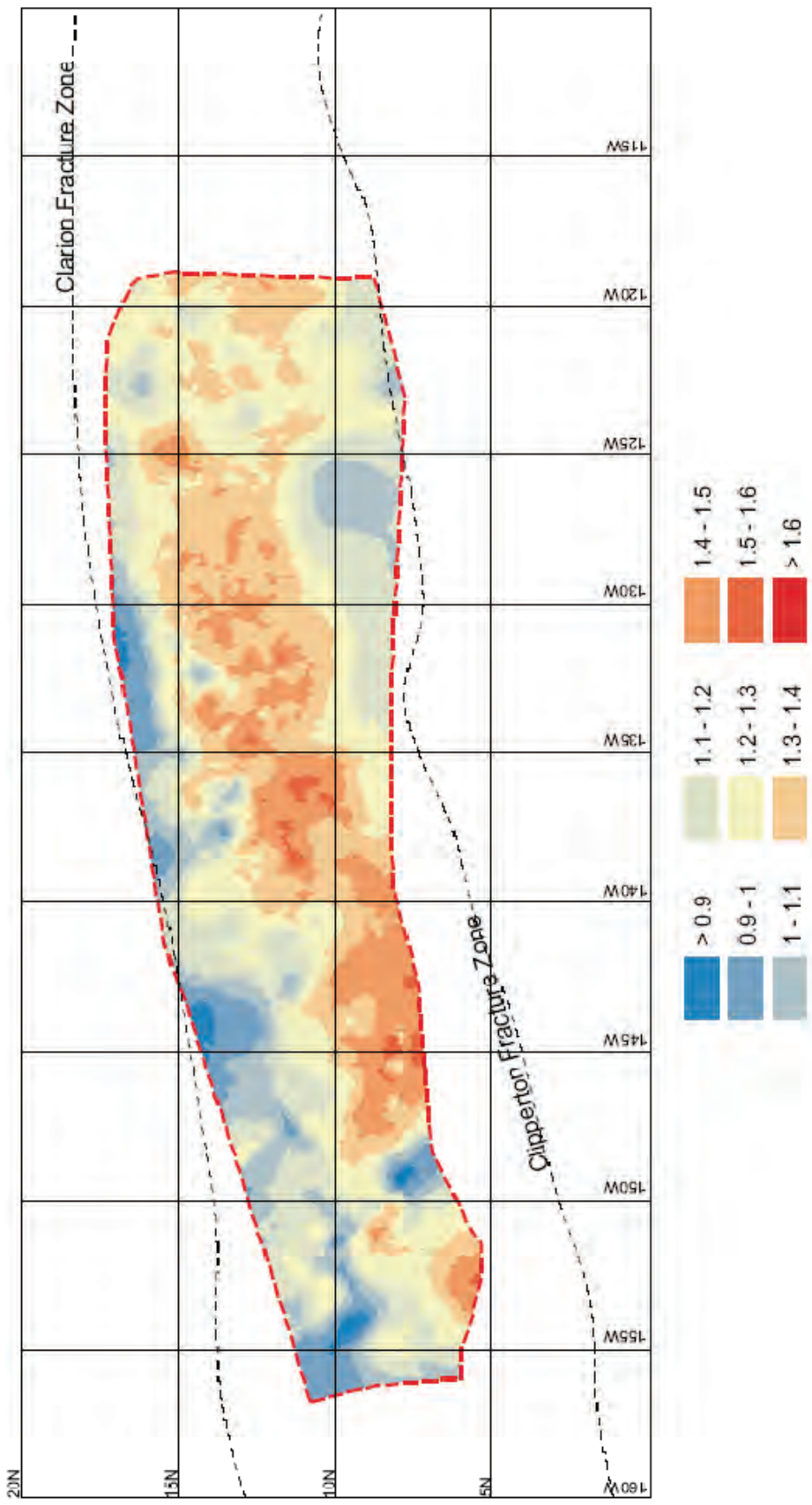
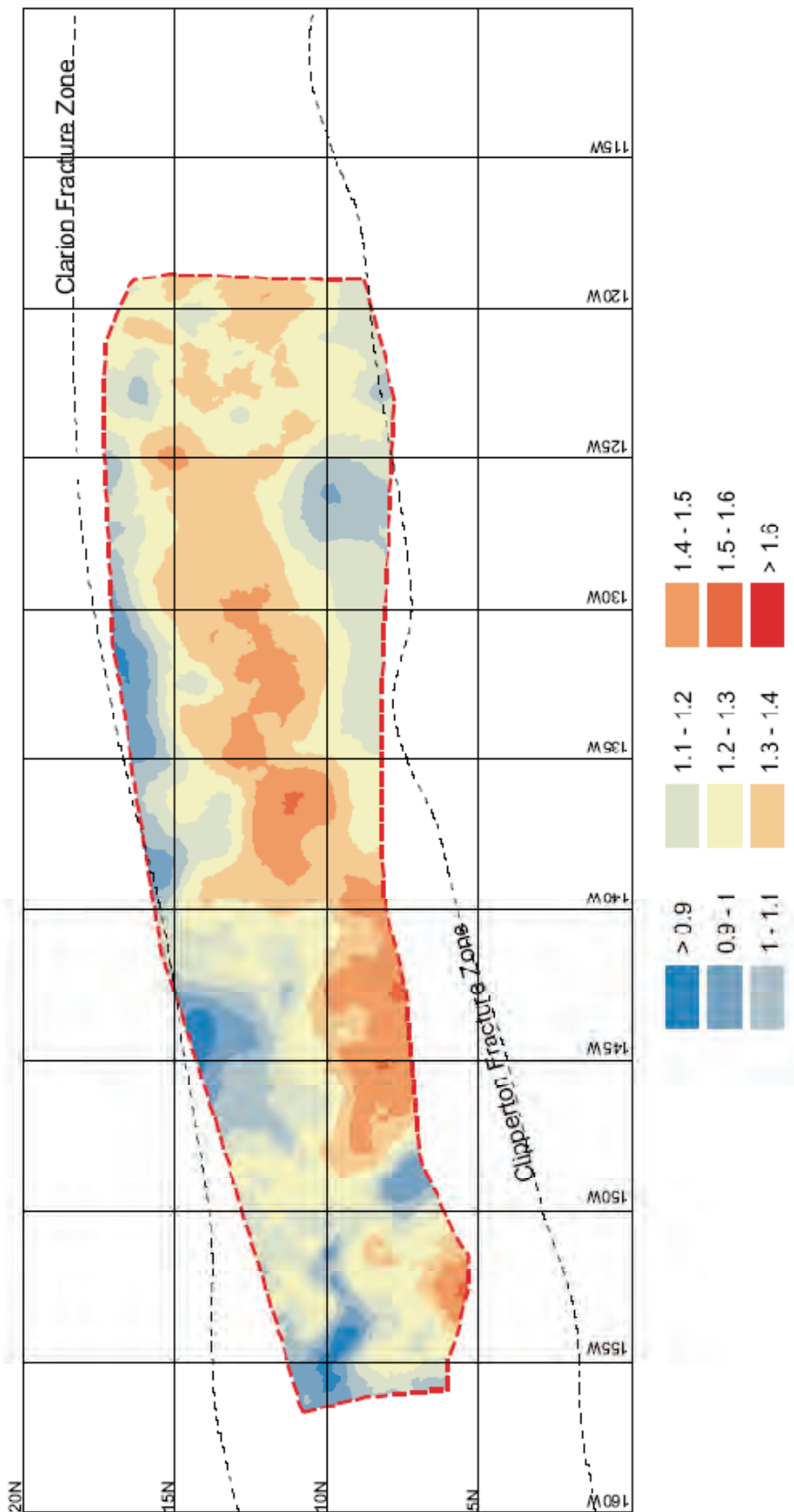


Figure 49. Nickel (dry weight percent): Original Data, Interpolated Contours



*Figure 50. Nickel (dry weight percent): Grid Block Data, Interpolated Contours*

### 8.1.5 Copper

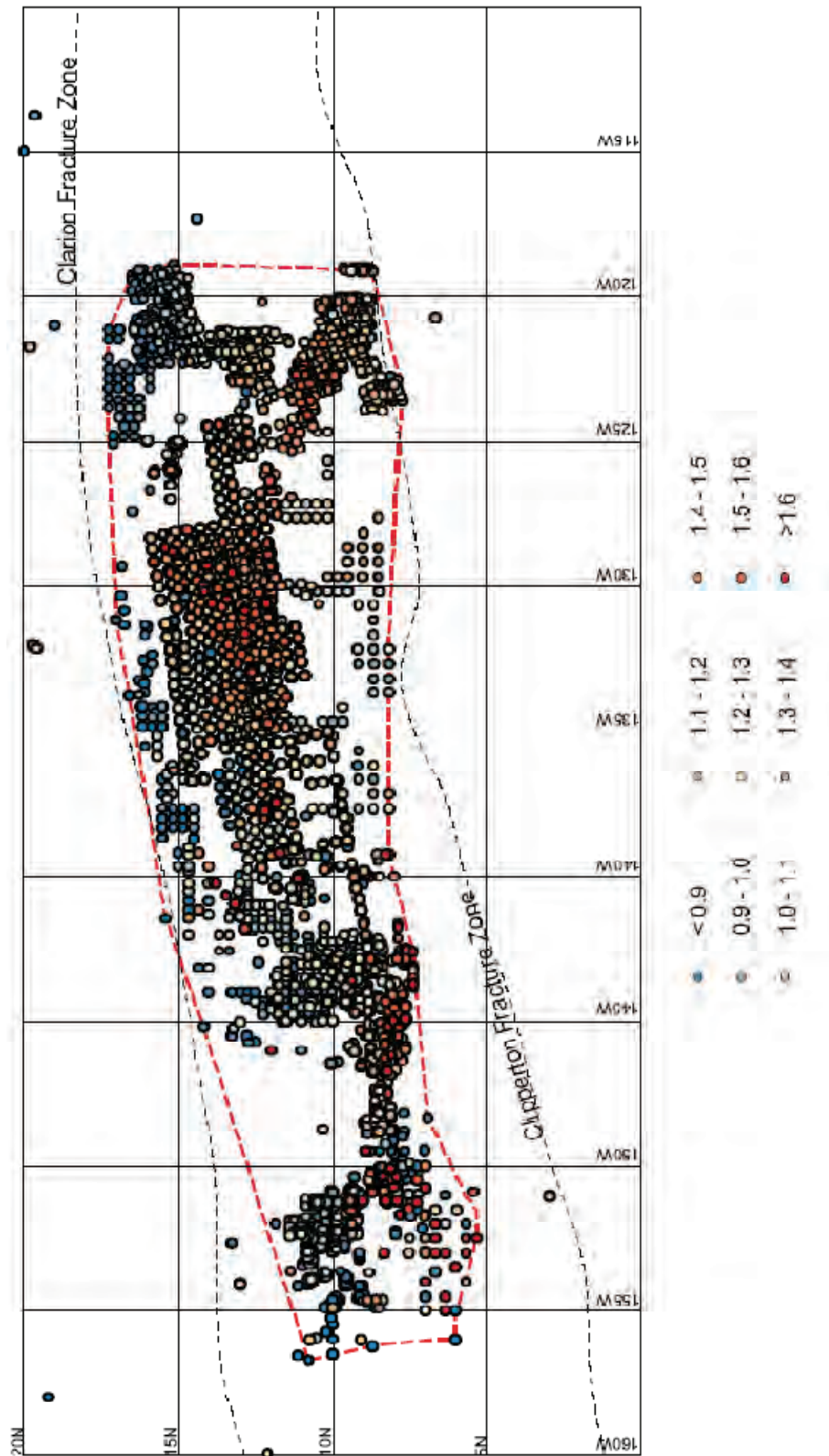


Figure 51. Copper (dry weight percent): Original Data Locations and Values

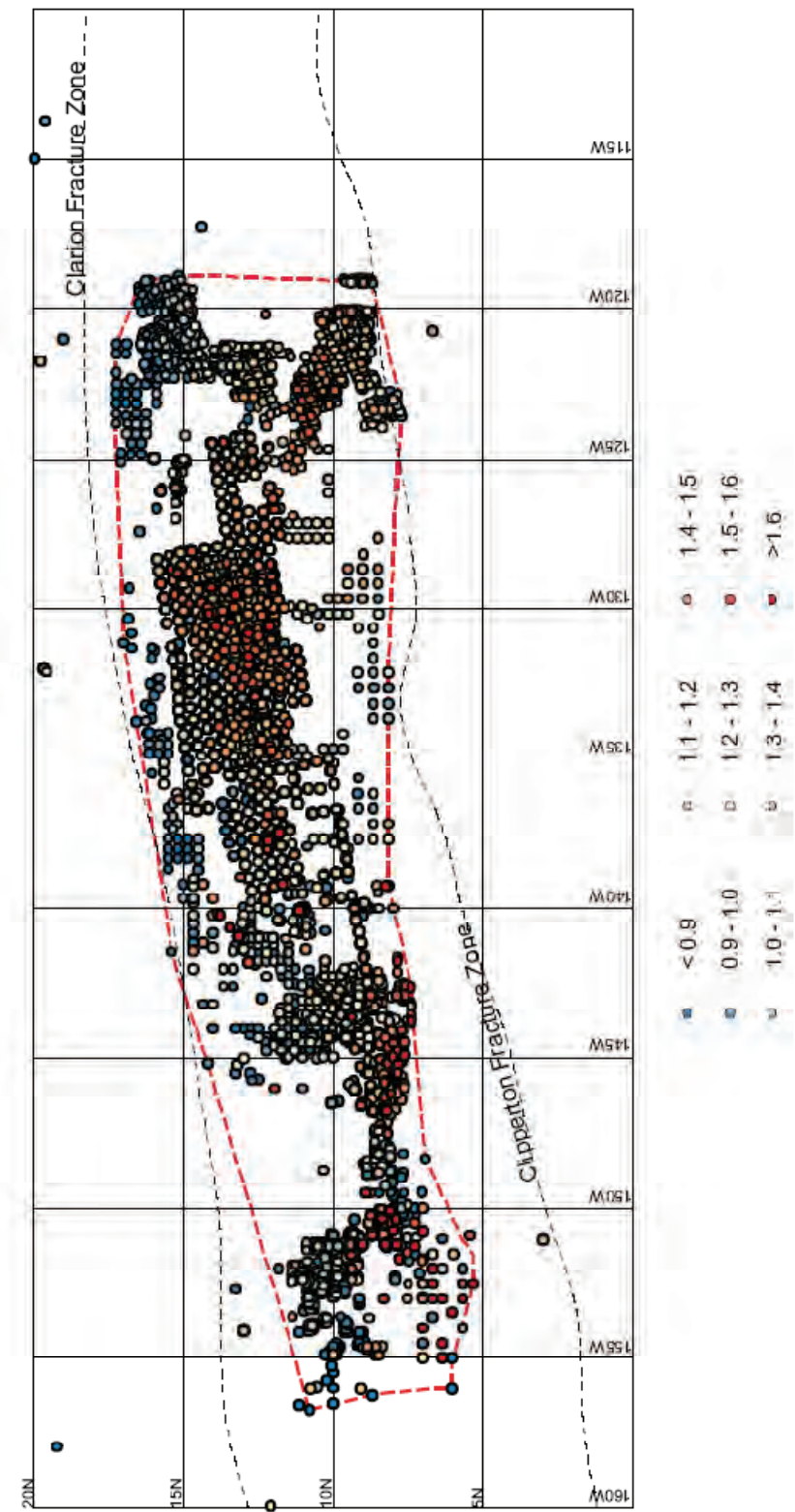


Figure 52. Copper (dry weight percent): Grid Block Data Locations and Values

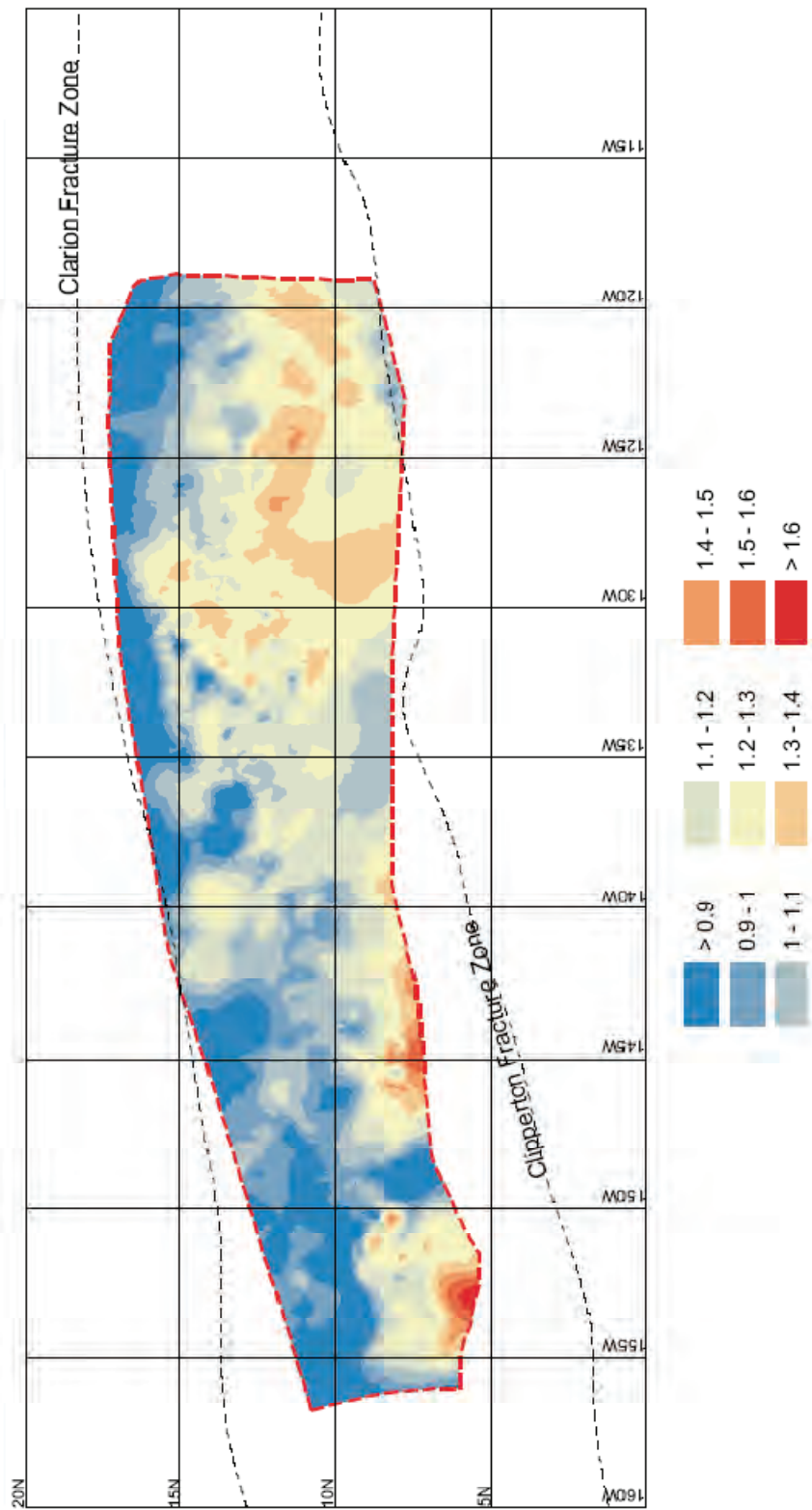


Figure 53. Copper (dry weight percent): Original Data, Interpolated Contours

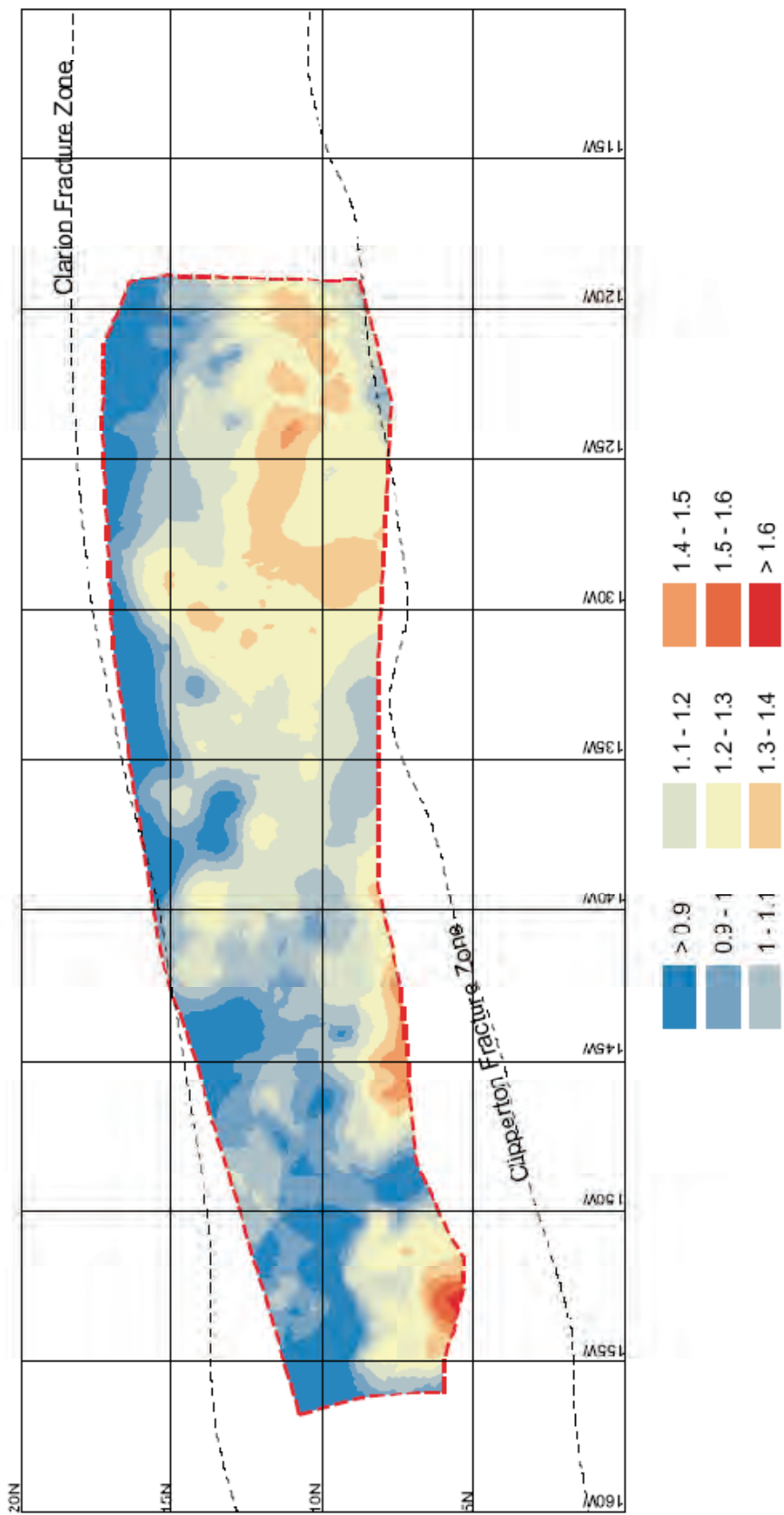
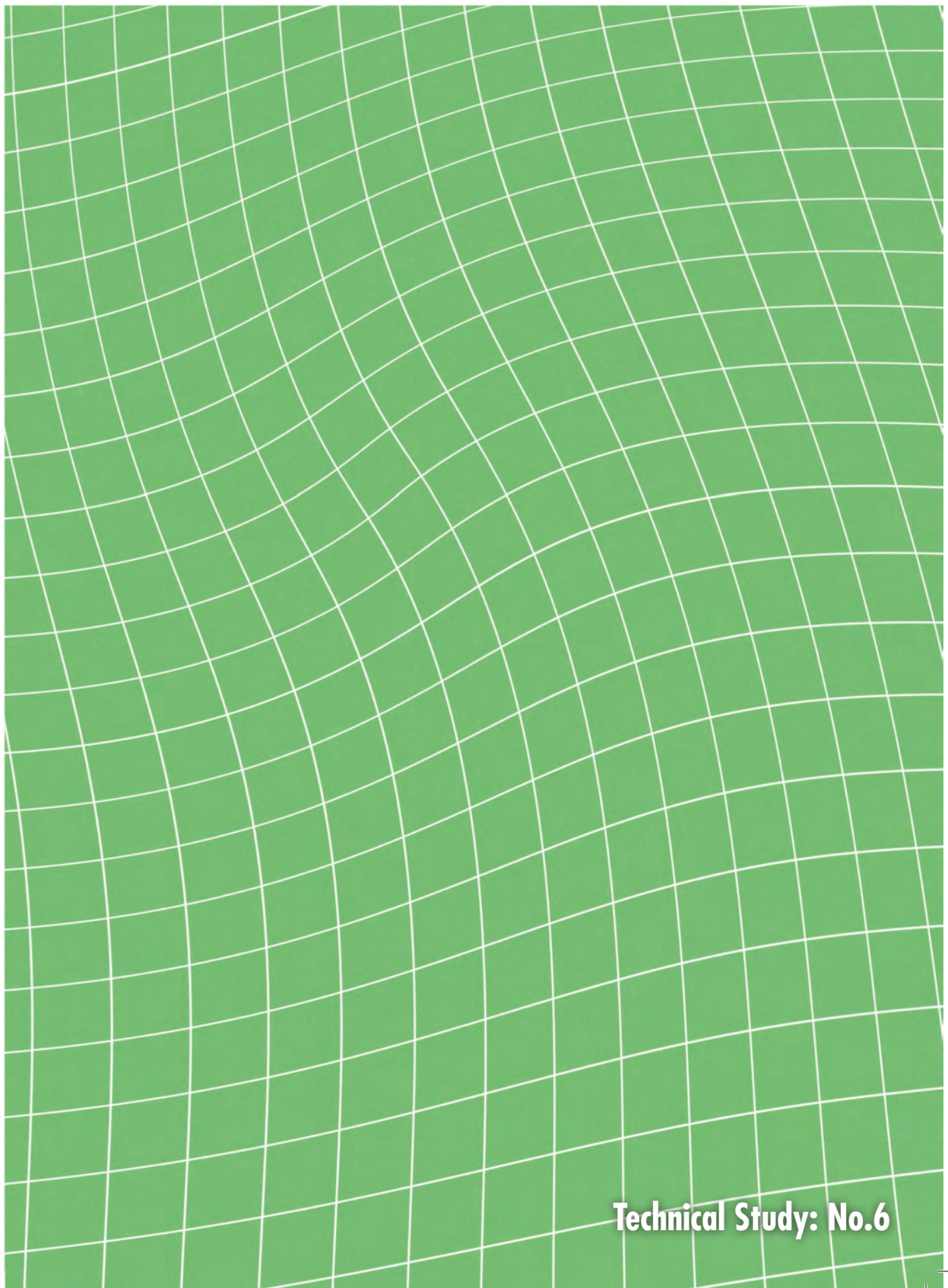


Figure 54. Copper (dry weight percent): Grid Block Data, Interpolated Contours



# PROSPECTOR'S GUIDE FOR POLYMETALLIC NODULE DEPOSITS IN THE CLARION CLIPPERTON FRACTURE ZONE



Technical Study: No.6



**PROSPECTOR'S GUIDE FOR  
POLYMETALLIC NODULE DEPOSITS IN THE  
CLARION-CLIPPERTON FRACTURE ZONE**



# TABLE OF CONTENTS

|   |            |
|---|------------|
| <i>List of Tables</i>   | <i>vi</i>  |
| <i>List of Figures</i>  | <i>vii</i> |
| <b>1. INTRODUCTION</b>  | <b>1</b>   |
| 1.1    Background and Objective                                       | 1          |
| <b>2. GRIDDED BATHYMETRY OF THE CCZ</b>                               | <b>3</b>   |
| 2.1    Introduction   | 3          |
| 2.2    Purpose  | 3          |
| 2.3    Existing Global Bathymetry Data Sets                           | 5          |
| 2.3.1    GEBCO (Global seafloor topography from ship depth soundings) | 5          |
| 2.3.2    Smith and Sandwell Predicted Bathymetry                      | 5          |
| 2.3.3    GEODAS   | 6          |
| 2.3.4    Rationale for using Smith and Sandwell Bathymetry            | 6          |
| 2.4    ISA Datasets   | 8          |
| 2.4.1    Available Data   | 8          |
| 2.5    Description of Work  | 8          |
| 2.5.1    Scanning   | 8          |
| 2.5.2    Digitizing   | 8          |
| 2.5.3    Processing, Editing and Selected Digital Data                | 9          |
| 2.5.4    Gridding   | 9          |
| 2.6    The Resulting Grids  | 9          |
| 2.6.1    One Minute Grid  | 9          |
| 2.7    Appendix A: ISA Data Sets                                      | 13         |
| <b>3. VOLCANIC, TECTONIC AND SEDIMENTARY FACTORS</b>                  | <b>14</b>  |
| 3.1    Static Factors   | 14         |
| 3.1.1    Bathymetry, Morphology and Tectonic Structure                | 14         |
| 3.1.2    Sediment Stucture and Lithology                              | 17         |
| 3.1.3    Occurrence of Polymetallic Nodules                           | 18         |
| 3.2    Dynamic Factors  | 20         |
| 3.2.1    Intra-Plate Seismic Activity                                 | 20         |
| 3.2.2    Intra-Plate Volcanism and Hydrothermal Activity              | 21         |
| 3.3    Model of CCZ Evolution and Nodule Formation                    | 23         |
| <b>4. A GROWTH MODEL FOR POLYMETALLIC NODULES</b>                     | <b>31</b>  |
| 4.1    Classification and Characteristics of CCZ Nodules              | 31         |
| 4.2    Growth Model   | 32         |
| 4.2.1    Supply of Metals   | 32         |
| 4.2.2    Presence of a Nucleus is Necessary                           | 33         |
| 4.2.3    Antarctic Bottom Water (AABW)                                | 33         |
| 4.2.4    Semi-Liquid Surface Layer                                    | 33         |

|           |   |           |
|-----------|---|-----------|
| 4.2.5     | Bioturbation  | 33        |
| 4.2.6     | Internal Nodule Stratigraphy  | 33        |
| <b>5.</b> | <b>NODULE COVERAGE, MORPHOLOGY AND DISTRIBUTION IN THE EASTERN CCZ</b>                  | <b>34</b> |
| 5.1       | Introduction  | 34        |
| 5.2       | Methods and Results   | 34        |
| 5.2.1     | Nodule Abundance and Coverage   | 34        |
| 5.2.2     | Genetic and Morphological Classification of Polymetallic Nodules                        | 35        |
| 5.2.3     | Nodule Morphology, Abundance, and Size  | 37        |
| 5.3       | Discussion and Conclusions  | 38        |
| 5.3.1     | Coverage and Abundance vs Seafloor Depth  | 38        |
| 5.3.2     | Nodule Abundance and Seafloor Morphology  | 40        |
| 5.3.3     | Regional Variability of Nodule Abundance and Morphology                                 | 41        |
| <b>6.</b> | <b>SEDIMENTS IN THE EASTERN CCZ</b>   | <b>43</b> |
| 6.1       | Geological Setting  | 43        |
| 6.2       | Bottom Morphology   | 44        |
| 6.3       | Bottom Sediments  | 45        |
| <b>7.</b> | <b>NODULE GENESIS AND SEDIMENT DISTRIBUTION IN THE REPUBLIC OF KOREA-ALLOCATED AREA</b> | <b>53</b> |
| 7.1       | Introduction  | 53        |
| 7.2       | Bathymetric Characteristics of the Study Area   | 54        |
| 7.3       | Nodule Characteristics  | 54        |
| 7.3.1     | Nodule Abundance  | 54        |
| 7.3.2     | Nodule Size Distribution  | 55        |
| 7.3.3     | Nodule Morphologies   | 55        |
| 7.3.4     | Nodule Surface Textures   | 57        |
| 7.3.5     | Summary of Polymetallic Nodule Characteristics  | 63        |
| 7.4       | Sediment Characteristics  | 63        |
| 7.4.1     | Sediment Distributions  | 63        |
| 7.4.2     | Mineral Composition   | 63        |
| 7.4.3     | Opal Content  | 64        |
| 7.4.4     | Age and Sedimentation Rate  | 64        |
| 7.4.5     | Chemical Composition  | 66        |
| 7.5       | Discussion  | 68        |
| 7.5.1     | Topography and Nodule Genesis   | 68        |
| 7.5.2     | Sedimentation Rate and Nodule Genesis   | 68        |
| 7.5.3     | Sediment Composition and Nodule Genesis   | 69        |
| 7.6       | Conclusions   | 69        |
| <b>8.</b> | <b>BATHYMETRY AND SEDIMENTATION IN THE COMRA CONTRACT AREA</b>                          | <b>71</b> |
| 8.1       | Bathymetry  | 71        |
| 8.1.1     | Sources of Data   | 71        |
| 8.1.2     | Depth Distributions   | 71        |
| 8.2       | Sediment Data Sources   | 71        |
| 8.3       | Sediment Type   | 71        |
| 8.3.1     | Siliceous Clay  | 72        |

|            |   |           |
|------------|---|-----------|
| 8.3.2      | Siliceous Ooze                                      | 74        |
| 8.3.3      | Siliceous-calcareous Ooze                           | 74        |
| 8.3.4      | Calcareous Ooze                                     | 74        |
| 8.4        | Sediment Distributions                              | 74        |
| 8.5        | Relationships Between Sediment Types and Bathymetry | 75        |
| <b>9.</b>  | <b>REGIONAL EXAMINATION OF SEDIMENTS</b>            | <b>77</b> |
| 9.1        | Data Sets and Classification Method                 | 77        |
| 9.1.1      | Data Sets Used                                      | 77        |
| 9.1.2      | Classification Method                               | 78        |
| 9.2        | Maps of Sediment Distribution                       | 79        |
| 9.2.1      | Relationships with Sediment Types                   | 82        |
| <b>10.</b> | <b>BENTHIC BIOLOGICAL DATA FROM THE CCZ</b>         | <b>83</b> |
| 10.1       | Available Data                                      | 83        |
| 10.2       | Abundance and Biomass of Benthic Organisms          | 83        |
| 10.3       | Geochemical Parameters                              | 86        |
| 10.4       | Geographical Gaps                                   | 86        |
| 10.5       | Preliminary Results                                 | 86        |
| <b>11.</b> | <b>REFERENCES CITED</b>                             | <b>91</b> |
| <b>12.</b> | <b>GLOSSARY OF TECHNICAL TERMS</b>                  | <b>96</b> |

## LIST OF TABLES

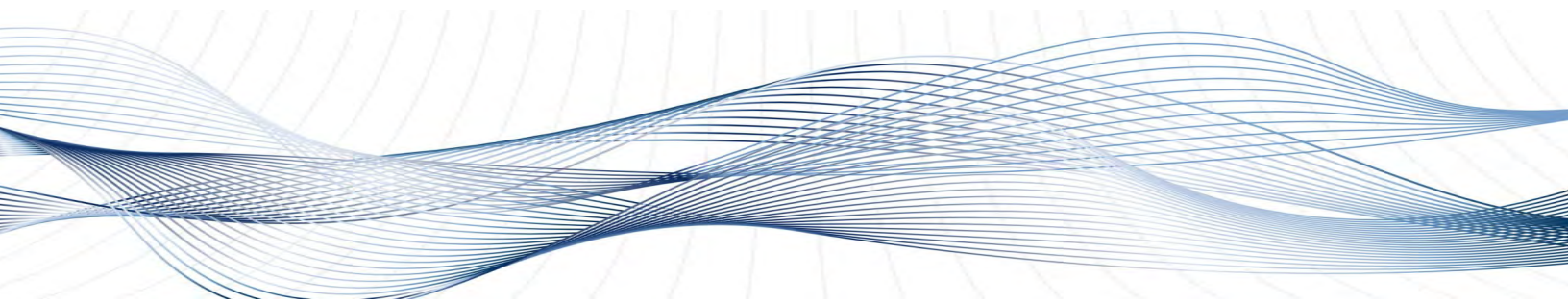
|          |  |    |
|----------|--|----|
| Table 1  | CCZ Metalliferous Sediment Compositions                        | 22 |
| Table 2  | Classification and Characteristics of CCZ polymetallic Nodules | 31 |
| Table 3  | Relationships Among Nodule Morphology, Abundance and Size      | 37 |
| Table 4  | Abundance and Coverage vs. Water Depth                         | 38 |
| Table 5  | Nodule Genetic Type vs. Water Depth                            | 39 |
| Table 6  | Nodule Abundance vs. Seafloor Morphology                       | 41 |
| Table 7  | Sediment Classification  | 47 |
| Table 8  | Sediment Lithological Composition and Stratigraphy             | 48 |
| Table 9  | Sediment Elemental Composition (ppm)                           | 49 |
| Table 10 | Sediment Fe, Ti and Mn Content                                 | 49 |
| Table 11 | Pore Water Composition   | 49 |
| Table 12 | Carbon and Nutrient Content in Sediments and Pore Waters       | 50 |
| Table 13 | Average Composition of Lithological Units                      | 67 |
| Table 14 | Data Sets Used in Study  | 77 |
| Table 15 | Sediment Classification Method Used                            | 78 |

# LIST OF FIGURES

|           |  |    |
|-----------|--|----|
| Figure 1  | Bathymetric Map of CCZ Based on Smith and Sandwell Bathymetry            | 4  |
| Figure 2  | Coverage of ISA Data Sets  | 4  |
| Figure 3  | Comparison of Ship Track Line Sources                                    | 7  |
| Figure 4  | One Minute Grid  | 9  |
| Figure 5  | Layout of the six sub-grids.   | 10 |
| Figure 6  | 0.5 Minute Grids   | 11 |
| Figure 7  | 0.1 Minute Grids   | 12 |
| Figure 8  | Major Features of the CCZ  | 15 |
| Figure 9  | Tectonic Sketch of the CCZ   | 16 |
| Figure 10 | Lithological Zonation of CCZ Surface Sediments                           | 17 |
| Figure 11 | Middle Miocene Unconformity  | 18 |
| Figure 12 | Sediment Facies and Nodule Abundance                                     | 19 |
| Figure 13 | Earthquake Epicenters in the CCZ (1991-2006)                             | 20 |
| Figure 14 | Recent Basalt Flows and Pavements in the CCZ                             | 22 |
| Figure 15 | Distribution of Recent Basalt Flows and Hydrothermal Deposits in the CCZ | 23 |
| Figure 16 | Modern Cross-Section of the CCZ  | 24 |
| Figure 17 | Paleo-Reconstruction of the CCZ Cross-Section, 5 Million Years Ago       | 24 |
| Figure 18 | Paleo-Reconstruction of the CCZ Cross-Section, 10 Million Years Ago      | 25 |
| Figure 19 | Paleo-Reconstruction of the CCZ Cross-Section, 15 Million Years Ago      | 25 |
| Figure 20 | Paleo-Reconstruction of the CCZ Cross-Section, 20 Million Years Ago      | 25 |
| Figure 21 | Paleo-Reconstruction of the CCZ 20 Million Years Ago                     | 26 |
| Figure 22 | Paleo-Reconstruction of the CCZ, 15 MYA                                  | 27 |
| Figure 23 | Paleo-Reconstruction of the CCZ, 10 MYA                                  | 28 |
| Figure 24 | Paleo-Reconstruction of the CCZ, 5 MYA                                   | 29 |
| Figure 25 | Diagram of Nodule Growth Processes                                       | 32 |
| Figure 26 | Nodule Coverage Determined from Photographs and Sample Recoveries        | 35 |
| Figure 27 | Histogram of Genetic Nodule Types in the Eastern CCZ                     | 36 |
| Figure 28 | Histogram of Nodule Morphological Types                                  | 36 |
| Figure 29 | Nodule Abundance vs. Morphology  | 37 |
| Figure 30 | Nodule Size Distribution vs. Morphology                                  | 38 |
| Figure 31 | Nodule Coverage vs. Water Depth  | 39 |
| Figure 32 | Nodule Abundance vs. Water Depth   | 40 |
| Figure 33 | Seabed Stations with No Nodules vs. Water Depth                          | 40 |
| Figure 34 | Nodule Abundance vs. Seafloor Morphology                                 | 41 |
| Figure 35 | Variation of Nodule Abundance with Latitude                              | 42 |
| Figure 36 | Variation of Nodule Genetic Morphology with Latitude                     | 42 |
| Figure 37 | Surface Sediments in the Eastern CCZ                                     | 43 |

|           |   |    |
|-----------|---|----|
| Figure 38 | Sedimentary Stratigraphy in the Eastern CCZ       | 44 |
| Figure 39 | Cumulative Sediment Grain Size Distributions      | 50 |
| Figure 40 | Down-Core Mineral Distributions                   | 51 |
| Figure 41 | Study Area and Bathymetry                         | 54 |
| Figure 42 | Nodule Mn/Fe Ratios                               | 55 |
| Figure 43 | Cu and Ni Content                                 | 56 |
| Figure 44 | Nodule Size Distribution                          | 57 |
| Figure 45 | Distributions of E- and D- Type Nodules           | 58 |
| Figure 46 | Distributions of P- and I- Type Nodules           | 59 |
| Figure 47 | Distributions of I+P- and E+D- Type Nodules       | 60 |
| Figure 48 | Distributions of s- and t- Type Nodules           | 61 |
| Figure 49 | Distributions of r- and d- Type Nodules           | 62 |
| Figure 50 | Illite and Smectite Content Variation with Depth  | 65 |
| Figure 51 | Opal Content Variations in Each Lithological Unit | 65 |
| Figure 52 | Opal Content of Surface Sediments                 | 66 |
| Figure 53 | COMRA East Area                                   | 72 |
| Figure 54 | COMRA West Area                                   | 72 |
| Figure 55 | East Area Bathymetry Histogram                    | 73 |
| Figure 56 | West Area Bathymetry Histogram                    | 73 |
| Figure 57 | Sediment Distribution in East Area                | 74 |
| Figure 58 | Sediment Distribution in West Area                | 75 |
| Figure 59 | Sediment Type vs. Bathymetry, East Area           | 76 |
| Figure 60 | Sediment Type vs. Bathymetry, West Area           | 76 |
| Figure 61 | Sediment Sample Stations Used in the Study        | 78 |
| Figure 62 | Station Sediment Classifications                  | 79 |
| Figure 63 | Nearest Neighbour Extrapolation                   | 80 |
| Figure 64 | Contours of Fine-Grained Sediments                | 80 |
| Figure 65 | Sediment Distribution and CCZ Bathymetry          | 81 |
| Figure 66 | Nodule Abundance and CCZ Bathymetry               | 81 |
| Figure 67 | Sediments vs Metal Content and Abundance          | 82 |
| Figure 68 | Map of stations sampled in and around the CCZ     | 85 |
| Figure 69 | Estimated Carbon Export Flux in the CCZ           | 87 |
| Figure 70 | Estimated Nitrogen Export Flux in the CCZ         | 87 |
| Figure 71 | Trend Surface Plane, Meiofauna                    | 88 |
| Figure 72 | Trend Surface Plane, Macrofauna                   | 88 |
| Figure 73 | Trend Surface Plane, Nematodes                    | 89 |
| Figure 74 | Trend Surface Plane, Polychaetes                  | 89 |
| Figure 75 | Trend Surface Plane, Tanaids                      | 90 |

# 1. INTRODUCTION



## 1.1 Background and Objectives

Submarine ferromanganese concretions were first discovered in the Kara Sea of Russia in 1868 (Earney, 1990). In the course of its round-the-world expedition from 1873 to 1876, HMS *Challenger* collected many small dark-brown balls, rich in manganese and iron, which were named polymetallic nodules (Manheim, 1978; Earney, 1990). Since the 1960s, manganese nodules (hereinafter referred to as ‘polymetallic nodules’, as many of the other metals of economic importance are to be found in these nodules) have been recognized as a potential source of nickel, copper, cobalt and manganese, which are likely to assume increasing importance as land-based deposits of these metals become increasingly depleted.

Polymetallic nodules are found on the seabed in many areas, and have been comparatively well studied because of their potential economic importance. The Clarion-Clipperton Fracture Zone (CCZ), the study area for this project, has been the focus of much international attention for many years (Mero, 1965; McKelvey *et al.*, 1979; Bernhard and Blissenbach, 1988). To date, the greatest concentrations of polymetallic nodules have been found in this region.

In March 2001 the International Seabed Authority (ISA) Secretariat met with representatives of the exploration Contractors (formerly known as ‘registered pioneer investors’) to discuss ways to improve the ISA’s resource assessment of polymetallic nodules in the CCZ. Some of the Contractor representatives suggested that the future work of the Secretariat would be enhanced through the development of a geological model of polymetallic nodule deposits for this region. This was in recognition of the paucity of nodule grade and abundance data for many areas of the CCZ.

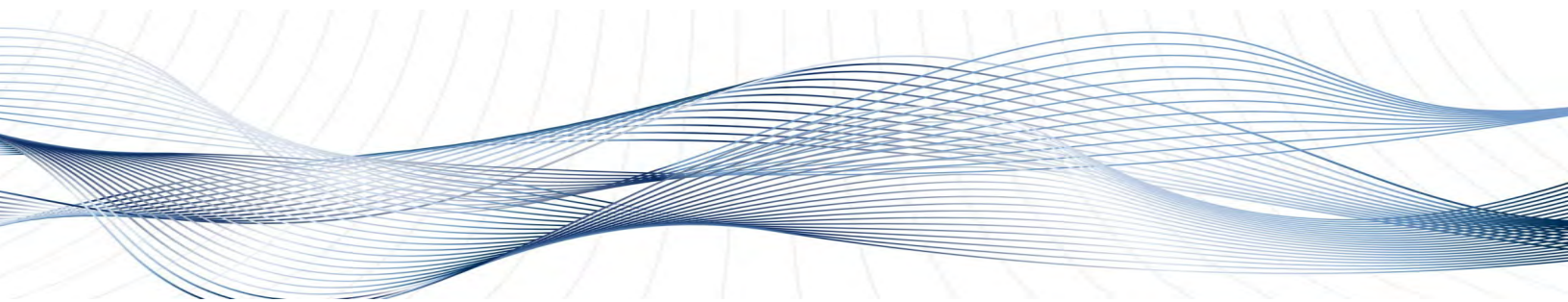
At the ninth session of the Authority in 2003, the members of the Authority’s Legal and Technical Commission recognized that such a model could directly benefit Contractors and Prospectors working in the CCZ by improving the resource assessment for the area, and could also contribute to a better general understanding of how economically interesting deposits form. The Authority convened a workshop between 13 and 20 May 2003 in Fiji, to consider the various data (metal content and abundance data and candidate proxies) that should be included in the effort. Experts from several relevant disciplines delivered technical presentations that identified candidate proxies that could be used and the major tasks that the Authority should undertake to establish the Geological Model.

The technical workshop produced general recommendations, a project strategy and key project components for the development of the Model. Between 6 and 10 December 2004, the Authority

convened a Group of Technical Experts to outline the scope of the work that would be involved, to ascertain the availability of data on selected proxies, to schedule the work required to gather, evaluate and incorporate suitable data sets into the model through mathematical algorithms.

Taking into account the results of the Fiji workshop, the Group of Technical Experts identified the approach that it would use to create the model and specified the proxy data that it would test for use in predicting polymetallic nodule metal content and abundance. The primary products from the effort are: (1) a ***Geological Model*** of polymetallic nodule deposits in the CCZ (presented in a separate report); and (2) a ***Prospector's Guide***, presented here, containing a narrative description of the key factors relevant to exploration for polymetallic nodules in the CCZ, including data and available information on known deposits. This report presents the results of nine independent studies that provide extensive geophysical, geological, oceanographic and biological information related to the CCZ deposits and general guidance, based on many years of study of these deposits, as to why these deposits occur where they do and criteria for seeking undiscovered deposits elsewhere.

## **2. GRIDDED BATHYMETRY OF THE CCZ**



### **2.1 Introduction**

The study area is located in the eastern central Pacific, to the southwest of the Hawaiian Islands. For the purposes of the study, the geographical limits of the study area have been taken to be 0° - 20°N x 115°W – 160°W. It is bounded to the north and south by the ENE-WNW trending Clarion and Clipperton Fracture Zones (Figure 1).

The seafloor lies mostly between 4,000 and 6,000 meters water depth in the study area and is characterized by a number of seamounts, some of which reach depths of less than 3,000 m. The wide-spread seafloor spreading fabric, oriented approximately orthogonal to the trend of the bounding fracture zones, provides a large number of flat-floored valleys, separated by irregular, often discontinuous ridges a few hundred meters high.

### **2.2 Purpose**

The reason for the work was to collect a number of surveys (Figure 2) carried out by the Pioneer Investors: France (IFREMER); Japan (DORD) data from a number of surveys; the Russian Federation (Yuzhmorgeologiya); China (COMRA); and Inter Ocean Metal Joint Organization (IOM) into combined bathymetric grids. These grids will be used to further the work of the ISA in the region, and particularly to develop a regional geologic model.

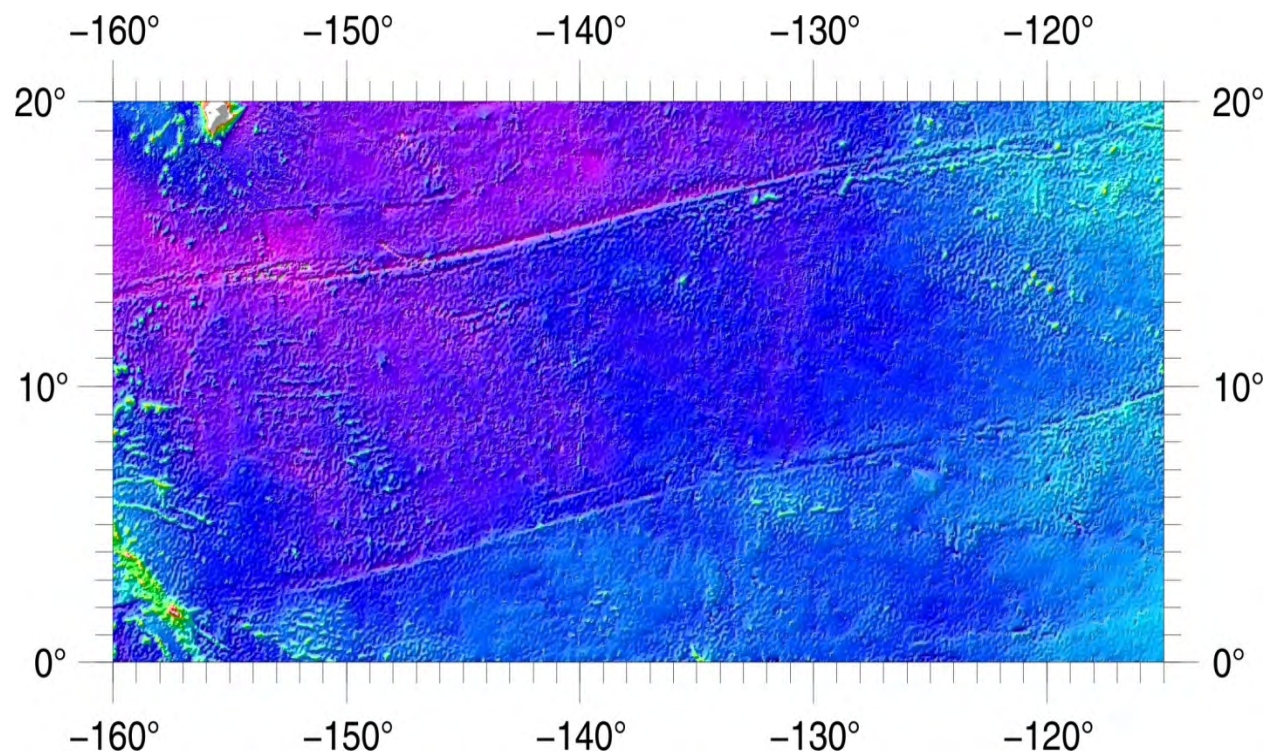


*Figure 1. Bathymetric Map of CCZ based on Smith and Sandwell Bathymetry*

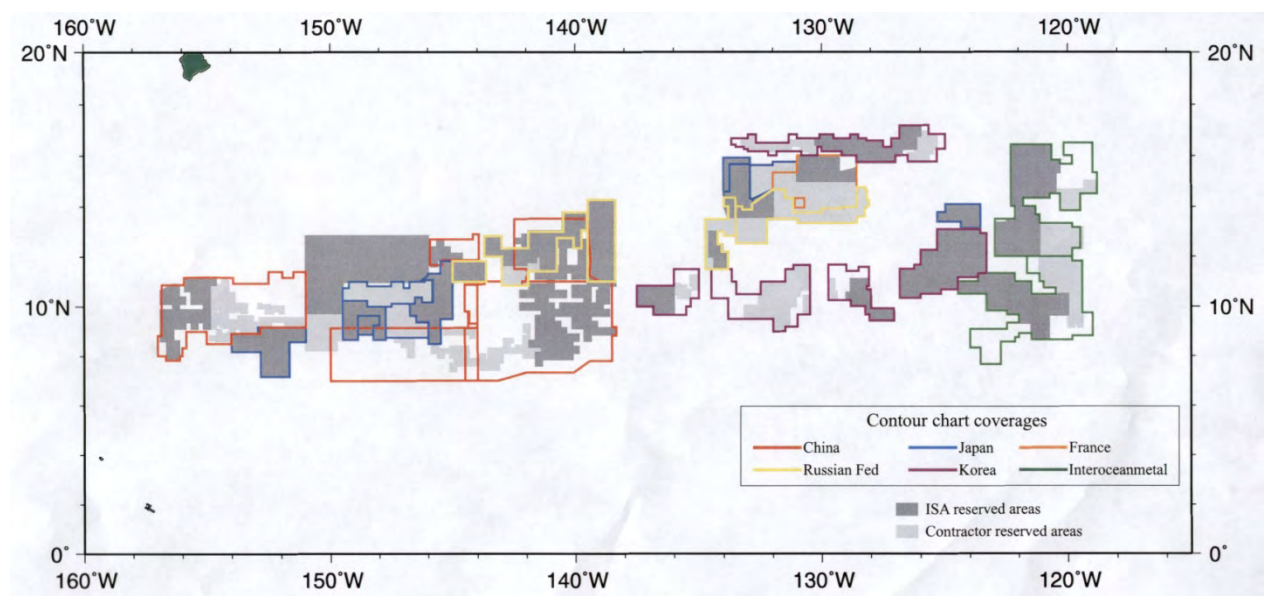


*Figure 2. Coverage of ISA Data Sets*

## 2.3 Existing Global Bathymetry Data sets

### 2.3.1 GEBCO (*Global seafloor topography from ship depth soundings*)

<http://www.ngdc.noaa.gov/mgg/gebco/gebco.html>

The GEBCO Digital Atlas (GDA), Centenary Edition, was published in 2003; it consists of two bathymetric products. The first comprises the digitized bathymetric contours, coastlines and track line control of the October 2002 version of the GEBCO Digital Atlas (GDA), based primarily on the digitized GEBCO Fifth Edition. The second is the GEBCO One Minute Bathymetric Grid, based primarily on the bathymetric contours of the October 2002 version of the GDA.

The contours of the GEBCO Fifth Edition were based on the collected soundings sheets provided by the volunteering Hydrographic Offices. These formed a unique data base on which to compile the Fifth Edition. However, because these sheets were compiled over a period of 30 to 40 years, the data recorded thereon varied considerably in accuracy, both in depth and position, depending on the sounding apparatus used, and the navigational methods employed by the numerous ships that had contributed data. Other data, including bathymetry from the GEODAS database were also used.

Although certain areas of the deep sea may be of sufficient commercial, military or scientific importance to be examined closely by saturated surveys, for the greater part of the deep oceans bathymetric charts can only be compiled from random track data of variable quality. The interpretation of such data relies on the expert understanding of marine geologists and geophysicists of the processes shaping the ocean floor. The latter quality is not exhibited in other global bathymetric datasets.

Additional control contours and sounding data were used in some areas to constrain the gridding process. It must be stressed that, although the GEBCO grid is presented at one minute intervals of latitude and longitude so as to replicate the GEBCO contours, this does not imply that knowledge is available on seafloor depth at this resolution - indeed the depth in most one minute squares of the world's oceans has yet to be measured!

In the study area most GEBCO data tracks run from north to south, many emanating from Hawaii. It is not unusual for there to be more than 100 km between adjacent data tracks.

### 2.3.2 Smith and Sandwell Predicted Bathymetry

[http://topex.ucsd.edu/www\\_html/mar\\_topo.html](http://topex.ucsd.edu/www_html/mar_topo.html)

The surface of the ocean bulges outward and inward, mimicking the topography of the ocean floor. The bumps, too small to be seen, can be measured by a radar altimeter aboard a satellite. Data collected by the European Space Agency ERS-1 altimeter, along with declassified data from the US Navy Geosat altimeter have provided detailed measurements of sea surface height over the oceans. These data provide the first view of ocean floor structures in many remote areas of the Earth. For scientific applications, the Geosat and ERS-1 altimeter data are comparable in value to the radar altimeter data recently collected by the Magellan spacecraft during its systematic mapping of Venus.

Walter Smith and David Sandwell used these dense satellite altimeter measurements in combination with sparse measurements of seafloor depth by ships to construct uniform resolution maps of seafloor topography. These maps do not have sufficient accuracy and resolution to be used to assess navigational hazards but they are useful for such diverse applications as locating the obstructions/constrictions to the major ocean currents and locating shallow seamounts where fish and lobster are abundant.

The satellite-derived gravity grids reveal all of the major structures of the ocean floor having widths greater than 10-15 km (6-9 miles). This resolution matches the total swath width of the much higher (in comparison to conventional echo sounders) multibeam mapping system on a ship (up to 100m resolution) so the gravity maps are the perfect reconnaissance tool for planning the more detailed shipboard surveys. The global gravity grids reveal all volcanoes on the seafloor greater than about 1,000m tall. It has been calculated that approximately half of these volcanoes had not been charted previously.

The depth values in the predicted bathymetry grid are coded according to their source. An even value is based on a satellite gravity measurement and an odd value is based on a depth measurement by a ship.

### **2.3.3 GEODAS**

<http://www.ngdc.noaa.gov/mgg/geodas/trackline.html>

The National Geophysical Data Centre (NGDC) GEODAS Marine Track line Geophysics database contains bathymetric (including multibeam), magnetic, gravity and seismic navigation data collected during marine cruises from 1953 to the present. Coverage is worldwide. Data sources include both US and foreign oceanographic institutions and government agencies.

These data have not been cleaned by NGDC. The cruise data files are accepted from the contributors 'as is' and is only checked for gross navigation errors, such as traveling across land.

### **2.3.4 *Rationale for using Smith and Sandwell bathymetry***

For this work, the Smith and Sandwell bathymetry was preferred to the GEBCO grid. A comparison of track line coverage (Figure 3) shows the Smith and Sandwell product to be based on a denser coverage of ship borne measurements as well as the satellite derived gravity values, making it a superior product for this work. Also, the emphasis of the dataset was on scattered data points rather than data points along contours.

GEBCO (top); Smith and Sandwell (middle); GEODAS (bottom)

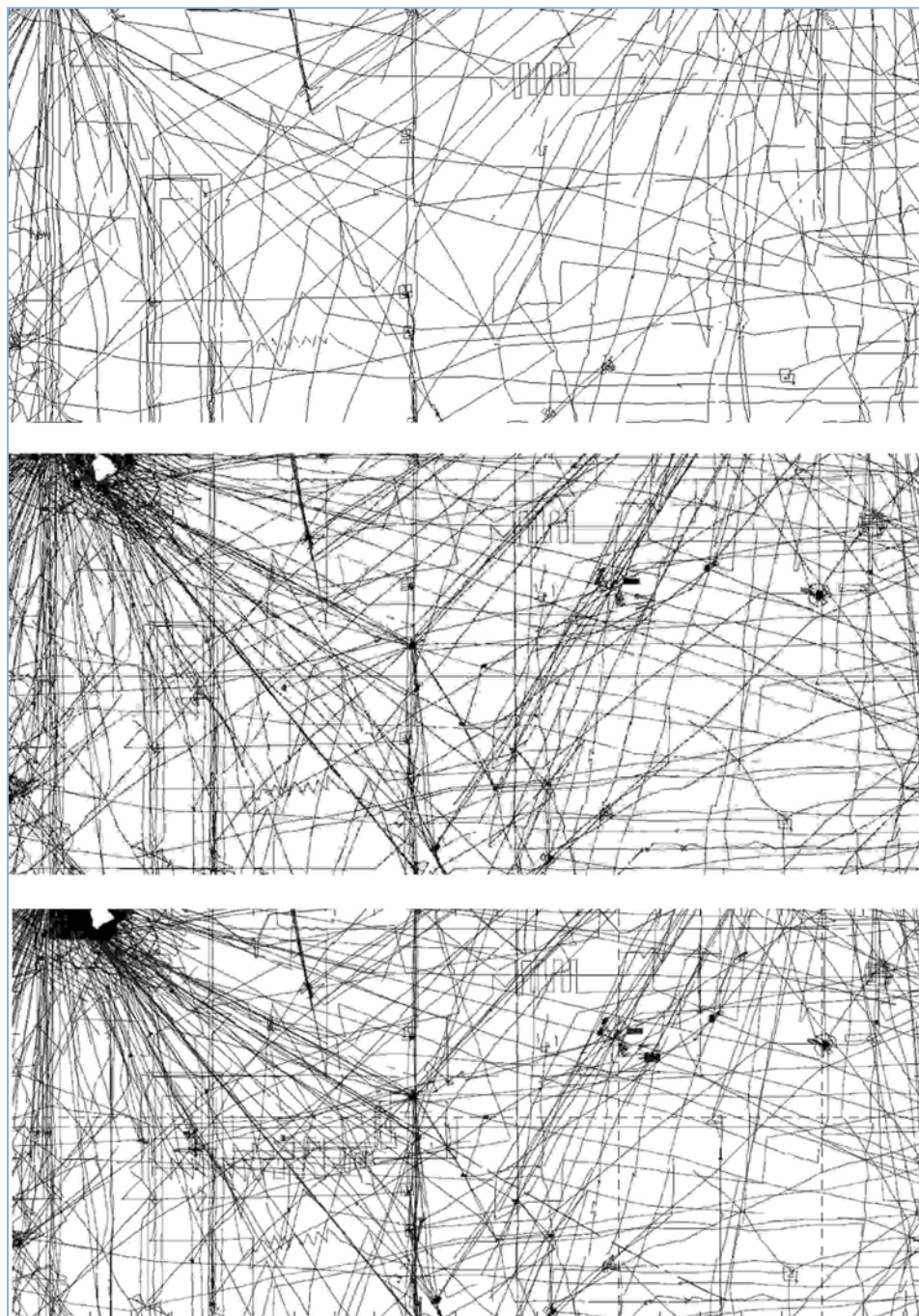


*Figure 3. Comparison of Ship Track Line Sources*

Further comparison of track line coverage with GEODAS bathymetry indicates that the Smith and Sandwell bathymetry has used most of the available ship borne bathymetric data in its creation.

## 2.4 ISA Datasets

### 2.4.1 Available Data

The ISA CCZ datasets (Appendix A) provided by the Pioneer Investors fell into three basic types:

- (i) Paper maps – on the Mercator projection at a variety of scales (mostly around 1:1,000,000) with contours depicted at various intervals (100, 200 and 500 m) to suit the map scale. Some maps also showed useful extreme soundings on lows and highs.
- (ii) Digital Grids at 0.5 minute and 500 and 200 m resolutions.
- (iii) Digital XYZ files in various ASCII formats.

These data are available digitally from the ISA as Excel spreadsheets.

## 2.5 Description of Work

The following sections discuss the procedures used to produce the final maps.

### 2.5.1 Scanning

The paper maps were scanned into 8-bit TIFF images using the large-format Colortrac 3680 Enhanced scanner at NOCS at 300 dpi resolution. The files were transferred to the project PC where they were cropped and converted to 1-bit (black and white) TIFF images using PhotoPaint software. The ArcGIS software requires these types of image in order to perform vectorizing operations.

Using ArcCatalog, the 1-bit images were exported to the ERDAS IMAGINE format used by the vectorizing software. Before vectorizing, the images were georeferenced using four points on the image whose map coordinates were known and were widely separated. This reduced any inaccuracies caused by unstable or badly copied paper maps.

### 2.5.2 Digitizing

#### Method 1

Georeferencing permitted conversion of values directly from the Mercator projected maps to digital Geographical (Latitude/Longitude) values. The entire image was automatically converted to vectors; these were then selected manually and assigned to individual contour layers that reflected their depth values. It was also possible to digitize manually any faint contours that had not automatically vectorized earlier.

These layers were saved as shapefiles, which were exported via a two-stage process to ASCII XYZ files.

#### Method 2

This was used to capture data from the scanned maps that were not sufficiently clear for the ArcGIS 9 method to work.

The 8-bit images were imported into Didger software. Didger permitted the images to be ‘calibrated’ before digitizing, and this converted values directly from the Mercator projected maps to digital Geographical values. The contours were then digitized manually to individual contour layers. These layers were exported to ASCII XYZ files.

The XYZ files produced by both digitizing methods described above were either gridded separately or concatenated into a single file for gridding.

### **2.5.3 Processing, editing and selecting digital data**

Microsoft Excel and word processing software were used to process, clean and select digital data.

### **2.5.4 Gridding**

Generic Mapping Tools (GMT) software was used to grid the data files. GMT was also used to create colour images, contour maps and to combine grids. Surfer software was used to visually inspect the grid values to identify anomalies etc. Fledermaus software was used to inspect the grids by creating 'fly-thru' scenes; GMT was used to create colour images and contour maps, and to check for errors. ArcGIS 9 was used to display the resulting grids in conjunction with the original data sets and the data sets created during the intermediate digitizing stages.

## **2.6 The Resulting Grids**

Grids have been produced by GMT (.grd files) and converted for import to ArcGIS/ArcView.

### **2.6.1 One Minute Grid**

#### Entire Area 0°-20°N x 160°-115°W

This grid (Figure 4) is a combination of the ISA-supplied datasets with depths derived from the Smith and Sandwell predicted bathymetry grid used as a background dataset to fill data gaps in and around the ISA datasets.

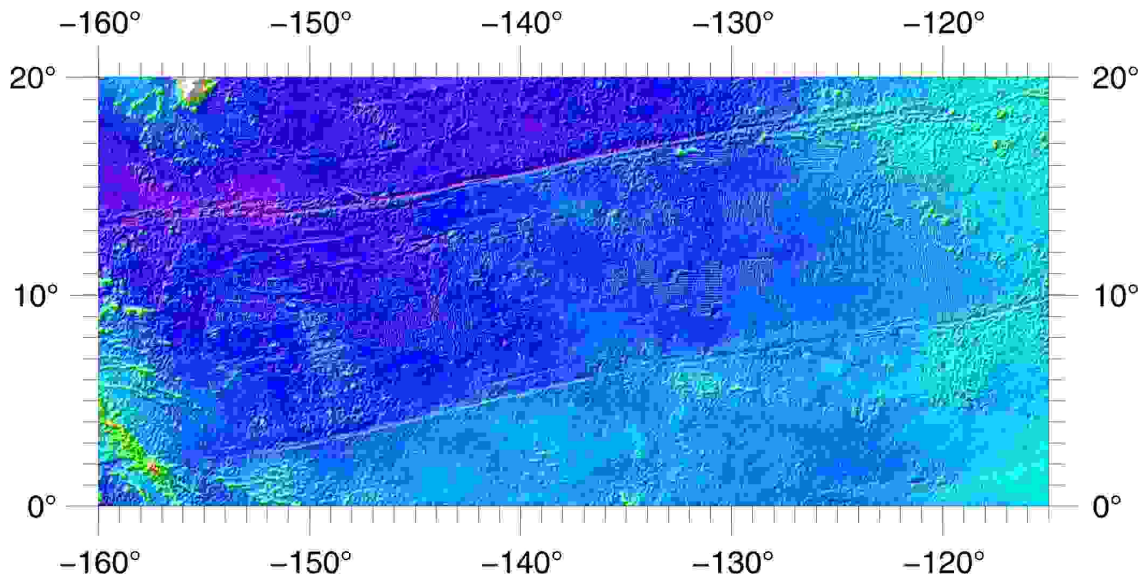


*Figure 4. One Minute Grid*

#### Sub-Grids

The work was split into six sub-grids (Figure 5).

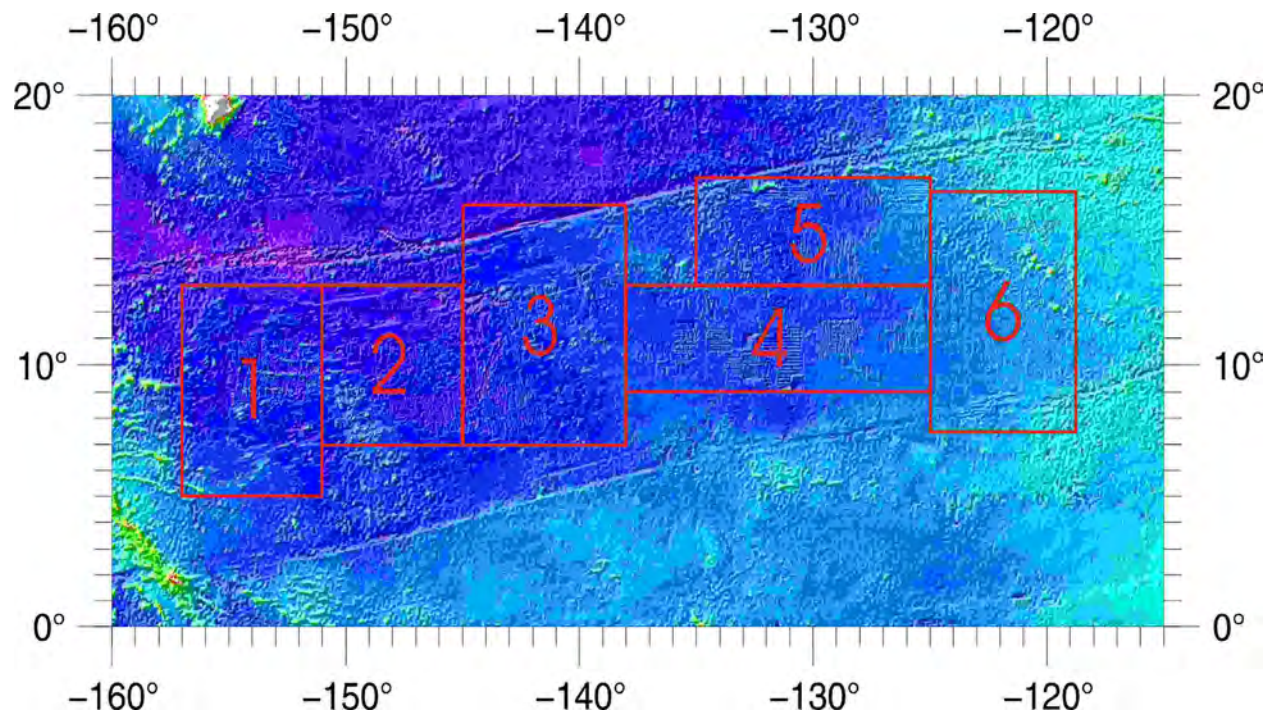


*Figure 5. Layout of the six sub-grids.*

These were selected to use the maximum amount of the ISA data in the best-shaped grids.

#### 0.5 Minute Grids

These grids (Figure 6) are a combination of the ISA-supplied datasets with depths derived from the Smith and Sandwell predicted bathymetry grid used as a background dataset to fill data gaps in and around the ISA datasets.

- *Area 1 5°-13°N x 157°-151°W*
- *Area 2 7°-13°N x 151°-145°W*
- *Area 3 7°-16°N x 145°-138°W*
- *Area 4 9°-13°N x 138°-125°W*
- *Area 5 13°-17°N x 135°-125°W*
- *Area 6 7.5°-16.5°N x 125°-118.5°W*

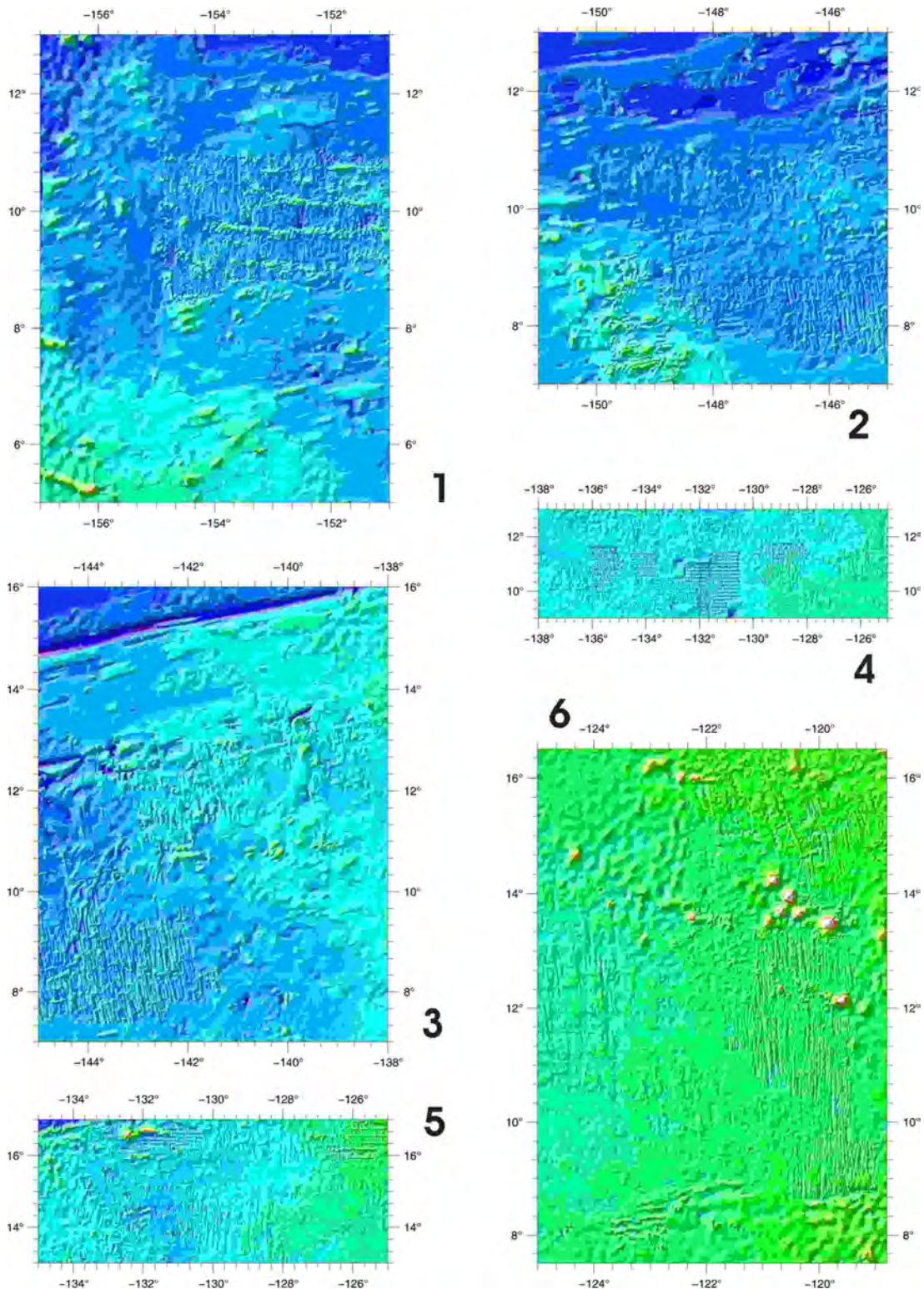


Figure 6. 0.5 Minute Grids

### 0.1 Minute Grids

These grids (Figure 7) are a combination of the ISA supplied datasets with depths derived from the Smith and Sandwell predicted bathymetry grid used as a background dataset to fill data gaps in and around the ISA datasets.

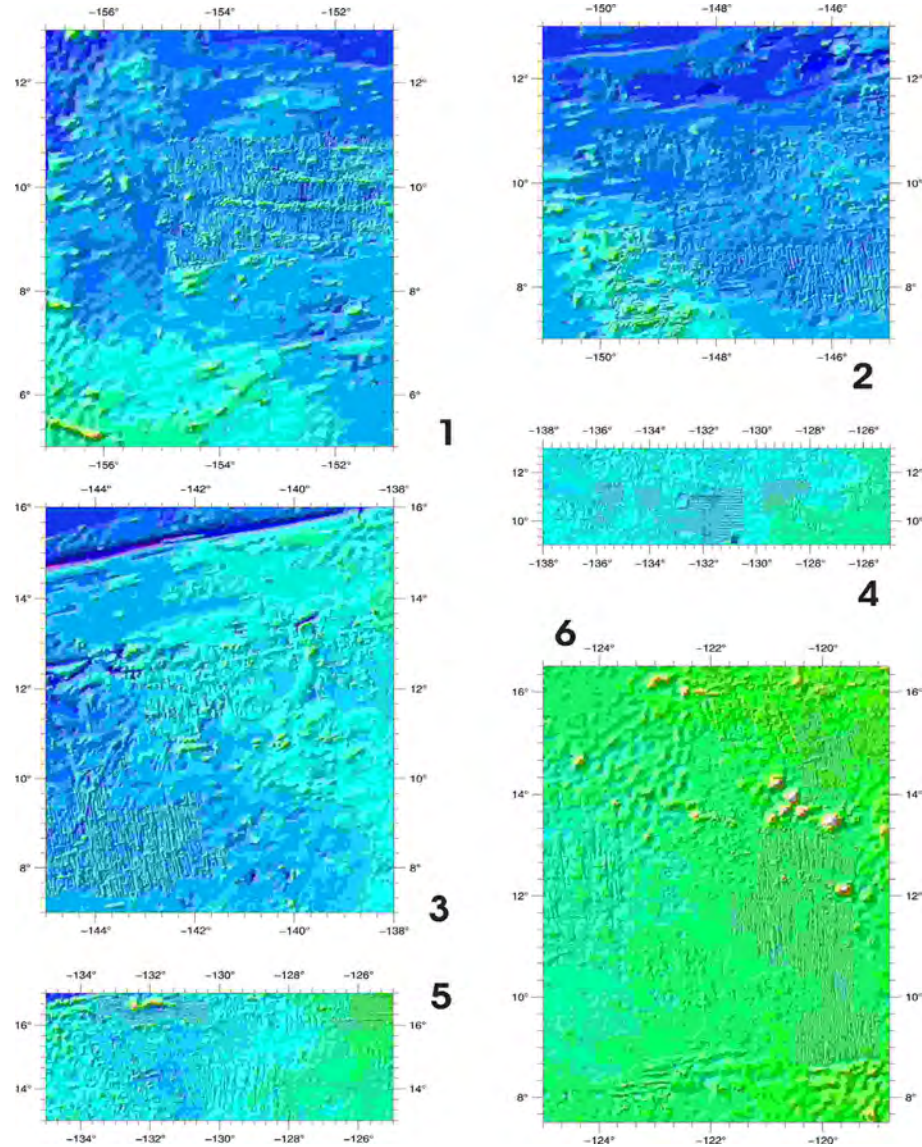


Figure 7. 0.1 Minute Grids

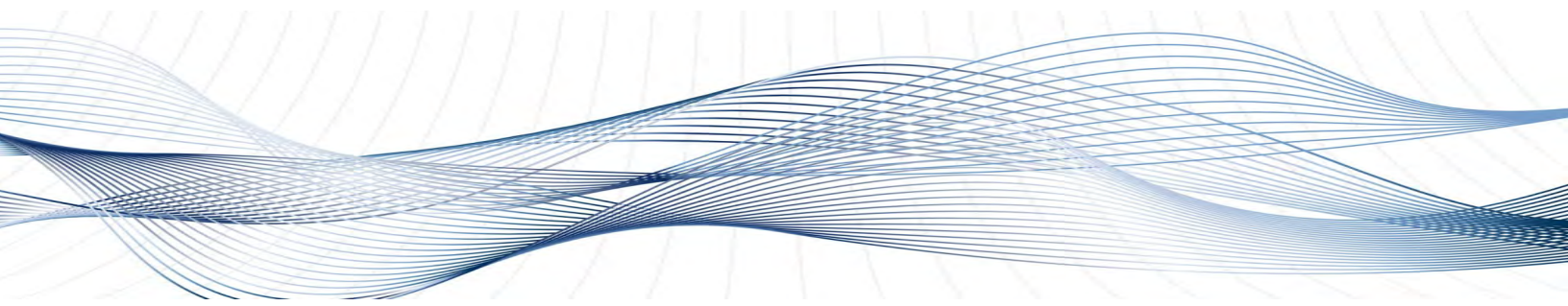
- Area 1 5°-13°N x 157°-151°W
- Area 2 7°-13°N x 151°-145°W
- Area 3 7°-16°N x 145°-138°W
- Area 4 9°-13°N x 138°-125°W
- Area 5 13°-17°N x 135°-125°W
- Area 6 7.5°-16.5°N x 125°-118.5°W

## 2.7 Appendix A: ISA Data sets

### International Seabed Authority Clarion Clipperton Fracture Zone Area

| Source              | Resolution | Datasets ( scans & ASCII )  | MinLon  | MaxLon  | MinLat | MaxLat | Geo Ref | Digitize | Grid |
|---------------------|------------|-----------------------------|---------|---------|--------|--------|---------|----------|------|
| CHINA<br>(COMRA)    | 100m + Ds  | CHI_fig31.tif               | -157    | -151    | 8      | 11.5   | Yes     | Yes      | Yes  |
|                     | 100m + Ds  | CHI_fig32.tif               | -146    | -144    | 11.5   | 13     | Yes     | Yes      | Yes  |
|                     | 100m + Ds  | CHI_fig33.tif               | -142.5  | -139    | 11     | 13.5   | Yes     | Yes      | Yes  |
|                     | 100m + Ds  | CHI_fig34.tif               | -150    | -144    | 7      | 11     | Yes     | Yes      | Yes  |
|                     | 100m + Ds  | CHI_fig35.tif               | -145.5  | -137.5  | 7      | 11     | Yes     | Yes      | Yes  |
|                     | 0.5 min    | Comra-east-multibeam.grd    | -149    | -141    | 7.4    | 10     | n/a     | n/a      | Yes  |
|                     | 0.5 min    | comra-east-sb-dep.xyz       | -149    | -141.3  | 7.3    | 10     | n/a     | n/a      | n/a  |
|                     | 0.5 min    | Comra-west-multbeam.grd     | -155    | -151    | 8.3    | 11     | n/a     | n/a      | Yes  |
|                     | 0.5 min    | comra-west-sb-dep.xyz       | -155    | -151    | 8.5    | 11     | n/a     | n/a      | n/a  |
|                     |            |                             |         |         |        |        |         |          |      |
| JAPAN<br>(DORD)     | 100m + Ds  | JAP_Additional1.tif         | -154    | -151    | 7.2    | 9.2    | Yes     | Yes      | Yes  |
|                     | 100m + Ds  | JAP_Additional2-3.tif       | -149.5  | -145    | 8.5    | 12     | Yes     | Yes      | Yes  |
|                     | 100m + Ds  | JAP_Additional4.tif         | -134    | -133    | 14.5   | 16     | Yes     | Yes      | Yes  |
|                     | 100m + Ds  | JAP_Res4Comm.tif            | -134    | -132.75 | 14     | 15.6   | Yes     | Yes      | Yes  |
|                     | 100m + Ds  | JAP_SelectedA.tif           | -147.75 | -146    | 8.75   | 10.1   | Yes     | Yes      | Yes  |
|                     | 100m + Ds  | JAP_SelectedByCommB1.tif    | -149    | -148    | 8.75   | 9.5    | Yes     | Yes      | Yes  |
|                     | 100m + Ds  | JAP_SelectedByCommB2.tif    | -125.5  | -123.5  | 13.1   | 14.1   | Yes     | Yes      | Yes  |
|                     | 100m + Ds  | JAP_SelfAllocate1.tif       | -149.5  | -145.75 | 10     | 11     | Yes     | Yes      | Yes  |
|                     | 100m + Ds  | JAP_SelfAllocate2.tif       | -133    | -131    | 14.25  | 15.75  | Yes     | Yes      | Yes  |
|                     | ~2 min ??  | Data for Geologic Model.xls | -149    | -131    | 8.75   | 15.77  | n/a     | n/a      | Yes  |
| FRANCE<br>(IFREMER) | 100m (mb)  | FRA_Carte6.tif              | -132    | -128.5  | 13.75  | 16     | Yes     | Yes      | Yes  |
|                     | 10m (mb)   | FRA_Carte7.tif              | -131.1  | -130.7  | 13.95  | 14.3   | Yes     | n/a      | n/a  |
| RUSSIA              | 100m       | RUS_sheet1.tif              | -145    | -139.5  | 11     | 13.75  | Yes     | Yes      | Yes  |
|                     | 100m       | RUS_sheet2.tif              | -139.5  | -133.5  | 11     | 14.25  | Yes     | Yes      | Yes  |
|                     | 100m       | RUS_sheet3.tif              | -133.5  | -128    | 12.5   | 14.75  | Yes     | Yes      | Yes  |
| KOREA               | ~500m      | 00_a2_noNaN.xyz             | -136.1  | -134.9  | 10.7   | 11.2   | n/a     | n/a      | Yes  |
|                     | ~500m      | 01_C1_noNaN.xyz             | -130.3  | -128.1  | 10.2   | 11.7   | n/a     | n/a      | Yes  |
|                     | ~500m      | 04_KR5_noNaNposs.xyz        | -132.8  | -131.5  | 9      | 10     | n/a     | n/a      | Yes  |
|                     | ~500m      | 95a2acinoNaNposs.xyz        | -134.5  | -133.5  | 10.5   | 11.5   | n/a     | n/a      | Yes  |
|                     | ~500m      | 95b2acinoNaNposs.xyz        | -136    | -135.25 | 9.85   | 10     | n/a     | n/a      | Yes  |
|                     | ~500m      | 95_B1noNaN.xyz              | -133.8  | -132    | 9.55   | 10     | n/a     | n/a      | Yes  |
|                     | ~500m      | 96_N1noNaN.xyz              | -133.5  | -130.25 | 16     | 16.9   | n/a     | n/a      | Yes  |
|                     | ~500m      | 96_N3noNaN.xyz              | -126.75 | -125    | 15.75  | 17.2   | n/a     | n/a      | Yes  |
|                     | ~500m      | 97_C1noNaN.xyz              | -129.75 | -128    | 10.5   | 11.7   | n/a     | n/a      | Yes  |
|                     | ~500m      | 98_99_00_B2noNaN.xyz        | -134.84 | -131.9  | 9.8    | 10.6   | n/a     | n/a      | Yes  |
|                     | ~500m      | b2areanoNaNposs.xyz         | -133    | -130.5  | 9.1    | 10     | n/a     | n/a      | Yes  |
|                     | 50m        | KOR_fig41a.tif              | -133.75 | -125    | 15.75  | 17     | Yes     | Yes      | Yes  |
|                     | 50m        | KOR_fig42a.tif              | -137.5  | -130.5  | 9      | 11.75  | Yes     | Yes      | Yes  |
|                     | 50m        | KOR_fig43a.tif              | -129.75 | -123.25 | 9.5    | 13     | Yes     | Yes      | Yes  |
|                     | 200m       | Bathymap 1.jpg              | -156    | -151    | 5      | 7      | Yes     | Yes      | Yes  |
|                     | 200m       | Bathymap 2.jpg              | -155    | -143.5  | 7      | 13     | Yes     | Yes      | Yes  |
|                     | 200m       | Bathymap 3.jpg              | -145    | -139    | 13     | 16     | Yes     | Yes      | Yes  |
| IOM                 | 100m       | IOM_sheet1.tif              | -123    | -118.75 | 12     | 16.5   | Yes     | Yes      | Yes  |
|                     | 100m       | IOM_sheet2.tif              | -124.5  | -119    | 7.75   | 12     | Yes     | Yes      | Yes  |
|                     | 200m       | iom_b1_bathy_grid.ascii     | -120.5  | -118.8  | 13.8   | 15.7   | n/a     | n/a      | Yes  |
|                     | 200m       | iom_b2_bathy_grid.ascii     | -121.7  | -118.9  | 8.6    | 13.4   | n/a     | n/a      | Yes  |

### 3. VOLCANIC, TECTONIC, AND SEDIMENTARY FACTORS



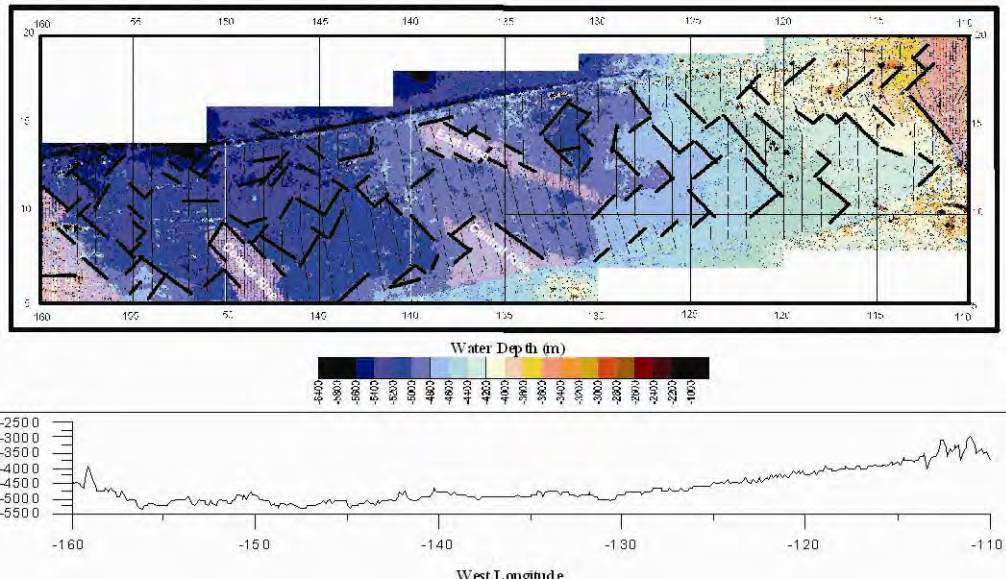
An analysis of the maps of volcanic and tectonic structural elements of the CCZ is provided in this part of the report. Its objective is to estimate the possible influences of static factors (i.e. bathymetry, geomorphology, tectonic structure and lithology), and dynamic factors (i.e. tectonic movements and volcanogenic, hydrothermal, sedimentary and erosive processes) on the growth of polymetallic nodules in the CCZ.

The methodology consists of a comparative analysis of the spatial distribution of the above-mentioned static factors, considered within the context of known dynamic factors, and their apparent relationships with the distribution of polymetallic nodule abundance and metal content. This approach has validated our evolutionary model of the CCZ in general, as well as the particular consequences for the distribution of polymetallic nodule abundance and metal content.

#### 3.1 Static Factors

##### ***3.1.1 Bathymetry, Morphology and Tectonic Structure***

The geomorphological structure of the CCZ conforms to the classical pattern of seabed structure typical for mid-ocean ridges and adjacent depressions (Figure 8).



Continuous red lines locate the traces of the Clarion and Clipperton Fracture Zones. Dashed red lines follow traces of non-transform discontinuities (such as the Mahi Mahi Fracture Zone), and dot-dash red lines indicate where extrapolation of the feature is yet to be supported by geophysical data. Bold black lines mark isochrones. Purple lines follow generalised trends possibly related to distribution of passive seismic events occurring in the region. Dotted red 'form' lines mark areas of anomalously shallow CCZ seafloor which we tentatively interpret to be an effect of additional crustal thickening due to local mantle thermal anomalies.

*Figure 8. Major Features of the CCZ*

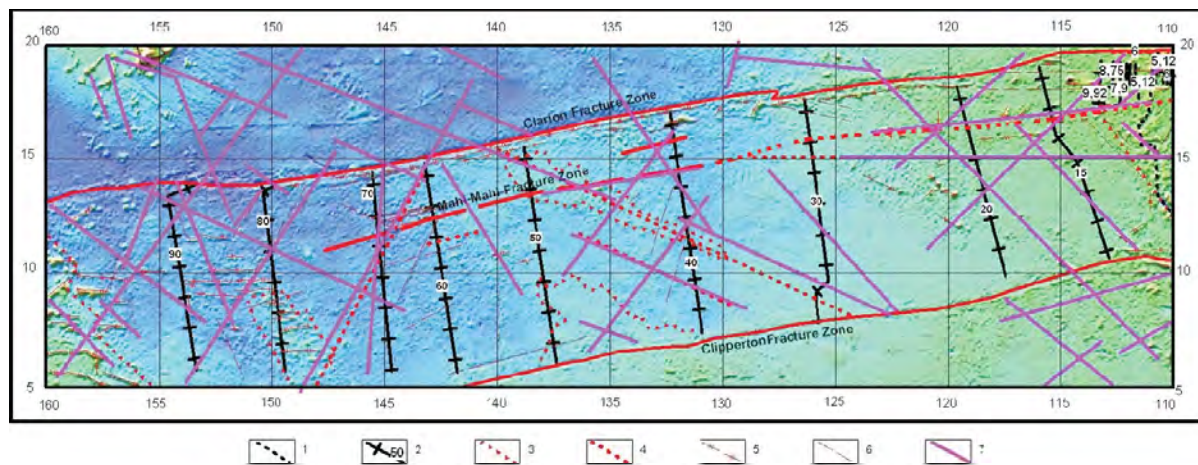
The Eastern Region (east of  $125^{\circ}$  W) consists mostly of the western slope of the Mathematicians Ridge. This structure is believed to be the western slope of the Paleo-East Pacific Rise (PEPR), which, up until five million years ago (5 Ma), was the spreading center (Klitgord and Mammerickx, 1982).

The average slope in this Eastern Region is close to  $\sim 0.57^{\circ}$  (1 m per km), which defines systematic increase of its average depth from 3,800 – 4,200 m at  $115^{\circ}$  W to 4,800-5,200 m at  $130^{\circ}$ W. Further westward the depth continues to increase at a gentler slope ( $\sim 0.35$  m per km- less than half a degree) to depths between 5,400 – 5,600 m at  $145^{\circ}$  W. The sea floor in this area also includes complicating elements that further subdue this overall trend. The largest of these are volcanic-tectonic swells, the Cooper Rise, Central Rise and East Rise.

Figure 8 shows that the regional variability of the bathymetric characteristics within the CCZ, including the areas of the above mentioned rises, obeys a pronounced order. This lies in the fact that isobaths are virtually always directed along one of two mutually orthogonal directions. The first direction has an azimuth of  $\sim 300^{\circ}$  - $315^{\circ}$ , near to the trend of the Hawaiian Archipelago. This may be termed the 'Hawaiian Trend'. The 'Ortho-Hawaiian' trend has a trend  $\sim 30^{\circ}$  - $45^{\circ}$  to the Hawaiian hotspot trend line. These features are indicated in Figure 8 as short, heavy line segments.

In addition, due to the general application by all the Contractors of high resolution, multi-beam echo-sounding systems, it is now apparent that, along the whole length of the CCZ, a more subtle but very persistent bathymetric pattern exists. This is the system of adjacent linear groups of ridges and valleys that are aligned approximately perpendicular to the bounding Clarion and Clipperton Fracture Zones. These systems generally exhibit crest-to-crest distances of 1-10 km and elevation extremes between tens to hundreds of meters. The overall trend lines of these features are indicated with light, parallel lines in Figure 9. Exceptions to this general seabed fabric are found in the vicinity of the larger tectonic and volcanic features.

Volcanic structures, represented by both single volcanoes and seamount chains ranging in height from hundreds of meters to a few kilometers, are distributed throughout the CCZ. However, most of them are concentrated in the West (the Cooper Rise) and East (PEPR slope at 120° W) sectors. Linearity is characteristic of a group of volcano-tectonic edifices. In most places, the orientation of the linearity is sub-latitudinal, near the orientations of the Clarion and Clipperton fracture zones. Some of these volcanic structures are oriented both in Hawaiian and Ortho-Hawaiian directions (see Figure 9).



1 - Extinct Rift of the Mathematicians Ridge; 2 - Basement Age (Isochrons in million years); 3 - Secondary level rise boundaries; 4 - Structural Lineations; 5 - Volcanic ridges and chains; 6 - Trenches or faults; 7 - Linear features indicated by seismic activity

*Figure 9. Tectonic Sketch of the CCZ*

The most extensive structure is a zone of sub-latitudinal fractures, registered by the GEBCO Committee as the Mahi-Mahi Fracture Zone (indicated by the dashed red line in Figure 9). Prior to the establishment of this nomenclature, Yuzhmorgeologiya called this fracture zone, remarkable for its partitioning of the relief, the Bezyimiyanni Fracture (Yubko, Stoyanov and Gorelik, 1990).

The Earth's crust in the Clarion-Clipperton Zone has a total thickness of 10.6 – 10.8 km (Golovinskiy 1985). It exhibits two layers: the upper part of the section is sediment cover with a thickness of 100 – 300 m; the lower part consists primarily of basalts. Coring and geophysical data show that the age of the basement successively decreases from West to East from  $90 \times 10^6$  years at 153° W to  $20 \times 10^6$  years at 118° W (Nisancioglu, 2003; ODP, 2002). As shown in Figure 9, isochrons of basement age are always nearly linear and oriented in sub-meridional directions, more or less parallel to the East Pacific Rise.

Nodule formation in the CCZ is subject to two different orientations of the bathymetric, geomorphological and tectonic structures. The first type is sub-meridional and is expressed by the patterns of the abyssal ridge valley structure, the isochrons indicating older crust to the west, and the general bathymetric trend of deeper seabed to the west. Without any doubt, these patterns are explained by the generation of the Pacific Plate spreading center, starting from the Late Cretaceous. We suggest that the second type of spatial order is the Hawaiian and Ortho-Hawaiian oriented structures, which are probably stress-release structures related to the overall drift of the Pacific Plate to the west-northwest.

### **3.1.2 Sediment Structure and Lithology**

A general model of lithologic units and stratigraphic boundaries in the sediment cover of a spreading ridge in the Pacific was proposed by T.H. Van Andel and G.R Heath as early as 1973 (DSDP 1973). The extensive surveys conducted by the ISA Contractors and others in the CCZ have repeatedly confirmed the basic aspects of this model. Lithologically, the model includes two end-members: carbonates (for example, carbonate silts and clays, carbonate oozes); and siliceous sediments (for example, red clays, siliceous ooze, siliceous silts and clays). Mixtures of these end members dominate the seabed in the CCZ and persist in nearly every setting, except where high rates of erosion, volcanic activity or other anomalous conditions occur.

The CCZ surficial sediments exhibit a unidirectional gradient perpendicular to the fracture zones, trending from predominant carbonate sediments in the southeastern extreme to predominant siliceous red clay in the west-northwest (Figure 10).

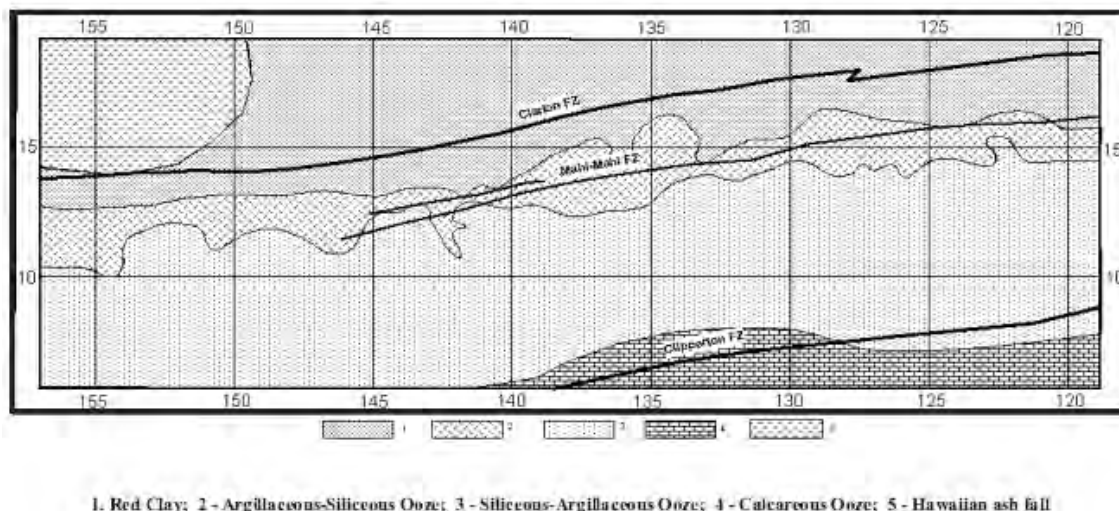
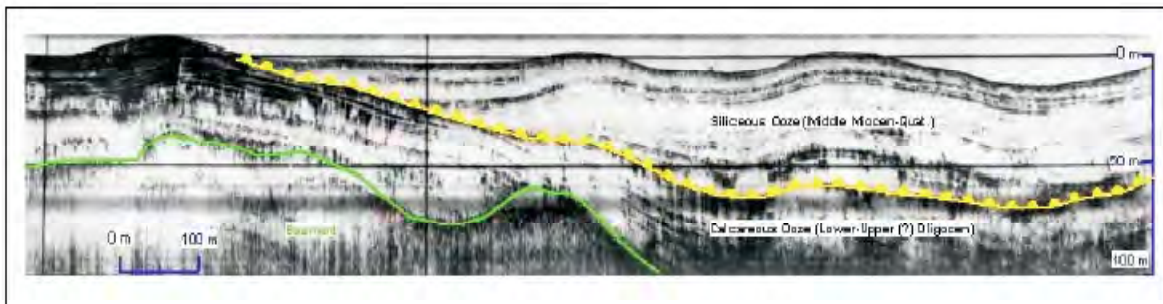


*Figure 10. Lithological Zonation of CCZ Surface Sediments*

This trend occurs despite the large differences in crustal age that occur from east to west, and is believed to be the culmination of two controlling factors; the north-south gradient of primary productivity, decreasing to the north; and the basic, tectonically controlled increase in water depth with distance from the EPR (Slater, Anderson and Bell, 1971). The east-west increase in water depth favours the persistence of siliceous sediments, since carbonate minerals become more and more soluble with increasing hydrostatic pressure (i.e. increasing water depth). In contrast, the north-south gradient in primary productivity favours higher concentrations of carbonates, since higher sediment rates can effectively overcome the dissolution rates.

With tectonic displacement and subsidence of the seabed westward, the seafloor at some point reaches a depth and latitude where the sedimentation rate and dissolution rate of carbonates are equal. This is defined as the Carbonate Compensation Depth (CCD). To the west and north of where these rates are balanced, carbonate sediments cannot accumulate on the seafloor. The primary result of these factors is expressed well in long cores recovered from the region. Within each core is found at some depth a facies transition from primarily siliceous sediments to primarily carbonate sediments, marking the transition of the coring site from above to below the CCD. As one would expect, this transition occurs at deeper depths in the sediments, marking successively older sediments from east to west. In the middle latitudes of the CCZ ( $10^{\circ}$  -  $12.5^{\circ}$  N), this transition occurs approximately at  $110^{\circ}$  -  $115^{\circ}$  W. Moving westward at this latitude, the transition occurs in successively older sediments (i.e. Miocene at  $120^{\circ}$  -  $125^{\circ}$  W and Oligocene at  $135^{\circ}$  -  $140^{\circ}$  W).

It is necessary to point out that within the sedimentary cover of the CCZ there are other facies changes besides this persistent siliceous-carbonate transition that are revealed on a regional scale. They include: 1) latitudinal zonation of a variety of young (Pleistocene-Holocene) sediment facies; and 2) a pronounced surface unconformity of Middle Miocene age, denoting an interruption of the sediment accumulation, dislocation and erosion of the earlier cumulated sediments (Figure 11).



Example of inclined and stratigraphic unconformities between Oligocene & Middle Miocene-Quaternary sediments (E-W profile near  $13^{\circ} 50'$  N,  $131^{\circ}$  W)  
Yellow Line - Miocene Unconformity; Green Line - Basement Rock

*Figure 11. Middle Miocene Unconformity*

### **3.1.3 Occurrence of Polymetallic Nodules**

Analysis of the spatial distribution of nodule abundance and metal concentration suggests an axial line of maximum abundance that is approximately parallel to and midway between the bounding fracture zones (see Figure 12).

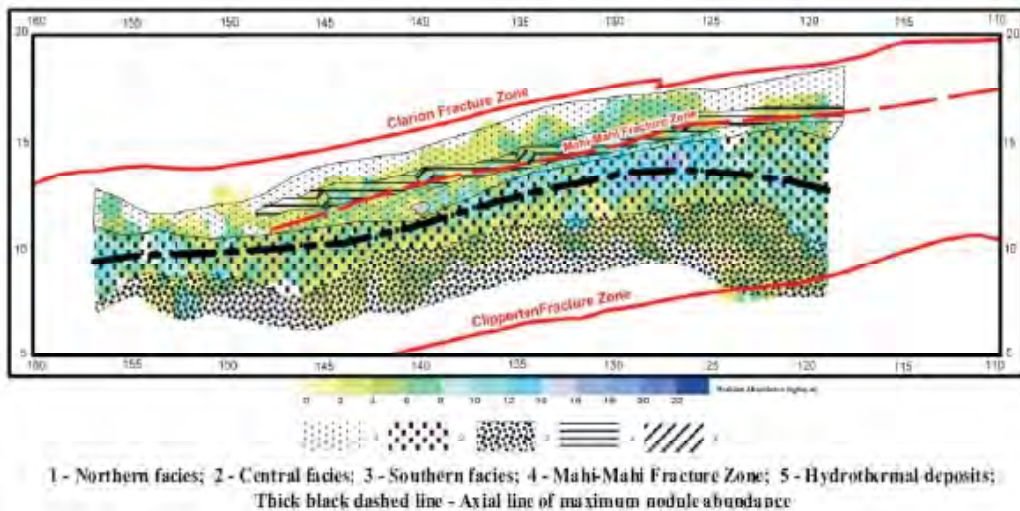


Figure 12. *Sediment Facies and Nodule Abundance*

The spatial distribution of metal content is different. The Mn/Fe ratio clearly increases from north-south, and, less distinctly, decreases from east to west.

As indicated in Figure 12, the polymetallic nodules in the CCZ can be divided into three distinct facies: (1) a northern facies that is characterized by the prevalence of small, often multi-nucleated nodules with smooth surfaces. The nodule abundance in this zone is, on average, relatively low. The nodules are relatively poor in Mn (19–26 per cent) and rich in Fe (6 to 10 per cent), poor in Ni and in Cu and relatively rich in Co (0.25 to 0.45 per cent). These are classified as ‘Type A’ nodules.

Within the middle zone the large (8–12 cm), discus and ovoid shaped nodules occur most frequently (2), generally with smooth surfaces on their upper sides and rough surfaces on their lower sides. These are richest in Ni (1.3 –1.5 per cent) and Cu (1.1 – 1.4 per cent), and are classified as ‘Type C’ nodules. Nodule abundance in the middle zone is the highest on average, and both ‘A’ and ‘C’ type nodules occur. In addition, within the middle zone, relatively large concentrations of polymetallic nodules can be found that exhibit characteristics that are intermediate between the A and C types. These can be termed as ‘Type B’ nodules. In the northern and middle zones, A, B and C types can be found. However, in the southern zone, only Type C deposits have been sampled.

It is interesting to note that the northern zone contains a linear area that exhibits relatively intensive (3) magmatic and hydrothermal activity. This area has been named the Mahi-Mahi Fracture Zone. Relatively young iron-rich mud, recent basaltic lavas, and massive sulfide minerals have been discovered along the trace of this fracture.

The inner structure of all the nodule types found in this area is fairly regular, consisting of a succession of thin, concentric layers. Generally, these layers form around a nodule nucleus, which can be composed of volcaniclastic debris, lithified sediment, detrital material or fragments of older nodules. The thickness of each layer ranges from 0.1 to 2 mm and is usually composed of one of two amorphous or crystalline mineral phases. The amorphous phase is an admixture of two oxide minerals: iron oxide (X-ray amorphous hematite); and 7Å manganese oxide (vernadite). The crystalline phase consists only of 10 Å manganese minerals such as buserite and todorokite. The amorphous phase is enriched in Fe and Co, and the crystalline phase is enriched in Mn, Cu and Ni. The bulk composition of nodules probably also depends on the ratio of crystalline and amorphous phases as well as the size and composition of the nucleus.

## 3.2 Dynamic Factors

### 3.2.1 *Intra-Plate Seismic Activity*

The Acoustic Monitoring Project of the VENTS Program performed continuous monitoring of ocean noise since August, 1991 using the U.S. Navy Sound Surveillance System (SOSUS) network and autonomous underwater hydrophones (PMEL 2006). That system has made it possible to estimate the intensity of seismic events with a Richter scale magnitude of 3-4 within the intra-plate regions of the oceanic basins. A description of the seismic activity of the CCZ and the surrounding areas has been prepared using this available information. On analyzing the information in the NOAA data base (PMEL 2006b), we determined that 4,679 seismic events took place within the area between  $110^{\circ}$  W - $160^{\circ}$  W and  $5^{\circ}$  N –  $20^{\circ}$  N between August 1991 and July 2006, including 402 events that occurred within the CCZ (see Figure 13).

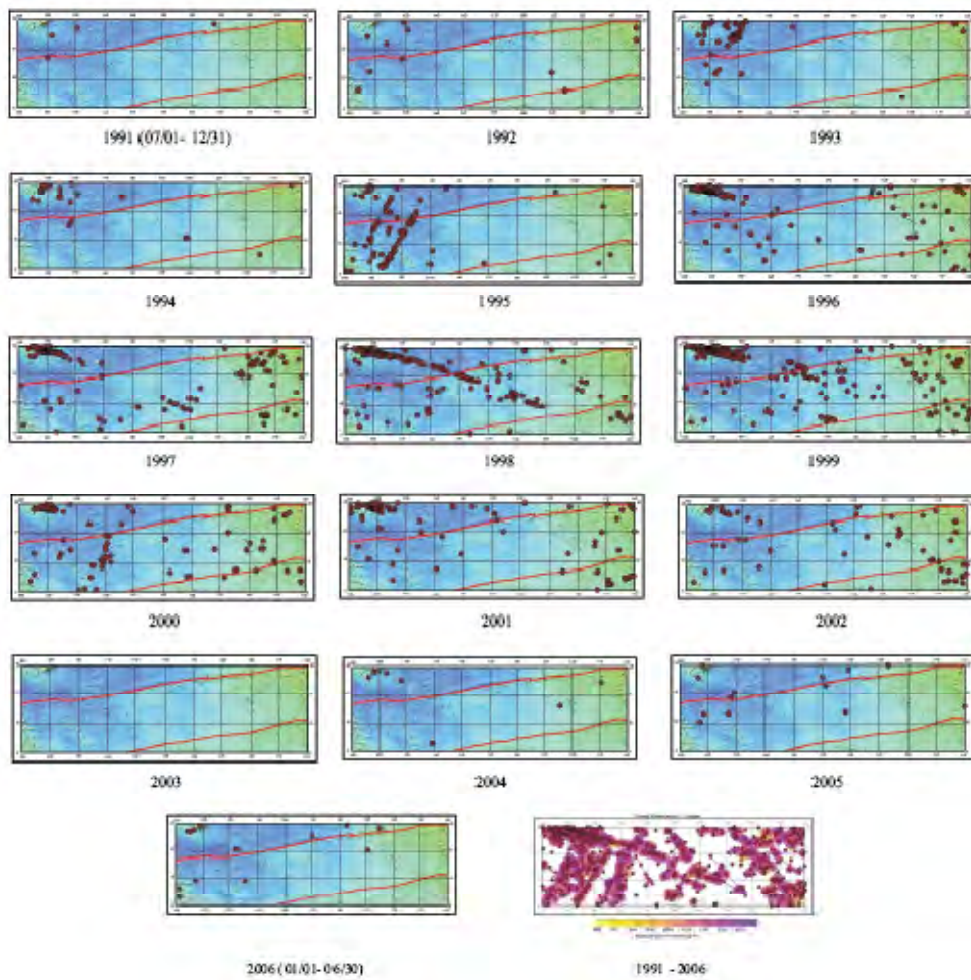


Figure 13. Earthquake Epicenters in the CCZ (1991-2006)

Examination of these data leads to the following conclusions:

- Seismic activity within the CCZ is irregular.
- The last period of high activity occurred between 1995 and 2002, with peak activity occurring in 1998-1999.
- Distribution of the seismic epicenters is along linear trend lines, with Hawaiian and Ortho-Hawaiian orientations.
- The seismic activity shows clear structure both in space and time. Initially, the lineations were Ortho-Hawaiian in orientation and took place near the Hawaiian Islands (Figure 13, 1991). They subsequently became more active, and the locus of activity shifted to the south east (Figure 13, 1992 – 1995). In 1996 the activity was predominantly oriented along the Hawaiian azimuth, and in the last phase of the high-level activity (1997 – 1998), the locus shifted again further southeast.

The general cause for this seismic activity is strike-slip and normal faulting associated with the release of stress caused by the motion of the Pacific Plate to the northwest.

### ***3.2.2 Intra-Plate Volcanism and Hydrothermal Activity***

The seismic activity described above is direct evidence of modern tectonic activity in the CCZ. There are other both direct and indirect indications of such activity occurring in the CCZ at different periods during its geological history. The most prominent evidence is the aforementioned multiple examples of angular and stratigraphic unconformities within the sedimentary cover, as well as appearances, within the CCZ area, of recent volcanism and associated hydrothermal activity.

The most tenable direct evidence of recent intra-plate volcanism in the CCZ is the basalt of Shimada Seamount, the crustal age of which is in the range of 16-17 million years. The seamount, (16° 50' N, 117° 30' W) is located within the eastern extension of the azimuth of the Mahi-Mahi Fracture Zone, 700 km west of the Paleo-EPR axis (1,150 km west of the present EPR axis). Its elevation is 3,900 m. Multiple lava flows of glassy basalts occur on the summit, slopes and near the base of this seamount (Gardner, Dean and Blakely, 1984).

Recent basalt flows of similar morphology were observed within the CCZ by Yuzhmorgeologiya (Figure 14, A and B) and Scripps Institution of Oceanography (Figure 14, C; SIO 1976). Recovered rock samples exhibit similar compositions to Shimada Seamount samples.

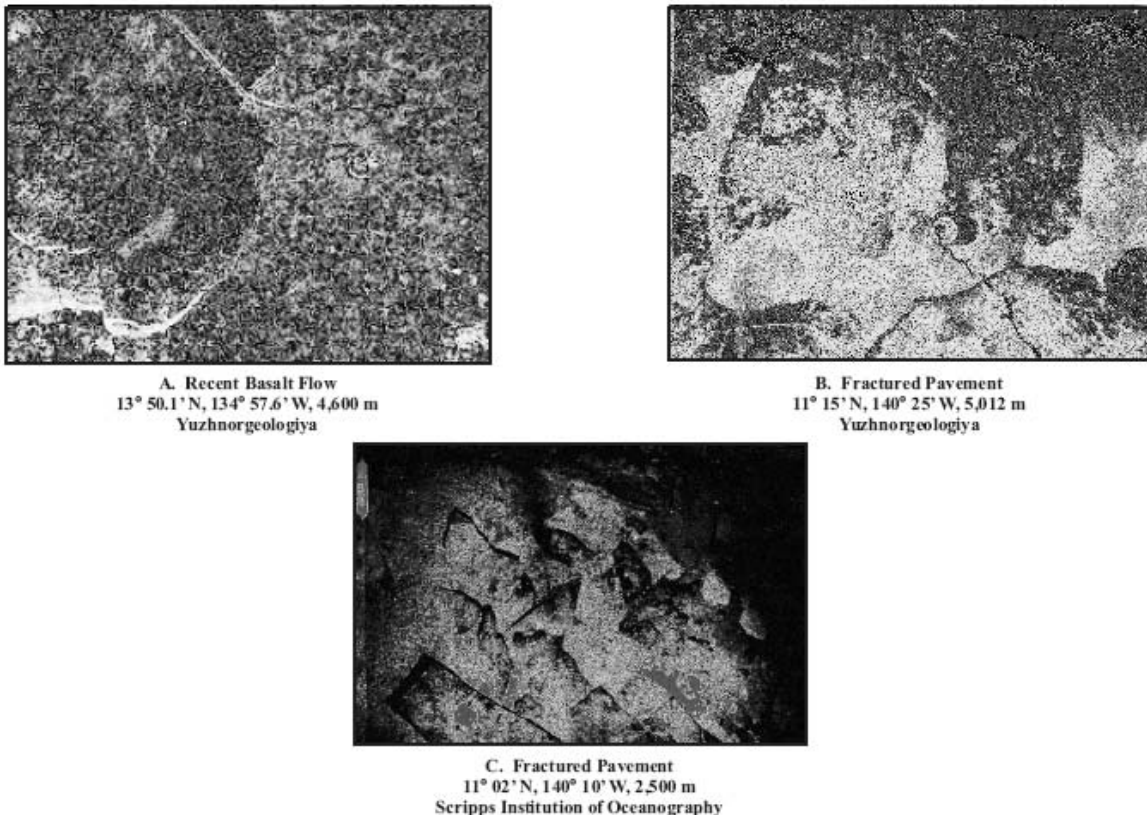


*Figure 14. Recent Basalt Flows and Pavements in the CCZ*

Direct evidence for potentially local sources of metals for the CCZ polymetallic nodules are found in metalliferous sediment and hydrothermal fluids discovered by Yuzhmorgeologiya (Table 1).

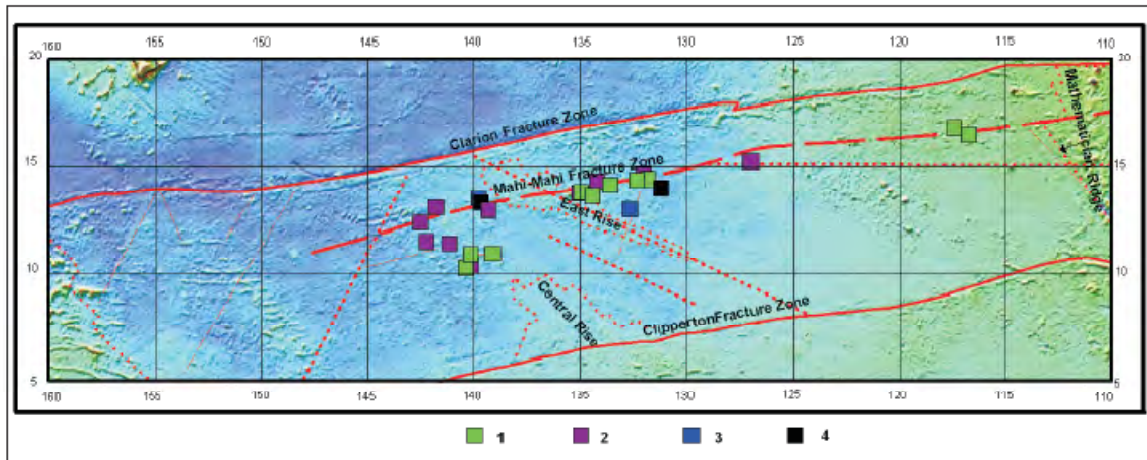
**Table 1. CCZ Metalliferous Sediment Compositions**

| Station ID | Coordinates |           | Metal Content (dry Wt. %) |      |      |      |      |      |
|------------|-------------|-----------|---------------------------|------|------|------|------|------|
|            | Lat. N      | Long. W   | Fe                        | Mn   | Ni   | Cu   | Co   | Zn   |
| 4207       | 12°58'3"    | 139°18'8" | 9.08                      | 1    | 0.1  | 0.07 | 0.02 | 0.02 |
| 4232       | 11°52'2"    | 139°42'4" | 15.4                      | 3.7  | 0.09 | 0.2  | 0.11 | 0.03 |
| 4307       | 13°06'9"    | 141°48'1" | 4.56                      | 4.14 | 0.23 | 0.22 | 0.02 | 0.06 |

In addition, Yuzhnogeologiya discovered unique deposits of massive hydrothermal-metasomatic sulphides (14° 00'6 N, 131°11'8 N) with the following composition: Fe – 15.5 per cent; Cu – 17.8 per cent; S – 17.8 per cent; Ag – 0.067 per cent; Ni – 0.085 per cent; Pb – 0.31 per cent%; Zn – 0.072 per cent; Co – 0.014 per cent; and Mn – 0.55 per cent. From microscopic examination of polished sections from these deposits, the following minerals were found: chalcopyrite – 60-65 per cent; bornite – 5 per cent; covellite – 4 per cent; galena – 1 per cent; and sphalerite – 0.5 per cent. Gangue minerals (quartz, carbonates) account for 25 per cent. Chalcopyrite forms nearly mono-mineral aggregates with

0.01-0.08 mm grain sizes and was formed after the gangue component. After etching it in a vapor of aqua regia, its anhedral-granular structure was revealed. Galena and bornite are mainly found together as xenomorphic grains of 0.01-0.1 mm size among the grains of chalcopyrite, and only in some places do they form independent aggregates. Covellite forms earthy masses, and partially replaces chalcopyrite and bornite, creating rims and filling fissures in chalcopyrite grains.

It is interesting that in most occurrences of young basaltic flows, metalliferous sediments, hydrothermal and hydrothermal-metasomatic deposits are spatially associated with the Mahi-Mahi Fracture Zone (Figure 15).



Recent basaltic flows (1), metalliferous sediments (2), hydrothermal flints (3), and hydrothermal-metasomatic sulfides (4) in the CCZ.

*Figure 15. Distribution of Recent Basalt Flows and Hydrothermal Deposits in the CCZ*

Mahi-Mahi Fracture Zone is playing the most important role in supplying metals for nodule formation, especially near its intersection with the East Rise, where the concentrations of recent lavas and hydrothermal deposits are high.

### 3.3 Model of CCZ Evolution and Nodule Formation

The preceding discussion supports the assertion that the development history of the geologic-geomorphologic structure of the CCZ is controlled by four types of geologic factors: hydrodynamic, sedimentation, volcano-tectonic and erosion-lithodynamic. Consistent with the time scale of these processes, two factors (hydrodynamic and sedimentation) can be considered as continuous, while the other factors are more sporadic.

The geodynamic factor is responsible for the formation of the CCZ basement. The second process controls the northward movement of the Pacific Plate, which reaches ever increasing depths of basement with age. Thus, those processes result in the formation of the principal features of relief, geomorphology and bottom depths within the CCZ.

Many investigators believe that the volcanogenic-hydrothermal activity of the East Pacific Rise (EPR) is one of the main sources of metals in polymetallic nodules as the result of complicated processes of dispersion and transportation to the bottom in dissolved and organic-fixed forms. This point of view is supported by the study.

The role of sedimentation is displayed in two ways. First, the initial relief is smoothed, which makes favourable conditions for polymetallic nodule formation. Second, it allows for the passage of metal-containing pore water, which can contribute to nodule formation.

As indicated in the preceding discussion, the most prominent events of the last 20 million years are connected with volcanogenic-hydrothermal and erosion-lithodynamic processes within the CCZ and are related to the middle Miocene unconformity, which included relatively high levels of magmatic activity, seabed erosion of sediments, and slope failures. In this evolutionary model of the CCZ, this event is of key importance because it started the processes that define the internal structure and geochemical zoning of the CCZ nodule deposits.

The key features of this model are presented in Figure 16 to Figure 20, showing modern (Figure 16) and reconstructed bottom sections of the CCZ for the periods of 5 (Figure 17), 10 (Figure 18), 15 (Figure 19) and 20 (Figure 20) million years.

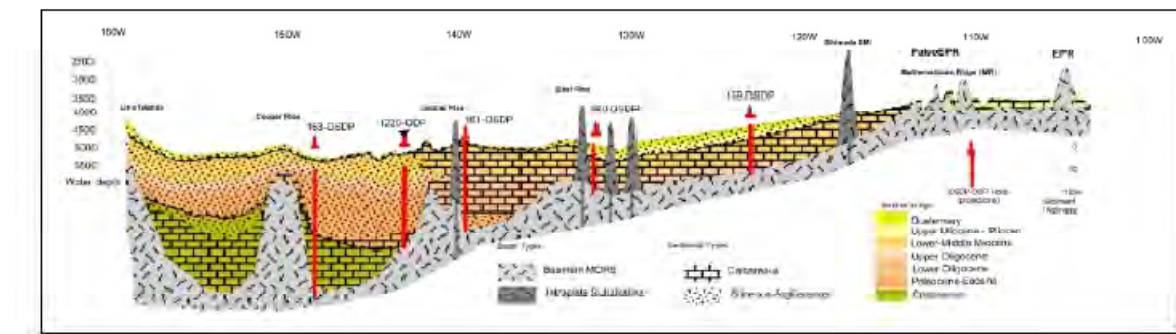


*Figure 16. Modern Cross-Section of the CCZ*

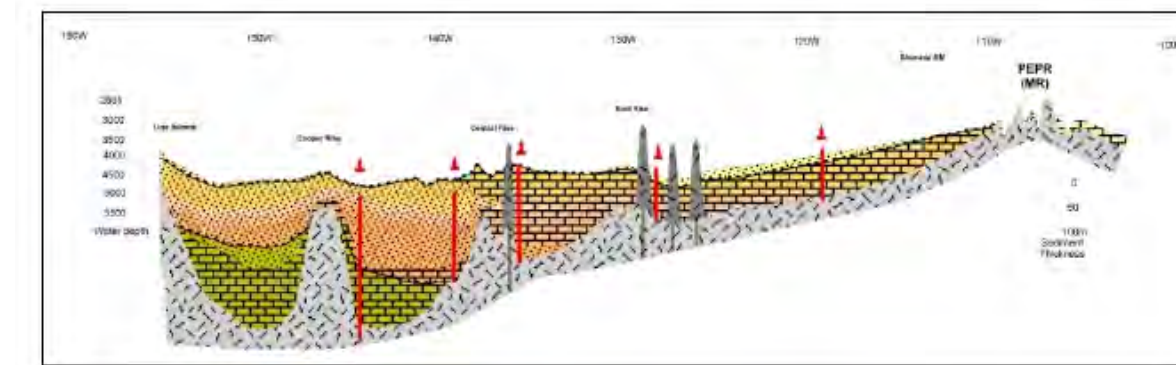


*Figure 17. Paleo-Reconstruction of the CCZ Cross-Section, 5 Million Years Ago*

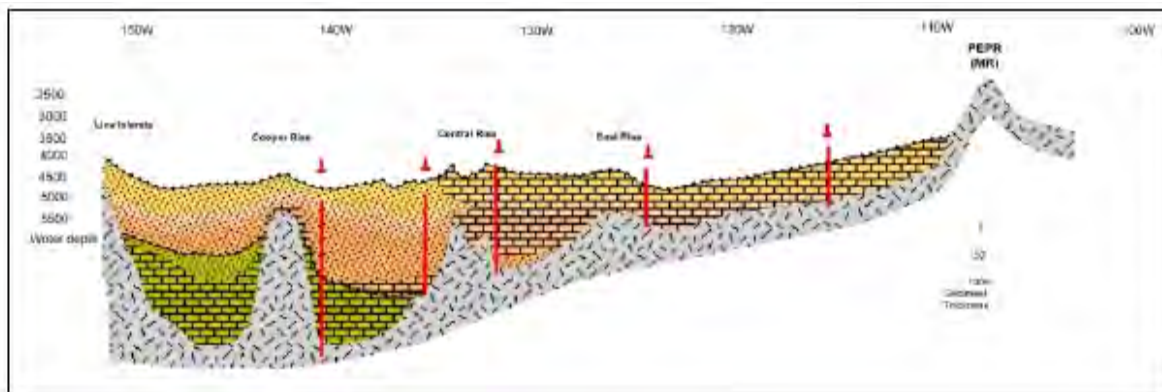


*Figure 18. Paleo-Reconstruction of the CCZ Cross-Section, 10 Million Years Ago*

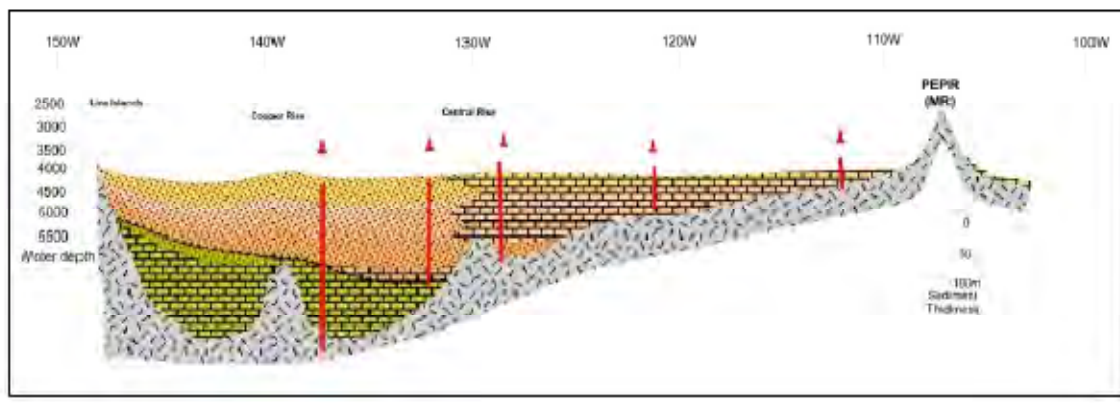


*Figure 19. Paleo-Reconstruction of the CCZ Cross-Section, 15 Million Years Ago*

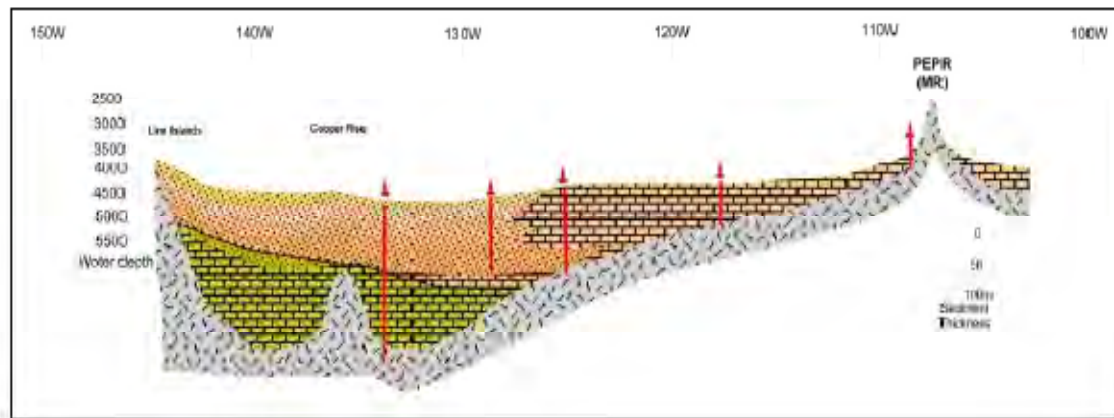
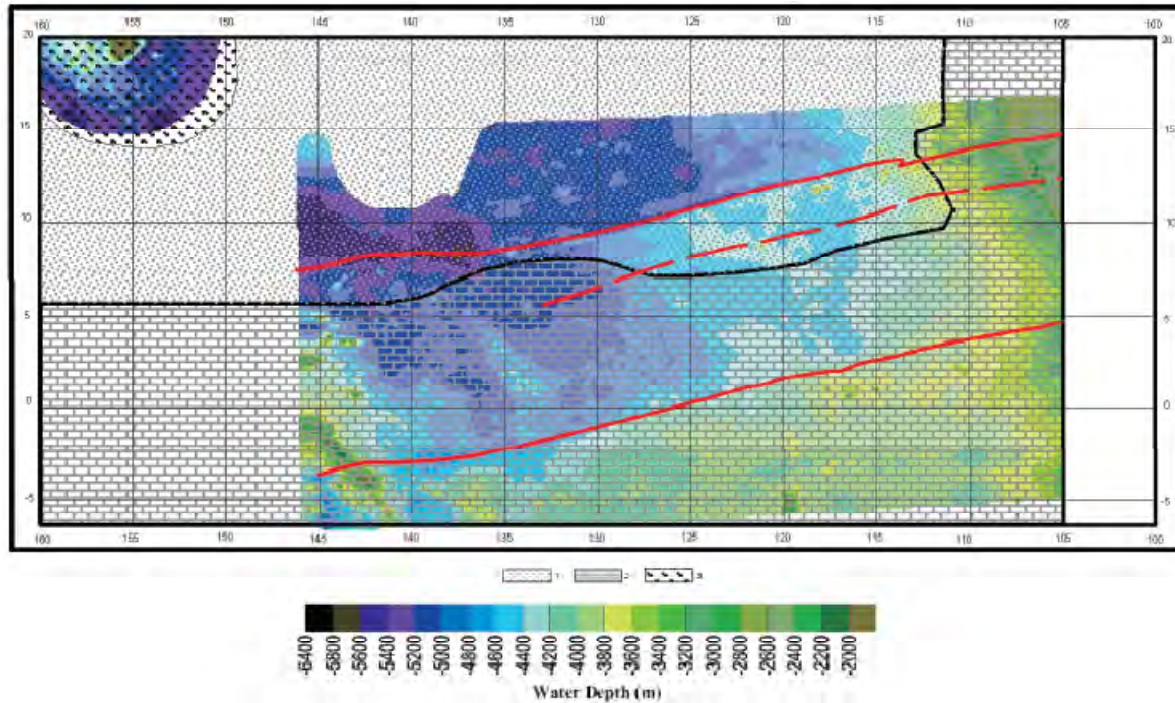


*Figure 20. Paleo-Reconstruction of the CCZ Cross-Section, 20 Million Years Ago*

All the sections are oriented along a line between  $17.5^{\circ}\text{N}$ ,  $110^{\circ}\text{W}$  in the east and  $7.5^{\circ}\text{N}$ ,  $160^{\circ}\text{W}$  in the west.

Changes in the geography of the axial area of the CCZ nodule field, connected with the northwest movement of the Pacific Plate, are shown in Figure 21.



1. Siliceous-Argillaceous Sediments; 2. Calcareous Sediments; 3. Hawaiian Ash Fall

*Figure 21. Paleo-Reconstruction of the CCZ 20 Million Years Ago*

The same figure illustrates changes in the position of the area relative to the CCZ lithological zoning outline, which is a reflection of the sedimentation zoning outline of the relevant fragment of the subequatorial area of the Pacific Ocean, geographically invariable all along the characterized period.

All paleo-reconstructions were made using specially developed software. Conclusions, based on these results, are as follows:

At about 20 million years ago (Ma), the axial area of the paleo-EPR (Mathematician Ridge) was located at a depth of 2.5-2.6 km, approximately along a longitude of  $107.5^{\circ}\text{W}$ . The western depression of the paleo-EPR was an arena of accumulation of carbonates (up to  $125^{\circ}\text{W}$ ) with a facies change westward to siliceous-argillaceous sediments (Figure 21).

The total thickness of the pre-20 Ma sediments demonstrates a consistent tendency toward increasing thickness from east to west, from tens of meters at  $110^{\circ}\text{W}$  to 300 m at  $135^{\circ}\text{W}$ , which is consistent with the lower local seabed relief occurring in the west and with the increasing crustal age from Upper Oligocene to Cretaceous .

Data supporting possible intra-plate volcano-tectonic activity in the CCZ are scarce and consist only of the known existence of the short north-south trending volcanic chains that rest on older basement rock. We believe that the most probable areas for such activity are at Cooper Rise and the system of volcanic ridges and chains located to the north of this rise.

Since the predominant part of the CCZ area at 20 Ma was within the zone of calcareous sedimentation, which was confirmed by the paleo-reconstructions (Figure 21), the prospects for nodule formation in the CCZ at that time are questionable.

Between 20 and 15 Ma, sedimentation within the CCZ was probably stable. In spite of the fact that at this time the area of CCZ was being shifted 250 km northwards, the major part of it remained within the zone of carbonate accumulation (Figure 22).

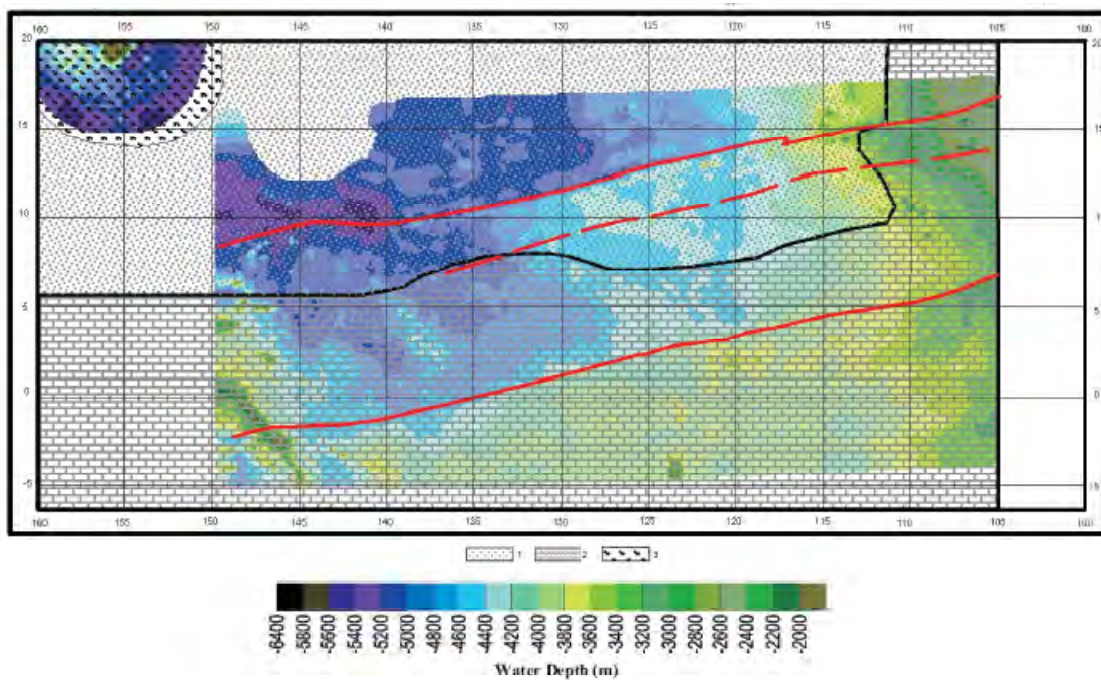


Figure 22. Paleo-Reconstruction of the CCZ, 15 MYA

Due to that fact, large-scale formation of polymetallic nodules did not occur during this period.

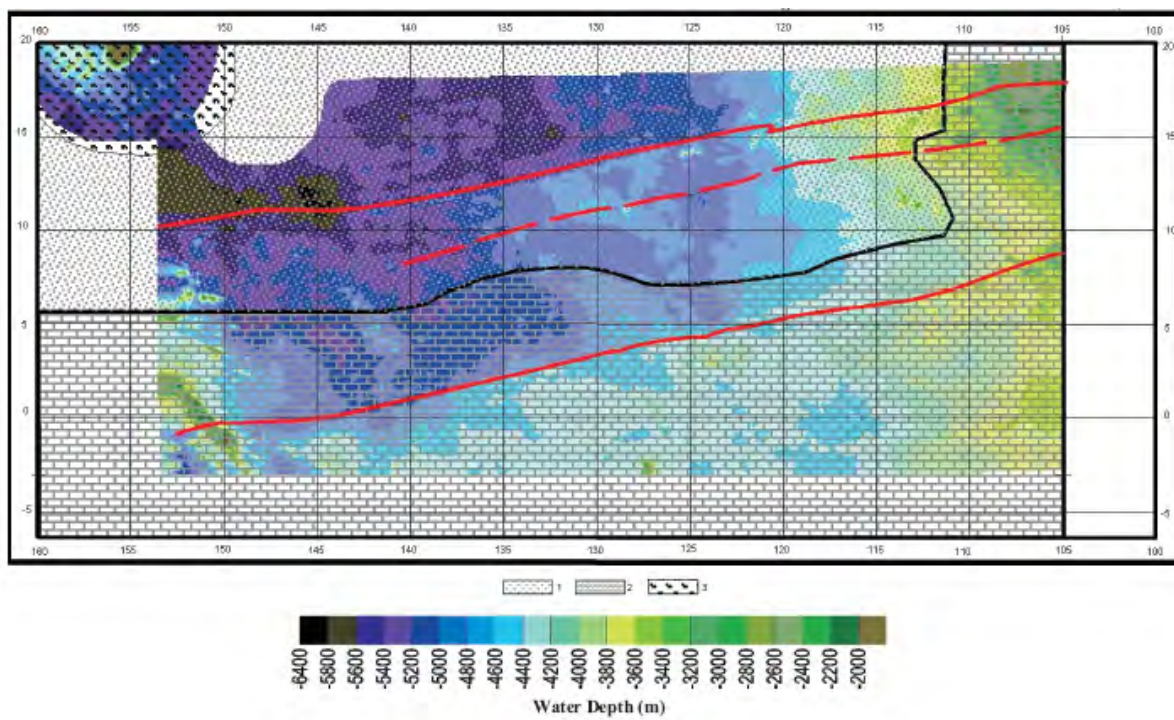
The most notable geological change within the CCZ between 15 and 1 Ma was a sharp increase of tectonic and sedimentary processes that influenced considerably the formation of the current geologic and geomorphologic structure of the CCZ, as well as the regional and local characteristics of nodule formation within the zone.

Intra-plate tectonic activity appears in three forms:

First, discontinuous dislocations along faults with amplitudes from 10-15 m to 100-150 m (in places to 300 m) were activated on the border of sub-meridional-orientated linear blocks of the initial basement structure. In many places this resulted in either a fracture with offset or in a near-fault dislocation within the sedimentary section, which produced inclined bedding. As a result, in many areas of the CCZ, sediments of various ages, down to the oldest, appear at the seabed.

Second, a tendency towards reorganization of the regional structural-geomorphology of the CCZ became more intensive with time producing increasingly well-defined topography of linear structural elements of the Hawaiian orientation. The Central Rise is the most striking example.

Third, along the Mahi-Mahi fracture zone, especially the area between  $130^{\circ}$  W and  $135^{\circ}$  W, increased magmatic-volcanogenic and related hydrothermal activity occurred. The intensity of the hydrothermal activity reached such a level, that it was sufficient to produce hydrothermal-metasomatic massive sulfide deposits. This suggests that at times an additional source of metals for manganese nodule formation could have been available within the CCZ. Taking into account that during this period nearly the entire the CCZ was siliceous-argillaceous sediment (Figure 23), it is believed that this marks the beginning for the formation of the major nodule deposits.



1. Siliceous-Argillaceous Sediments; 2. Calcareous Sediments; 3. Hawaiian Ash Fall

Figure 23. Paleo-Reconstruction of the CCZ, 10 MYA

Moreover, in parallel with the already mentioned favourable factors for nodule formation, some unfavourable conditions developed within the current period. The first of these was intensive erosion of mechanically weakened sediment dislocations (Nisancioglu, 2003; Ujiie, 1984). Most researchers believe that global climate change occurred as a result of the formation of the Antarctica ice cap. The influence of this event on near-bottom currents and water composition resulted in an increase in the velocities of near-bottom flow (up to 10-15 cm/s), a simultaneous decrease of the near-bottom water temperature, and an increase in the CCD (Ujiie 1984). Such a combination of conditions is not favourable to the stability of sediments, especially carbonates.

The attraction of such an interpretation of the events at the beginning of the middle Miocene for this study is that it provides a reasonable explanation for the sediment thickness related to erosional troughs, and an understanding that currently the overwhelming majority of ancient erosional troughs

and slopes are buried under the sediments, the most ancient of which is not more than 15 Ma. Basically, they are siliceous-argillaceous radiolarian silts and zeolite-containing clays.

Thus, the major geological events happened within the period of 15-10 Ma and resulted in a new structural-geomorphology of the seafloor, one of the main elements of which is the middle Miocene unconformity (Figure 11). All known major nodule-bearing areas of the CCZ are hosted by these Neogene sediments.

The 10-5 Ma period was characterized by the gradual attenuation of these erosional processes, by filling in lows with sediment. Since nearly the whole CCZ is within the zone of siliceous-argillaceous sediments (Figure 24), the post-erosion sediments match the sediments. However, the thickness of the sediments is generally only a few meters.

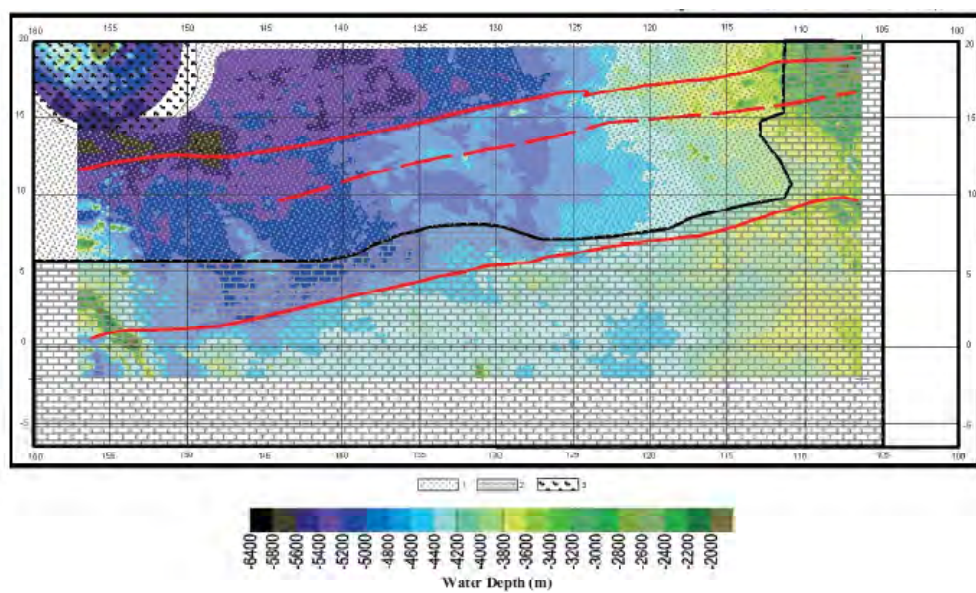


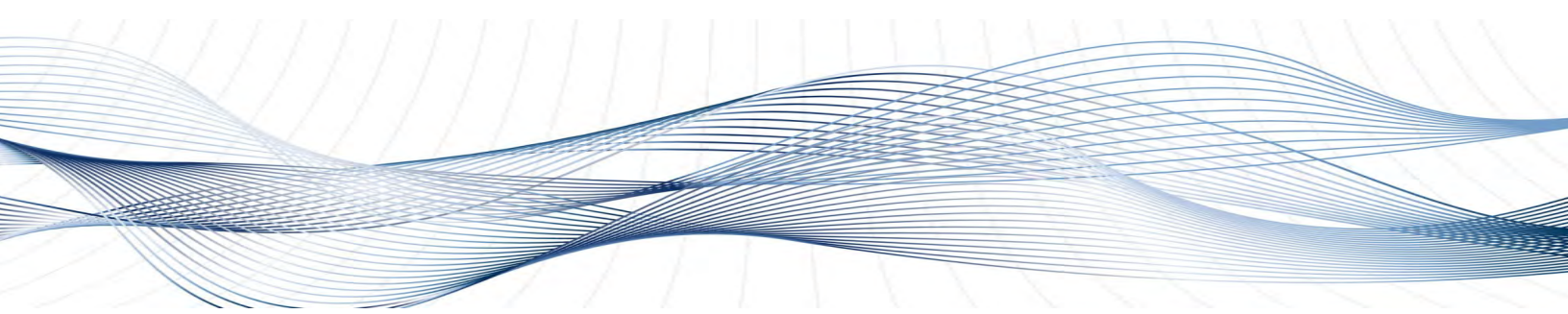
*Figure 24. Paleo-Reconstruction of the CCZ, 5 MYA*

There are still indications of the intra-plate volcano-tectonic activity of the CCZ, generated 5 Ma by the tectonic activity leading up to and including the re-alignment of spreading-center axis from the PEP to the current position of the EPR (Figure 16). During this period the conditions for nodule formation became more favourable, and the process of nodule formation entered an active phase including almost the entire CCZ area. This process was accelerated by the additional delivery of metals from the contemporaneous intra-plate volcanogenic-hydrothermal activity of the CCZ, concentrated along the Mahi-Mahi Fracture Zone. This influence would be expected to result in a relative enrichment of iron and an impoverishment of manganese, due to the relatively close proximity of the source to the forming nodule deposits. This might account for the increasing Mn/Fe ratio from north to south.

During the last 5 Ma, the process of burial of the post-middle-Miocene relief has been steady. The nature of the sedimentation has been similar to current times. Sediment accumulation differed from earlier times by only moderate hydrodynamic activity of near-bottom waters, in the form of low-velocity flow (1-2 cm/s) confined to the central parts of the troughs, which was enough however for local erosion, down to several tens of centimeters. At the same time, redistribution of sediment took place on steep slopes and sediment shifted to lows, contributing to the formation of increased

thicknesses of post-erosional sediments. Intra-plate volcano-tectonic activity in the CCZ has either remained constant for the past 5 Ma, or it might have increased during the past million years. The Holocene volcanism of Shimada Seamount (Figure 16) is the most reliable example of this activity. Thus, during the last 5 Ma, both the sediment facies that favour nodule formation and the tectonic and volcanic activities that may supply additional sources of metals suggest that the nodules are currently actively growing.

## 4. A GROWTH MODEL FOR POLYMETALLIC NODULES



### 4.1 Classification and Characteristics of CCZ Polymetallic Nodules

Polymetallic nodules are composed of both nuclei and concentric layers of iron and manganese hydroxides and oxides. Generally, according to factors including their morphology, size and texture, polymetallic nodules are classified into three types: Smooth (S-type), Rough (R-type) and Smooth-Rough mixed (S-R-type). The characteristics of these three types in the CCZ are presented in Table 2.

**Table 2. Classification and Characteristics of CCZ Polymetallic Nodules**

| <b>Classification</b> | <b>Surface shape</b>  | <b>Morphology</b>  | <b>Mineralogy</b>  | <b>Chemical Make-up</b>   | <b>Occurrence</b>                        | <b>Genesis</b>   |
|-----------------------|---|--|--|---|--|--|
| <b>S-type</b>         | Smooth  | Spherical, aggregate with poly-nucleus, irregular          | Vernadite  | Rich in Fe, Co, poor in Mn, Cu, Ni, ratio of Mn/Fe is less than 2 | Exposure on surface layer                | <u>Hydro-genous;</u> forming from seawater   |
| <b>R-type</b>         | Rough, grainy, papillate shape                                  | Spherical, kidney  | Todorokite and vernadite                                   | Rich in Mn, Cu, Ni, ratio of Mn/Fe is larger than 5               | Buried or mostly buried in surface layer | <u>Diagenetic,</u> forming from pore waters  |
| <b>S-R type</b>       | Smooth on the top side surface, rough on the lower side surface | Generally asymmetric elliptical, some tabular or irregular | Top similar to S-type and the lower side similar to R-type | Top similar to S-type but the lower side is similar to R-type     | Semi- buried in surface layer            | <u>Mixed Genesis;</u> hydrogenous for the top side and diagenetic for the lower side |

## 4.2 Growth Model

Polymetallic nodules in the CCZ generally grow very slowly, at rates of 1-10 mm per  $10^6$  yr (Beiersdorf *et al.*, 2003). The processes believed to be responsible for nodule growth are illustrated in Figure 25. The six factors believed to control these processes are discussed in the following sections.

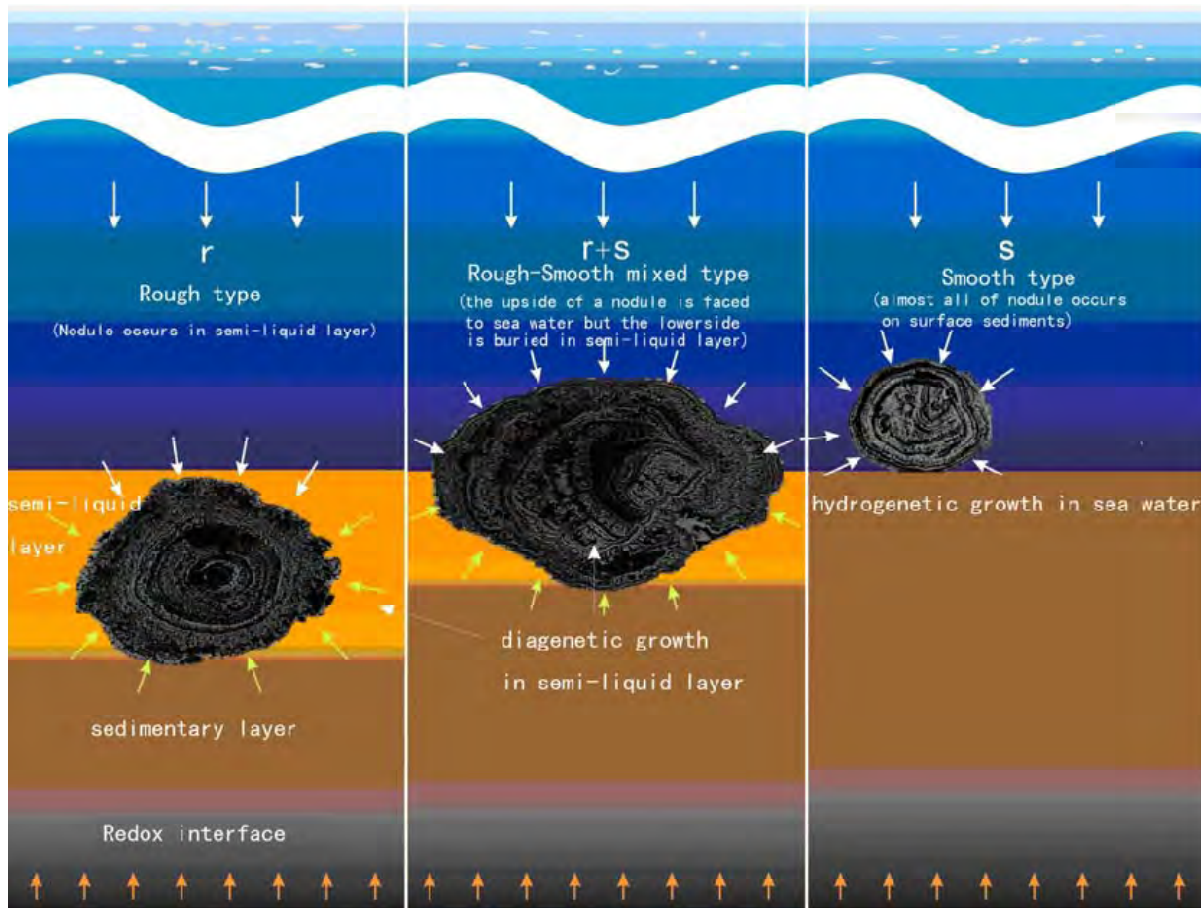


Figure 25. Diagram of Nodule Growth Processes

### 4.2.1 Supply of Metals

One of the key controls for nodule growth is the supply of the metals. It is estimated that the total reactive and soluble Mn entering into oceans is 1.2-14.7 million tons per year (Mt/yr), which includes contributions from rivers (0.2-0.4 Mt/yr), the atmosphere (0.05-0.3 Mt/a), seafloor hydrothermal venting (1-10 Mt/yr), and re-mobilization of buried metal through diagenesis (0.4-4 Mt/yr; Lisitsin, 1978; Elderfield, 1976; Baturin, 1988). The total Mn from these sources that is delivered to the deep seabed (depths > 3,000 m) is estimated to be about 7.4-8.35 Mt/yr. The total Mn in all polymetallic nodules discovered to date is much less than this value, delivered over a period of several million years (Baturin, 1988). Thus, nodule formation is probably not limited by the availability of manganese.

Concentration of metals such as Fe, Mn, Cu, Co, Ni and Zn in sediments is very low compared to metal concentrations in polymetallic nodules. However, the accumulation rate of sediments is three orders of magnitude higher than the growth rate of nodules. Radioactive dating has shown that, except

for the accumulation rate of Fe, V, Cr and Ti, which accumulate more rapidly in sediments than in nodules, the accumulation rate of Mn, Cu, Co, Ni and Zn in sediment is the same as the accumulation rate of these metals in nodules (Baturin, 1988). Thus, the supply of metals is not the limiting factor for the formation of polymetallic nodules. As discussed below, the environment of formation and other factors are key to the formation and growth of the nodules.

#### ***4.2.2 Presence of A Nucleus is Necessary***

Nodule nuclei consist of fragments of old nodules, cemented or consolidated sediment, volcaniclastic rocks, fish teeth etc. In fact, all materials which are slightly harder than sediment on the seafloor can serve as nuclei for nodule formation. It is likely that the occurrence of nucleus material is strongly related to the number of polymetallic nodules in the CCZ.

#### ***4.2.3 Antarctic Bottom Water (AABW)***

Late Cenozoic sedimentary unconformity, and especially the middle to late Miocene sedimentary unconformity, was caused by the corrosive and erosive forces of AABW (Demidova, 1998). This erosion and removal of fine sediments generated abundant fragmental materials that served as nuclei for the formation of polymetallic nodules. Moreover, the elevated concentration of oxygen in AABW kept the bottom waters well oxygenated. Any components from surface waters or sedimentary pore water were oxidized to oxides or hydroxides and accumulated on the nodules in this environment of very low sedimentary rates.

#### ***4.2.4 Semi-Liquid Surface Layer***

Smooth type polymetallic nodules occur on the seafloor surface with no or minimal semi-liquid layer, and their metal supply is primarily from overlying sea water. Rough type polymetallic nodules occur in a semi-liquid layer and their ore-forming materials are mainly from sediment pore waters. The physical and chemical differences between the semi-liquid layer and near-bottom sea water account for the different minerals found in the two types of polymetallic nodules. These different minerals cause the different percentages of metals (Mn, Fe, Cu, Co, Ni) in nodules. For example, vernadite is enriched in Co, while todorokite is enriched in Cu and Ni.

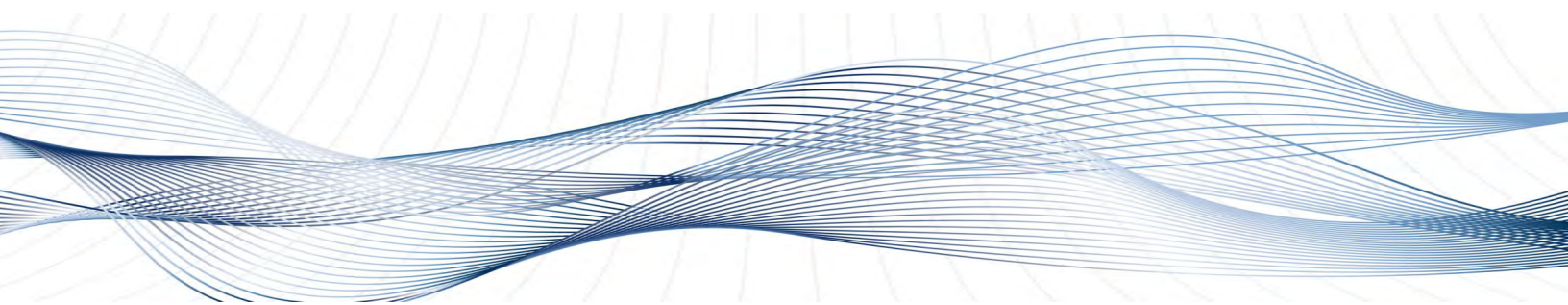
#### ***4.2.5 Bioturbation***

Recently deposited sediments in the benthos are greatly affected by fauna. This bioturbation is a dominant process in the pelagic sediments of the CCZ. Because the growth rate of polymetallic nodules is three orders of magnitude slower than the accumulation rate of sediments, the movement of nodules by benthos every 500 years or so may be sufficient to keep nodules on the sediment surface (Beiersdorf *et al.*, 2003).

#### ***4.2.6 Internal Nodule Stratigraphy***

The complexity of growth histories of polymetallic nodules is reflected by the pronounced variation of mineralogy and chemical composition observed in their concentric layers. During the long term geological history of deep-sea sedimentary basins, the topography, sedimentation rate, semi-liquid layers, water currents and biological activity vary at different temporal and spatial scales. These variations cause not only the variety of chemical compositions and micro textures/structures in single nodules, but also changes in the distribution of nodule type, nodule size and nodule abundance at local and regional scales.

## 5. NODULE COVERAGE, MORPHOLOGY AND DISTRIBUTION IN THE EASTERN CCZ



### 5.1 Introduction

The study area examined covers more than 810,000 km<sup>2</sup> in the eastern part of the CCZ, between 8° 38' 77'' – 16° 52.76' N latitude and 118° 52.5' – 125° 19.75' W longitude. Data and information from 926 stations, sampled with a box corer and grabs and collected during the prospecting and exploration activity of the IOM, were compiled for further processing in future. A total of 262.6 km of digital photographic coverage, obtained by the 'NEPTUNE' deep-tow system was used to estimate nodule coverage and distribution.

In order to understand nodule distribution within this study area, an analysis was made to determine the correlations between such nodule-related factors as coverage, abundance, morphology, size, genetic type, and water depth, bottom morphology, and geographic region

### 5.2 Methods and Results

#### 5.2.1 *Nodule Abundance and Coverage*

Sediment samples were collected from a total of 926 stations; 49 of these (about 5.2 per cent) contained no polymetallic nodules. Polymetallic Nodule abundances in excess of 20 kg/m<sup>2</sup> were reported at 25 stations (with a recovered maximum of 43.6 kg/m<sup>2</sup>), while at 332 stations the nodule abundance was higher than 10 kg/m<sup>2</sup>. Nodule coverage varied between 0 to 99 per cent. High nodule coverage (more than 50 per cent) was found at 128 stations, including 7 stations with coverage of more than 80 per cent.

Seafloor polymetallic nodule coverage for 737 stations was estimated both from seafloor photographs and ground-truth data determined from box-core and grab sample recoveries. There are substantial differences between the two methods (Figure 26). Nodule blanketing by sediment is a characteristic feature in the entire study area, and, as shown by these results, it is not recommended to use only bottom photographs for nodule coverage estimation.

Besides partially sediment-covered nodules, completely buried nodules were found at 81 sampling stations, located between 119° 50' W and 120° 50' W, and at depths > 4,300m (90.2 per cent), including 42.7 per cent of all stations located at depths > 4,400 m (Kotliński and Stoyanova, 2007).

Completely buried polymetallic nodules in box-cores were found as deep as 45 cm in sediment. However, the stations studied for geotechnical parameters showed 140 cm to be the maximum depth at which buried nodules were found. Factors and conditions responsible for buried nodules are still unknown, and future nodule research may bear evidence of the complexity and length of processes leading to their burial, as well as the specific features of the deep-sea environment.

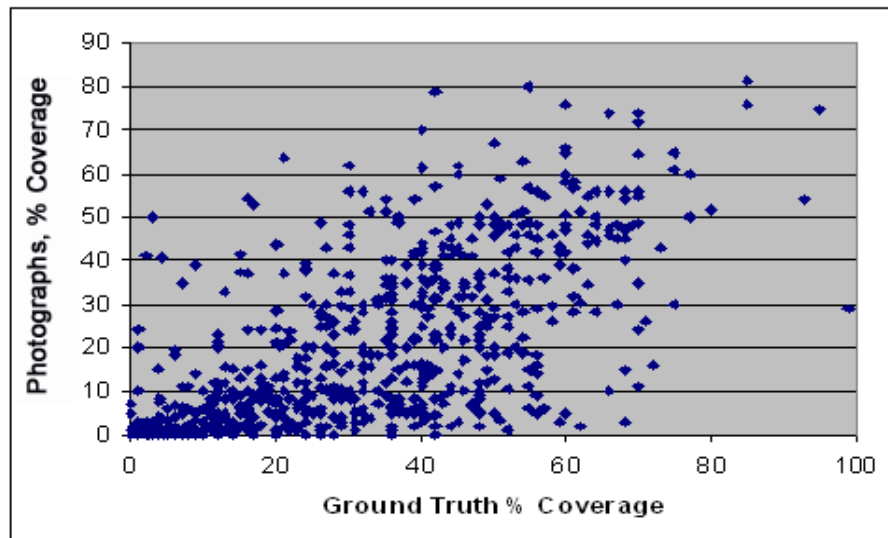


*Figure 26. Nodule Coverage Determined from Photographs and Sample Recoveries*

### **5.2.2 Genetic and Morphological Classification of Polymetallic Nodules**

The eastern part of the CCZ features all the genetic and morphological classifications of polymetallic nodules known in the entire region.

#### Genetic Classifications:

- **H**, hydrogenetically grown
- **HD**, hydrogenetic-diagenetic features
- **D**, diagenetically grown
- **D1**, diagenetic, with Cu>Ni
- **C**, crusts, grown on hard substrates

#### Morphological Classifications

- **D**, discoidal
- **E**, ellipsoidal
- **S**, spheroidal
- **T**, tabular
- **P**, poly-nucleic aggregate

- **I**, irregular shaped
- **F**, fragments

The distribution of the different genetic types of polymetallic nodules from 839 stations showed that the D-type and its D1-subtype are dominant within the entire eastern part of the CCZ (Figure 27).

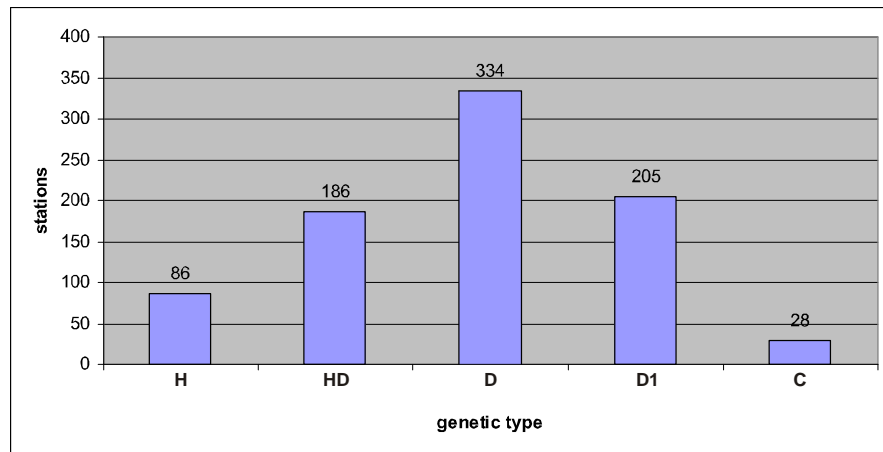


*Figure 27. Histogram of Genetic Nodule Types in the Eastern CCZ*

Throughout the study area, discoidal and ellipsoidal polymetallic nodules and their fragments are dominant (Figure 28). More than 70 per cent of studied sample stations consist of those morphological types, followed by the spheroidal type (about 15 per cent), and the pooled contribution of nodules of other morphologies does not exceed 15 per cent.

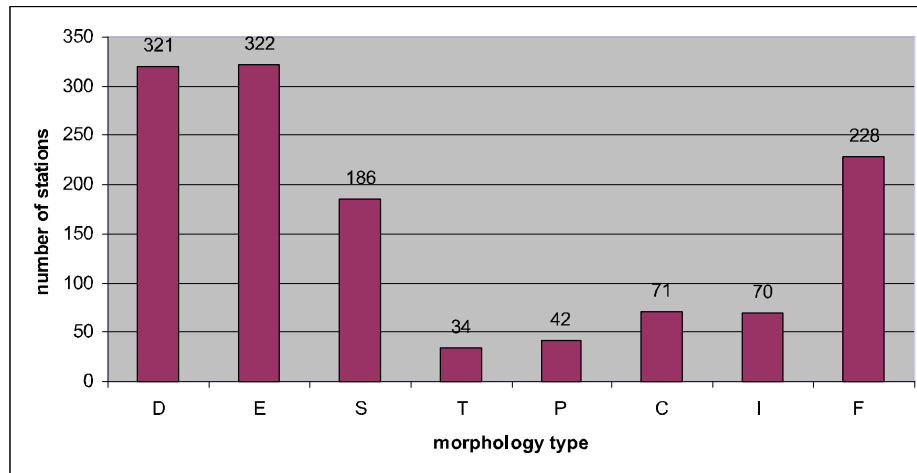


*Figure 28. Histogram of Nodule Morphological Types*

### 5.2.3 Nodule Morphology, Abundance and Size

Data collected from 824 stations allowed an examination of the relationships among nodule morphologies and the abundance and size of the deposits (Table 3).

**Table 3. Relationships among Nodule Morphology, Abundance and Size**

| Morphological Type | No. Stations | Mean Abundance (kg/m <sup>2</sup> ) | Size (cm) |      | % Relative Weight of Size Fraction (cm) |       |       |       |      |
|--------------------|--------------|-------------------------------------|-----------|------|---|-------|-------|-------|------|
|                    |              |                                     | Min.      | Max. | < 2                                     | 2 - 4 | 4 - 6 | 6 - 8 | >8   |
| D                  | 321          | 8.0                                 | 2.7       | 7.0  | 6.2                                     | 30.9  | 26.1  | 26.1  | 50.6 |
| E                  | 322          | 7.3                                 | 1.5       | 6.1  | 7.8                                     | 43.9  | 27.1  | 20.7  | 45.8 |
| S                  | 186          | 6.6                                 | 1.4       | 6.0  | 18.5                                    | 58.4  | 27.8  | 20.8  | 40.1 |
| T                  | 34           | 5.7                                 | 1.6       | 7.0  | 20.9                                    | 51.3  | 27.6  | 28.9  | 29.8 |
| P                  | 42           | 9.5                                 | 0.4       | 5.4  | 21.3                                    | 64.0  | 20.4  | 21.3  | 4.2  |
| I                  | 70           | 9.5                                 | 2.3       | 6.1  | 9.6                                     | 23.2  | 18.5  | 20.3  | 63.0 |
| F                  | 228          | 11.1                                | 2.3       | 7.2  | 6.2                                     | 25.7  | 27.4  | 26.2  | 38.1 |

Nodules representing the different morphological types show that aggregated type P are most abundant (based on data from 42 sampling stations), followed by discoidal and ellipsoidal nodule types (see Figure 29).

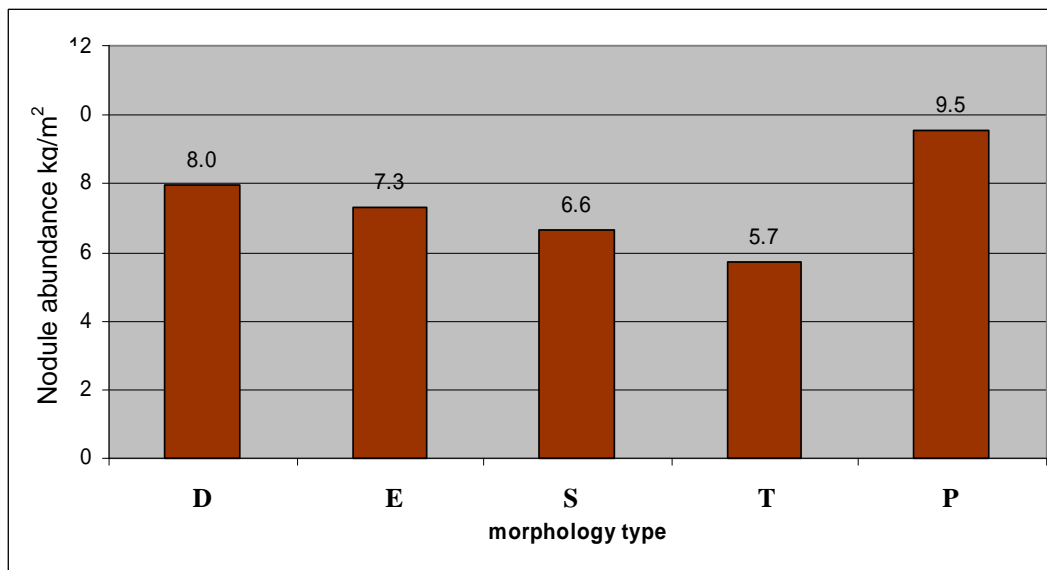


*Figure 29. Nodule Abundance vs. Morphology*

The nodule size distribution throughout the study area is bimodal, with peaks involving sizes 2-4 cm and larger than 8 cm size intervals for most morphologies (Figure 30). Only the poly-nucleated, aggregate (P) type exhibits a relatively low frequency of the largest (> 8 cm) size class of nodules.

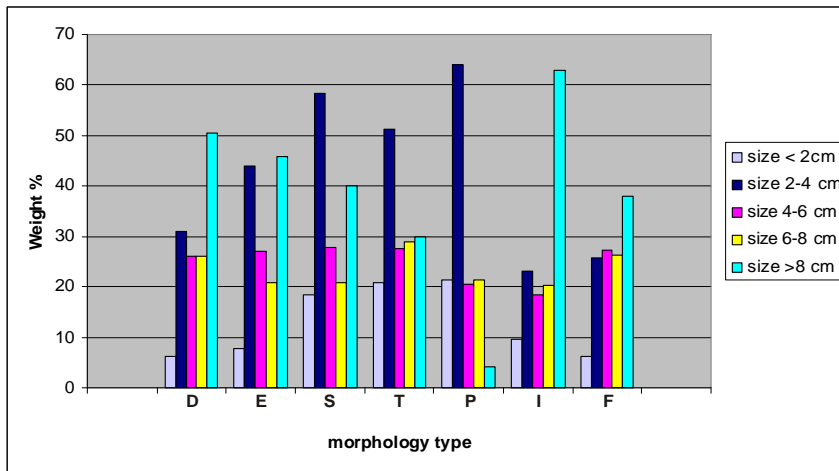


Figure 30. Nodule Size Distribution Versus Morphology

## 5.3 Discussion and Conclusions

### 5.3.1 Coverage and Abundance vs. Seafloor Depth

Table 4 shows the distribution of nodule coverage and abundance at different water depths. Mean abundance increases steadily up to depths of 4,500 m, and then decrease significantly.

Table 4. Abundance and Coverage vs. Water Depth

| Depth Range (m) | No. Stations | Nodule Coverage, % |      |      | Nodule Abundance, kg/m <sup>2</sup> |      |      |
|-----------------|--------------|--------------------|------|------|-------------------------------------|------|------|
|                 |              | Mean               | Min. | Max. | Mean                                | Min. | Max. |
| 3,470 - 4,100   | 51           | 31.7               | 3    | 80   | 7.0                                 | 0.0  | 22.5 |
| 4,101 - 4,200   | 63           | 33.0               | 0    | 85   | 7.6                                 | 0.1  | 18.0 |
| 4,201 - 4,300   | 154          | 29.9               | 0    | 75   | 8.0                                 | 0.0  | 22.5 |
| 4,301 - 4,400   | 348          | 29.6               | 0    | 99   | 8.6                                 | 0.0  | 30.0 |
| 4,401 - 4,500   | 196          | 30.0               | 0    | 77   | 8.8                                 | 0.00 | 43.6 |
| > 4,500         | 112          | 23.8               | 0    | 61   | 5.4                                 | 0.0  | 22.9 |

The mean nodule coverage, as estimated from ground-truth measurements with box-core and grab samples, is highest in the seafloor depth range of 4,100-4,200 m and the highest nodule coverage occurred between 4,300-4,500 m (Table 5, Figure 31, Figure 32). Almost all the stations with no nodule coverage were found deeper than 4,300 m (Figure 33; Kotliński and Stoyanova, 2005).

**Table 5. Nodule Genetic Type vs. Water Depth**

| <i>Genetic Type</i> | <i>No. Stations</i> | <i>Depth Interval (m)</i> |
|---------------------|---------------------|---------------------------|
| <b>H</b>            | 86                  | 3,753 - 4,703             |
| <b>HD</b>           | 186                 | 3,955 - 4,690             |
| <b>D</b>            | 334                 | 3,996 - 4,939             |
| <b>D1</b>           | 205                 | 4,199 - 4,694             |
| <b>C</b>            | 28                  | 3,490 - 4,622             |

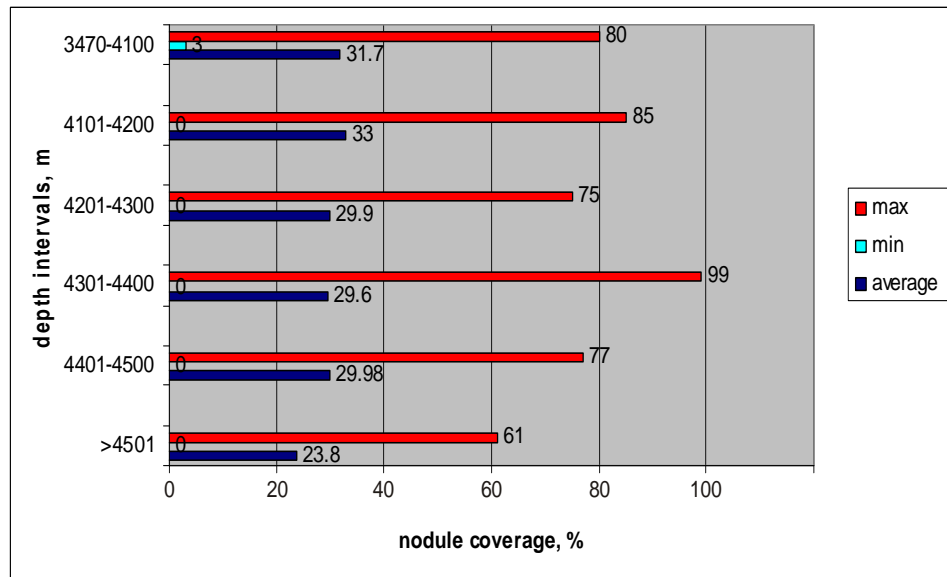


*Figure 31. Nodule Coverage vs. Water Depth*

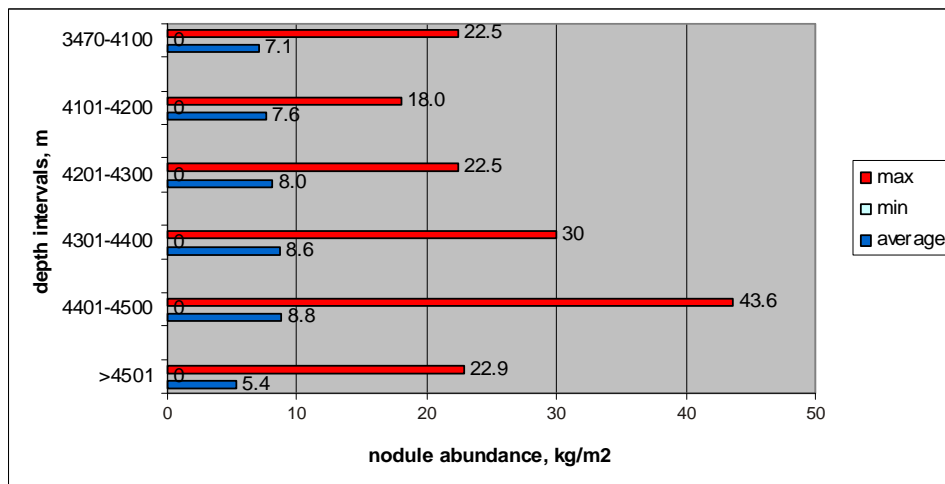


Figure 32. Nodule Abundance vs. Water Depth

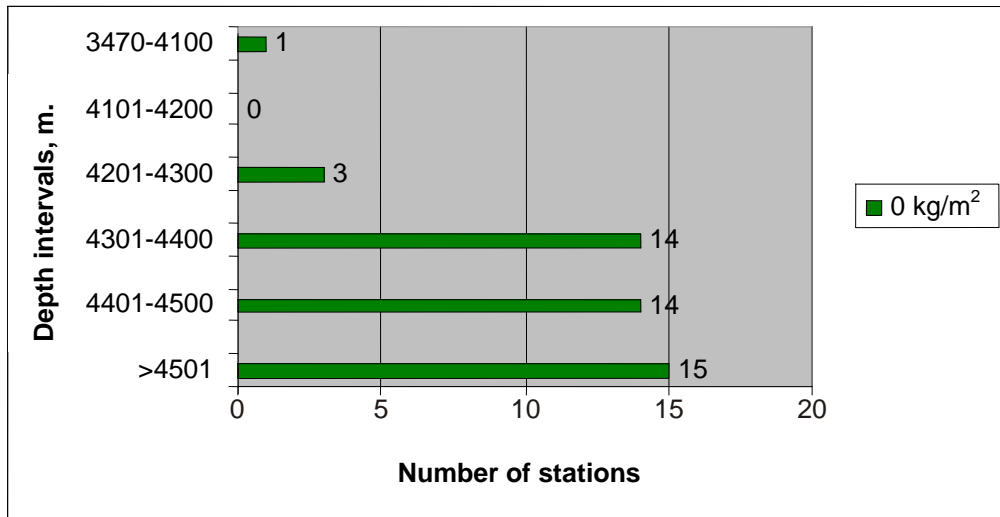


Figure 33. Seabed Stations with No Nodules vs. Water Depth

Data collected from 839 sampling stations were used to estimate the distribution of the genetic nodule types by seafloor depth intervals (Table 5). Nodules representing genetic types H and HD were found within the shallow depth range of 3,750 – 3,950 m, while the type D and subtype D1 were occurred at a minimum seafloor depth of 3,995 m.

### 5.3.2 Nodule Abundance and Seafloor Morphology

In general, stations that yielded high nodule abundances were found on all types of seafloor morphology (Table 6, Figure 34). 332 stations had nodule abundances higher than 10 kg/m<sup>2</sup>. Of these, 129 occurred on undulating plains, 80 on horst slope areas, and 52 on trough slope areas. The remaining 71 stations were distributed among the other seafloor types.

**Table 6. Nodule Abundance vs. Seafloor Morphology**

| Seafloor Morphology               | No. Stations | Nodule Abundance ( $\text{kg}/\text{m}^2$ ) |      |      |
|-----------------------------------|--------------|---|------|------|
|                                   |              | Mean  | Min. | Max  |
| Undulating Plain (up)             | 303          | 8.6   | 0    | 43.6 |
| Horst Trough (ht)                 | 87           | 8.6   | 0    | 28.4 |
| Horst Slope (hs)                  | 227          | 8.3   | 0    | 30.0 |
| Trough Axis (ta)                  | 57           | 6.8   | 0    | 20.2 |
| Trough Slope (ts)                 | 145          | 8.3   | 0    | 23.7 |
| Slope (vs)                        | 20           | 8.7   | 0    | 22.5 |
| Plains among Volcanic Hills (pvh) | 7            | 10.6  | 0.1  | 20.8 |

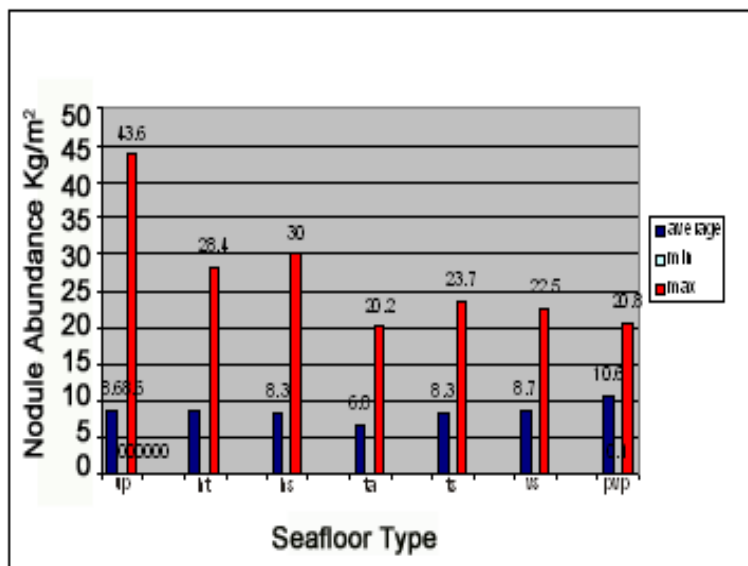


**Figure 34. Nodule Abundance vs. Seafloor Morphology**

### 5.3.3 Regional Variability of Nodule Abundance and Morphology

Data collected from 934 sample stations allowed examination of the spatial trends of nodule abundance and morphology in the study area. The stations with the highest mean abundance and with the highest maximum value are situated between  $12 - 16^\circ \text{N}$  (Figure 35). A total of 189 stations in this zone (representing about half of all stations in this latitudinal band) showed nodule abundances in excess of  $10 \text{ kg}/\text{m}^2$ . North of  $16^\circ \text{ N}$  and south of  $12^\circ \text{ N}$ , the nodule abundance evidently decreases, consistent with the axial line of high abundance described above in Section 5.2.3.

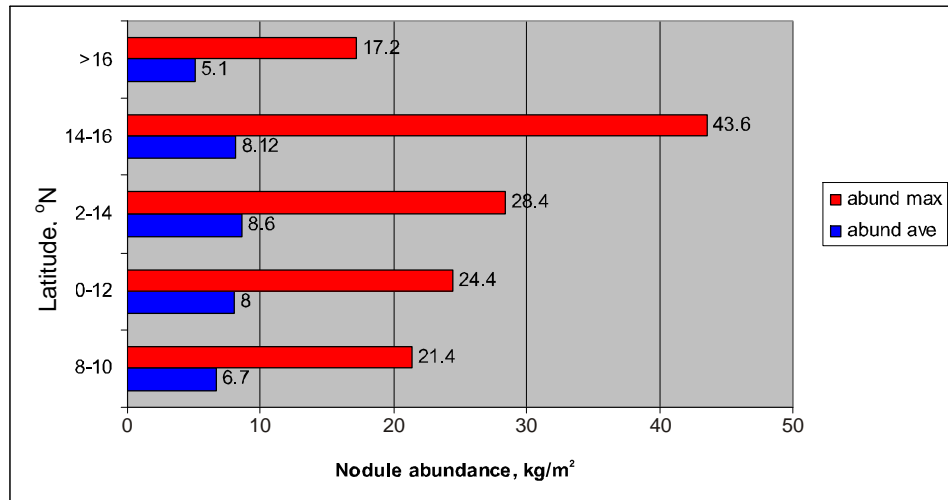


*Figure 35. Variation of Nodule Abundance with Latitude*

As shown in Figure 36, the distribution of nodule genetic types shows virtually no variation with latitude in the study area. The nodule genetic types **H**, **HD**, and **D** were most uniformly distributed across a latitude range of  $8.66^{\circ}$  to  $16.88^{\circ}$  N, while the **D1** type has a range of between  $8.65^{\circ}$ -  $14.63^{\circ}$  N.

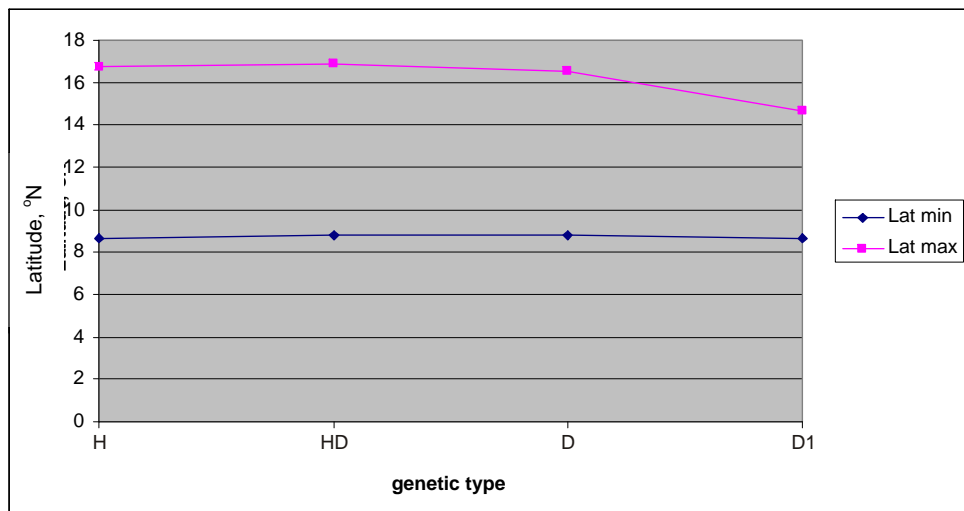
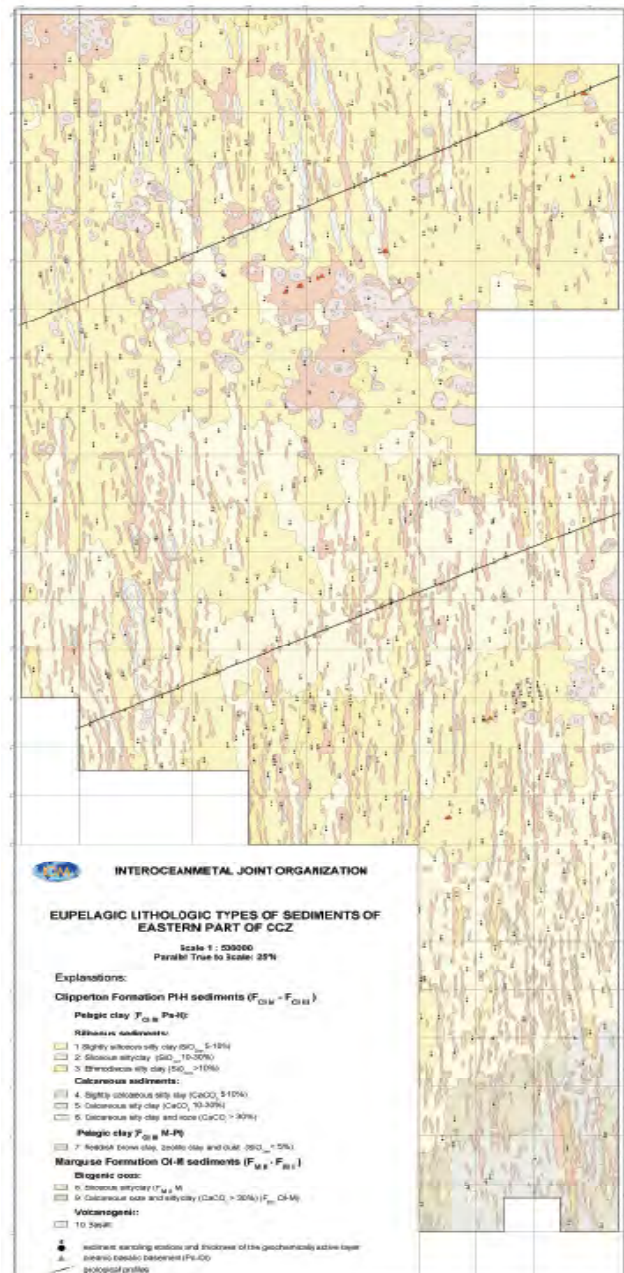


*Figure 36. Variation of Nodule Genetic Morphology with Latitude*

This study covers only some features of nodule morphology, coverage and abundance relevant to the eastern part of the CCZ nodule field. The relationships discussed here demonstrate the complexity of the factors that control nodule formation in the study area and the entire CCZ.

## 6. SEDIMENTS IN THE EASTERN CCZ

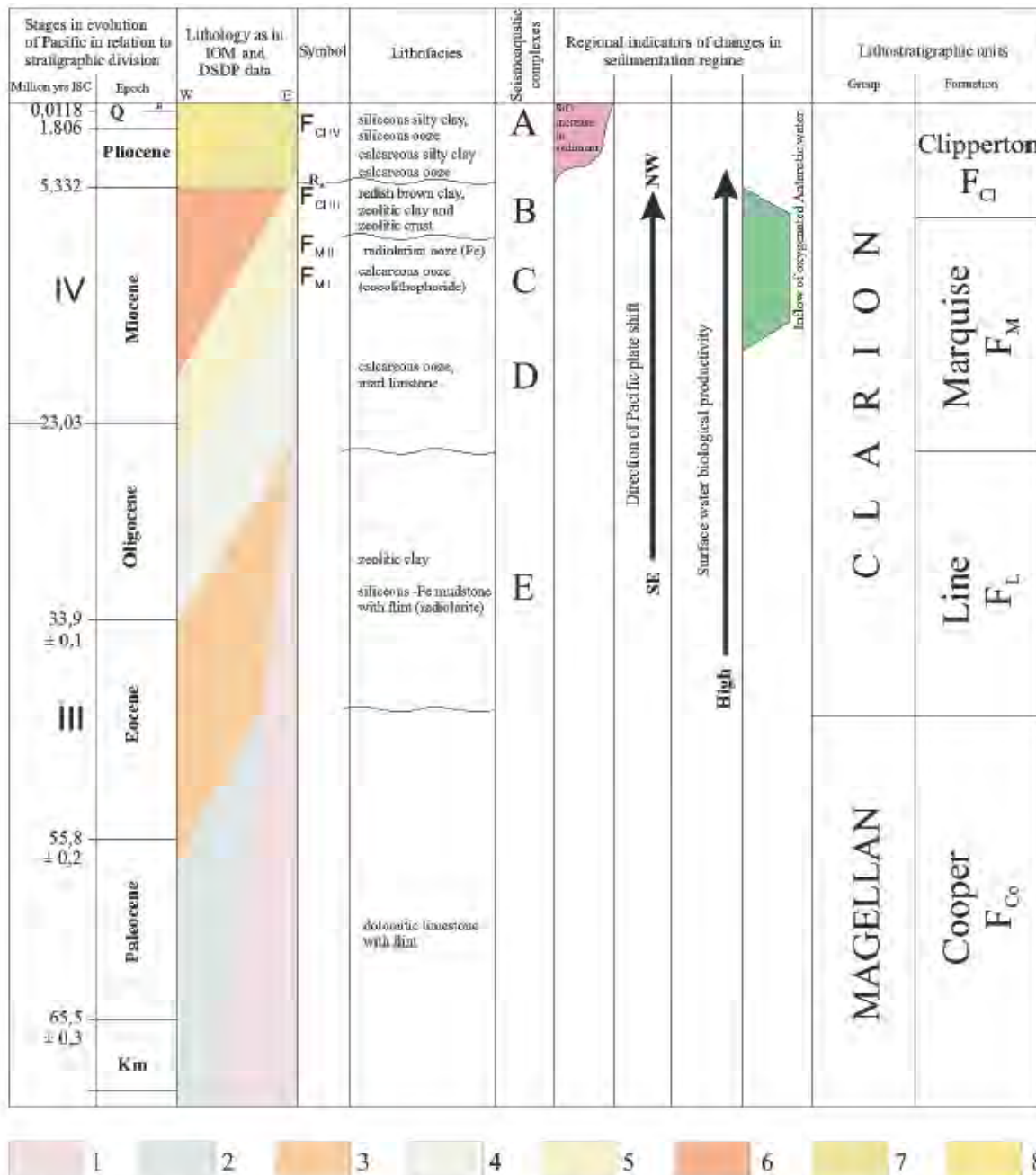


### 6.1 GEOLOGICAL SETTING

One study area is north of the equator in the eastern part of the northeastern Pacific Basin, between the Clarion and Clipperton Fracture Zones. It has been examined in detail by InterOcean Metal (IOM) since 1988. Sediment samples were recovered with grab samplers, box corers, multi-corers and gravity corers. The age of the basement of this area is Oligocene-Miocene, as determined from the drill core samples at DSDP site 159 and magnetic lineation patterns (DSDP 1973).

The topography of the area is characterized by NW-SE to NNW-SSE trending elongated seabed structures. A seismic reflection survey of the area revealed that two predominant reflectors A' and B' form the boundary between Miocene through Holocene siliceous clay/ooze and C' and D' sediment of Oligocene age. The surface sediments consist of Pleistocene and Holocene (made up of siliceous silty clay and ooze) underlain by Miocene through Pliocene (made up of pelagic clay, zeolitic clay, zeolitic crust), and hiatuses of Pliocene through Pleistocene and Late Miocene ages (see Figures 37 and 38).

Figure 37. Surface Sediments in the Eastern CCZ



1. oceanic basaltic basement,
2. dolomitic limestone with flint
3. siliceous Fe mudstone with flint radiolarite,
4. calcareous ooze, marl limestone,
5. calcareous ooze (cocolithophorides),
6. reddish brown clay, zeolitic clay and zeolitic crust,
7. calcareous silty clay and ooze,
8. siliceous silty clay, siliceous ooze,

Figure 38. Sedimentary Stratigraphy in the Eastern CCZ

## 6.2 Bottom Morphology

A majority of seabed structure of the eastern part of the CCZ is typically represented by three structures. These structures are, meridian-oriented volcano-tectonic blocks, formed by a combination of sub-latitudinal and longitudinal fractures including transform faults. Sub-latitudinal fractures are tracked by volcanic ridges, and longitudinal fractures are tracked by horsts and grabens. The

morphological structure of the ocean floor was formed during the Oligocene and Miocene periods that are characterized by the age of underlying basalt. In the late Miocene and Pliocene periods an outburst of volcanic-tectonic activity occurred, further changing the bottom topography. The evidence for this activity is superimposed volcanic complexes of sub-latitudinal trend (Kotliński, 1999; Kotliński and Zadornov, 2002). The bottom depth is generally deeper from the north and south towards the middle, and insignificant deepening from east to west characterizes the study area.

The ocean floor is a hilly plain - plateau (4,300 – 4,400 m water depth), crossed by a strictly north-south system of horsts (4,100 – 4,300 m) and grabens (4,400 – 4,750 m) (Kotliński and Stoyanova, 2006). The primary morphological structure consists of these horsts and grabens occurring along fault zones. The surface relief of this hilly plain is generally less than 100 m, with hills and ridges exceeding 100 m on plains. Less common are volcanic structures, characterized by slopes of more than 7°.

The base line for this hill-and-ridge topography is at the 4,300 m isobath. The horst width varies between 1.0 and 1.5 km, with lengths ranging from 7 to 70 km. The widest and the longest horsts are formed in the central and southern parts of the region. The horsts are both symmetrical and asymmetrical. In the latter case, the slopes of the horsts are very steep (over 45°). The horsts reach a maximum height of 200 m (in the north), and the minimum height is 75 m (in the western part of the central area).

The base line for the grabens is at 4,400 m water depth. The width of the basins (along the 4,500 m isobath) varies between 0.8 and 50 km, and their length ranges between 4.5 and 150 km. The profile of the depression floor is predominantly trough shaped. The graben depth varies between 225 m in the south and 310 m in the west of the central part (Kotliński, 2003). The depressions support basins up to 210 m deep, and ranging in size from 0.8x1.4 km to 3x18 km. The depression axes are *en echelon*, and some grabens often have several axes. The slopes of the depressions are steep (some are nearly vertical). The cross profile of the depressions is often symmetrical. Undulation of axes is typical for both horsts and depressions.

### 6.3 Bottom Sediments

As shown by the classification of eupelagic sediments (Table 7), polygenetic clays contain less than 30 per cent microfossils. If microfossils comprise less than 5 per cent, the sediment is classified as pelagic clay, with the < 4 µm grain-size fraction making up more than 75 per cent. Pelagic silty clays contain < 30 per cent microfossils, while the group of oozes contains more than 30 per cent microfossils. If sediment contains more than 50 per cent siliceous or calcareous microfossils, it is placed within either siliceous or calcareous ooze subtypes (for example, Foraminiferal ooze).

The sediment profile is topped by slightly siliceous silty clay and siliceous silty clay. The top 1-15 cm layer comprises the geochemically active layer, which is the environment of nodule formation (see Table 8. This layer consists of sediments with 3.04-28.6 per cent amorphous silica content. Contents of chemical elements in this sediment and pore waters are presented in Tables 9 - 12.

In terms of the origin of the sediments and their amorphous silica and calcium carbonate contents, the eastern part of the CCZ may be fairly reliably regarded as supporting reddish brown clay and zeolitic clay (less than 5 per cent amorphous silica content), slightly siliceous (with 5-10 per cent amorphous silica) and siliceous (10-30 per cent amorphous silica) silty clay, and slightly calcareous (5-10 per cent amorphous silica) and calcareous (10-30 per cent CaCO<sub>3</sub>) silty clay. The uppermost part of the sediment profile features predominantly siliceous silty clay, which grades down core into slightly siliceous silty clay. Calcareous silty clay and calcareous ooze occur only in the southern part of the study

area. In terms of grain size distribution, the sediments are classified mostly as clay or silty clay. The  $< 4 \mu\text{m}$  clay fraction accounts for 88.6 per cent of the sediments presented in Table 8. Down-core distributions of the common minerals observed in these sediments are presented in Figure 40.

Reddish brown pelagic clay is particularly common in the northern part of the area. It is yellow-brown in color, with various gray shades. With increasing microfossil content, its colour changes gradually from dark brown to gray yellow. The silt ( $4-63 \mu\text{m}$ ) content is usually below 25 per cent. The average contents of  $\text{SiO}_2 + \text{Al}_2\text{O}_3$ , amorphous  $\text{SiO}_2$ , and  $\text{C}_{\text{org}}$  are more than 70 per cent, less than 5 per cent, and 0.02-0.75 per cent, respectively.

Towards the equator, changes in sedimentation pattern are reflected in a gradually increasing biosilica content. There is also a concurrent increase in the deposit thickness, from several centimeters to several tenths of meters. Horizontal changes in lithological heterogeneity in relation to bathymetric variations also occur. The sediment often shows signs of bioturbation.

Siliceous clayey silt and silty clay are brown-yellow and show conspicuous bioturbation. Radiolarian remains are particularly abundant in the  $> 64 \mu\text{m}$  grain size fraction. Microfossils in this environment are re-deposited and gradually dissolve. The sediment often contains mixtures of micronodules and terrigenous (or clastic? or detrital?) components. They also contain barite and gypsum, the content of which increases with depth, and phillipsite, quartz, feldspar, pyroxene and apatite. Zeolite and silica contents do not exceed 5 and 10 per cent, respectively. Plagioclase is also present. Compared to brown pelagic clay, the sediment group discussed above shows a higher barite content (< 5 per cent), lower zeolite content, and is distinct in its higher micronodule content (up to 10 per cent). Grains of the clay fraction ( $< 4 \mu\text{m}$ ) are characteristic in that they contain di-octahedral hydromuscovite (2M illite) with an ordered texture, kaolinite plus chlorite (13-18 per cent), and montmorillonite (20-30 per cent). Typical of montmorillonite is its mixed-layered structure with illite packets, a low  $\text{Fe}^{+2}$  content, and di-octahedral structure similar to that of products of igneous rock weathering, which suggests its eolian and detrital origins.

Calcareous ooze and calcareous silty clay contain coccoliths and foraminifera. The average content of  $\text{SiO}_2 + \text{Al}_2\text{O}_3$  is about 63 per cent, and  $\text{CaCO}_3$  is less than 47 per cent.

**Table 7. Sediment Classification** (Kotliński 1998, modif. Kotliński 2008)

| SEDIMENT GROUP   | 6.1 SEDIMENT<br>7.0 SUBGROUP | Quantify Fraction <4µm (%)   | Lithologic Sediment Type  | Lithogenic and authigenic components <sup>1,2</sup> %<br><25 - >4µm  | Biogenic Fossil Components %           |                              | Remarks                     |  |
|--|------------------------------|--|---|--|--|------------------------------|-----------------------------|--|
|  |                              |  |   |  | Siliceous SiO <sub>2</sub> amorph.     | Calcareous CaCO <sub>3</sub> |                             |  |
| <b>POLYGENIC</b>   | Pelagic clay                 | >75  | Reddish Brown clay  | <10  | $\leq 5 \text{ CaCO}_3 + \text{SiO}_2$ |                              | below SCD                   |  |
|  |                              |  | Zeolitic clay   | Zeolites >5  |  |                              |                             |  |
|  | Pelagic Silty clay           | 75≤4µm >50   | Slightly siliceous  | ≤25  | 5-10                                   | +                            | below CCD                   |  |
|  |                              |  | Siliceous   |  | 10-30                                  | +                            |                             |  |
|  |                              |  | Slightly calcareous   |  | +                                      | 5-10                         | above CCD                   |  |
|  |                              |  | Calcareous  |  | +                                      | 10-30                        |                             |  |
| <b>BIOGENOUS</b>   | Calcareous ooze              | 75≤4µm ≥25   | Foraminiferan silty clay  | ≤25  | +                                      | >30                          | Foraminiferans <sup>3</sup> |  |
|  |                              |  | Coccolithophoride silty clay  |  | >30                                    |                              | Coccolithophores            |  |
|  | Siliceous ooze               |  | Radiolarian silty clay  |  |  |                              | Radiolarians <sup>4</sup>   |  |
|  |                              |  | Diatom/ Ethmodiscus silty clay  |  |  |                              | Diatoms/ Ethmodiscus        |  |
|  |                              |  |   |  |  |                              |                             |  |
| <b>LITHOGENIC COMPONENTS<sup>1</sup>:</b><br><i>Clay minerals (Illite, Montmorillonite, Kaolinite, Chlorites), Quartz, Feldspar, Pyroxene, Apatite, volcanogenic material and others.</i>              |                              | <b>Autogenic components<sup>2</sup>:</b><br>Manganese Micronodules<br>Zeolite (Phillipsite, Clinoptilolite)<br>Barite, Gypsum, Calcium | <b>Biogenic fossils:</b><br><b>Calcareous:</b><br>Foraminiferans (Planktonic)<br>Coccolithophorides<br>Pteropodes<br><b>Siliceous</b><br>Diatoms, Ethmodiscus<br>Radiolarians<br>Sponge spicules<br>Silicoflagellates | <b>Foraminiferan silty clay<sup>3</sup>:</b><br>$\geq 50\%$ Foraminiferans<br><b>Diatom-Radiolarian clayey silt<sup>4</sup>:</b><br>30-50% Diatoms<Radiolarians<br><b>Ethmodiscus silty clay<sup>5</sup>:</b><br>$= \geq 10\%$ Ethmodiscus rex |  |                              |                             |  |
| <b>REMARKS:</b><br><i>Diagenic (Hemipelagic) sediments<br/><math>\geq 25\%</math> of fraction &gt;4µm<br/>consist lithogenic<sup>1</sup> and authigenic<sup>2</sup><br/>components /Berger, 1974/.</i> |                              |  |   |  |  |                              |                             |  |

**Table 8. Sediment Lithological Composition and Stratigraphy (IOM data, 2005)**

| Litho-stratigraphic units (age) | Lithofacies (lithologic type)   | Origin                          | Thickness cm | pH        | Eh mV   | SiO <sub>2</sub> am. % | CaCO <sub>3</sub> % | C <sub>org.</sub> % | Quantify Fraction <4μm % | Water Content W <sup>1</sup> % | Density ρ g/cm <sup>3</sup> |
|---------------------------------|---|---------------------------------|--------------|-----------|---------|------------------------|---------------------|---------------------|--------------------------|--------------------------------|-----------------------------|
| F <sub>GIV</sub> (Ps-H)         | <b>Geochemically active layer</b><br>(Siliceous silty clay, Slightly siliceous clayey silt) | eluvial-deluvial                | 1-15         | 6.47-8.17 | 343-622 | 3.04-28.64             | < 14.1              | 0.13-0.78           | 5.1-88.6                 | 248-470                        | 1.15-1.23                   |
|                                 | (Siliceous silty clay/clayey silt)  |                                 | 41           | 6.87-8.14 | 390-666 | 2.10-25.67             | < 9.60              | 0.09-0.75           | 6.1-86.0                 | 210-437                        | 1.16-1.28                   |
|                                 | Biogenic Ooze/silty clay<br>(Ethmodiscus silty clay)  |                                 | 480          | 7.27-7.81 | 422-600 | 1.73-32.15             | < 0.976             | 0.02-0.31           | 30.6-84.7                | 205-309                        | 1.20-1.28                   |
|                                 | (Slightly calcareous silty clay)  | eluvial-deluvial                | 39           | 7.19-8.05 | 396-592 | 13.78-32.54            | < 0.083             | 0.21-0.40           | 71.9-84.3                | 224-434                        | 1.16-1.24                   |
|                                 | (Calcareous silty clay)   |                                 | 24           | 7.42-8.31 | 443-584 | 7.95-12.1              | 5.09-9.67           | 0.40-0.68           | 64.9-81.3                | 265-424                        | 1.17-1.23                   |
| F <sub>GIII</sub> (M-Pl)        | <b>Pelagic Clay</b><br>(Reddish Brown Clay, Zeolithic clay and Zeolithic crust)             | eluvial                         | 408          | 7.01-7.96 | 389-615 | 0.48-8.80              | < 3.178             | 0.02-0.75           | 47.6-88.4                | 85-303                         | 1.16-1.60                   |
| F <sub>MII</sub> (M)            | <b>Biogenic</b><br>(Siliceous silty clay, Radiolarian clayey silt))                         | eluvial                         | 255          | 7.19-8.02 | 476-625 | 0.90-16.29             | < 4.767             | 0.05-0.15           | 38.9-80.2                | 255-599                        | 1.12-1.25                   |
| F <sub>M I</sub> (Ol-M)         | <b>Biogenic</b><br>(Calcareous Ooze, Calcareous silty clay)                                 | Primarily biogenic accumulation | 70           | 7.47-8.09 | 505-625 | 0.50-7.75              | 18.40-71.14         | 0.01-0.23           | 45.1-78.9                | 150-165                        | 1.33-1.37                   |

**Table 9. Sediment Elemental Composition (ppm)**

| <b>Element</b>  | <b>Sr</b>  | <b>Co</b> | <b>Ni</b>  | <b>Zn</b> | <b>Cu</b>  | <b>Zr</b>  | <b>Mo</b> | <b>V</b>   | <b>Cr</b> | <b>Pb</b> | <b>As</b> | <b>Ba</b>    |
|---|------------|-----------|------------|-----------|------------|------------|-----------|------------|-----------|-----------|-----------|--------------|
| <b>Geochemically active sediment layer (66 samples)</b> |            |           |            |           |            |            |           |            |           |           |           |              |
| <b>Mean</b>   | <b>400</b> | <b>67</b> | <b>173</b> | <b>90</b> | <b>337</b> | <b>125</b> | <b>9</b>  | <b>98</b>  | <b>45</b> | <b>32</b> | <b>44</b> | <b>7,806</b> |
| <b>Maximum</b>  |            | 130       | 400        | 260       | 580        | 190        | 32        | 140        | 60        | 50        | 90        | 10,500       |
| <b>Minimum</b>  | 260        | 28        | 71         | 50        | 210        | 86         | 3         | 62         | 28        | 16        | 20        | 3,900        |
| <b>Underlying sediment (68 samples)</b>                 |            |           |            |           |            |            |           |            |           |           |           |              |
| <b>Mean</b>   | <b>432</b> | <b>53</b> | <b>107</b> | <b>94</b> | <b>308</b> | <b>134</b> | <b>9</b>  | <b>101</b> | <b>47</b> | <b>33</b> | <b>44</b> | <b>8,362</b> |
| <b>Maximum</b>  | 1,200      | 240       | 460        | 190       | 960        | 220        | 35        | 150        | 70        | 58        | 90        | 15,000       |
| <b>Minimum</b>  | 4          | 6         | 47         | 40        | 160        | 80         | 3         | 47         | 10        | 12        | 10        | 1,600        |

**Table 10. Sediment Fe, Ti and Mn Content**

| <b>Element</b>  | <b>Fe</b> | <b>Ti</b> | <b>Mn</b> |
|---|-----------|-----------|-----------|
| <b>Geochemically active sediment layer (66 samples)</b> |           |           |           |
| <b>Mean</b>   | 3.9       | 0.3       | 0.5       |
| <b>Maximum</b>  | 4.7       | 0.45      | 0.88      |
| <b>Minimum</b>  | 2.7       | 0.19      | 0.09      |
| <b>Underlying sediment (68 samples)</b>                 |           |           |           |
| <b>Mean</b>   | 4.2       | 0.3       | 0.2       |
| <b>Maximum</b>  | 5.4       | 0.58      | 1.57      |
| <b>Minimum</b>  | 1.8       | 0.076     | 0.03      |

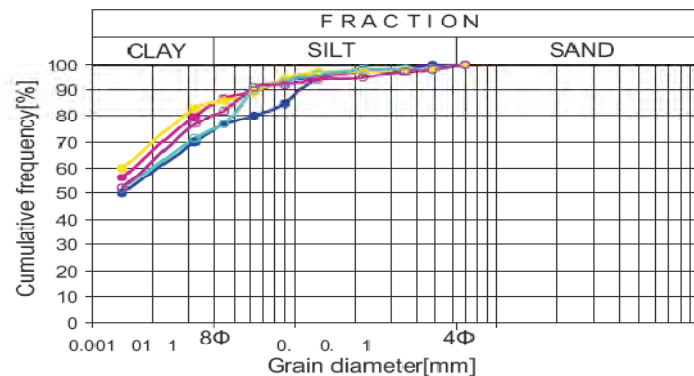
**Table 11. Pore Water Composition**

| <b>Element</b>  | <b>Fe</b> | <b>Mn</b> | <b>Co</b> | <b>Ni</b> | <b>Cu</b> | <b>Zn</b> | <b>Pb</b> | <b>Cd</b> | <b>As<sup>3+</sup></b> |
|---|-----------|-----------|-----------|-----------|-----------|-----------|-----------|-----------|------------------------|
| <b>Geochemically active sediment layer (64 samples)</b> |           |           |           |           |           |           |           |           |                        |
| <b>Mean</b>   | 1.74      | 4.43      | 0.037     | 2.41      | 5.67      | 9.52      | 3.09      | 0.56      | 2.72                   |
| <b>Maximum</b>  | 10.14     | 72.54     | 0.174     | 17.01     | 23.1      | 40.4      | 16.5      | 4.03      | 6.64                   |
| <b>Minimum</b>  | 0.25      | 0.34      | 0.003     | 0.57      | 0.50      | 4.35      | 1.22      | 0.10      | 0.23                   |
| <b>Underlying sediment (64 samples)</b>                 |           |           |           |           |           |           |           |           |                        |
| <b>Mean</b>   | 1.73      | 3.55      | 0.025     | 1.69      | 3.12      | 8.79      | 3.01      | 0.51      | 2.33                   |
| <b>Maximum</b>  | 7.43      | 15.29     | 0.12      | 8.56      | 21.59     | 72.5      | 8.51      | 1.78      | 8.37                   |
| <b>Minimum</b>  | 0.28      | 0.23      | 0.001     | 0.36      | 0.19      | 3.24      | 1.15      | 0.04      | 0.45                   |

**Table 12. Carbon and Nutrient Content in Sediments and Pore Waters**

| 1.2 Component                              | 1.3 Sediment            |                        |                     |                        | 1.4 Pore Water ( $\mu M$ )   |                              |                               |                                |
|--|-------------------------|------------------------|---------------------|------------------------|------------------------------|------------------------------|-------------------------------|--------------------------------|
|  | C <sub>carb</sub> (ppt) | C <sub>org</sub> (ppt) | CaCO <sub>3</sub> % | SiO <sub>2</sub> dry % | NO <sub>2</sub> <sup>-</sup> | NO <sub>3</sub> <sup>-</sup> | PO <sub>4</sub> <sup>3-</sup> | SiO <sub>3</sub> <sup>2-</sup> |
| <b>Geochemically active sediment layer</b> |                         |                        |                     |                        |                              |                              |                               |                                |
| <b>No. samples</b>                         | 69                      | 70                     | 70                  | 68                     | 67                           | 67                           | 67                            | 67                             |
| <b>Mean</b>                                | 0.05                    | 0.44                   | 0.45                | 9.04                   | 0.18                         | 35.7                         | 2.32                          | 328.7                          |
| <b>Maximum</b>                             | 1.92                    | 0.75                   | 16.01               | 18.81                  | 0.4                          | 45.8                         | 3.75                          | 455.6                          |
| <b>Minimum</b>                             | 0.01                    | 0.14                   | 0.06                | 0.5                    | 0.04                         | 27.2                         | 1.78                          | 252.8                          |
| <b>Underlying sediment</b>                 |                         |                        |                     |                        |                              |                              |                               |                                |
| <b>No. samples</b>                         | 69                      | 70                     | 70                  | 67                     | 65                           | 64                           | 65                            | 65                             |
| <b>Mean</b>                                | 0.33                    | 0.233                  | 2.68                | 8.89                   | 0.14                         | 35.7                         | 2.4                           | 388.2                          |
| <b>Maximum</b>                             | 8.53                    | 0.84                   | 71.1                | 32.54                  | 0.32                         | 45.22                        | 4.06                          | 492.7                          |
| <b>Minimum</b>                             | 0.01                    | 0.01                   | 0.067               | 0.48                   | 0.05                         | 25.01                        | 1.7                           | 311.4                          |

**Reddish BrownClay**



**Siliceous SiltyClay**

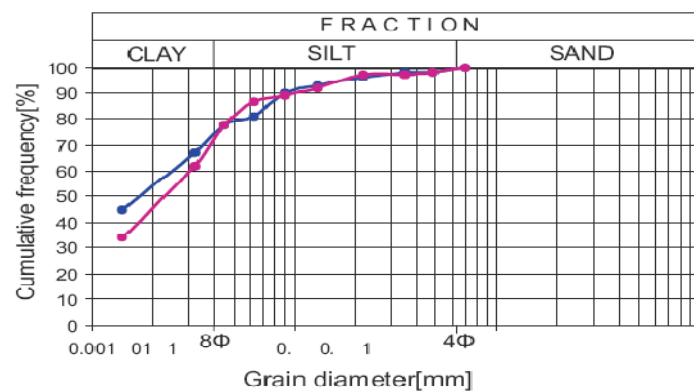


**Figure 39. Cumulative Sediment Grain Size Distributions**

Radiolarian ooze and diatom ooze are bright yellow-brown to brown-yellow, some samples have gray shades and commonly show mottles. They show a lower correlation between Mn and Co or Cu contents, or between contents of Fe and Co. It is possible that the main source of Cu and Ni is skeletons of the radiolaria that fully dissolved after deposition. The sediments discussed cover vast areas of the bottom and occur to about 11° N.

The top, geochemically active layer, 1-15 cm thick, consists mainly of radiolarian and diatom silty clay. It is homogenous in texture and has viscosities higher than that of the underlying layer. The underlying layer, up to 30-40 cm thick, consists mainly of siliceous silty clay. It is plastic, and its texture is heterogeneous. It contains pale yellow-brown to yellow-green mottles. The mottles are 0.5-7 cm in diameter and comprise about 20-40 per cent of the sediment by weight. These mottles may have resulted from redox processes taking place in the sediment. In addition, the sediment layer contains numerous bioturbation structures. The presence of ichnocoenoses trace fossils is related to well oxidized water, a low energy environment, and slow sedimentation rates.

Eupelagic sediments covering the seafloor of the eastern part of the CCZ consist of the Marquise and Clipperton formations (Table 8). Based on the origin and composition of the sediments, they can be divided into four litho-stratigraphic units (Table 8). The lowest lithofacies ( $F_{M\text{ I}}$ ) consists of biogenic calcareous ooze (foraminifera silty clay and coccolith-foraminifera silty clay, which are the products of primarily biogenic accumulation). The lithofacies is 70 cm thick and its amorphous silica content amounts to 1.36-7.75 per cent (Table 8).

The overlying lithofacies ( $F_{M\text{ II}}$ ) is made up of radiolarian silty clay, which is X-ray amorphous. These sediments are biogenic, pelagic and detrital, and produced in part by halmyrolysis and erosion of basalt.  $F_{M\text{ II}}$  is 255 cm thick, its amorphous silica content amounting to 0.90-16.3 per cent (Table 8). Sediments of these two lithofacies are thought to represent the Marquise formation (Oligocene and Miocene age).

Lithofacies  $F_{Cl\text{ III}}$  is represented by zeolitic clay (phillipsite) or reddish brown clay and denser zeolitic crusts of Miocene and Pliocene age. The zeolitic clay layer is 273 cm thick, and its amorphous silica content ranges between 0.48-8.8 per cent.

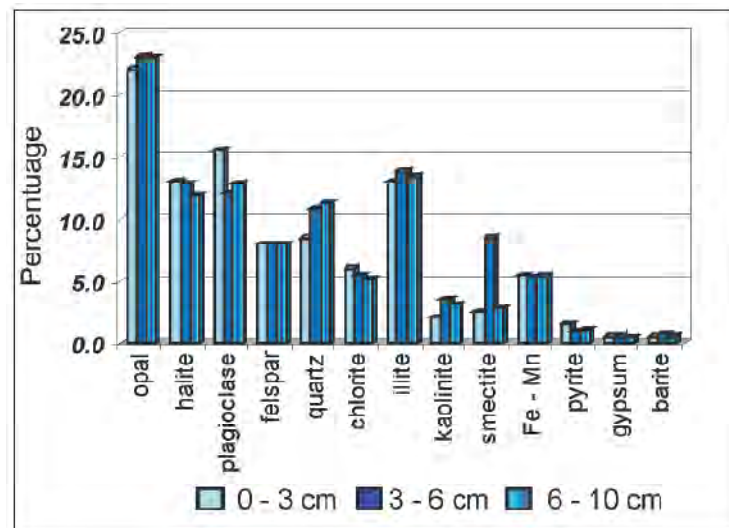


Figure 40. Down-Core Mineral Distributions

Higher up in the section are sediments assigned to lithofacies  $F_{Cl\text{ IV}}$  (Table 8). Sediments are siliceous silty clay, ethmodiscus clay, and alcareous silty clay. This section features a distinct top layer, 41 cm thick, consisting of siliceous silty clay which, down section, grades into lighter-coloured sediment with a mottled appearance. Genetically, this is a biogenic and detrital section. Sediments of lithofacies III and IV have been attributed to the Clipperton formation.

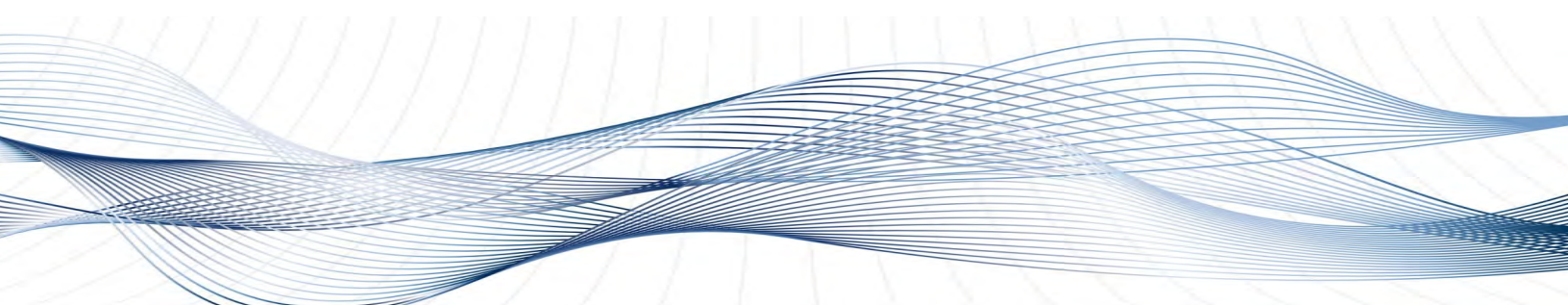
In addition, reworked Ethmodiscus silty clay occurs that is typically lacking in polymetallic nodules. The Ethmodiscus silty clay layers are 39 cm thick, their amorphous silica contents ranging from 13.88 to 32.5 per cent.

Results of chemical analysis of bottom sediments of the study area can be summarized as follows:

- Sediments of lithofacies  $F_{M\text{ I}}$  and ethmodiscus silty clay are impoverished in metals and elements.
- The highest contents of base metals are typical of the geochemically active sediment layer.
- The sediment iron content is virtually identical with the iron content of the nodules.
- The lithofacies  $F_{Cl\text{ IV}}$  sediment in the vertical profile (below 40 cm depth) shows a sharp reduction in the base metal contents; no pronounced variations were found in the underlying sediments.
- Contents of the base metals in the sediment are higher in nodule-bearing areas compared to nodule-free areas.

Nodule abundance is not dependent on the thickness of the geochemically active sediment layer.

## 7. NODULE GENESIS AND SEDIMENT DISTRIBUTION IN THE REPUBLIC OF KOREA - ALLOCATED AREA



### 7.1 Introduction

Nodule genesis and growth are affected by many environmental factors, especially: (1) supply of biogenic, terrigenous and hydrogenetic material to the sediment and to the nodules; (2) deposition and reworking of sediments due to seafloor morphology; (3) bottom water composition and movement; and (4) bioturbation (von Stakelberg and Beiersdorf, 1991). These factors are all or partly related to sediment supply rates and composition in the area of interest, and are indicative of the importance of sediment supply and distribution in nodule genesis. In this report we investigate nodule occurrence (i.e., abundance, shape, surface texture and metal content) in terms of the chemical and mineral composition of sediments, sedimentation rates and sediment distribution patterns, in order to better understand the potential effects of sediments on nodule genesis.

For the study area, we selected two blocks (KR2 and KR5) of the Korea Allocated Area located in the southern ( $9^{\circ}$  N~ $11^{\circ}$  N) and northern parts ( $16^{\circ}$  N~ $17^{\circ}$  N) of the CCZ, and between  $130^{\circ}$  W ~  $133^{\circ}$  W meridians (Figure 41). These sediment characteristics are compared with nodule characteristics on a regional scale rather than local details so that we can examine the regional-scale controls on nodule genesis. This work is based on the sampling and analysis of 117 sites in KR2 and 228 sites in KR5 for nodule characteristics. For sediment characteristics, multiple cores were collected at 17 sites in KR2 and 75 sites in KR5.

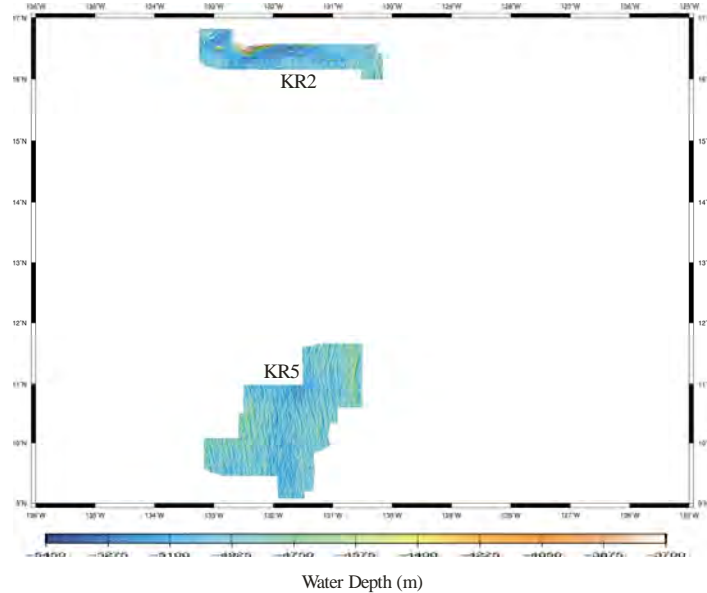


*Figure 41. Study Area and Bathymetry*

## 7.2 Bathymetric Characteristics of the Study Area

KR2 and KR5 are located at similar longitudes but show different bathymetric characteristics (Figure 41). KR2 is characterized by the presence of small-scale seamounts. Because of this, the area shows a highly variable bathymetric pattern. KR5 shows a relatively flat bathymetric pattern and is characterized by the repetitive occurrence of abyssal ridges and valleys oriented in a NNW to SSE direction. In general, the eastern and western parts of KR5 are shallower than the central part.

## 7.3 Nodule Characteristics

### 7.3.1 *Nodule Abundance*

In general, KR2 shows higher nodule abundance than KR5. In KR2, the western part has higher nodule abundance than the eastern part, while in KR5 the central part shows higher nodule abundance than the eastern and western parts. In both areas, nodule abundances are generally higher in topographic lows.

#### Nodule Metal Content

Mn/Fe ratios of polymetallic nodules are higher in KR5 than in KR2 (Figure 42), which suggests that nodules in KR5 were more affected by diagenetically-derived metals than those of KR2. In KR2, the western part with higher nodule abundances showed lower Mn/Fe ratios than the eastern part. In this block, Mn/Fe ratios show a weak negative correlation with nodule abundance. The same trend is also observed in KR5, where Mn/Fe ratios are lower in the central part with higher nodule abundances. Cu and Ni contents, supplied mainly from sediments, show distribution patterns similar to Mn/Fe ratios, although the reason for the observed decrease in Ni content in the central part of KR5 is not clear (Figure 43).

### 7.3.2 Nodule Size Distribution

Nodule size is slightly larger ( $5.3 \text{ cm} \pm 1.9$  on average) in the southern block (KR5) than in the northern block (KR2;  $3.7 \text{ cm} (\pm 1.9)$  on average) (Figure 44). However, nodule size is not correlated with either abundance or metal content.

### 7.3.3 Nodule Morphologies

The polymetallic nodules collected were classified into six groups based on their morphologies: D-(discoidal); E- (ellipsoidal); S- (spheroidal); I- (irregular); P- (poly-nucleated nodule); and T- (tabular) types. Nodules show dominant morphological shapes that depend upon bathymetric settings. For example, E- and D- type nodules are dominant on abyssal plains while P- and I-types are dominant near seamounts.

In general, D-and E-type nodules are abundant in the southern block (KR5) and less abundant in the northern block (KR2; Figure 45). In detail, however, the central part of KR5 block, characterized by relatively low Mn/Fe ratios and Cu and Ni contents, shows low occurrences of D-type nodules. Moreover, the western part of KR2, characterized by low Mn/Fe and Cu and Ni content, shows low occurrences of D- and E-type nodules.

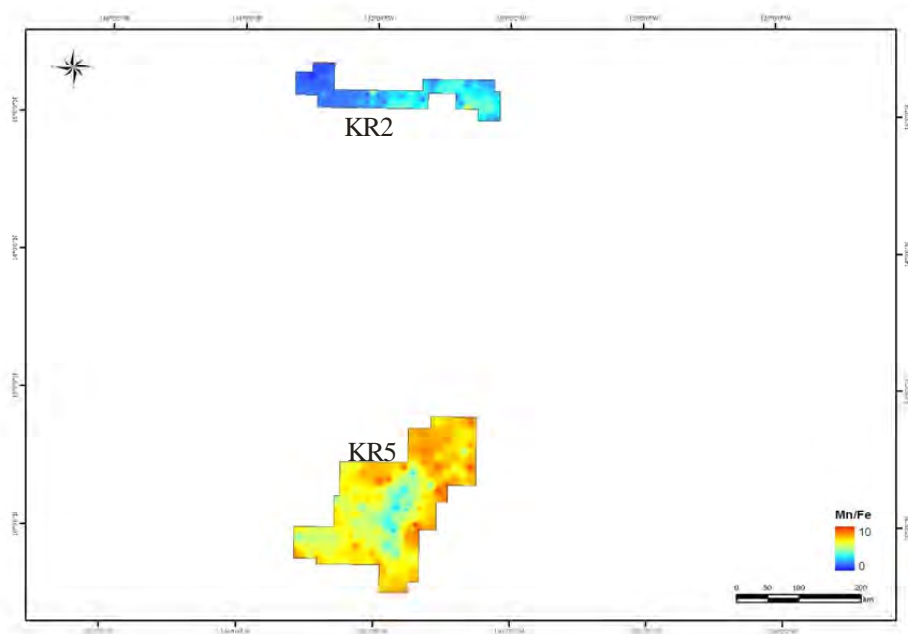


Figure 42. Nodule Mn/Fe Ratios

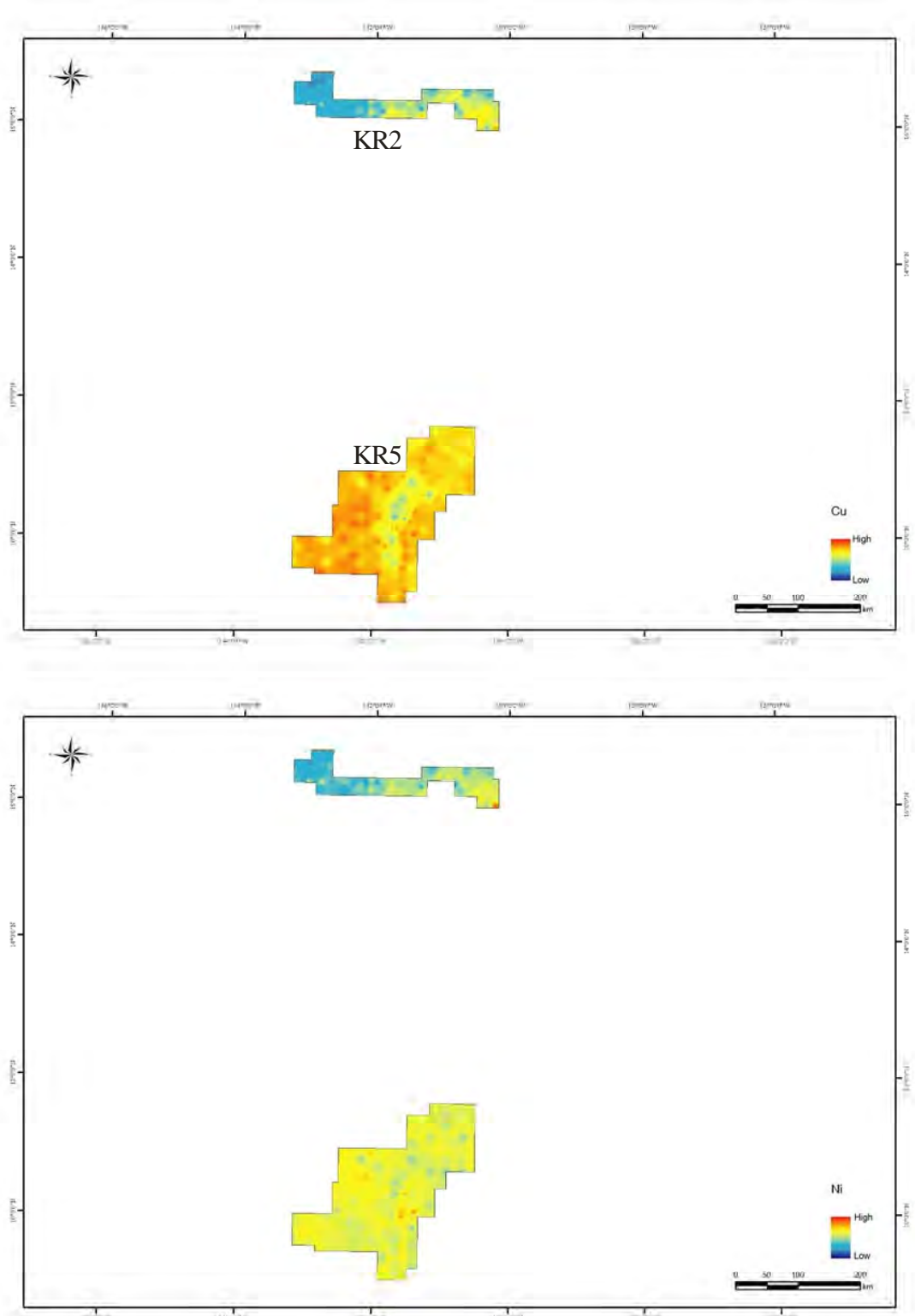
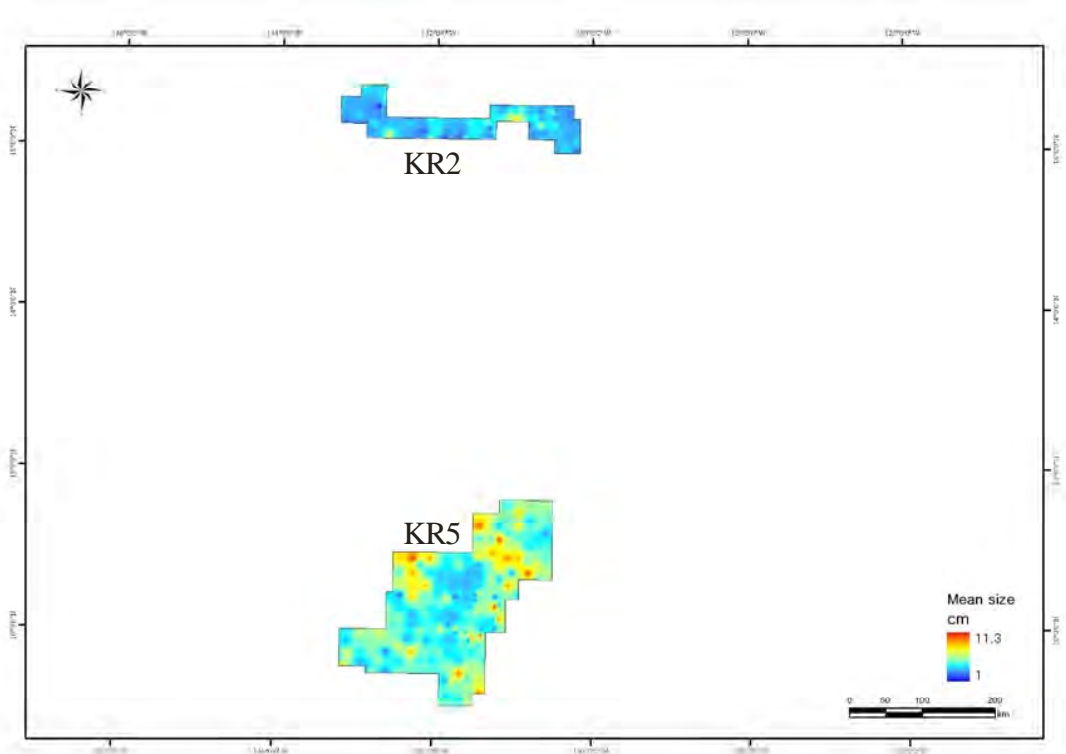


Figure 43. Cu (top) and Ni (bottom) Content



*Figure 44. Nodule Size Distribution*

P- and I-type nodules are more frequently encountered in the northern block (KR2) than in the southern block (KR5) (Figure 46). In KR5, the central part shows higher occurrences of P- and I-types than the eastern and western parts. In KR2, the western part, with more variable topographic settings due to the adjacent seamounts, shows higher occurrences of I-type than the eastern part. T-type nodules show occurrences restricted to local areas, and S-type nodules are rarely encountered in either block. In summary, P- and I-types are dominant in KR2 while E- and D-types are dominant in KR5. Figure 47 *Figure* contrasts the sum of P- and I-type nodules with the sum of E- and D-types throughout the study area.

#### **7.3.4 Nodule Surface Textures**

The collected polymetallic nodules were classified into four types based on their surface textures: d-(dimorphic), r- (rough), s- (smooth), and t-types (transitional). Dimorphic nodules show both r and s textures, whereas transitional nodules show textures that are intermediate between r and s. Nodule surface textures are believed to be related to their growth conditions. For example, diagenetic nodules are dominated by r- and d- type, while hydrogenetic nodules are dominated by s- and t-types.

S-type nodules are much more common in the northern block (KR2) than in the southern block (KR5) (Figure 48). In KR5, the central part shows a relatively high percentage of s-type compared to the eastern and western parts. The t-type nodule shows a distribution pattern similar to that of the s-type, but it is more widely distributed in the southern block than the s-type nodule. Distribution of r and d type nodules is shown in Figure 49.

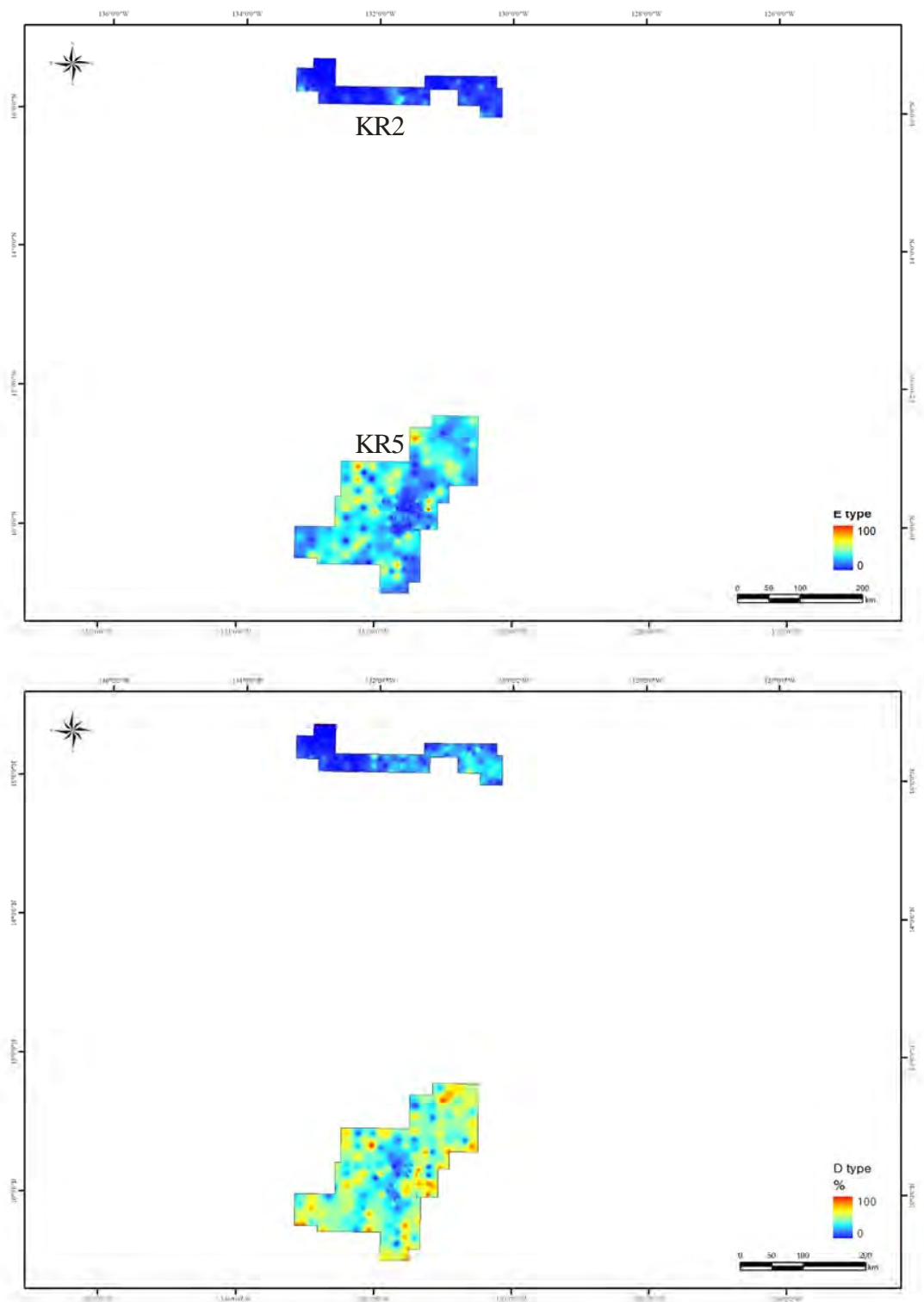


Figure 45. Distributions of E- and D- Type Nodules

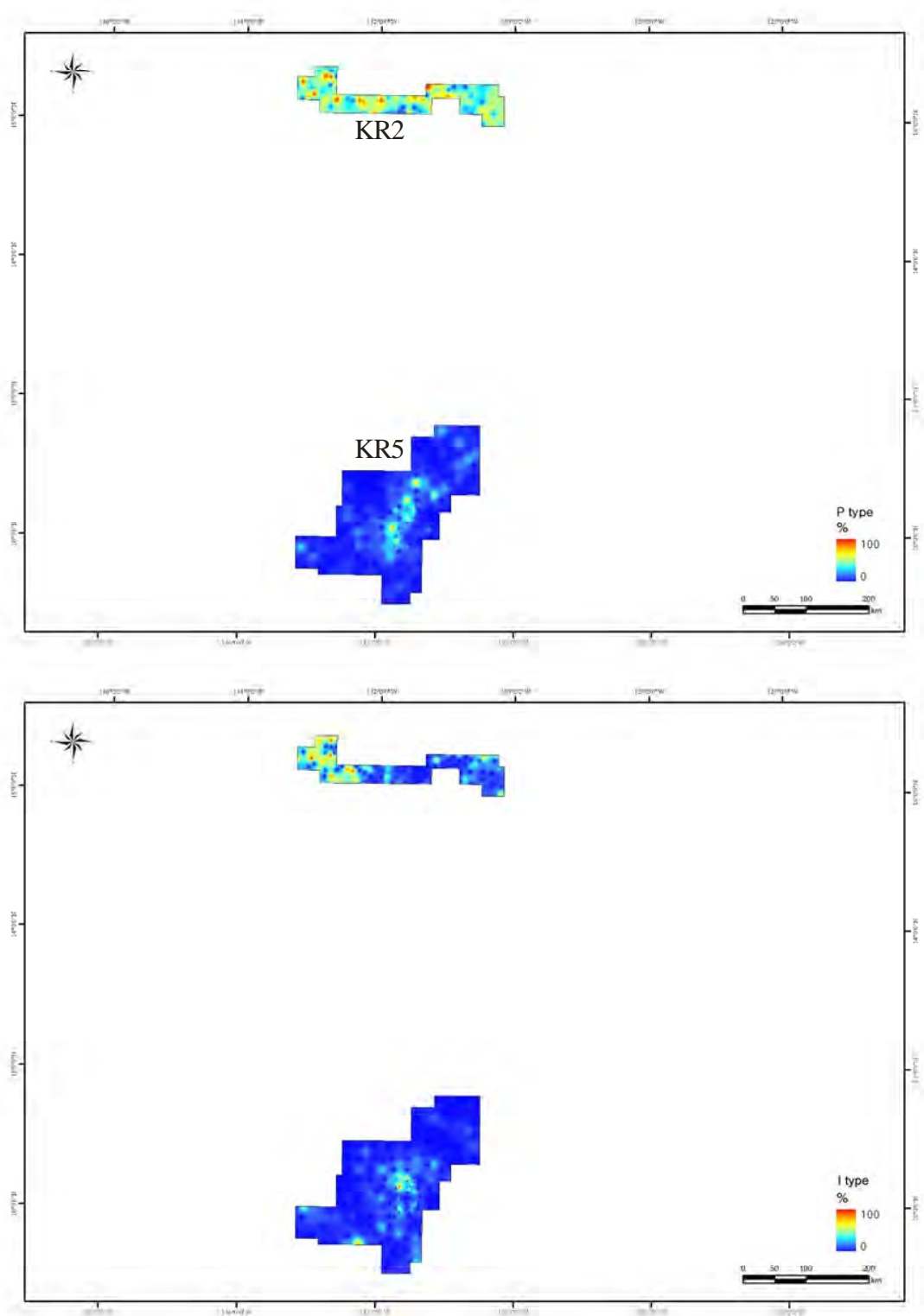


Figure 46. Distributions of P- and I-Type Nodules

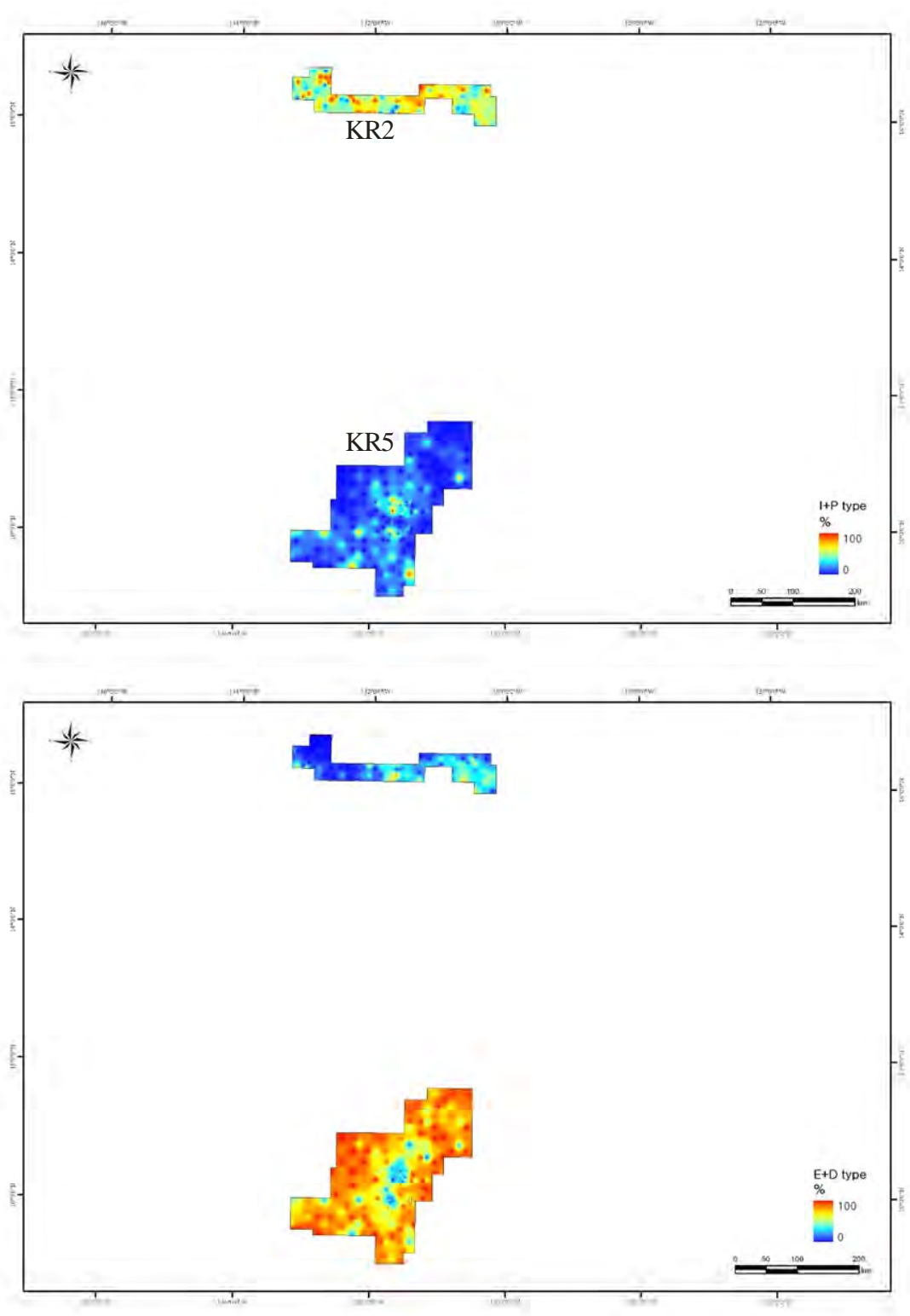


Figure 47. Distributions of I+P- and E+D- Type Nodules

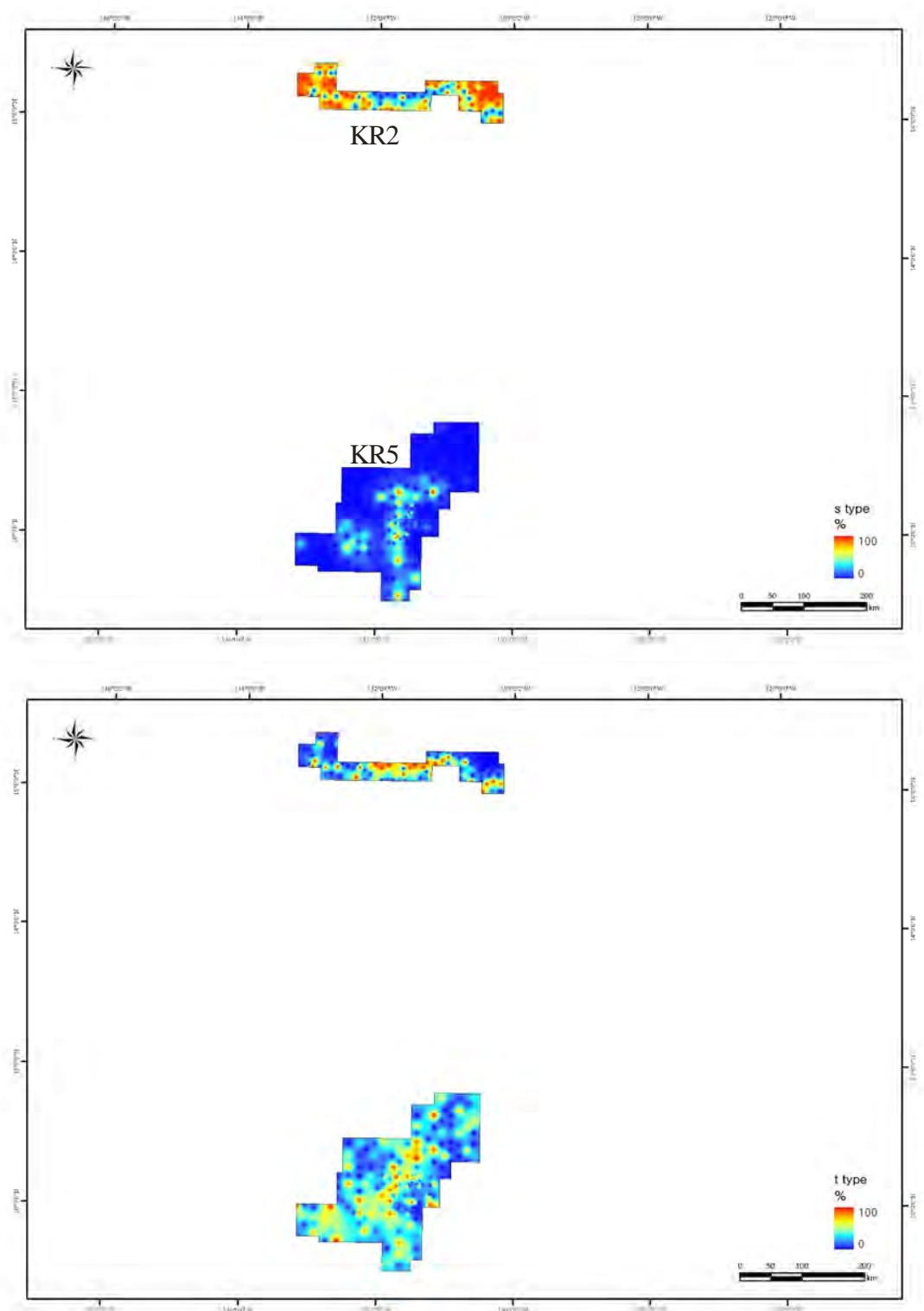


Figure 48. Distributions of *s*- and *t*- Type Nodules

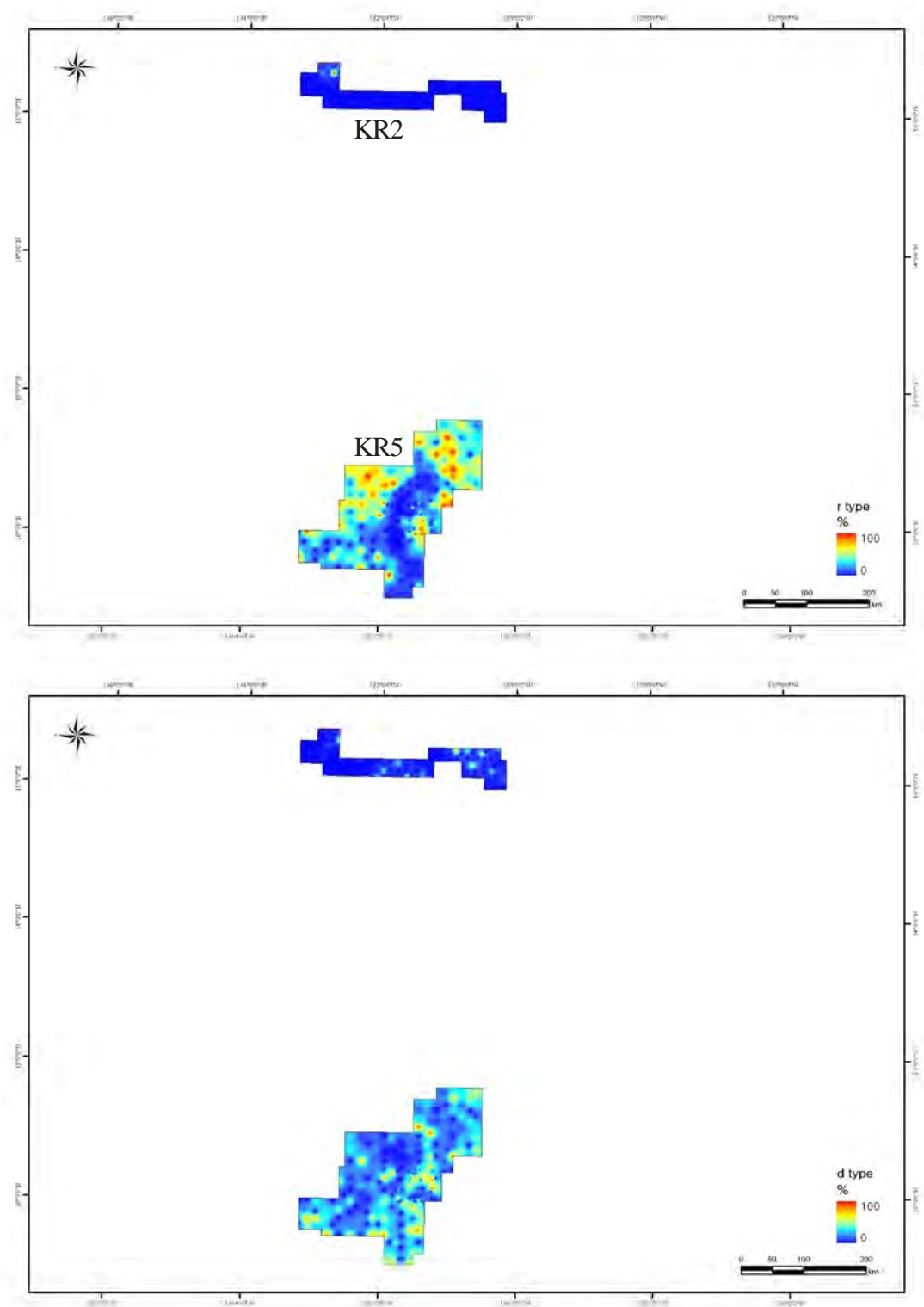


Figure 49. Distributions of r- and d- Type Nodules

### **7.3.5 Summary of Polymetallic Nodule Characteristics**

The morphological and textural characteristics of polymetallic nodules in the study area are summarized as follows. The northern block (KR2) is characterized by relatively high nodule abundances, low Mn/Fe ratios, low Cu and Ni content and high Fe and Co contents. In morphology, P- and I-type nodules are dominant. In texture, s- and t-types are abundant. All these characteristics indicate that hydrogenetic precipitation has been dominant over diagenetic processes in the northern block. Taking account of the relatively slow growth rate of hydrogenetic nodules, the presence of smaller nodules in the northern block is consistent with other chemical, morphological and textural characteristics.

In contrast, the southern block (KR5) is characterized by relatively low nodule abundances, high Mn/Fe ratio, high Cu and Ni content, and low Fe and Co contents. D- and E-type and r- and d-type nodules are the dominant morphological and textural nodule types in the southern block. All these characteristics indicate that diagenetic processes have dominated over hydrogenetic precipitation in the southern block.

## **7.4 Sediment Characteristics**

### **7.4.1 Sediment Distributions**

Sediments in the study area consist of three major lithological units – Units 1, 2 and 3 – which are distinctive in colour and texture. Unit 1 comprises the topmost layer and is dark grayish brown (10YR4/2) to dark brown (10YR3/4). It is homogenous mud characterized by very high water content. In some cores, dark brown sediments underlie Unit 1 or Unit 2. This dark layer was included in Unit 1 because of its colour and lithology, which are similar to Unit 1, but it contains a much lower water content compared to Unit 1. Unit 2 lies below or alternates with Unit 1 in most cores. It consists of yellowish brown (10YR4/6) to brown (10YR3/5) mud and includes many burrows filled with overlying Unit 1 sediments. Burrow densities decrease downward. Unit 3 underlies Unit 2 in most cores where it occurs and is very dark brown to black (10YR3/2 to 10YR2/1).

KR2 and KR5 blocks show big differences in Unit 1 thickness and lithological associations. KR5, the southern block, includes a great number of lithological units, and Unit 1 thickness is relatively thin, from 2 to 14 cm. In the northern block, Unit 1 sediments predominate down to 60 cm depth – the maximum core length obtainable with multiple cores used by KORDI. Unit 2 is not observed at all in the collected cores, but Unit 3 occurs in a few cores. In a piston core collected at similar latitude to KR2, the thickness of Unit 1 reaches 250 cm. So, the apparent absence of Unit 2 in KR2 is likely attributed to its deeper occurrence, which exceeds the multiple corer sampling depth (~60 cm).

### **7.4.2 Mineral Composition**

The studied sediments are classified into three lithological units, as described above, each of which shows a distinctive mineral composition and opal content. All the samples are mainly composed of quartz, feldspar, smectite, illite, kaolinite and chlorite, but their relative abundances distinguish these lithological units. Unit 1, the topmost layer, is dominated by quartz (15 – 27 per cent) and illite (39 – 54 per cent), which feature a mineral composition similar to that of North Central Pacific surface sediments. Unit 3 is characterized by high content of smectite, reaching a maximum of 68 per cent of total clay. This Unit's quartz content is slightly less than that of Unit 1. It is also characterized by the occurrence of clinoptilolite, a zeolite mineral.

Unit 2 shows a variable mineral composition site to site. It shows a mineral composition similar to Unit 1 at a site where Unit 3 is missing. Where Unit 3 occurs, it shows a mineral composition similar to Unit 3 or an intermediate mineral composition between Unit 1 and Unit 3. Based on the mineral composition of Unit 2, it is further divided into Unit 2a and 2b. Unit 2a has mineral and chemical compositions similar to Unit 1, while Unit 2b has mineral and chemical compositions similar to Unit 3.

Mineral composition shows systematic changes with depth in the sediments under investigation. In general, quartz and illite dominate in the upper section and smectite increases downward and comprises a dominant mineral phase in the lower sections (Figure 50). This down-core variation is due to the common facies association that Unit 1 exhibits, i.e. abundant in illite and quartz in the top of the sections. Unit 2 and/or Unit 3 are characterized by high smectite content. Surface sediments, Unit 1, of the study area, also show a systematic change with latitude in illite and smectite contents, in which illite content decreases toward the equator while smectite content increases, compensating for the reduction of illite content..

#### **7.4.3 Opal Content**

The studied samples also show distinctive opal contents that vary with the lithological units and sampling locations. Unit 1 is highest in biosilica, varying from 8.0 – 16.5 per cent. Unit 3 shows the lowest opal content, varying from 1.8 – 8.7 per cent (Figure 51). In the southern block (KR5), opal content of Unit 1 varies from 8.0 – 16.5 per cent and decreases to 1.8 – 8.7 per cent. This trend is accompanied by the lithological change to Unit 2 and/or Unit 3 (Figure 52). On the other hand, in the northern block (KR2), opal content is very low compared to the low latitude region, ranging from 3.1 to 10.7 per cent. There is also an apparent depth- and/or lithology-dependent trend found in the low latitude region, but not in the northern block. In a plot against depth in the sediment, opal content decreases with depth while smectite increases with depth; as a result, these two variables comprise a mirror image. This suggests opal dissolution as a potential source for smectite, as suggested by researchers in the 1970s.

#### **7.4.4 Age and Sedimentation Rate**

Ages were determined using  $^{10}\text{Be}/^{9}\text{Be}$  ratios of sediments in KR5 block and  $^{87}\text{Sr}/^{86}\text{Sr}$  ratios of fish teeth present in the sediments of a piston core collected close to the KR2 block. Based on the age data, linear sedimentation rates are estimated to vary between 0.07 - 0.13 mm/kyr for Unit 2b and Unit 3.  $^{10}\text{Be}/^{9}\text{Be}$  ratios of Units 1 and 2a were rather uniform, probably because of mixing by bioturbation; a consistent, decreasing trend in  $^{10}\text{Be}/^{9}\text{Be}$  ratios with depth is lacking. Unit 2b and Unit 3 have ages of 1.5 ~ 3 Ma and older than 3 Ma, respectively. Based on the estimated age of Unit 2b and Unit 3 and the thickness of Unit 1 and 2a, the sedimentation rates of Unit 1 and 2a are estimated to be similar to those of Unit 3 at around 0.1 mm/kyr. In KR2, the sedimentation rate of Unit 1 (extending to 250 cm depth) is estimated at 0.32mm/kyr, three to four times higher than in the southern block. Unit 2 of the same piston core, below 250 cm, showed a linear sedimentation rate of 0.11 mm/kyr, three times less than the overlying Unit 1 layer, but similar in magnitude to Units 2b and 3 in the southern block. In the northern block, the age of Unit 1 extends to 5 to 7 Ma. This indicates that Unit 1 started to accumulate in the northern part earlier than the southern part.

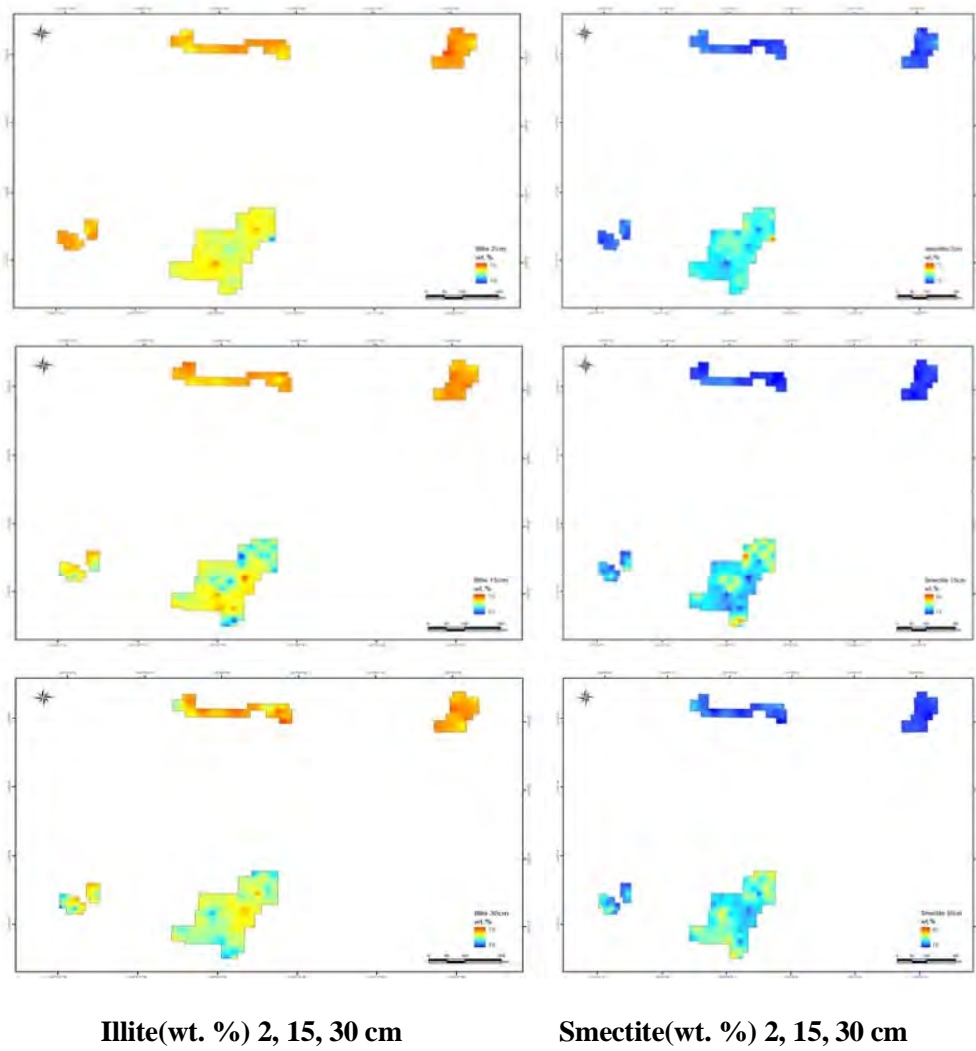


*Figure 50. Illite and Smectite Content Variation with Depth*

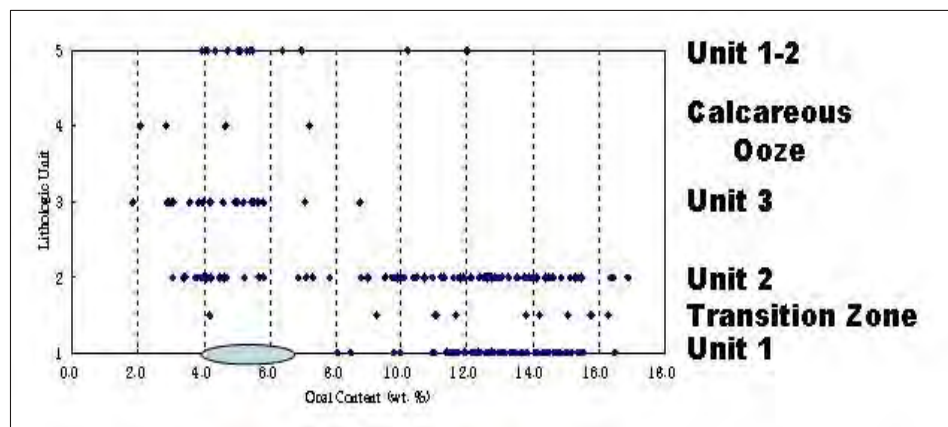


*Figure 51. Opal Content Variations in Each Lithological Unit*

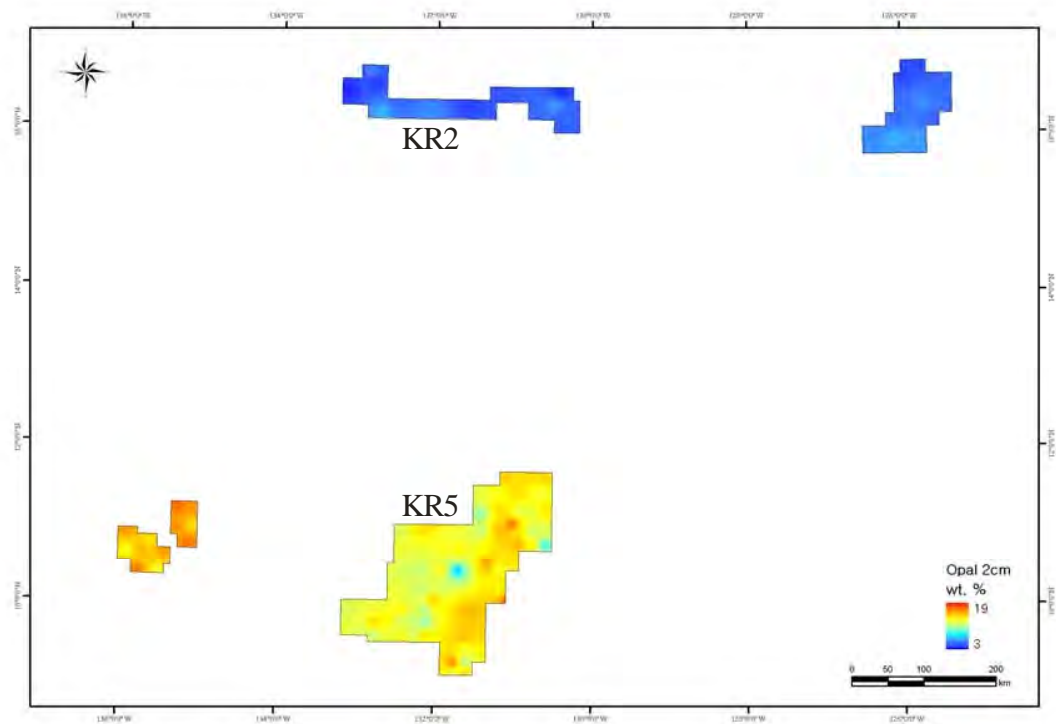


*Figure 52. Opal Content of Surface Sediments*

#### 7.4.5 Chemical Composition

Units 1 and 2a are similar in major elemental composition, but metal (Mn, Ni and Zn) contents are slightly higher in Unit 1 than in Unit 2. These two rock units are clearly differentiated by Ni/Cu ratios, where the Ni/Cu ratios of Unit 1 are significantly higher than those of Unit 2a. Units 2b and 3 have very high Mn, Ni, Cu, Zn, Fe and rare earth element contents compared to the other two overlying units (Table 13).

**Table 13. Average Composition of Lithological Units**

|                                    | Unit I       |      |    | Unit 2a      |      |    | Unit 2b      |      |    | Unit 3       |      |    |
|------------------------------------|--------------|------|----|--------------|------|----|--------------|------|----|--------------|------|----|
|                                    | Mean         | std. | N  |
| Major elements (wt.%)              |              |      |    |              |      |    |              |      |    |              |      |    |
| <i>Na<sub>2</sub>O</i>             | -            | -    | -  | -            | -    | -  | -            | -    | -  | -            | -    | -  |
| <i>MgO</i>                         | <b>3.09</b>  | 0.32 | 78 | <b>2.95</b>  | 0.4  | 72 | <b>4.33</b>  | 0.4  | 11 | <b>3.58</b>  | 0.50 | 56 |
| <i>Al<sub>2</sub>O<sub>3</sub></i> | <b>11.36</b> | 1.22 | 78 | <b>11.94</b> | 1.3  | 72 | <b>14.90</b> | 1.1  | 11 | <b>10.84</b> | 1.81 | 56 |
| <i>K<sub>2</sub>O</i>              | <b>2.45</b>  | 0.33 | 78 | <b>2.52</b>  | 0.4  | 72 | <b>3.13</b>  | 0.2  | 11 | <b>2.18</b>  | 0.35 | 56 |
| <i>CaO</i>                         | <b>1.14</b>  | 0.12 | 78 | <b>1.03</b>  | 0.1  | 72 | <b>1.99</b>  | 0.5  | 12 | <b>1.69</b>  | 0.36 | 56 |
| <i>MnO</i>                         | <b>0.55</b>  | 0.11 | 78 | <b>0.15</b>  | 0.1  | 72 | <b>0.23</b>  | 0.1  | 12 | <b>1.43</b>  | 0.92 | 56 |
| <i>Fe<sub>2</sub>O<sub>3</sub></i> | <b>5.66</b>  | 0.71 | 78 | <b>5.90</b>  | 0.8  | 72 | <b>8.63</b>  | 0.7  | 11 | <b>6.96</b>  | 1.75 | 56 |
| <i>TiO<sub>2</sub></i>             | <b>0.50</b>  | 0.06 | 78 | <b>0.53</b>  | 0.1  | 72 | <b>0.64</b>  | 0.0  | 11 | <b>0.47</b>  | 0.08 | 56 |
| <i>P<sub>2</sub>O<sub>5</sub></i>  | <b>0.32</b>  | 0.08 | 78 | <b>0.26</b>  | 0.0  | 72 | <b>0.79</b>  | 0.2  | 12 | <b>0.58</b>  | 0.21 | 56 |
| Trace Elements (ppm)               |              |      |    |              |      |    |              |      |    |              |      |    |
| <i>Sc</i>                          | <b>15</b>    | 2.02 | 29 | <b>15</b>    | 3.4  | 35 | -            | -    | -  | <b>17</b>    | 5.0  | 31 |
| <i>V</i>                           | <b>85</b>    | 8    | 78 | <b>88</b>    | 6.0  | 72 | <b>64</b>    | 7.3  | 12 | <b>90</b>    | 22.6 | 53 |
| <i>Cr</i>                          | <b>46</b>    | 5.16 | 78 | <b>48.9</b>  | 4.6  | 72 | <b>48</b>    | 8.0  | 12 | <b>29</b>    | 8.0  | 53 |
| <i>Co</i>                          | <b>67</b>    | 10.5 | 78 | <b>38.8</b>  | 14   | 72 | <b>27</b>    | 13   | 12 | <b>108</b>   | 68.5 | 53 |
| <i>Ni</i>                          | <b>156</b>   | 39   | 78 | <b>70</b>    | 33   | 72 | <b>114</b>   | 24   | 12 | <b>267</b>   | 112  | 53 |
| <i>Cu</i>                          | <b>406</b>   | 76   | 78 | <b>343</b>   | 87   | 72 | <b>1066</b>  | 123  | 12 | <b>750</b>   | 256  | 53 |
| <i>Zn</i>                          | <b>130</b>   | 33   | 78 | <b>118</b>   | 23   | 72 | <b>229</b>   | 16   | 12 | <b>166</b>   | 54   | 53 |
| <i>Rb</i>                          | <b>126</b>   | 43   | 78 | <b>131</b>   | 43   | 72 | <b>163</b>   | 10   | 12 | <b>116</b>   | 31   | 53 |
| <i>Sr</i>                          | <b>273</b>   | 57   | 78 | <b>242</b>   | 44   | 72 | <b>787</b>   | 185  | 12 | <b>402</b>   | 180  | 56 |
| <i>Y</i>                           | <b>67</b>    | 30   | 63 | <b>55</b>    | 17   | 67 | -            | -    | -  | <b>101</b>   | 42   | 44 |
| <i>Zr</i>                          | <b>161</b>   | 39   | 78 | <b>160</b>   | 33   | 72 | <b>325</b>   | 28   | 11 | <b>176</b>   | 72   | 52 |
| <i>Ba</i>                          | <b>4695</b>  | 2041 | 77 | <b>5358</b>  | 2111 | 72 | <b>8370</b>  | 7588 | 10 | <b>7609</b>  | 3205 | 56 |
| <i>La</i>                          | <b>39</b>    | 6.93 | 57 | <b>43</b>    | 5.5  | 45 | <b>121</b>   | 52   | 12 | <b>94</b>    | 28   | 22 |
| <i>Ce</i>                          | <b>71</b>    | 8.17 | 57 | <b>78</b>    | 8.6  | 45 | <b>104</b>   | 25   | 12 | <b>83</b>    | 16   | 22 |
| <i>Pr</i>                          | <b>13</b>    | 2.62 | 57 | <b>14</b>    | 1.8  | 45 | <b>40</b>    | 13   | 12 | <b>32</b>    | 10   | 22 |
| <i>Nd</i>                          | <b>54</b>    | 11   | 57 | <b>56.9</b>  | 7.4  | 45 | <b>172</b>   | 58   | 12 | <b>135</b>   | 46   | 22 |
| <i>Sm</i>                          | <b>13</b>    | 2.83 | 57 | <b>14</b>    | 1.6  | 45 | <b>43</b>    | 14   | 12 | <b>32</b>    | 11   | 22 |
| <i>Eu</i>                          | <b>4.3</b>   | 1.37 | 57 | <b>4.7</b>   | 1.2  | 45 | <b>12</b>    | 3.1  | 12 | <b>10</b>    | 2.9  | 22 |

| Cont'd               | Unit I     |      |    | Unit 2a     |      |    | Unit 2b    |      |    | Unit 3     |      |    |
|----------------------|------------|------|----|-------------|------|----|------------|------|----|------------|------|----|
|                      | Mean       | std. | N  | Mean        | std. | N  | Mean       | std. | N  | Mean       | std. | N  |
| Trace Elements (ppm) |            |      |    |             |      |    |            |      |    |            |      |    |
| <b>Gd</b>            | <b>14</b>  | 3.80 | 57 | <b>15</b>   | 2.6  | 45 | <b>51</b>  | 15   | 12 | <b>36</b>  | 13   | 22 |
| <b>Tb</b>            | <b>2.3</b> | 0.72 | 57 | <b>2.4</b>  | 0.5  | 45 | <b>7</b>   | 2.3  | 12 | <b>5.8</b> | 1.8  | 22 |
| <b>Dy</b>            | <b>13</b>  | 3.58 | 57 | <b>13.5</b> | 2.3  | 45 | <b>42</b>  | 14   | 12 | <b>32</b>  | 11   | 22 |
| <b>Ho</b>            | <b>2.6</b> | 0.90 | 57 | <b>2.7</b>  | 0.6  | 45 | <b>8</b>   | 2.5  | 12 | <b>6.4</b> | 2.0  | 22 |
| <b>Er</b>            | <b>7.1</b> | 2.01 | 57 | <b>7.4</b>  | 1.3  | 45 | <b>22</b>  | 7.3  | 12 | <b>18</b>  | 5.3  | 22 |
| <b>Tm</b>            | <b>1.0</b> | 0.28 | 57 | <b>1.1</b>  | 0.2  | 45 | <b>3</b>   | 1.1  | 12 | <b>2.4</b> | 0.7  | 22 |
| <b>Yb</b>            | <b>6.5</b> | 1.59 | 57 | <b>6.8</b>  | 0.9  | 45 | <b>18</b>  | 6.5  | 12 | <b>15</b>  | 4.3  | 22 |
| <b>Lu</b>            | <b>1.0</b> | 0.27 | 57 | <b>1.1</b>  | 0.2  | 45 | <b>2.7</b> | 0.9  | 12 | <b>2.3</b> | 0.6  | 22 |
| <b>Hf</b>            | <b>3</b>   | 0.33 | 42 | <b>3</b>    | 0.3  | 40 | -          | -    | -  | <b>4</b>   | 0.5  | 13 |
| <b>Pb</b>            | <b>7.6</b> | 4.98 | 58 | <b>8.3</b>  | 5.7  | 66 | -          | -    | -  | <b>7.0</b> | 7.7  | 44 |

## 7.5 Discussion

### 7.5.1 Topography and Nodule Genesis

As discussed in Section 7.3, the northern block (KR2) is dominated by hydrogenetic nodules, while the southern block (KR5) is dominated by diagenetic nodules. Piper and Blueford (1982) and Usui *et al.* (1987) suggested that hydrogenetic nodules are abundant on and around hills such as seamounts, while diagenetic nodules dominate in abyssal plain areas. At a regional scale, the distribution of nodules with different origins agrees well with their suggestion; hydrogenetic nodules in KR2 are found in relatively uneven areas, while the diagenetic nodules in KR5 occur on relatively flat areas.

However, on a more local scale, the central part of KR5 block shows a distribution pattern that opposes this trend. The central part of KR5 shows more hydrogenetic nodule characteristics – closer to those of the northern block – than the eastern and western parts of KR5, but topographically the eastern and western parts show more resemblance to the northern block. Therefore, it requires a more detailed study to understand nodule genesis in terms of topography.

### 7.5.2 Sedimentation Rate and Nodule Genesis

Von Stackelberg and Beiersdorf (1991) suggested that the manganese nodule facies shows low nodule abundance and low metal (Cu+Ni+Co) grade in the northern part, but high abundance and grade in the south close to the highly productive equatorial zone. For consideration of this aspect, metal content and abundance of nodules should be dealt with separately, because high nodule abundance does not correspond to high metal grade in the study area. The metal content of nodules is generally high and abundance low in the southern block, which is dominated by diagenetic processes, and metal content is low and abundance high in the northern block, which is dominated by hydrogenetic process. A similar situation is apparent for nodule abundance within the KR5 area, in which the central part, with high nodule abundance, shows lower metal contents than the eastern and western parts of the block.

In terms of average sedimentation rate, the northern block, further away from the equator, shows three to four times higher sedimentation rates since 7 Ma. Prior to 7 Ma, the sedimentation rates were identical in both blocks within the time frame analyzed in this study. This unexpected trend is likely due to the dissolution of dissolution-prone biogenic components in the southern block, supported by a rapid drop in opal content with depth, and higher supply of aeolian dust that is resistant to dissolution in the northern block, supported by proximity to the source area. Thus, it is difficult to discuss the effect of sedimentation rates on nodule genesis where sedimentation has been affected by dissolution processes. With respect to organic matter supply, it is reasonable to consider that the southern block, closer to the highly productive equatorial zone, experiences higher sedimentation rates than the northern block. So, the higher metal contents of nodules in the southern block in this study are consistent with von Stackelberg and Beiersdorf's (1991) suggestion. However, the nodule abundance seems to disagree with their suggestion, because the northern block and the central part of KR5 are characterized by relatively metal poor nodules and exhibit higher nodule abundances.

### **7.5.3 Sediment Composition and Nodule Genesis**

Von Stackelberg and Beiersdorf (1991) attributed the occurrence of metal-rich nodules to the higher supply of organic matter. Careful examination of the sediment distribution and composition of the study blocks suggests that the flux of organic matter to the seafloor is a potential controlling factor of nodule genesis. This possibility is considered in two aspects – the thickness of Unit 1 and the metal-rich chemical composition of Units 2b and 3.

Metal-poor Unit 1 is generally thicker in the northern block than in the southern block. If metals are supplied from the sediment column and not from decomposition of organic matter at the seabed, as suggested by von Stackelberg and Beiersdorf (1991), the metals are likely derived from the deeper lying metal-rich Units 2b and 3 rather than the metal-poor Unit 1, which is in contact with the nodules. If this is true, the presence of Unit 1 will prevent the supply of metals to be remobilized from Units 2b and 3 to the surface by precipitating micro-nodules, which are ubiquitous in Unit 1. This is consistent with our observation that metal-rich nodules in the southern block have a thin Unit 1 and metal-poor nodules in the northern part have a thick Unit 1. So, we suggest the thickness of Unit 1 is a potential controlling factor of genesis for nodules distributed in the study blocks. Unfortunately, this process does not explain the low metal content of nodules in the central part of KR5, which may be controlled by processes suggested by previous studies. Moreover, the thickness of Unit 1 does not show any coherent pattern with nodule abundance either. This indicates that there must be other processes affecting nodule abundance and genesis, which require further detailed study.

## **7.6 Conclusions**

For a better understanding of factors controlling nodule genesis, two blocks (KR2 and KR5), located in the southern ( $9^{\circ}$  N –  $11^{\circ}$  N) and northern ( $16^{\circ}$  N –  $17^{\circ}$  N) parts of the CCZ between  $130^{\circ}$  W –  $133^{\circ}$  W meridians were investigated with respect to nodule and sediment characteristics.

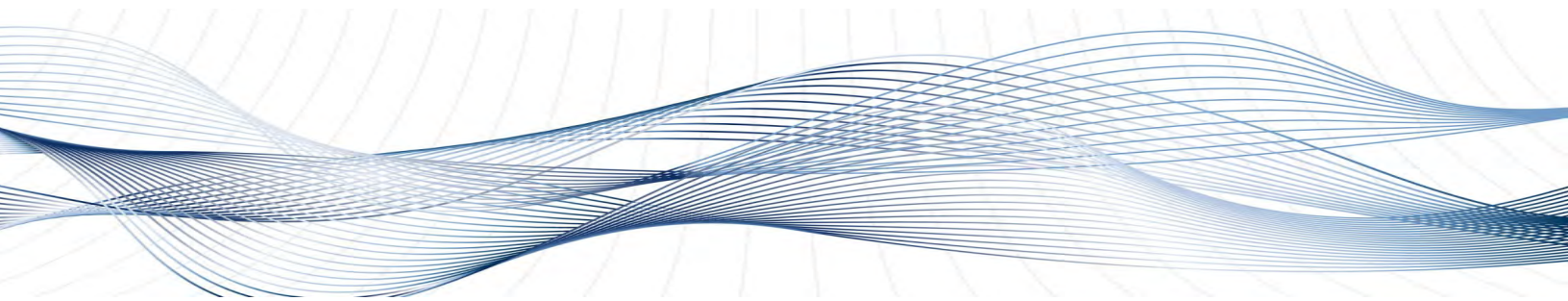
The northern block (KR2) is dominated by hydrogenetic nodules. In contrast, the southern block (KR5) is dominated by diagenetic nodules. The northern block is characterized by a thick metal-poor Unit 1, while, Unit 1 is thin in the southern block, which places metal-rich Units 2b and 3 close to the surface.

Despite discrepancies in detail, the distribution of different nodule genetic types in the northern and southern blocks can be explained by variations in topography and sedimentation rate. It is known that hydrogenetic nodules formed preferentially in areas with high topographic variation and low

sedimentation rates, consistent with dominant nodule types and geological settings found in the northern block. Diagenetic nodules are known to be formed preferentially in flat abyssal areas with high sedimentation rates. The southern block has a geological setting more conducive to diagenetic nodule formation than the northern block.

The nodule distribution in the study blocks might also be explained by the distribution of metal-poor Unit 1 and metal-rich Units 2b and 3. The northern block with a thicker Unit 1 has more abundant hydrogenetic nodules. This might be due to the role of Unit 1 in preventing the supply of metals remobilized from underlying metal-rich Units 2b and 3 to reach the seabed where the nodules are forming.

## 8. BATHYMETRY AND SEDIMENTATION IN THE COMRA CONTRACT AREA



### 8.1 Bathymetry

#### 8.1.1 Sources of Data

The bathymetry of the China Ocean Mineral Resources R&D Association (COMRA) pioneer investor area, including its exclusive exploration area designated by contract with the International Seabed Authority, was determined at high resolution using SeaBeam multi-beam echo-sounding systems.

The area explored includes two non-contiguous portions, an East Area (Figure 53) and a West Area (Figure 54). Water depth in the East Area ranges from 3,901.8 m to 5,590.7 m, with a median of 5,170.9 m. The West Area ranges in depth from 2,969.1 m to 5,986.6 m, with a median of 5,182.9 m. The area deeper than 5,300 m covers about 8.5 per cent of the East Area and about 11 per cent of the West Area. The area less than 5,000 m water depth covers about 3.8 per cent of the East Area and about 12.3 per cent of the West Area. That is, water depth in both portions of the COMRA area, is mostly between 5,000 m and 5,300 m (Figures 55 - 56).

#### 8.1.2 Depth Distributions

There are three types of topography in the COMRA area: abyssal hills; seamount chains; and abyssal basins (Figures 53 and 54). Seamount chains are most obvious in the West Area. There are four main seamount chains trending east-west in the West Area. Several seamount chains also occur in the eastern and southwestern parts of the East Area.

### 8.2 Sediment Data Sources

Sediment data from the COMRA area were collected from 1,606 stations by grab samplers; 849 stations are from the East Area and 757 stations from the West Area.

### 8.3 Sediment Types

There are generally four types of surface sediment in the COMRA area, including siliceous clay, siliceous ooze, siliceous-calcareous ooze, and calcareous ooze. Each is discussed in the following sections.

### 8.3.1 Siliceous clay

Siliceous clay is the dominant sediment type in the COMRA area and includes about 65 per cent of the sample station recoveries. The siliceous clay is brown and Filemot (colour of a dry faded leaf). The biogenic silica content is 10-30 per cent, which is composed of radiolarians and diatoms. The median grain size is 8.8-9.0φ. The clay mineral content is less than 70 per cent. The fragmental mineral content is less than 1 per cent. There are frequently agglomerate and cricoid (ring-shaped) structures, which are presumably the cavities and relics of biological activity.

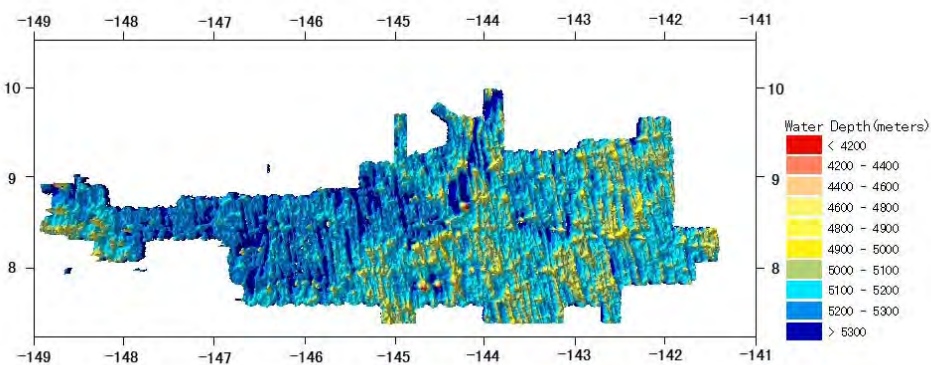


Figure 53. COMRA East Area

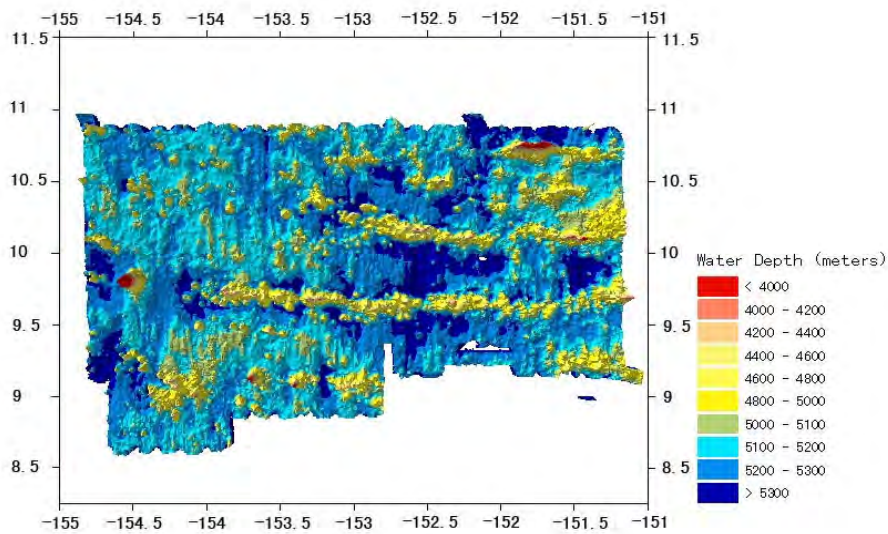


Figure 54. COMRA West Area

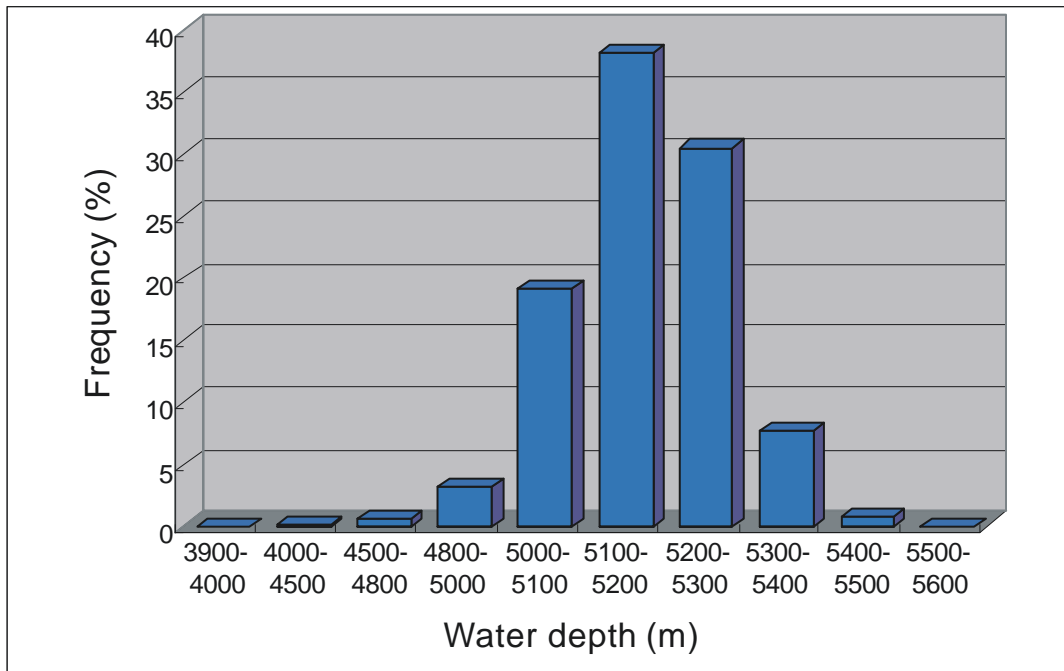


Figure 55. East Area Bathymetry Histogram

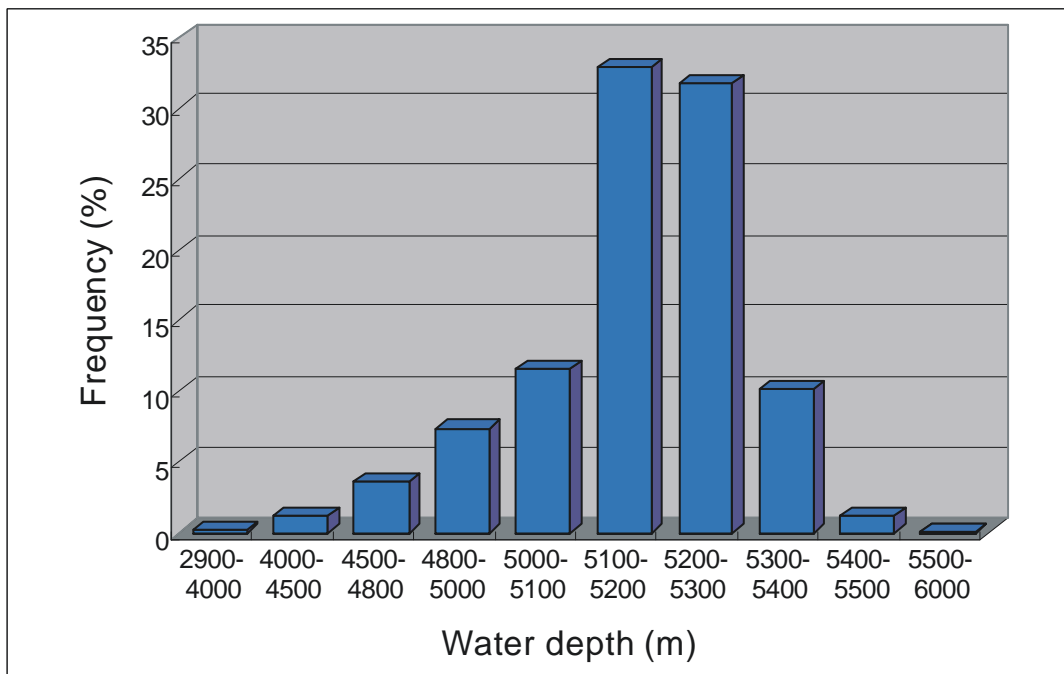


Figure 56. West Area Bathymetry Histogram

### **8.3.2 Siliceous ooze**

Siliceous ooze was found in about 30 per cent of sampled stations in the COMRA area. The colour of siliceous ooze is similar to that of siliceous clay. The biosilica content is 30-50 per cent, which is mostly composed of radiolarian shells, with secondary diatoms, and some sponge spicules and teeth. The clay mineral content is 40-70 per cent, which is mainly illite, accounting for more than 55 per cent of clay minerals. Other clay minerals are montmorillonite, chlorite and kaolinite. The median grain size is 8.5-8.9φ. Agglomerate and cricoid structures occur commonly.

### **8.3.3 Siliceous-calcareous ooze**

Deep yellow – yellow siliceous-calcareous ooze covers 2.3 per cent of sampled stations in the COMRA area. Calcareous shell content is 30-45 per cent and vbiosilica content is 10-25 per cent. The predominant calcareous shells are foraminifera. Clay mineral content is between 40-60 per cent, composed mostly of illite.

### **8.3.4 Calcareous ooze**

Pearl gray to white calcareous ooze ? covers only about 2 per cent of sampled stations in the COMRA area. It is poorly consolidated with low viscosity. Biological calcareous fragments comprise more than 95 per cent of this material. Both foraminifera and nannofossils are major components. The median grain size is 4.3-6.7φ. Clay mineral content is less than 5 per cent, of which illite is 65-70 per cent, montmorillonite is 10-16 per cent%, chlorite is 10-11 per cent, and kaolinite is 10-11 per cent.

## **8.4 Sediment Distributions**

Siliceous sediments, including siliceous clay and siliceous ooze, are the most abundant sedimentary types in the East Area. Siliceous clay covers 72 per cent of the area and siliceous ooze 22 per cent (Figure 57). Siliceous clay is mainly distributed on abyssal hills and plains with an average water depth of 5,096 m. Siliceous ooze is mostly distributed in transitional areas between siliceous clay and calcareous ooze in the southeastern part of the East Area, with an average water depth of 5,094 m. The area of siliceous ooze is a little less than 10,000 km<sup>2</sup>. Calcareous sediment is limited to seamounts in southeastern and western parts of the East Area, with an average water depth of 4,500-4,900 m.

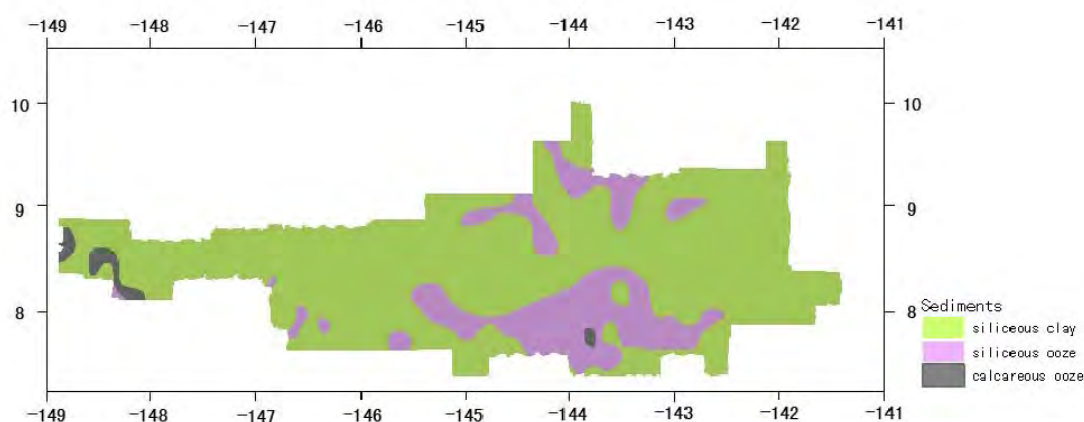


*Figure 57. Sediment Distribution in East Area*

Siliceous sediments cover 70-80 per cent of the seabed in the West Area, a little less than that of the East Area (Figure 58). Siliceous clay is primarily distributed in abyssal basins and hills between seamount chains, with an average water depth of 5,096 m. Siliceous ooze is almost zonally distributed along the margin of basins that trend east-west. Its boundaries with siliceous clay are transitional. Calcareous ooze is distributed on the top of seamounts, and the sizes of areas covered are determined by the abundance of seamounts and seamount chains. Calcareous sediment covers about 5 per cent of the West Area.

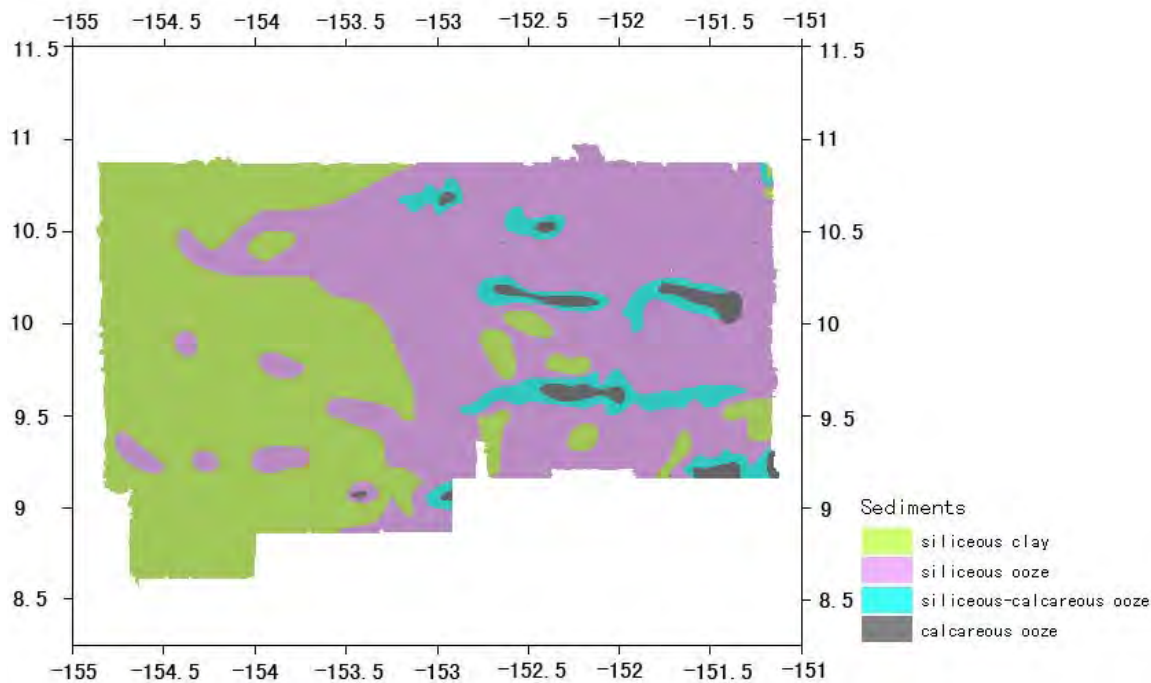


*Figure 58. Sediment Distribution in West Area*

The type of sediment is controlled by both water depth and the production of biosilica. Distribution characteristics of sediments are as follows:

- (1) Vertically, with depth in sediment sections, and with the increase in water depth, types of sediments change from calcareous ooze to siliceous ooze, and then to siliceous clay.
- (2) Horizontally, from east to west and from south to north, biosilica content of sediments decreases with increases of both clay and volcaniclastic content.

## 8.5 Relationships Between Sediment Types and Bathymetry

Calcareous ooze is located on the top of seamounts, and siliceous ooze and clay are distributed in the other regions of the COMRA East area (Figure 59).

In the COMRA West Area, calcareous ooze is located on the top of seamounts, and both siliceous ooze and clay are distributed in the other regions, and the siliceous-calcareous ooze is clearly located between siliceous and calcareous oozes (Figure 60).

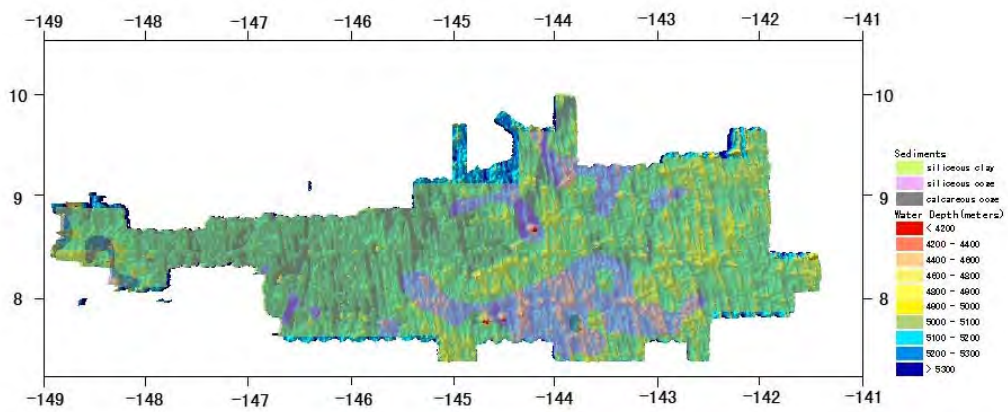


Figure 59. Sediment Type vs. Bathymetry, East Area

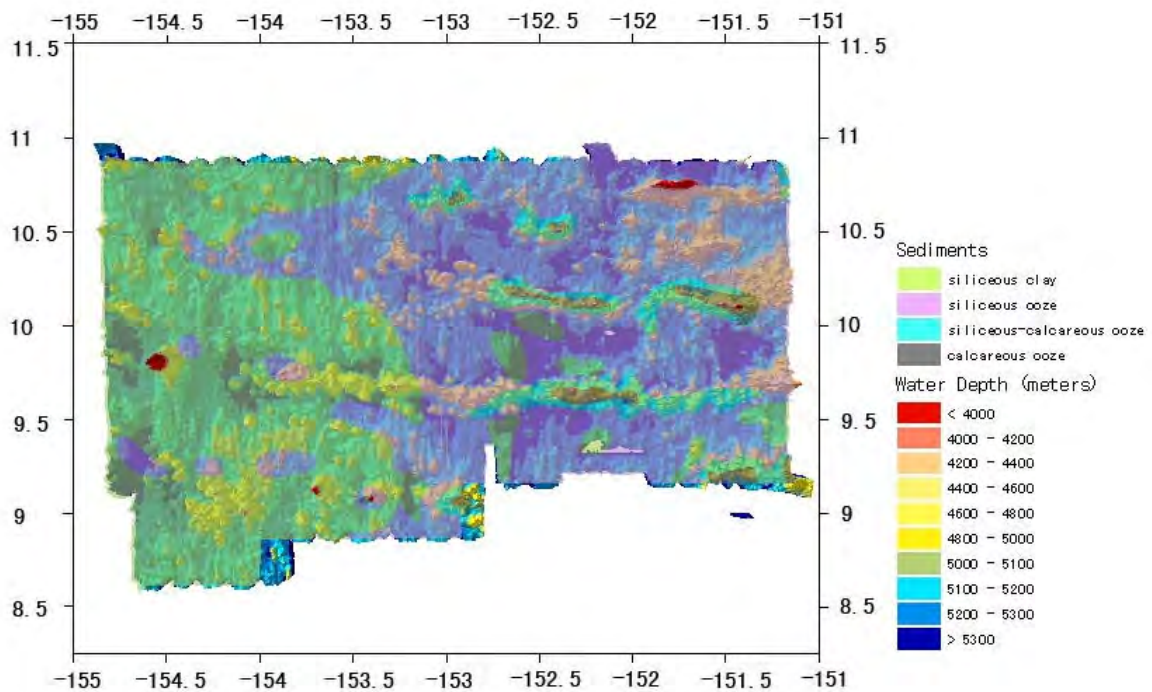
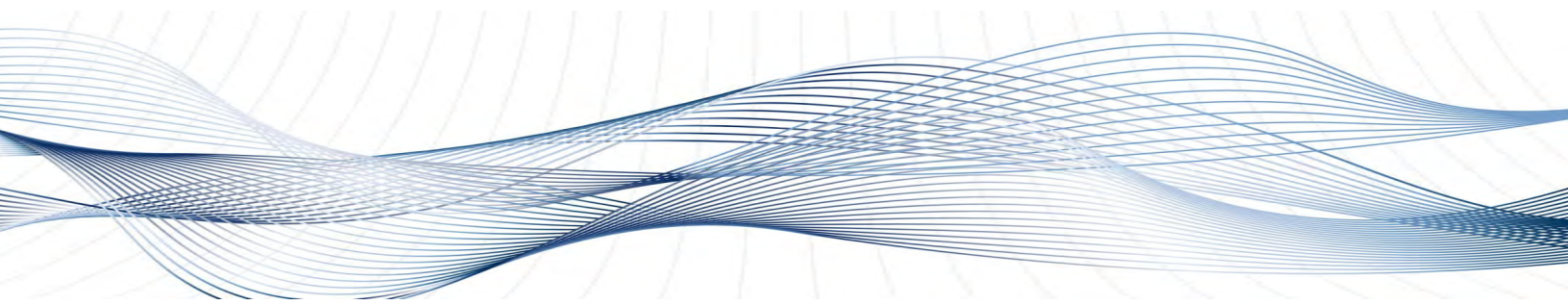


Figure 60. Sediment Type vs. Bathymetry, West Area

## 9. REGIONAL EXAMINATION OF SEDIMENTS



### 9.1 Data Sets and Classification Method

#### 9.1.1 *Data Sets Used*

Data sets were provided to the study by three Contractors in the Area: the IFREMER, France; the Chinese consortium COMRA; and the multi-national consortium IOM. In addition, publically available sediment data within the CCZ study area were downloaded from the U.S. National Geophysical Data Center (NGDC).<sup>1</sup> Table 14 summarizes the particulars of these data sources.

**Table 14. Data Sets Used in Study**

| <i>Source</i>  | <i>File Names</i>   | <i>Number of Stations</i> |
|----------------|---|---------------------------|
| <i>IFREMER</i> | Sed-stations20-28.xls<br>Sed-frotis20-28.xls  | 1,750                     |
| <i>COMRA</i>   | China sediments type.xls  | 951                       |
| <i>IOM</i>     | Depth,nod.abund and sediments(230 stations).xls<br>depth,nodtype and sediment(310 stations).xls | 540                       |
| <i>NGDC</i>    | ArcIMS® ArcView® shape files  | 1,443                     |
| <b>Total</b>   |   | <b>4,684</b>              |

<sup>1</sup>. <http://www.ngdc.noaa.gov/mgg/geolin/geolin.html>

The locations of these stations are shown in Figure 61.

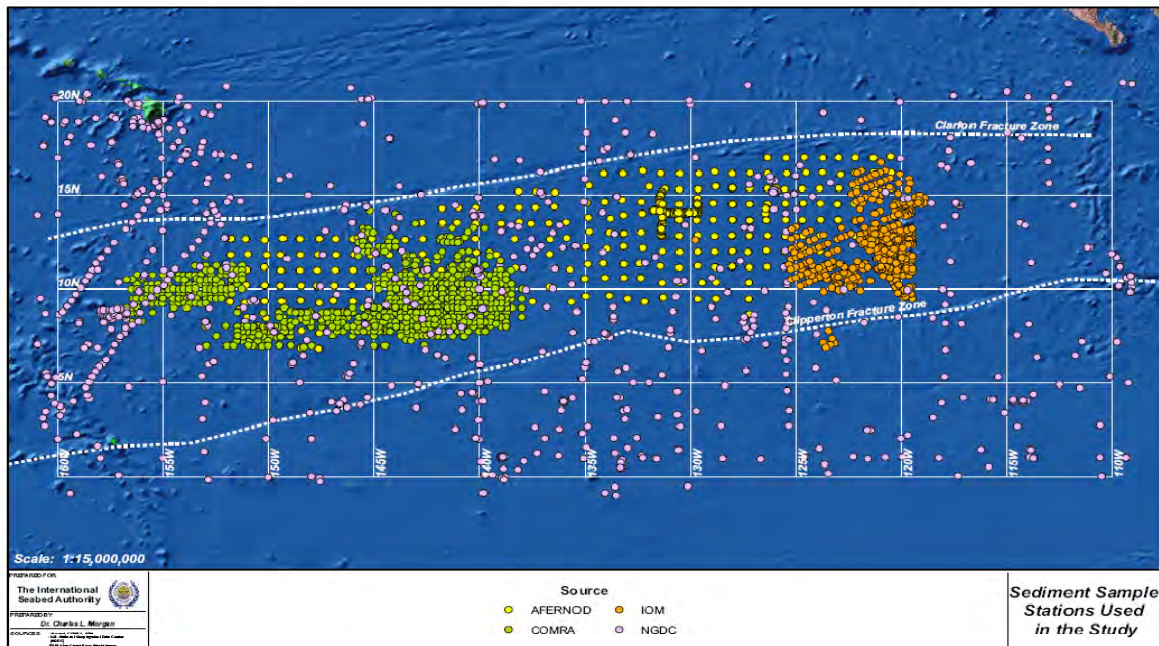


Figure 61. Sediment Sample Stations Used in the Study

### 9.1.2 Classification Method

In order to incorporate these distinct data sets into a single file, it was necessary to simplify the sediment classifications used so that the common features of all data sources provide the basis of the classification. Because most of the data do not include the quantitative percentages of different components, the classification is primarily qualitative. It is summarized in Table 15.

Table 15. Sediment Classification Method Used

| Code | Dominant Constituents       | Criteria (when available)                         |
|------|-----------------------------|---|
| 1    | Ooze, Calcareous            | Dominant Biogenic Carbonate                       |
| 2    | Mud, Calcareous             | Mud ≥ 25%; Biogenic Carbonate ≥ 25%               |
| 3    | Ooze, Calcareous, Siliceous | Dominant Biogenic Carbonates & Bio. Silica; Ca>Si |
| 4    | Mud, Calcareous, Siliceous  | Mud ≥ 25%; Silica ≥ 25%; Carbonate ≥ 25%; Ca>Si   |
| 5    | Mud, Siliceous, Calcareous  | Mud ≥ 25%; Silica ≥ 25%; Carbonate ≥ 25%; Si>Ca   |
| 6    | Ooze, Siliceous, Calcareous | Dominant Biogenic Silica & Carbonates; Si>Ca      |
| 7    | Mud, Siliceous              | Mud ≥ 25%; Biogenic Silica ≥ 25%                  |
| 8    | Ooze, Siliceous             | Dominant Biogenic Silica                          |
| 9    | Mud                         | Grain size < 0.004 mm                             |
| 10   | Mud, Volcanic               | Mud ≥ 25%; Volcanic debris ≥ 25%                  |
| 11   | Silt                        | Grain size 0.004 mm – 0.063 mm                    |
| 12   | Sand                        | Grain size 0.063 mm – 2.00 mm                     |
| 13   | Gravel                      | Grain size > 2.00 mm                              |
| 14   | Large rock or no recovery   |   |

## 9.2 Maps of Sediment Distribution

Using the data set defined above, the following maps were generated to characterize the distribution of sediment types across the CCZ.

Figure 62 shows the distribution of sediment types from the assembled data set. Figure 63 shows a nearest-neighbour extrapolation where the entire area is coloured to indicate the sediment classification of the closest station. Figure 64 shows a kriged interpolation of the fine-grained sediment types (excluding silt, sand and gravel; see Table 15). Since these classifications are gradational, this kind of contouring can generate meaningful results. Figure 65 is a three-dimensional overlay of the contoured sediment values on the bathymetry.

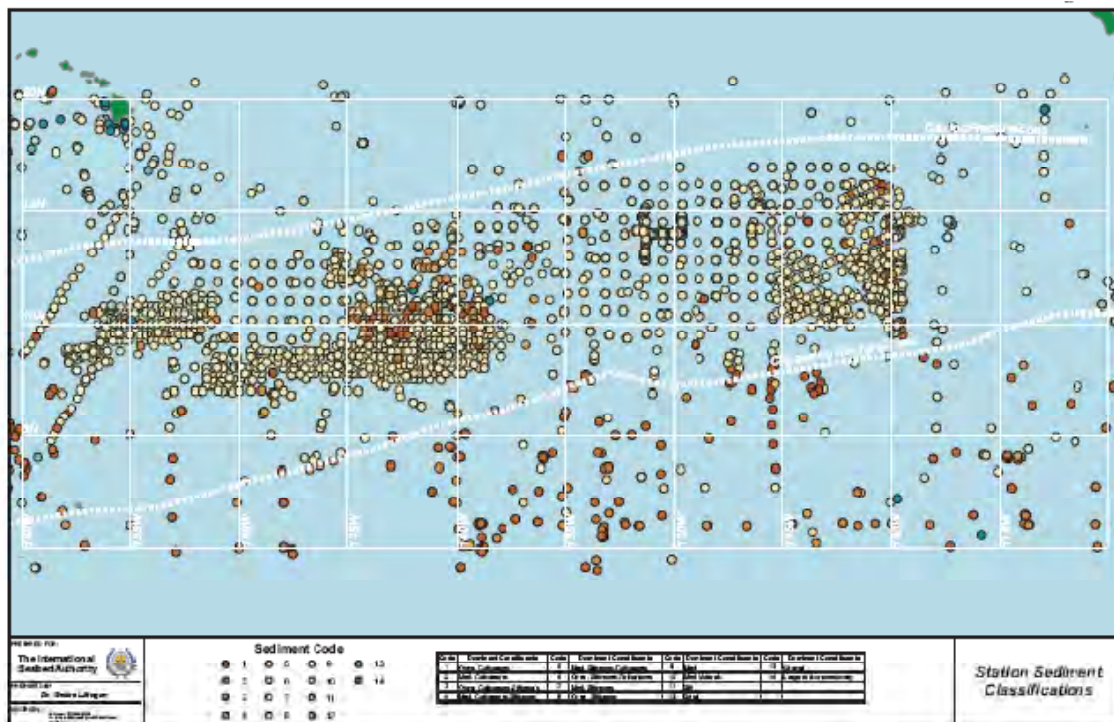
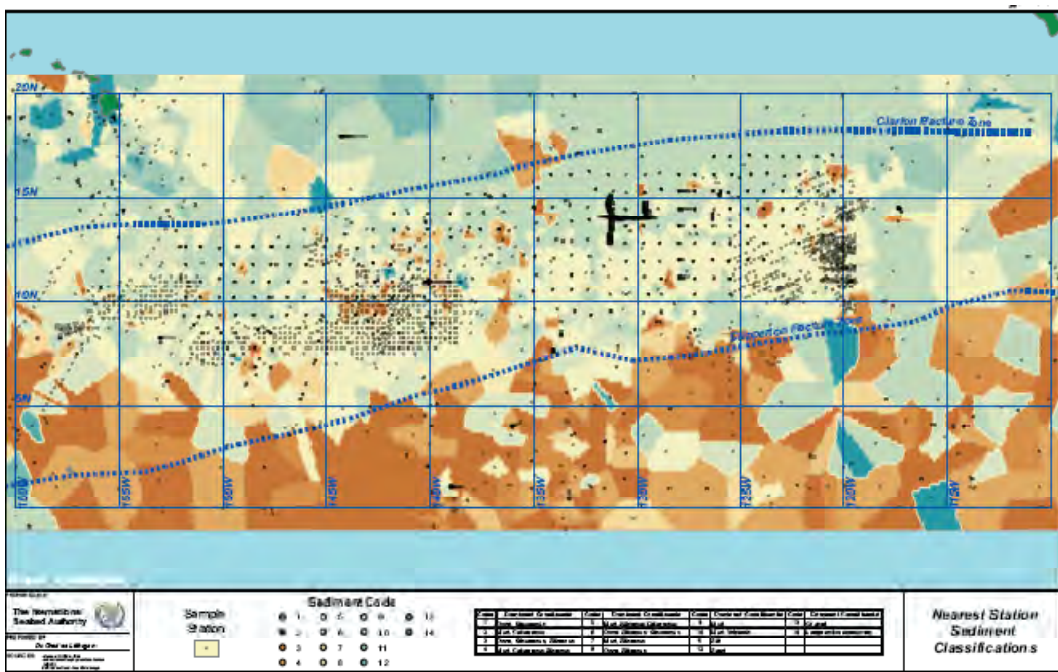
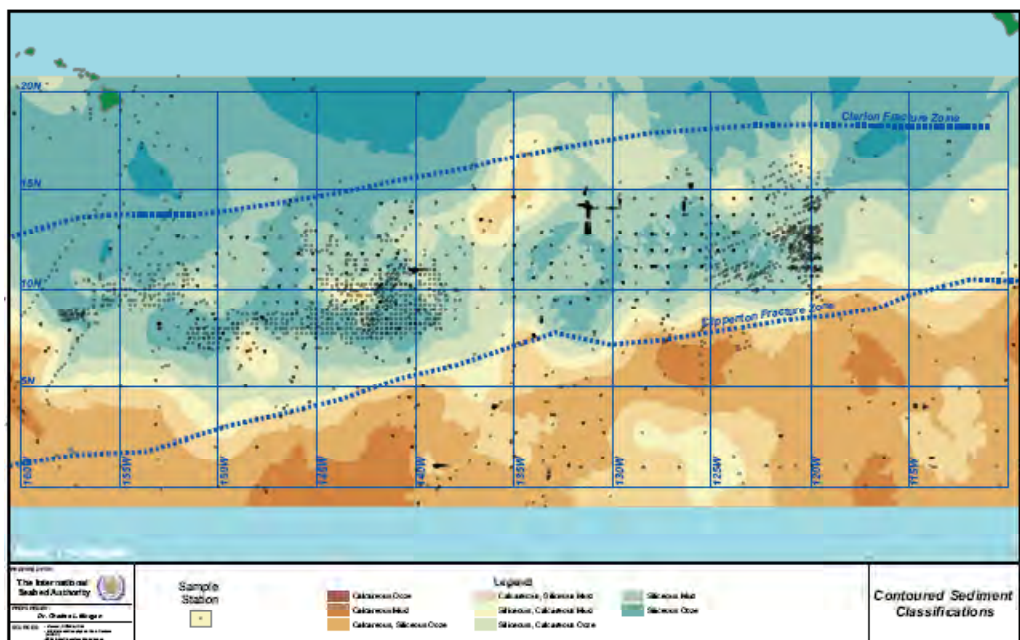


Figure 62. Station Sediment Classifications



*Figure 63. Nearest Neighbour Extrapolation*



*Figure 64. Contours of Fine-Grained Sediments*

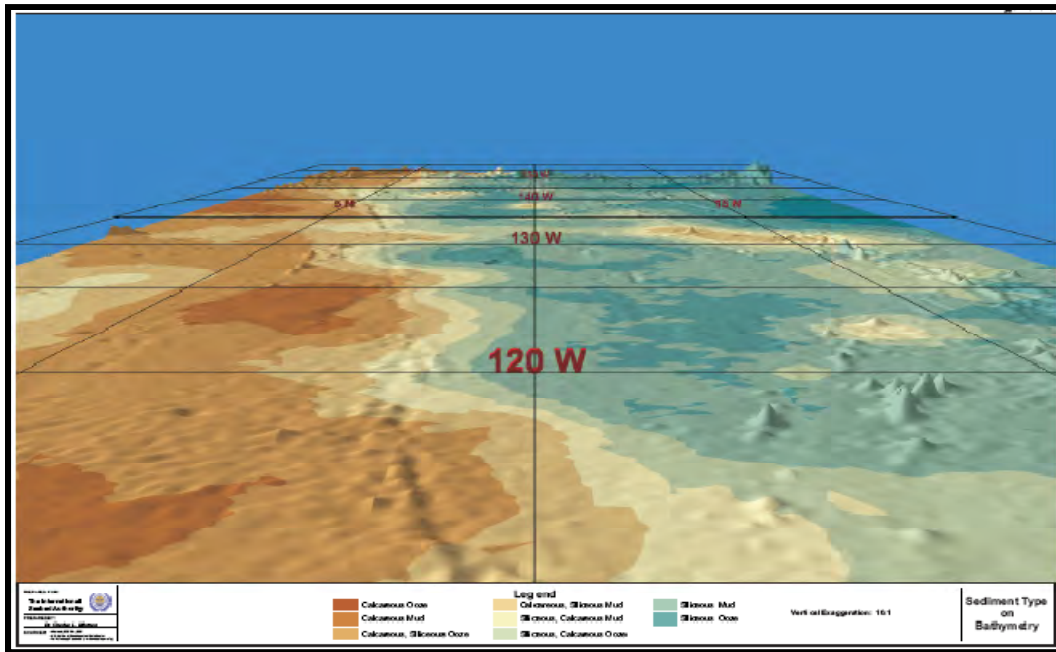


Figure 65. Sediment Distribution and CCZ Bathymetry

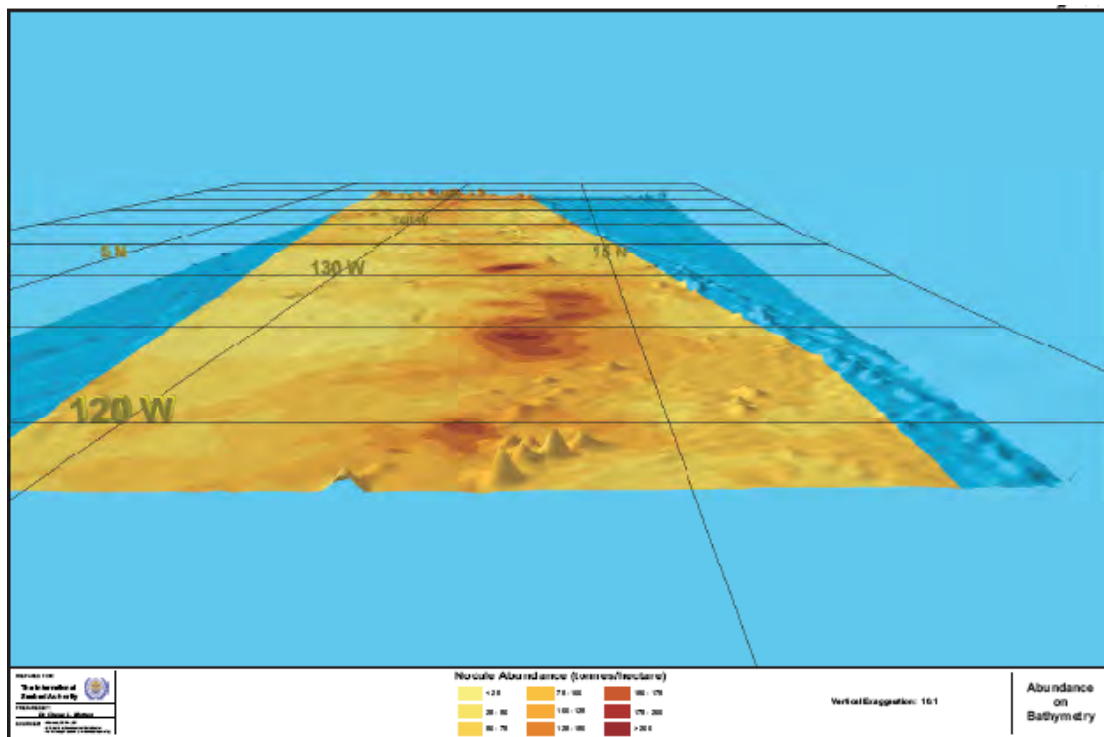


Figure 66. Nodule Abundance and CCZ Bathymetry

### 9.2.1 Relationships with Sediment Types

In order to investigate the relationships between the sediment type and nodule abundance and metal content, sediment type was interpolated for each of the  $0.1^{\circ}$  grid points where nodule data are available. Then, the average metal content and abundance of nodules for each sediment type represented in the data set was calculated. The results of these calculations are presented in Figure 67. These results generally confirm the qualitative conclusions noted by Horn, Horn and Delach (1973) and others for many years, such as that the highest abundances of nodules occur in the siliceous sediments and not in the calcareous sediments. However, somewhat surprisingly on a finer scale, siliceous calcareous muds host the highest abundances and the siliceous oozes have surprisingly low abundances, in contrast to the common knowledge previously assumed by this author.

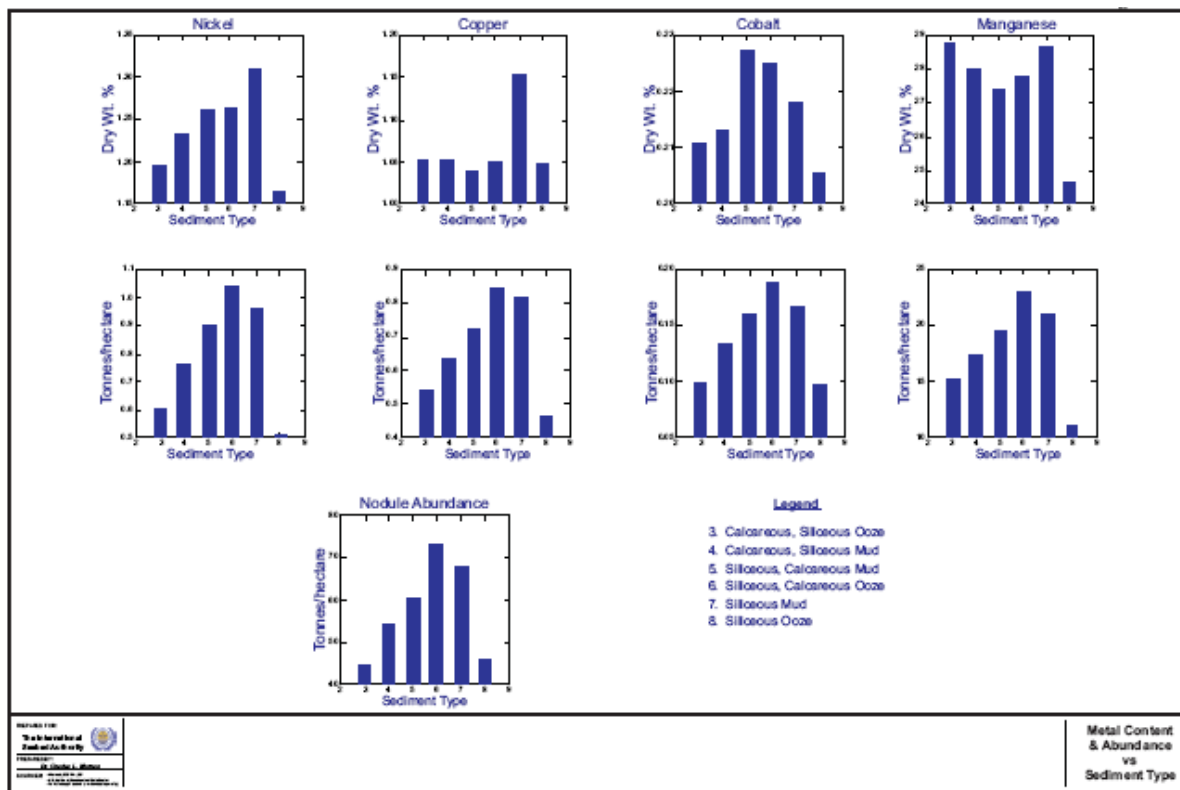
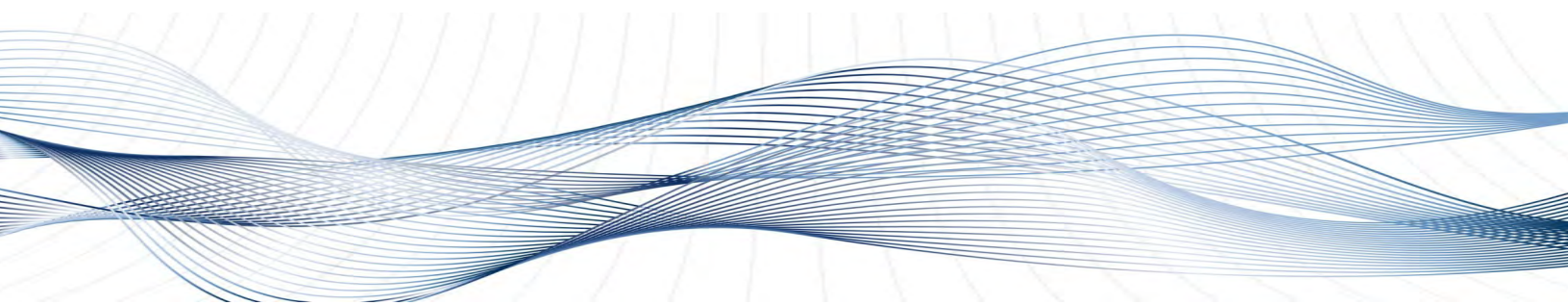


Figure 67. Sediments vs Metal Content and Abundance

# 10. BENTHIC BIOLOGICAL DATA FROM THE CCZ



The flux of particulate organic carbon (POC) is thought to influence the quality and abundance of polymetallic nodules in the CCZ, and is thus a key parameter to be included in geological models of the nodule province. However, direct measurements of POC flux are extremely difficult to obtain. Fortunately, a number of benthic biological parameters appear to be tightly correlated with the flux of POC to the seafloor (for example, Smith *et al.*, 1997), and may thus make suitable proxies for this problematic measurement. These parameters include: (1) abundance and/or biomass of benthic organisms in various size classes; (2) sediment community oxygen consumption (SCOC), or respiration rate of the sediment community; and (3) depth of sediment mixed layer due to bioturbation (for example, Smith and Rabouille, 2002; Smith and Demopoulos, 2003). This chapter attempts to (a) summarize the results of search of public domain for data for each of these parameters in the general region of the CCZ (0 to 31° N; 100 to 160° W); (b) identify geographical gaps in the data set; (c) suggest potentially untapped data resources; and (d) summarize the preliminary trends observed to date.

## 10.1 Available Data

A number of research programmes have sampled the abyssal North Pacific seafloor, many of which collected data for multiple parameters of interest to biogeochemical modeling efforts. The available station locations are plotted on the map in Figure 68. Overall, meiofaunal (63-300 µm) and macrofaunal (300 µm-3 mm) abundances and/or biomass represent the most widely sampled biological parameters in this region, and these data sets also exhibit the greatest consistency in collection methods across field programmes. Most of the faunal abundance data (including meiofauna, macrofauna and megafauna) were collected within, or slightly south of, the CCZ, with another small cluster of samples collected north of the Hawaiian Islands (~30° N, 155° W) available for comparison (Figure 68). The bulk of the SCOC and bioturbation data were collected south of the CCZ, with a comprehensive data set along a longitudinal transect 140°W from the equator to 9°N.

## 10.2 Abundance and Biomass of Benthic Organisms

Meiofaunal sampling sites are well distributed throughout the CCZ. In addition, a few data are available from the mid-Pacific gyre region (MPG, and CLIMAX-II sites). All samples were collected from multi-cores, or from subsamples taken from a 0.25 m<sup>2</sup> box core (or a combination of the two), and preserved in formalin. Most studies quantified total meiofauna (Hecker and Paul 1977; Bernstein *et al.*, 1978; Hecker and Paul, 1979; Snider *et al.*, 1984; Wilson and Hessler, 1987; Renaud-Mornant and Gourbault, 1990; Wilson 1992; KORDI, unpublished data; P. Martinez, unpublished data; Radziejewska *et*

*al.*, 2001), while data from the EqPac sites are restricted to nematode abundance, biomass and diversity (Brown *et al.*, 2001; Lambshead *et al.*, 2002). Data from the DOMES (Hecker and Paul, 1977; Hecker and Paul, 1979), CLIMAX-II (Bernstein *et al.*, 1978), and PRA (Wilson, 1992) sites are problematic due to the use of unusually large sieve sizes ( $\sim 300\text{ }\mu\text{m}$ ). However, additional stations were sampled in close proximity to all these sites, so exclusion of the questionable data should not significantly impact upon modeling efforts.

Macrofauna were also well sampled within the CCZ, and comprehensive data sets are available from Kaplan, EqPac, ECHO-1 and PRA sites (C. Smith, unpublished data; Wilson and Hessler, 1987; Wilson, 1992; Smith *et al.*, 1997; Glover *et al.*, 2002; Smith and Demopoulos, 2003). Most of these studies include abundance data for total macrofauna, although data are also available for specific taxa (especially polychaetes and copepods) (C. Smith, unpublished data; Wilson 1987; Wilson, 1992; Glover *et al.*, 2002). All studies used  $\sim 300\text{ }\mu\text{m}$  sieves and formalin or ethanol fixaton techniques, and measurements appear generally to be comparable. DOMES data also include macrofaunal abundances (Hecker and Paul, 1977; 1979), but sample-washing techniques may have led to large losses, and these data should probably be excluded from modeling efforts, although it is possible that a statistical normalization could allow their inclusion. Again, other programmes have sampled sites adjacent to DOMES stations. Mid-Pacific gyre data are also available for comparison from the CNP, MPG and CLIMAX stations (Hessler and Jumars, 1974; Snider *et al.*, 1984; Smith, 1987), and from the HOT station (polychaetes only, Glover *et al.*, 2002).

Megafaunal abundances are available from four studies, each sampling a different region across the middle of the CCZ ( $\sim 10\text{-}14^\circ\text{ N}$ ,  $120\text{-}145^\circ\text{ W}$ ) (Nichols *et al.*, 1984; Fukushima *et al.*, 2000; Radziejewska and Stoyanova 2000; Hoover and Smith, unpublished Equatorial Pacific data). The most comprehensive of these surveys was conducted by OMCO (Nichols *et al.*). However, variations in equipment used and methods of photo analysis may make comparisons more subjective than with meiofaunal or macrofaunal data.

Data codes (a,b,c,d,e) refer to parameters measured at each station (see legend at bottom). Data are from published literature and ISA contractors.

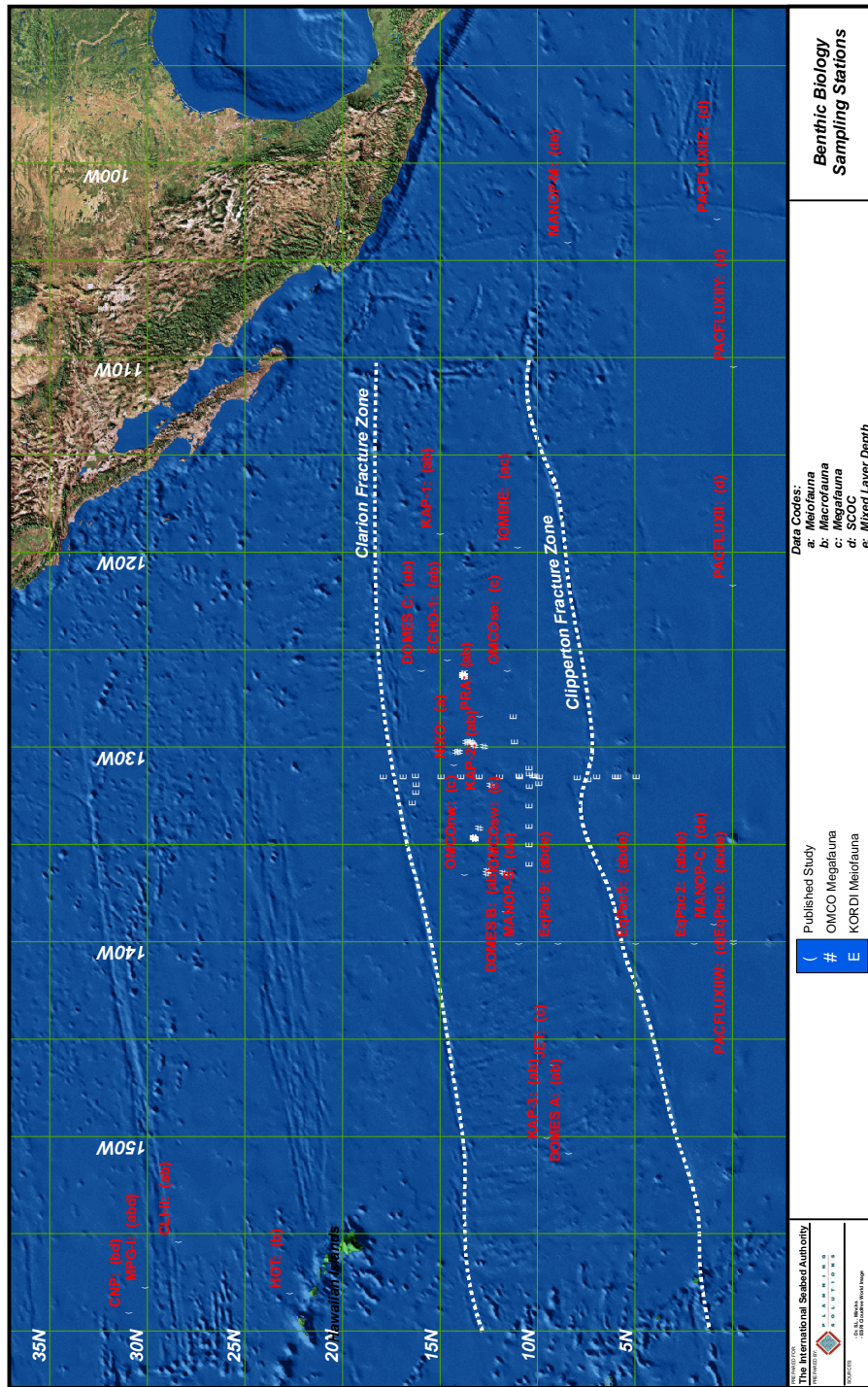


*Figure 68. Map of stations sampled in and around the CCZ*

### 10.3 Geochemical Parameters

Geochemical data are unfortunately not well represented within the boundaries of the CCZ, with the exception of sediment community oxygen consumption (SCOC) rates at EqPac sites along 140° W (Berelson *et al.*, 1994; Hammond *et al.*, 1996) and the MANOP site S (Berelson *et al.*, 1990). Data are widely distributed outside the CCZ, including the mid-Pacific gyre sites (Smith, 1987; Smith *et al.*, 1983; 1992), and the equatorial region south of the CCZ (Berelson *et al.*, 1990; Berelson *et al.*, 1994; Hammond *et al.*, 1996). All these studies collected *in situ* measurements of SCOC using benthic landers. Additional estimates of SCOC modeled from pore water oxygen measurements are also available from MANOP sites C and S (Reimers *et al.*, 1984), the VERTEX station in the mid-Pacific gyre (Murray and Kuivila, 1990), and along a transect from 15° S to 11° N at ~135° W (Martin *et al.*, 1991). Pore water data were also collected well east of the immediate area of primary interest, along a transect from 5° S, 164° W to 8° N, 169° E (Grundmanis and Murray, 1982), as well as at eight stations slightly west of the nodule area (10° N, 90-100° W) (Jahnke *et al.*, 1982). Pore water measurements are considered a less accurate measure of oxygen consumption (for example, Jahnke and Jackson, 1992), but are likely to be roughly comparable to data from benthic landers.

Bioturbation data in and around the CCZ are very scarce, with radiotracer profiles available only at EqPac and MANOP sites C and S (0-9° N, 140° W), and MANOP site M near the continental slope (Cochran, 1985; Smith and Rabouille, 2002). Smith and Rabouille (2002) used published radiotracer data from the EqPac and PACFLUX region (Hammond *et al.*, 1996; Pope *et al.*, 1996) to model bioturbation depths ( $L$ ). Additional values of  $L$  can be modeled from radiotracer data published by Cochran (1985).

### 10.4 Geographical Gaps

Biological data are reasonably well distributed within the CCZ, although increased resolution will certainly enhance model accuracy. For the area of maximum nodule abundance (roughly 13-15° N, 120-125° W), no data exist in the public domain. In addition, biological data are lacking from regions at the west end of the CCZ and along northern and southern boundaries. Geochemical measurements, including sediment respiration and sediment mixed layer depth, are sparse throughout the CCZ.

### 10.5 Preliminary Results

The preliminary examination of the data indicates that, in general, the abundance of these benthic fauna is roughly proportional to the flux of nutrients available in particles settling from the surface.

Figures 69 and 70 present, respectively, estimated export fluxes of carbon and nitrogen from the upper 500 m of the water column. Figures 71 to 75 present simple trend surface planes of observed numerical abundance for the major groups of benthic fauna.

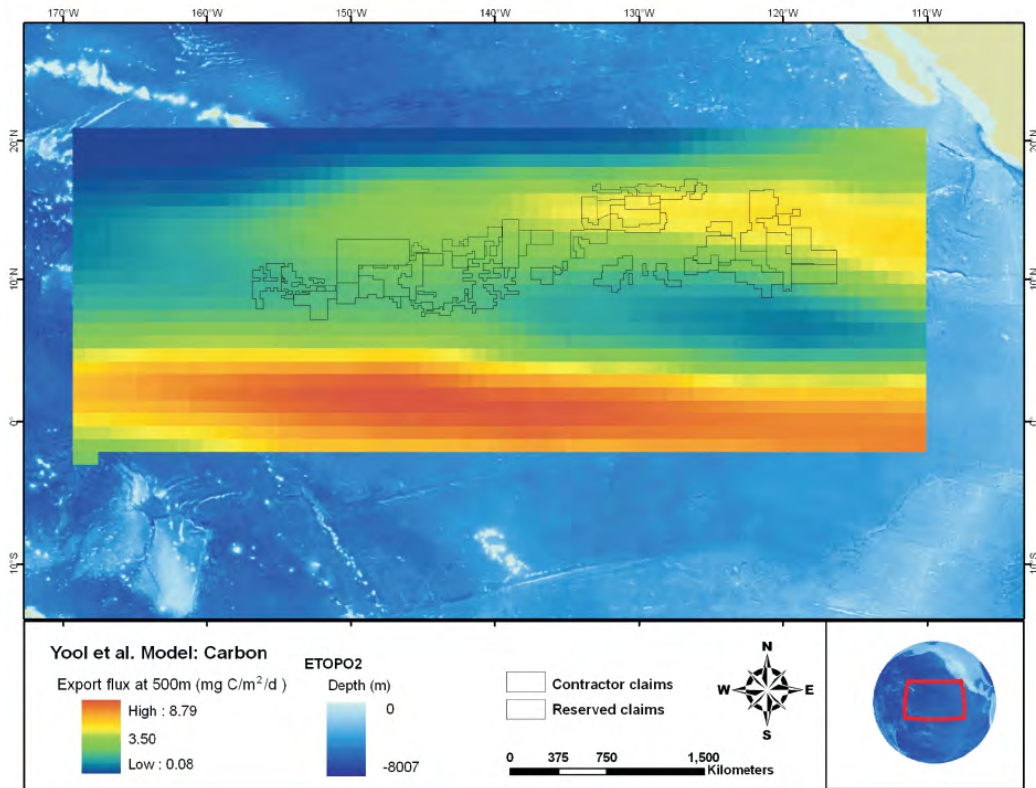


Figure 69. Estimated Carbon Export Flux in the CCZ

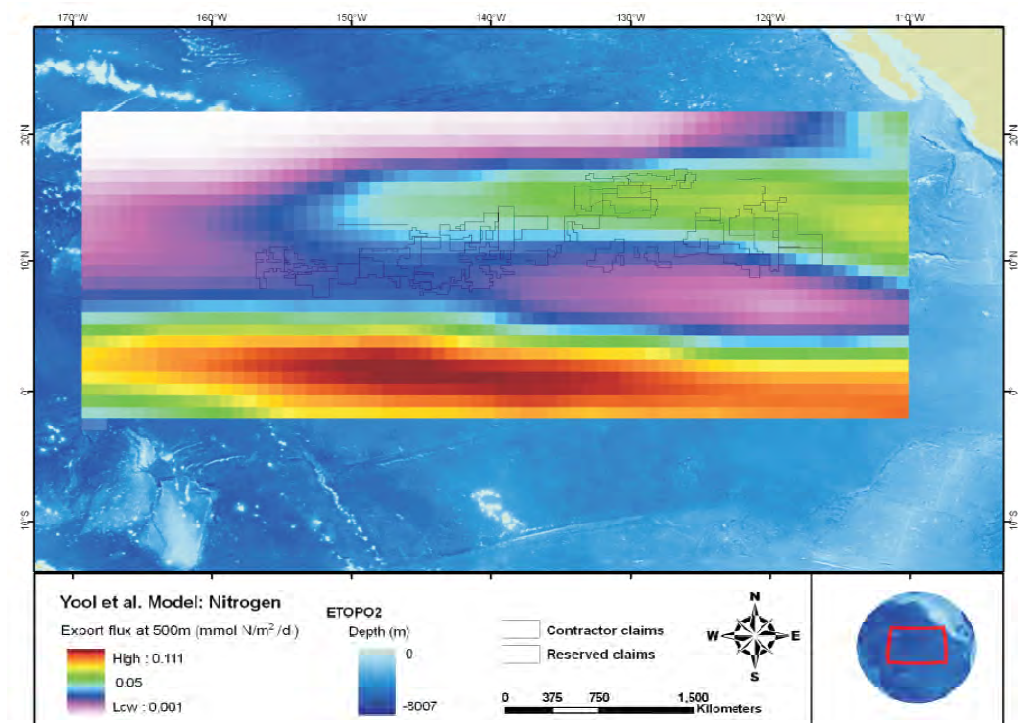
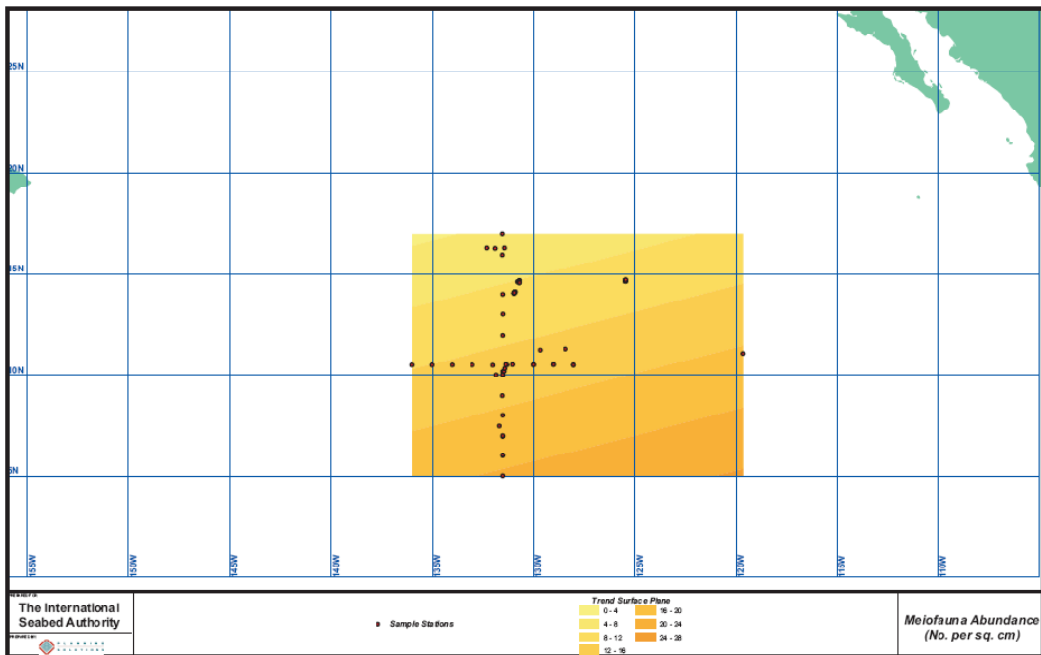
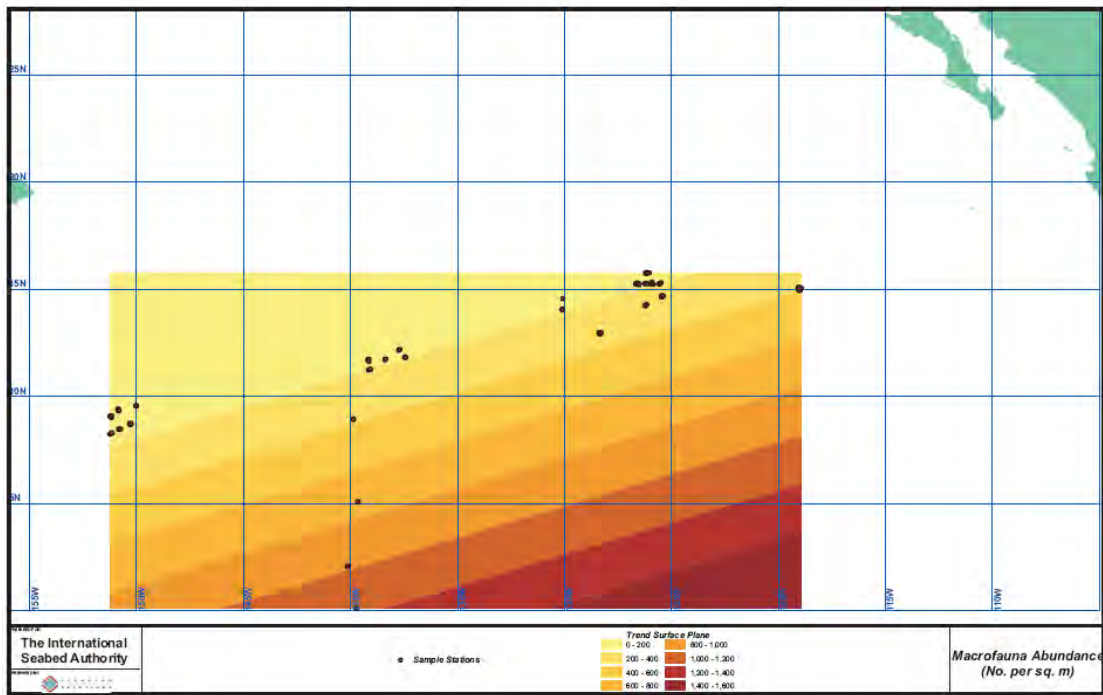


Figure 70. Estimated Nitrogen Export Flux in the CCZ



*Figure 71. Trend Surface Plane, Meiofauna*



*Figure 72. Trend Surface Plane, Macrofauna*

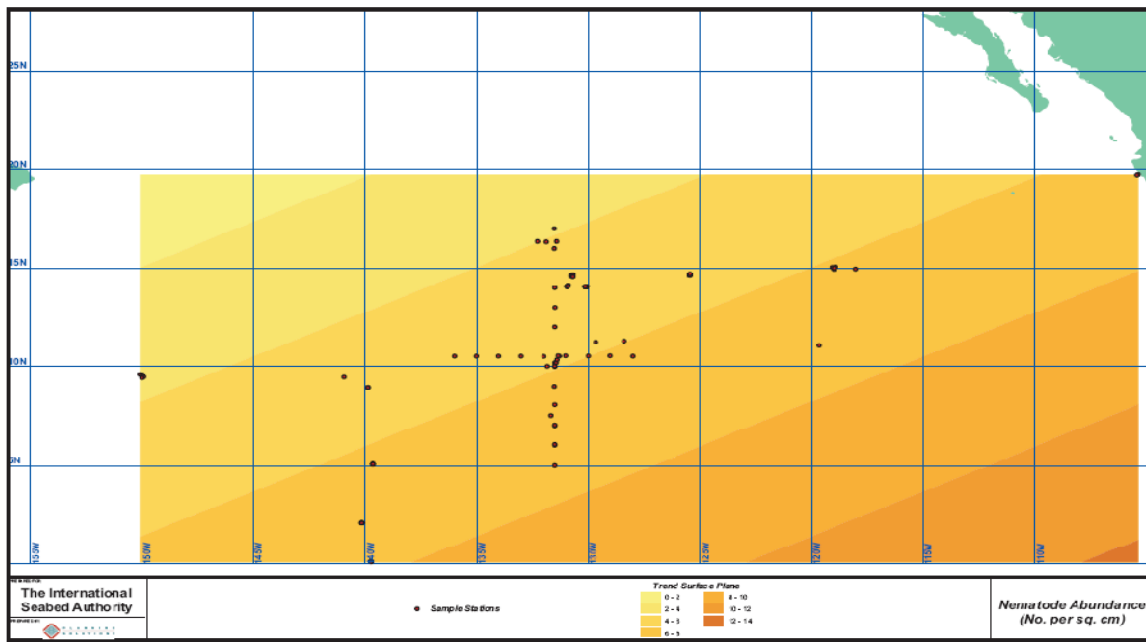


Figure 73. Trend Surface Plane, Nematodes

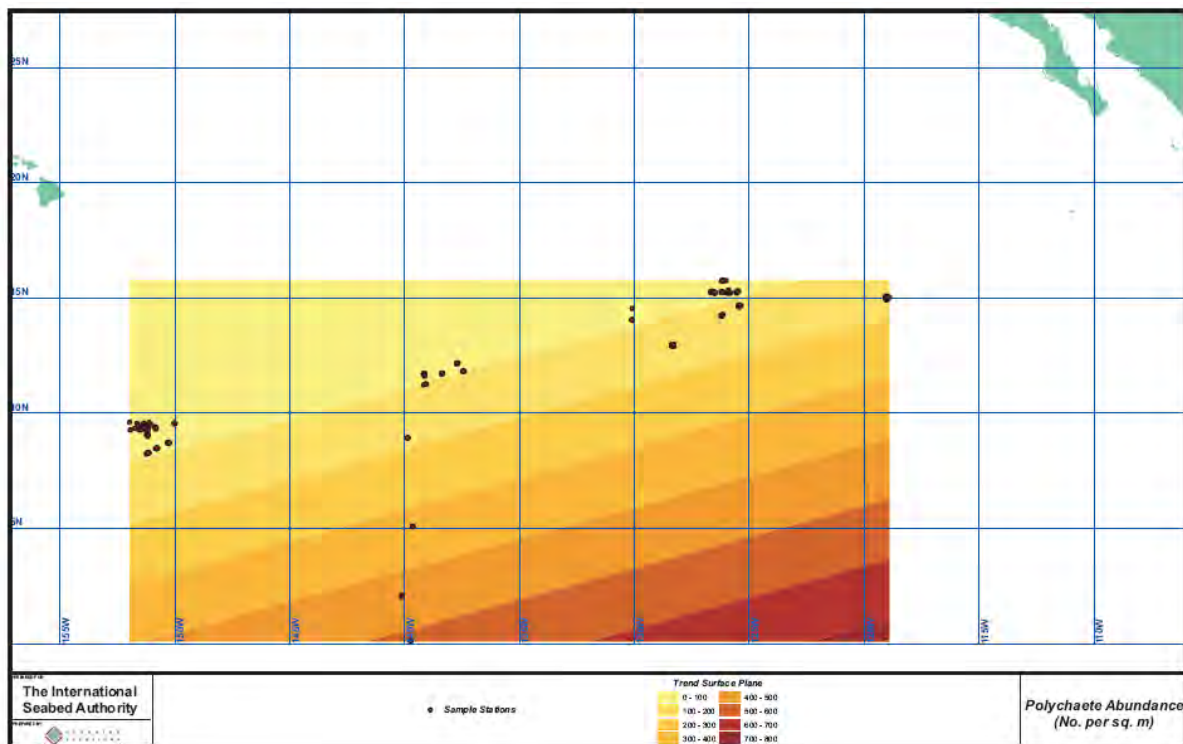


Figure 74. Trend Surface Plane, Polychaetes

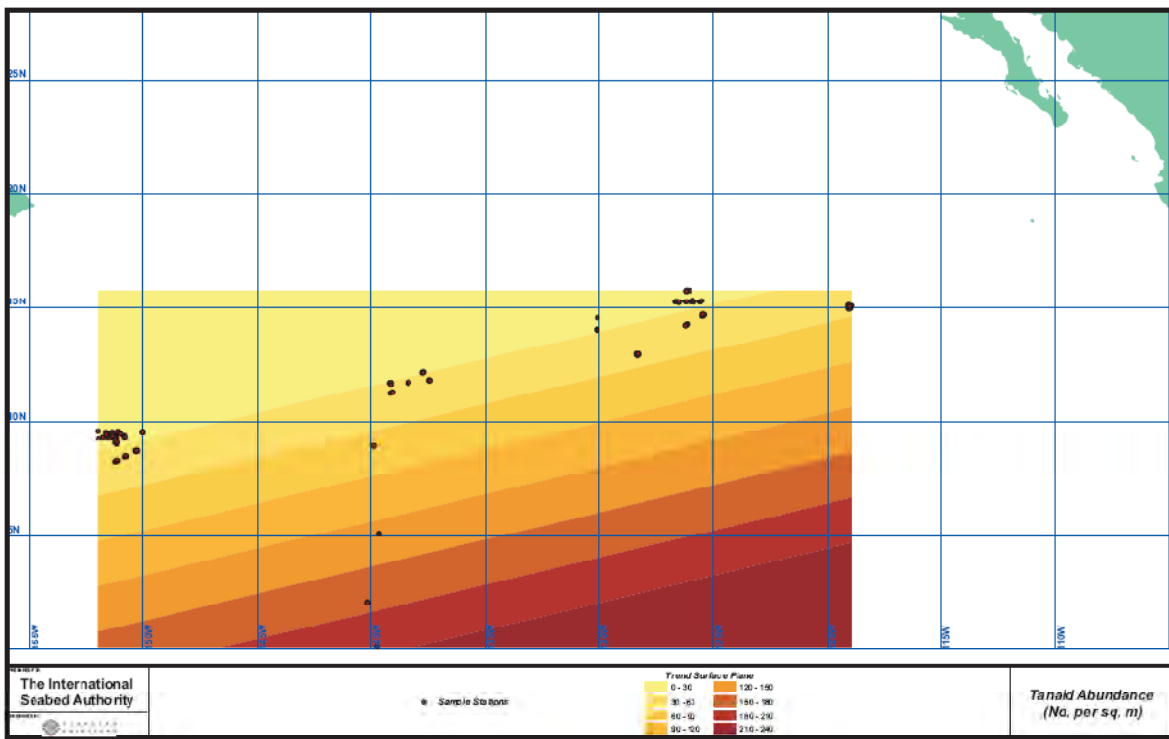
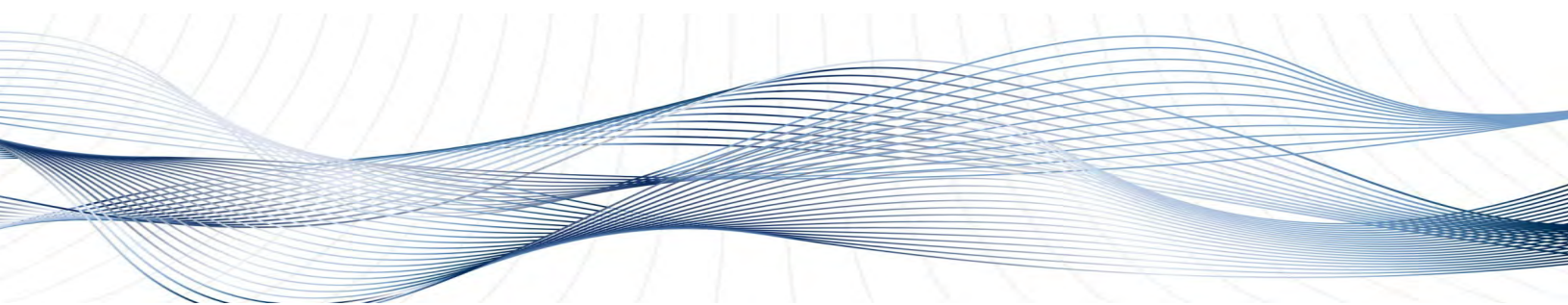


Figure 75. Trend Surface Plane, Tanaids

## 11. REFERENCES CITED



- Baturin, G.N. (1988), *The Geochemistry of Manganese and Manganese Nodules in the Ocean*, D. Reidel Publishing Company, Dordrecht, Boston, Lancaster and Tokyo, 342 p.
- Beiersdorf, H., U. von Stackelberg and M.W. Hombach (2003), 'Scientific challenges related to the development of a geological model for the manganese nodule occurrences in the Clarion-Clipperton Zone (Equatorial North Pacific Ocean)', unpublished report.
- Berelson, W.M. et al. (1994), Dissolution kinetics of calcium carbonate in equatorial Pacific sediments, *Global Biogeochem. Cycles* 8(2), p. 219-235.
- Berelson, W.M. et al. (1990), Benthic fluxes and pore water studies from sediments of the central equatorial north Pacific: Nutrient diagenesis, *Geochim Cosmochim Acta* 54, p. 3001-3012.
- Bernstein, B.B. et al. (1978), Spatial dispersion of benthic Foraminifera in the abyssal central North Pacific, *Limnol Oceanogr* 23(3), p. 401-416.
- Brown, C.J. et al. (2001), Phytodetritus and the abundance and biomass of abyssal nematodes in the central, equatorial Pacific, *Deep-Sea Res* 48, p. 555-565.
- Cochran, J.K. (1985), Particle mixing rates in sediments of the eastern equatorial Pacific: Evidence from  $^{210}\text{Pb}$ ,  $^{239,240}\text{Pu}$  and  $^{137}\text{Cs}$  distributions at MANOP sites, *Geochim Cosmochim Acta* 49, p. 1195-1210.
- Demidova T. (1998), 'The physical environmental in nodule provinces of the deep sea', in *Deep-seabed polymetallic nodule exploration: development of environmental guidelines*, Jamaica, International Seabed Authority, p. 79-116.
- DSDP (1973), *Reports of the Deep Sea Drilling Program*, V. 16, p. 937-949.
- EarthSearch.net (2008) URL:  
<http://www.earthsearch.net/featureIndex.php?type=int&start=2981000&end=2982000>
- Elderfield, H. (1976), Manganese fluxes to the ocean, *Marine Chemistry* 4(2), p. 103-132.
- Fukushima, T., Y. Shirayama and E. Kuboki (2000), The characterization of deep-sea epifaunal megabenthos community two years after an artificial rapid deposition event, *Publ Seto Mar Biol Lab* 39(1), p. 17-27.

- Gardner J.V., W.E. Dean and R.J. Blakely (1984), Shimada Seamount: an example of recent mid-plate volcanism, *Bull. Geol. Soc. Amer.* 95(7), p.855-862.
- Glover, A.G., et al. (2002), Polychaete species diversity in the central Pacific abyss: Local and regional patterns, and relationships with productivity, *Mar Ecol Prog Ser* 240, p. 157-170.
- Golovinskiy, B.I. (1985), *Tectonics of the Pacific Ocean* M., Nedra, 199 p. (In Russian).
- Grundmanis, V., and J.W. Murray (1982), Aerobic respiration in pelagic marine sediments, *Geochim Cosmochim Acta* 46, p. 1101-1120.
- Hammond, D.E. et al. (1996), Early diagenesis of organic material in equatorial Pacific sediments: Stoichiometry and kinetics, *Deep-Sea Research II* 43(4-6), p. 1365-1412.
- Hecker, B. and A.Z. Paul (1977), Benthic base-line survey of the DOMES area, NOAA: 115 p.
- Hecker, B. and A.Z. Paul (1979), Abyssal community structure of the benthic infauna of the eastern equatorial Pacific: DOMES sites A, B, and C, in Bischoff, J.L. and D.Z. Piper (eds.), *Marine Geology and Oceanography of the Pacific Manganese Nodule Province*, Plenum Press, New York, NY, p. 287-308.
- Hessler, R.R. and P.A. Jumars (1974), Abyssal community analysis from replicate box cores in the central North Pacific, *Deep-Sea Res* 21, p. 185-209.
- Horn, D.R., B.M. Horn and M.N. Delach (1973), Copper and Nickel Content of Ocean Ferromanganese Deposits and their Relation to Properties of the Substratein Morgenstein, M. (ed.), *Papers on the Origin and Distribution of Manganese Nodules in the Pacific and Prospects for Exploration*, Hawai'i Institute of Geophysics, University of Hawai'i, 175 p.
- IOM (2005), IOM's review of the implementation of plan of work for exploration for the period 2001-2005 (ISA).
- Jahnke, R.A., S.R. Emerson and J.W. Murray (1982), A model of oxygen reduction, denitrification, and organic matter mineralization in marine sediments, *Limnol Oceanogr* 27(4), p. 610-623.
- Jahnke, R.A. and G.A. Jackson (1992), The spatial distribution of sea floor oxygen consumption in the Atlantic and Pacific Oceans in Rowe, G.T.V. and Pariente (eds.), *Deep-Sea Food Chains and the Global Carbon Cycle*, Kluwer Academic Publishers, Dordrecht, Netherlands, p. 295-307.
- Klitgord, K.D. and J. Mammerickx (1982), Northern East Pacific Rise: Magnetic anomaly and bathymetric framework, *Journal of Geophysical Research*, 87(B8), p. 6725-6750.
- Kotliński R. and M.M. Zadornov (2002), Osobiennosti konkrecijenosnosti wostocznoj czasti polia Klarion-Klipperton (Razwedocznyj rajon SO Interokeanmetall) – International Conference “Minerals of the Ocean”, St. Peterburg, Russian Federation, 2002: 1-5.
- Kotliński, R. (1999), Metallogenesis of the world’s ocean against the background of oceanic crust evolution, *Polish Geological Institute Special Papers* 4, Warszawa, p. 1-70.
- Kotliński, R. (2003), Relationships Between Nodule Genesis and Topography in the Eastern Area of The C-C region, ‘Meeting of Scientists for the Preparation of a Programme of Work for the Development of a Geological Model of the Clarion-Clipperton Fracture Zone’, International Seabed Authority, Nadi, Fiji, 2003.

- Kotliński, R. and V. Stoyanova (2005), Control factors of polymetallic nodules distribution within the Eastern area of the Clarion-Clipperton Zone (CCZ), 'VI ISOPE Ocean Mining Symposium'; Changsha, China, 9-13 October, 2005, pp. 1-11.
- Kotliński, R. and V. Stoyanova (2006), Buried and Surface Polymetallic Nodule Distribution in the Eastern Clarion-Clipperton Zone: Main Distinctions and Similarities, 'AOGS 2006 Conference, Singapore, 2006.
- Kotliński, R. and V. Stoyanova (2005), Control factors of polymetallic nodules distribution within the Eastern area of the Clarion-Clipperton Zone (CCZ), '6th ISOPE Ocean Mining Symposium ; Changsha, China, 9-13 October, 2005, p. 1-11.
- Kotliński, R. and V. Stoyanova (2007), Buried and Surface Polymetallic Nodule Distribution in the Eastern Clarion-Clipperton Zone: Main distinctions and similarities, *Advances in Geosciences* 9, p.67-74.
- Lambshead, P.J.D. et al. (2002), Latitudinal diversity patterns of deep-sea marine nematodes and organic fluxes: A test from the central equatorial Pacific, *Mar Ecol Prog Ser* 236, p. 129-135.
- Lisitsin, A. P. (1978), Processes of oceanic sedimentation, Moscow, *Nauka*, 392 p. (In Russian).
- Martin, W.R. et al. (1991), Benthic organic carbon degradation and biogenic silica dissolution in the central equatorial Pacific, *Deep-Sea Res* 38(12), p. 1481-1516.
- Murray, J.W. and K.M. Kuivila (1990), Organic matter diagenesis in the northeast Pacific: Transition from aerobic red clay to suboxic hemipelagic sediments, *Deep-Sea Res* 37(1), p. 59-80.
- Nichols, J.A., C.L. Morgan and D. Pawson (1984), 'Megabenthos abundance in the Clarion-Clipperton region and possible coupling with surface productivity, unpublished report.
- Nisancioglu, K.H. (2003), Reorganization of Miocene deep water circulation in response to the shoaling of the Central American Seaway, *Paleoceanography* 18(1), p. 1006.
- ODP (2002), Preliminary Report of ODP Leg 199, Shipboard Scientific Party, 2002 – URL: [http://www-dp.tamu.edu/publications/prelim/199\\_prel/prel7.html](http://www-dp.tamu.edu/publications/prelim/199_prel/prel7.html)
- Pautot, G. and M. Hoffert (1984), *Nodules from the central Pacific in their geological environment. COPANO cruises 1979*, ArchiMer, Institutional Archive of IFREMERURL: <http://www.ifremer.fr/docelec/notice/1984/notice1144-EN.htm>
- Piper, D. Z. and J.R. Blueford (1982), Distribution, mineralogy and texture of manganese nodules and their relation to sedimentation at DOMES site A in the equatorial Pacific, *Deep-Sea Research* 29, p. 927-952.
- PMEL (2006a), URL: <http://www.pmel.noaa.gov/vents/acoustics.html>
- PMEL (2006b), URL: <http://autochart.pmel.noaa.gov:1776/autochart/GetPosit.html>
- Pope, R.H. et al. (1996), Rapid bioturbation in equatorial Pacific sediments: Evidence from excess  $^{234}\text{Th}$  measurements, *Deep-Sea Research II* 43(4-6), p. 1339-1364.
- Radziejewska, T. and V. Stoyanova (2000), Abyssal epibenthic megafauna of the Clarion-Clipperton area (NE Pacific): Changes in time and space versus anthropogenic environmental disturbance, *Oceanological Studies* 29(2), p. 83-101.

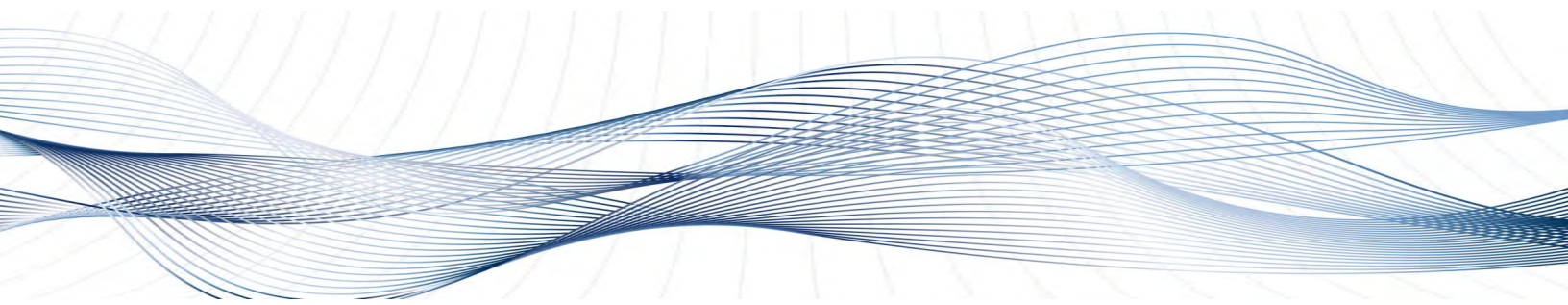
- Radziejewska, T., J. Rokicka-Praxmajer and V. Stoyanova (2001), 'IOM BIE revisited: Meiobenthos at the IOM BIE site 5 years after the experimental disturbance', Proc Fourth Ocean Mining Symposium, Szczecin, Poland, International Society of Offshore and Polar Engineers.
- Reimers, C.E. et al. (1984), Oxygen consumption rates in pelagic sediments from the Central Pacific: First estimates from microelectrode profiles, *Geochim Cosmochim Acta* 48, p. 903-910.
- Renaud-Mornant, J. and N. Gourbault (1990), Evaluation of abyssal meiobenthos in the eastern central Pacific (Clarion-Clipperton Fracture Zone), *Prog Oceanogr* 24, p. 317-329.
- Sclater, J.G., R.N. Anderson and M.L. Bell (1971), Elevation of Ridges and Evolution of the Central Eastern Pacific, *Journal of Geophysical Research* 76(32), p. 7888-7915.
- SIO (1976), *Preliminary Cruise Report of R/V Melville (Pleiades Expedition Leg 04 MN76-01)*, Prepared by The Manganese Nodule Project Coordinator's Office Scripps Institution of Oceanography La Jolla, California for the Manganese Nodule Project Seabed Assessment Program, IDOE-NSF Technical Report No. 15 December 1976, (ISA library.)
- Smith, C.R. et al. (1997), Latitudinal variations in benthic processes in the abyssal equatorial Pacific: control by biogenic particle flux, *Deep-Sea Research II* 44(9-10), p. 2295-2317.
- Smith, C.R. and A.W.J. Demopoulos (2003), 'The Deep Pacific Ocean Floor', in Tyler, P.A. (ed.), *Ecosystems of the Deep Oceans* 28, Elsevier Science, Amsterdam, Netherlands, p. 179-218.
- Smith, C.R. and C. Rabouille (2002), What controls the mixed-layer depth in deep-sea sediments? The importance of POC flux, *Limnol Oceanogr* 47(2), p. 418-426.
- Smith, K.L. (1987), Food energy supply and demand: A discrepancy between particulate organic carbon flux and sediment oxygen consumption in the deep ocean, *Limnol Oceanogr* 32(1), p. 201-220.
- Smith, K.L., R.J. Baldwin and P.M. Williams (1992), Reconciling particulate organic carbon flux and sediment community oxygen consumption in the deep North Pacific, *Nature* 359, p. 313-316.
- Smith, K.L., M.B. Laver and N.O. Brown (1983), Sediment community oxygen consumption and nutrient exchange in the central and eastern North Pacific, *Limnol Oceanogr* 28(5), p. 882-898.
- Snider, L.J., B.R. Burnett and R.R. Hessler (1984), The composition and distribution of meiofauna and nanobiota in a central North Pacific deep-sea area, *Deep-Sea Res* 31(10), p. 1225-1249.
- Ujiiie, H. (1984), A middle Miocene hiatus in the Pacific region: its stratigraphic and paleoceanographic significance, *Palaeogeography, Palaeoclimatology, & Palaeoecology*, 46(1-3), p. 143-146.
- Usui, A. et al. (1987), Local variability of manganese nodule facies on small abyssal hills of the central Pacific basin, *Mar. Geol.* 74, p. 237-275.
- Von Stackelberg, U. and H. Beiersdorf (1991), The formation of manganese nodules between the Clarion and Clipperton fracture zones southeast of Hawaii, *Mar. Geol.* 98, p. 411-423.
- Wilson, G.D.F. (1987), 'Crustacean communities of the manganese nodule province: DOMES Site A compared with DOMES Site C', Scripps Institution of Oceanography, La Jolla, CA, Report for the NOAA Office of Ocean and Coastal Resource Management (Ocean Minerals and Energy) on Contract NA-84-ABH-0030, 44 p.

Wilson, G.D.F. (1992), Biological evaluation of a preservational reserve area: Faunal data and comparative analysis, *Australian Museum*, Sydney, 60 p.

Wilson, G.D.F. and R. Hessler (1987), 'The effects of manganese nodule test mining on the benthic fauna in the North Equatorial Pacific', in Speiss, F.N. et al. (eds.), *Environmental Effects of Deep Sea Dredging*, SIO Reference Number 87-5, La Jolla, CA, Scripps Institution of Oceanography, p. 24-86.

Yubko B.M., B.B. Stoyanov, and I.M. Gorelik (1990), Geological structure and ore-bearing characteristics of the Clarion-Clipperton Zone of the Pacific Ocean, *Soviet Geology* 12, p.72-80. (In Russian).

## 12 GLOSSARY OF TECHNICAL TERMS



**10 Å-Manganate.** A general designation for manganese oxide minerals commonly found in deep seabed polymetallic nodules; one of which is todorokite. They are generally identified in a geological sample through a prominent 10- Å X-ray diffraction peak, diagnostic of the spacing ( $1 \text{ \AA} = 10^{-10} \text{ m}$ ) between sheets of  $\text{MnO}_2$  within the mineral structure.

**7 Å-Manganate.** A general designation for manganese oxide minerals commonly found in deep seabed polymetallic nodules; one of which is birnessite. They are generally identified in a geological sample through a prominent 7-Å X-ray diffraction peak.

**Abundance.** Areal density (usually with units of kilograms of nodules per square meter of seafloor) of polymetallic nodules on the seafloor.

**Abyssal.** Pertaining in general to the great depths of the oceans; specifically referring to 3,500 m to 6,000 m.

**Accuracy.** Describes the nearness of a measurement to the standard or true value. Usually contrasted with “precision”, which is a measure of the deviation of a measurement about an average value. Precision can be expressed as an error estimate, such as a standard deviation about an average value. Specification of accuracy requires an independent knowledge of what a true value should be beyond the measurement being made.

**Adsorption.** The assimilation of gas, vapor, or dissolved matter by the surface of a solid. In this context, the assimilation of dissolved metals onto small particles of sediment or plankton skeletal remains.

**Aerosol.** A suspension of fine droplets of liquid in a gas.

**Algorithm.** A specific set of computer instructions where succeeding terms are generated by application of formulas to preceding terms.

**Area or international seabed Area.** Defined in the Law of the Sea Convention as “the seabed and ocean floor and subsoil thereof, beyond the limits of national jurisdiction”. Exploration for and exploitation of mineral resources in the Area may only be carried out through the International Seabed Authority in accordance with the extensive provisions of the Convention and the rules, regulations, and procedures adopted by the Authority.

**Argillaceous.** Containing clay minerals.

**Amorphous Silica.** See “Opaline skeletons”.

**Average Value.** A number that typifies a set of values from which it is calculated. For example,

Arithmetic mean: Sum of the set values divided by the number of values used to calculate the sum.

Median: The number in the set of numbers that is less than half of the rest of numbers and greater than the other half (or the arithmetic mean of the two middle numbers, for a set size that is an even number).

**Benthic.** Of or pertaining to the immediate vicinity of the seafloor.

**Biogeochemical Model.** A predictive model that uses biological, geological and chemical concepts and processes to explain natural observations.

**Bioproductivity.** Primary productivity; the generation of organic matter through photosynthesis. In the deep ocean primary productivity is carried out almost exclusively by photosynthetic plankton.

**Bioturbation.** The mixing of seabed sediments through the actions of benthic animals. For example, sea cucumbers (holothurians) cause extensive bioturbation by ingestion and excretion of sediments to extract organic matter for nutrition.

**Birnessite.** One of the 7-Å manganate minerals.

**Calcareous Ooze.** Seafloor sediments composed primarily of the calcium carbonate ( $\text{CaCO}_3$ ) exo-skeletal remains of plankton.

**CCD.** Carbonate Compensation Depth; the depth within the ocean water column at which the rate of dissolution of calcium carbonate (a rate that increases with water depth) is balanced by the rate of calcium carbonate sedimentation. When the seafloor is below the CCD, long-term accumulation of carbonate sediments will not occur.

**CCZ.** Clarion-Clipperton Zone; the region of seafloor in the northeastern tropical Pacific Ocean bounded on the north by the Clarion Transform Fault, on the south by the Clipperton Transform Fault, on the east by the East Pacific Rise, and on the west by the Line Island chain. The largest accumulations of deep seabed polymetallic nodule deposits found to date are within this region.

**Chlorophyll in Surface Waters:** Concentration of chlorophyll-a pigment (units usually mg of chlorophyll per  $\text{m}^3$  of seawater). In the deep ocean, this concentration is directly proportional to the density of photosynthetic plankton in the water and therefore also directly proportional to primary productivity. It is estimated using color scanner measurements of the characteristic green pigment color intensity collected by satellites.

**Cobalt.** A metallic element (atomic number 27) found in polymetallic nodules. It is used in the formulation of high-strength steels and other specialty alloys.

**Confidence Level.** Statistical measure of the fraction of test results that can be expected to be within a specified range. For example, a confidence level of 95% means that the result of an action will probably meet expectations 95% of the time.

**Continental Runoff.** All dissolved and suspended materials carried into the ocean by rivers, streams, ground water, and storm water runoff. In this context, the runoff comes from the western side of the North American continent.

**Copper.** A metallic element (atomic number 29) found in polymetallic nodules. It is used extensively in construction for electric wire and in land-based exterior applications (structural roofs, rain gutters) that need to be resistant to weathering.

**Correlation.** A measure of statistical linear relationship between two paired variables. In this context we use the Pearson correlation coefficient ( $r$ ) for this measure. It is calculated as follows:

$$r = \sqrt{\frac{(\sum(x_i - m_x)(y_i - m_y))^2}{\sum(x_i - m_x)^2 \sum(y_i - m_y)^2}}$$

Where:

$x$  and  $y$  are the two variables, each of which is available for every sample included in the calculation;

$m_x$  and  $m_y$  are the arithmetic means of the two variables, and

$i$  is the number of cases (i.e. samples) for which both variables have been measured.

The value of the  $r$  coefficient varies between zero, indicating that there is no linear relationship observed between the two variables, and one, indicating that a scatter plot of the two variables plotted against each other will form a perfect line. The square of the Pearson correlation coefficient is called the “coefficient of determination,” and it can be shown mathematically that this coefficient (symbol commonly used: “ $R^2$ ”) represents the proportion of the total variance of one of the two variables that can be accounted for by the other.

**Crusts (Ferromanganese, Manganese, Cobalt).** Polymetallic hydroxide/oxide deposits that form on hard substrates (i.e. rocks, not sediments) on the seafloor. They consist mostly of manganese oxides and iron oxyhydroxides and are found with up to about 2% cobalt and smaller percentages of nickel, copper, and minor but significant concentrations of titanium, nickel, platinum, molybdenum, tellurium, cerium and other metallic and rare earth elements.

**Deterministic model.** A mathematical model in which outcomes are precisely determined through known relationships among states and events, without any room for random variation. In such models, a given input will always produce the same output, such as in a known chemical reaction. In contrast, stochastic models use ranges of values for variables in the form of probability distributions and generate series of probabilities for potential outcomes.

**Deviation.** Difference between an observed value and an expected one. A standard deviation is a particular estimate of this predicted difference between measured values and expected values (usually assumed to be some measure of the average value).

**Diagenesis.** Any chemical, physical, or biological change undergone by a sediment after its initial deposition. In this context it usually refers to the chemical and biological seafloor processes that transfer metals from the surfaces of sediment particles to the surfaces of polymetallic nodules.

**Dissolution.** The incorporation of materials from the solid state into a liquid. Generally in this context, it refers to solid materials dissolving in seawater.

**EPR.** East Pacific Rise; This geological feature bounds the CCZ on its eastern margin with a persistent, volcanic ridge. It separates the Pacific Plate to the west from (north to south) the North American

Plate, the Rivera Plate, the Cocos Plate, the Nazca Plate, and the Antarctic Plate. It runs from an undefined point near Antarctica in the south northward to its termination at the northern end of the Gulf of California in the Salton Sea basin in southern California. The geological classification for the EPR is a “spreading center” also called a “mid-ocean ridge.” Its volcanism generates the Pacific oceanic crustal rocks.

**Erosion.** The physical and chemical processes that wear down the landscape. In the ocean, benthic ocean currents can erode the seafloor, suspending and transporting fine-grained sediment particles and leaving behind larger sediments, rocks, and polymetallic nodules.

**Error Propagation.** When estimating a numerical value from a computation of measured variables, the uncertainty, or error, of estimation is a function of the uncertainties of the measured variables. That is, the errors associated with the variables used in the computation propagate into the error for the Statisticians have developed a series of methods for estimating the uncertainties of various calculated quantities, depending on the specific type of calculation. For example, if the value sought is a sum of two measured variables, then the estimate for the error for the calculated value is the square root of the sum of squares of the uncertainties for the two measured values.

**Error.** The uncertainty assigned to any measured variable, based usually on repetitive collections of measurements of the variable. A common error estimate is the standard deviation.

**Exploration Contractor.** An investor in deep seabed mining, which may be a State Party to the Law of the Sea Convention, a state entity, or any other entity having a legal personality and sponsored by a State Party, that holds a 15-year exploration contract with the International Seabed Authority granting exclusive rights for exploration for a specified class of mineral resource in a specified area of the international seabed Area. Currently (2009), contracts are held by qualifying entities from China, France, Germany, India, Japan, Republic of Korea, Russian Federation, and a consortium co-sponsored by Bulgaria, Cuba, Czech Republic, Poland, Russian Federation, and Slovakia.

**Fauna.** The animals living in any particular habitat. In the ocean, this term usually includes all non-photosynthetic organisms.

**Fecal Pellets.** Animal excretions. In the deep ocean, the fecal pellets from zooplankton (non-photosynthetic plankton) comprise an important mechanism for the removal of fine-grained materials from suspension in the water column to sedimentation on the seafloor.

**Flux (metals).** Generally, the transport of mass or energy through space. In this context, flux refers to the transport of Mn, Ni, Cu and other materials from surface waters or laterally distant locations to the seafloor where they are available for uptake into polymetallic nodules.

**Free-Fall Grab Sampler.** An un-tethered oceanographic tool used to collect samples of surface deposits on the seafloor. Free-fall grabs are deployed from research ships, usually sequentially in groups of four to six. They fall to the seafloor rapidly because of ballast weights that make them negatively buoyant. Contact with the seafloor triggers the closing of the sampler jaws and drops the ballast weights. With the loss of the ballast weights, floats in the sampler make it positively buoyant, and thus it then returns to the surface carrying its seafloor sample. Free-fall grab samplers were the primary tool used by Exploration Contractors to recover polymetallic nodules from the seafloor.

**Fuzzy Logic.** The term "fuzzy logic" emerged in the development of the theory of fuzzy sets by Lotfi Zadeh. A fuzzy subset A of a (crisp) set X is characterized by assigning to each element x of X the degree of membership of x in A (e.g., X is a group of people, A the fuzzy set of old people in X). Now

if  $X$  is a set of propositions then its elements may be assigned their degree of truth, which may be “absolutely true”, “absolutely false” or some intermediate truth degree: a proposition may be more true than another proposition. It is one of the techniques of soft-computing, i.e. computational methods tolerant to sub-optimality and imprecision (vagueness) and giving quick, simple and sufficiently good solutions.<sup>2</sup>

**Generation (Growth Stage).** A period of active accumulation of manganese oxide minerals, reflected in the nodule texture as a series of concentric, 0.5-3 cm thick, micro-laminae; each successive series overlays another and is distinctly separated from it, thus evidencing a hiatus in nodule growth; commonly in the CCZ, each nodule goes through three growth stages.

**Growth Rate.** The accumulation rate of material in polymetallic nodules, usually estimated as mm/ $10^6$  years of increasing thickness around the nucleus of the nodule.

**High-Grade Nodules.** Nodules in which the sum percentages of nickel, copper, and cobalt ( $\text{Ni} + \text{Cu} + \text{Co}$ ) is higher than 2.5%.

**Holocene.** The most recent geological Epoch including geological deposits that were deposited within the last 12,000 years.

**Hydrogenetic.** Forming directly from seawater; in this context it refers to the accumulation of metals in polymetallic nodules that come directly from seawater with no intermediate period spent in sediments.

**Hydrothermal.** Forming from hot fluids; in this context, it refers to metals that come from the leaching of rocks by hot fluids along spreading ridges. Seawater is heated up as it approaches magma at the spreading ridges and then it returns to the seafloor, where it is expelled into the ocean carrying relatively high concentrations of leached metals.

**Hydrothermal Plume.** An emission of relatively warm, metal-rich water (hydrothermal fluid) from the seafloor. Hydrothermal plumes are commonly produced near the East Pacific Rise, and evidence for their recent occurrence at some distance from the EPR is discussed in the Prospector’s Guide. Hydrothermal plumes generally have significantly elevated concentrations of manganese.

**International Seabed Authority.** The international organization established by the Law of the Sea Convention to organize and control all activities of exploration for and exploitation of mineral resources in the Area, including making due provision for protection and preservation of the marine environment from such activities. Established in 1994 upon entry into force of the Convention, the Authority currently (2009) have 160 members.

**Iron.** A metallic element (atomic number 26) found in polymetallic nodules. Iron is second the most common metal in the Earth’s crust (aluminum is the most common) and the primary component of steel. Its occurrence in polymetallic nodules is generally not considered to be economically interesting.

**Iron-Oxyhydroxide.** The main iron phase in nodules, which consists of iron oxide and hydroxide and is commonly written as  $\text{FeO(OH)}$ ; the most common types with regard to nodules are feroxyhyte and goethite.

---

<sup>2</sup> Stanford Encyclopedia of Philosophy; <http://plato.stanford.edu/entries/logic-fuzzy/>

**Kriging.** Refers to a group of techniques used to generate interpolated maps (i.e. assign values to places between sites where samples have been collected) describing the spatial coverage of some variable (e.g. nodule abundance or metal content) from relatively sparse data sets. Kriging techniques use spatial covariance (i.e. the observed relationships between different observations of the same variable collected at different distances apart from each other) to determine how to calculate the interpolated values.<sup>3</sup> Kriging techniques are commonly used by mining companies to assess resources from metal content estimates derived from cores or other samples.

**Manganese.** A metallic element (atomic number 25) found in polymetallic nodules. After iron, it is the most abundant transition metal in the Earth's crust. In the deep seabed nodule deposits, it is almost always the most common metal found in the deposit, reaching concentrations of greater than 30% in some deposits.

**Mid-Ocean Ridge.** Mid-Ocean Ridges are places where the Earth's tectonic plates are gradually moving apart, and as they do, magma rises up to fill the gap, sometimes leading to submarine volcanic eruptions. This shallow magma provides a heat source that creates many seafloor hot springs along the ridges which transport heat and chemicals into the ocean.<sup>4</sup> The East Pacific Rise is a mid-ocean ridge.

**Miocene.** A geological Epoch, pertaining to geological deposits formed between 5.3 and 23 million years before the present.

**Neural Network.** Inspired by the structure of the brain, a neural network consists of a set of highly interconnected entities, usually defined within a computer algorithm, called nodes or units. Each unit is designed to mimic its biological counterpart, the neuron. Each accepts a weighted set of inputs and responds with an output.

**Nickel.** A metallic element (atomic number 28) found in polymetallic nodules. It is currently believed to be the most commercially interesting metal in these deposits. It is used primarily in steel production, especially stainless steels.

**Nodule (Ferromanganese, Manganese, Polymetallic).** Deposits of manganese and other metal oxides that accumulate in deep seabed sedimentary environments as sub-spherical or discoid-shaped deposits. When individual nodules are cut into sections, they usually exhibit distinct, roughly concentric structures, strongly suggestive of growth rings in tree sections, which suggests an accretionary growth history at the surface of the nodule

**Nodule Growth.** The accumulation of metal oxides and entrained materials at the surface of polymetallic nodules.

**Nucleus.** The center of the concentric growth structures in a nodule, consisting in the CCZ deposits of a rock, a fragment of an older nodule, or some other hard substrate.

**Oligocene.** A geological Epoch, pertaining to geological deposits formed between 23 and 33.9 million years before the present.

**Opaline Skeletons.** Components of biogenic sedimentation, represented by radiolarian skeletons and diatom frustules.

<sup>3</sup> A good text book describing these techniques is Journel, A.G. and Huijbregts, C.J. 1978. *Mining Geostatistics*. Academic Press, London, 600 p.

<sup>4</sup> <http://www.pmel.noaa.gov/vents/geology/MOR.html>

**Oxygen Minimum Zone.** The Oxygen minimum zone is the zone in which oxygen saturation in seawater in the ocean is at its lowest, caused by the consumption of oxygen through oxidation of organic matter sinking through the water column. This zone occurs at depths of about 500 to 1,000 meters, depending on local circumstances. In the deep ocean, the presence of oxygen in the seawater is a remnant of when that water mass was located at or near the surface of the ocean. Most deep water masses have their origin in the seas around the Arctic or Antarctica, where oxygen-rich cold water sinks down and flows north or south. The oxygen in this abyssal water is no longer replenished after sinking down, since no photosynthesis can take place at these depths due to lack of sunlight and no exchange with the Earth's atmosphere is possible.

The oxygen content in deep water is dependent on the amount of oxygen it had when it reached that depth, minus depletion by deep sea organism metabolism or chemical oxidation processes. In the CCZ, in water depths above 500 meters, replenishment of oxygen by air and from photosynthesis is still possible, while below about 1,000 meters, there are too few organisms present to exhaust the supply.

**Pelagic Clay.** Seafloor sediments consisting primarily of fine-grained clay minerals, organic particles, and iron and manganese oxides. Clay minerals are the primary weathering products of rocks and include a variety of platy aluminum silicate minerals (e.g. illite, montmorillonite, chlorite and kaolinite).

**Permeability.** The capability of a porous rock or sediment to permit the flow of fluids through its pore spaces.

**Pioneer Investor.** An interim arrangement adopted by the Third United Nations Conference on the Law of the Sea that was designed to protect those entities that had already made a large investment in seabed mining. This so-called Pioneer Investor Protection regime allows a State, or consortium of mining companies, to be sponsored by a State and registered with the International Seabed Authority as a Pioneer Investor. Registration reserves for the Pioneer Investor a specific mine site in which the registered Investor is allowed to explore for, but not exploit, polymetallic nodules. Registered Investors are also obligated to explore a mine site reserved for the Enterprise and undertake other obligations, including the provision of training to individuals to be designated by the Preparatory Commission. Seven pioneer investors were registered: China, France, India, Japan, the Republic of Korea, the Russian Federation, and a consortium known as the Interoceanmetal Joint Organization (IOM).

**Plankton.** Animals and plants, generally microscopic, whose primary form of horizontal mobility is drifting with the ambient water body, though many plankton species exhibit daily vertical excursions. Phytoplankton are plants that generate organic matter through photosynthesis; zooplankton are animals that consume other organisms or organic detritus for their nutrition. Calcareous plankton form protective exoskeletons of calcium carbonate, while siliceous plankton have exoskeletons made of hydrated silica ( $\text{SiO}_2 \cdot n\text{H}_2\text{O}$ ).

**Polymetallic.** Containing more than one metal. Polymetallic nodules contain major concentrations (> 5%) of manganese and iron, minor concentrations (>0.1%) of nickel, copper, cobalt, and other metals, and trace concentrations of rare earths and many other metals.

**Poly-nodules.** Polymetallic nodules that appear to have more than one nucleating site.

**Porosity.** The percentage of void spaces containing seawater in rocks or sediments. If the void spaces are generally connected to each other, the material is also permeable.

**Precipitation.** Transformation of dissolved materials into solids.

**Precision.** A measure of the deviation of a measurement about an average value. Precision can be expressed as an error estimate, such as a standard deviation about an average value (see “Accuracy”).

**Prediction.** An estimate of values for variables of interest at sites where no sample data exist. If the prediction is made between existing sample stations, the prediction is also an interpolation; if not it is an extrapolation.

**Proxy.** A variable that is believed to indicate potential for the occurrence of deposits. Using proxy variables in modeling of deposit occurrence consists of determining or assuming a relationship between the variable and the deposit occurrence and using the values for the proxy variable to predict values for the deposit variables where sample data are not available.

**Quaternary.** The most recent Period in the geological time scale, including the Pleistocene and Holocene Epochs, and including the geological deposits formed approximately in the past 2.6 million years.

**Radiolaria.** Siliceous zooplankton species of the biological Order Radiolaria.

**Red-Brown Deep Sea Clay.** Deep seabed sedimentary deposits consisting primarily of clay minerals, organic particles, and iron and manganese oxides. These deposits are most common in the western and northwestern portions of the CCZ.

**Redox Boundary or Interface.** A level within a sediment column denoted by a relatively pronounced chemical gradient between sediment pore water rich in oxygen with pore water that is depleted in oxygen or other redox-sensitive species. Many metals are more stable in solution in oxygen-poor water than in oxygen-rich water. Thus, in the deep seabed, when pore waters flow from the oxygen-poor (low redox potential) to oxygen-rich (high redox potential) regions, dissolved metals, and particularly manganese, can precipitate to form manganese-oxide nodules.

**Regression.** Computational techniques that determine potential statistical relationships between paired variables (see “Correlation”).

**Reserved Area.** The UN Convention on the Law of the Sea requires each applicant for an exploration area to specify two areas of the seabed, estimated to be of equal commercial value. One of these is to be used for exploration by the applicant the other, the Reserved Area, will be held for future development by developing countries.

**Resource Estimation.** Methods of estimating the amount of mineral resources that occur within a specified area. This study uses kriging techniques to develop resource estimates for the polymetallic nodule resources within the CCZ.

**Scavenging.** The processes that effectively concentrate metals in polymetallic nodules. They include Adsorption and incorporation into the mineral matrix of the nodules.

**Seamount.** A seafloor elevation above the surrounding terrain that does not reach the sea surface.

**Sedimentation Rate.** The accumulation rate (e.g. millimeters of sediments per thousand years) of sediments of the seafloor.

**Semi-Liquid Layer.** Uppermost 1 to 10 cm thick and very soft layer of deep-sea sediments (siliceous clay to siliceous ooze) with very low shear stress values (0.2 to 2 kPa) and very high water content (75 to 85 %). The semi-liquid layer contains the major portion of benthic life and has a sharp transition to the sub-oxic deeper sediment layer. The mixed type and diagenetic polymetallic nodules rest, in general, in this layer.

**Significance Level.** A statistical estimate of the probability that a conclusion, based on the statistical analysis of observations, is true. The Chi-square, f- and t- statistics are all different methods of estimating the significance level for different situations.

**Siliceous Mud.** Seafloor sediments composed primarily of fine-grained biosiliceous materials.

**Siliceous Ooze.** Seafloor sediments composed primarily of fine-grained, biologically formed siliceous materials such as radiolarian tests and diatom frustules.

**Slope Failure.** The movement of bottom sediments caused by slopes that are too steep to be stable. This can be caused by erosion at the base of the slope or normal faulting. The result of slope failure on the seafloor is usually a flow of suspended sediments, called a turbidity flow.

**Smectite.** Used for a group of clay mineral, the most important of which are montmorillonite, beidellite, nontronite, saponite and hectorite. These and several other less common types are usually formed from the chemical weathering of volcanic rocks.

**Suboxic.** Refers to sediments where concentrations of oxygen and sulfide are both extremely low and show no perceptible gradients. Many scientists believe that much of the growth of polymetallic nodules occurs within suboxic sediments, commonly recognized to be <4.5 µM (about 0.1 ml/L) oxygen.<sup>5</sup>

**Thermocline.** The layer in the ocean in which temperature changes most rapidly with depth. The thermocline may be thought of as an invisible blanket that separates the upper mixed layer from the calm deep water below.

**Todorokite.** One type of 10-Å manganate.

**Transform Fault.** Locations in the seabed crust where two plates slide past one another. The fracture zone that forms a transform plate boundary is known as a transform fault. Most transform faults, such as the Clarion and Clipperton Fracture Zones, are found in the ocean basin and connect offsets in the mid-ocean ridges.

**Turbidity Flow.** A swift downhill flow of dense, sediment laden water, triggered by a slope failure and driven by the relatively high density of the sediment suspension compared with seawater. Turbidity flows can cause significant erosion and damage, similar to an avalanche on land.

**Types Of Nodules (E.G. Mixed Type Etc.).** Groupings of nodules similar in morphology (appearance, size, and the character of outer surface). The CCZ nodules are most commonly classified into three genetic types:

H (hydrogenetic) - small nodules [up to 4 cm in diameter; most frequently spheroidal and with smooth surfaces (S)]; the major Mn mineral is δ-MnO<sub>2</sub> (vernadite), present as Co-enriched amorphous phase; as a rule, the Mn/Fe ratio is lower than 3;

---

<sup>5</sup> Morrison et al. (1999) The oxygen minimum zone in the Arabian Sea during 1995. *Deep-Sea Res. II* 46: 1903–1931.

D (diagenetic) - large nodules [6-12 cm in diameter; predominantly discoidal and ellipsoidal in shape and with rough surfaces (R)]; the major Mn mineral is 10-Å manganate (todorokite), present as Cu+Ni-enriched crystalline phase; as a rule, the Mn/Fe ratio is higher than 5;

HD (hydrogenetic-diagenetic) - nodules intermediate in size, with smooth upper and rough lower surface (S+R), predominantly ellipsoidal, flattened, plate-shaped; the major Mn mineral is 7-Å manganate (birnessite), represented by variable proportions of amorphous and crystalline phases; the Mn/Fe ratio varies between 3 and 5.

**Variables.** Something that takes on different values that can be counted or measured. An independent variable is one that has values that are specified by measurements. A dependent variable is one that can be calculated from values of independent variables.

**Variogram.** A plot of the mean of the square of the differences between variable values measured at specified distances from each other. It is one way to display the spatial covariance of a variable and it is the primary tool used in kriging to weigh the values used to interpolate between measured locations.

**Vernadite.** A manganese oxide that occurs typically in land-based deposits and is similar to the marine mineral phase called  $\delta$ -MnO<sub>2</sub>, the phase that characterizes hydrogenetic precipitation. The crystallographers would call this phase turbostratically disordered hexagonal birnessite.

**Volcanogenic.** Forming as a result of volcanic activity.

As part of its mandate to conduct resource assessments of prospective mineral deposits in the Area, the Authority, together with its Contractors and their scientists, joined forces with a group of technical experts to establish and develop a Geological Model of polymetallic nodule deposits in the CCZ.

The primary product of this combined effort are a Geological Model of polymetallic nodule deposits in the Clarion Clipperton Zone; and a Prospectors Guide containing a narrative description of the key factors relevant to exploration for polymetallic nodules in the Clarion-Clipperton Zone together with data and available information on known deposits.

The Geological Model consists of a set of digital and hard copy maps and tables describing the predicted metal content and abundance of deposits in the Clarion-Clipperton fracture zone, along with associated error estimates.

The Prospector's Guide examines all potential proxy data variables identified as important indicators of metal content and abundance, and outlines specific data sets that qualify for use in the Geological Model and data information on all known nodule deposits in the Clarion-Clipperton Fracture Zone.

The area of interest for this study is 110° - 160° W Longitude and 0° - 20° North Latitude. The Authority's effort to mode the polymetallic nodule resources in the Clarion-Clipperton Fracture Zone, an area covering nearly 12 million square kilometers, is the largest and most complex undertaking to date.

ISBN 978-976-95268-2-2



9 789769 526822